2020

Structural Performance Evaluation of Dynamic Message Signs with Adhesive and Welded Joints

Ibin Amatya
South Dakota State University

STRUCTURAL PERFORMANCE EVALUATION OF DYNAMIC MESSAGE SIGNS WITH ADHESIVE AND WELDED JOINTS

BY

IBIN AMATYA

A thesis in partial fulfillment of the requirements for the

Master of Science

Major in Civil Engineering

South Dakota State University

2020

THESIS ACCEPTANCE PAGE

Ibin Amatya

This thesis is approved as a creditable and independent investigation by a candidate for the master's degree and is acceptable for meeting the thesis requirements for this degree. Acceptance of this does not imply that the conclusions reached by the candidate are necessarily the conclusions of the major department.

Advisor Date

Nadim Wehbe
Department Head Date

Dean, Graduate School Date

ACKNOWLEDGEMENTS

I would like to thank Dr. Junwon Seo for being my advisor. I highly appreciate his professional guidance and encouragement for my research work. His continued motivation always encouraged me to be productive and sincere towards my study and research. I am grateful to Dr. Seo for all the supervision provided by him for all the written work relating to this research. I would also like to thank Dr. Burckhard and Dr. Letcher for being part of my thesis committee.

I would like to thank Daktronics, Mountain-Plains Consortium, and United State DOT for sponsoring the research. I would like to acknowledge the Project Committee: Dan Bierschbach, Toby Pulscher, Jeff Haliburton, John Syrstad, and Eric Johns at Daktronics for their invaluable comments and support for this work. I am also grateful to Dr. Todd Letcher for his help with the small-scale testing and to Mr. Gutzmer for his guidance over the full-scale testing of dynamic message signs (DMS). I would like to thank my research colleagues Brian Kidd and Euiseok Jeong for all their help in my research.

I would like to express love for my my wife Anisha Dangol, who was always supportive and kind during this research. I would like to thank my parents Guru Das Amatya and Indira Amatya, my sister Isha Amaya, and my brother-in-law Pradeep Raj Regmi for their continuous love, support, and encouragement during my studies. I would like to provide special thanks to Dinesh Shrestha, Sujan Parajuli, Sandip Rimal, Bikash Khanal, Puskar Dahal, Kush Thaiba, and Sandip Ojha for their guidance and supports during my graduate school journey.

TABLE OF CONTENTS

LIST OF FIGURES

LIST OF TABLES

ABSTRACT

STRUCTURAL PERFORMANCE EVALUATION OF DYNAMIC MESSAGE SIGNS WITH ADHESIVE AND WELDED JOINTS

IBIN AMATYA

2020

The ultimate objective of this study was to determine the structural performance of the Dynamic Message Sign (DMS) bonded with chemical adhesive in terms of ultimate strength and fatigue strength. To achieve this objective, this study first investigated the effects of various parameters, including humidity and temperature on tensile, shear, peel, and cleavage strength through small-scale tests of adhesive specimens with variation in specimen width. The tensile, shear, peel, and cleavage specimens were conditioned in a temperature-humidity controlled chamber prior to its testing. The tensile, shear, peel, and cleavage specimens with different widths were tested according to American Society for Testing and Materials (ASTM) after conditioning them in different temperature and humidity conditions. Numerous data resulting from the tests were analyzed through graphical comparisons and statistical analysis, in order to explore the effect of the considered parameters on each of the strengths. As part of the statistical analysis, two separate regression models, Multiple Linear Regression (MLR) and Response Surface Metamodels (RSM), were developed. It was found that humidity and width were the most significant parameters negatively affecting the tensile and peel strength, respectively. The MLR and RSM regression models developed in this study can be used for the prediction of tensile, shear, peel, and cleavage strength of the adhesive joints for different

temperature and humidity conditions that aid the design of adhesive joints in the DMS. Welded specimens were also tested at the same condition as in the adhesive specimen testing, and the results were compared with those from the adhesive testing. In addition to the small-scale tests, four full-scale DMS tests were performed to examine their structural performance. Specifically, the ultimate strength testing was carried out on one DMS with adhesive joints and one with typically welded connections, and the fatigue testing was also conducted for one DMS system with adhesive joints and one with welded connections. For the ultimate strength testing, a monotonic loading was applied to each DMS until failure, whereas for the fatigue testing, each of the DMSs were applied by a load of 0.818 kN equivalent to natural wind gust up to 500,000 cycles. The ultimate strength testing demonstrated that the adhesive DMS failed at 125 kN, while the weld DMS failed at 146 kN. During the fatigue test, stress ranges observed in the panel were much below the threshold of the aluminum panel of the DMS. No sign of damage was observed in both adhesive and welded DMSs from the fatigue tests. The results indicated that DMS with adhesively bonded connections is relatively better than welded DMS with respect to the stress induced in the aluminum panel.

INTRODUCTION

An adhesive has the potential to increase the production of Dynamic Message Signs (DMSs) due to its efficient applications, less labor work, and the ability to join different metals. The majority of the clients such as State Departments of Transportation prefer welded connections for connecting the aluminum back-skin with the frame of the DMS. The adhesive is a decent alternative to join lightweight metals with different melting points. In adhesive joints, loads are more homogeneously distributed than in welded joints. Different complexities such as difficulties in joining irregular seams and panel distortion (Tsai et al. 1999) have been observed in the course of manufacturing of welded connections. Further, the probability of noticing residual stresses and distortion is also high in welded connections. Even with such high potential of adhesive joints, limited experimental studies (Çolak et al. 2009, Agarwal et al. 2014, Savvilotidou et al. 2017, Kim et al. 2012, Goglio and Rezaei 2014, Silva et al. 2016, Sousa et al. 2018, Moussa et al. 2012, Da Silva et al. 2009, Neto et al. 2012) have been carried out to study the adhesive joint performance of DMSs.

To further examine the structural performance of DMS with adhesive joints, this study conducted small- and full-scale testings. For the small-scale testing, an experimental program was initially designed to examine the tensile, shear, peel, and cleavage strength of the adhesive and welded specimens at different temperature and humidity conditions. All the specimens with different specimen widths were tested according to American Society for Testing and Materials (ASTM) after conditioning them in different temperature and humidity conditions. Note, the welded specimens were

fabricated following the guideline from American Welding Society (AWS). Numerous data resulting from each of the small-scale tests were analyzed through graphical comparisons and statistical analysis, so as to investigate the effect of the temperature, humidity, and width on the tensile, shear, peel, and cleavage strengths. As part of the statistical analysis, Multiple Linear Regression (MLR) and Response Surface Metamodels (RSM) for adhesive specimens were utilized not only to determine statistically significant parameters (i.e., temperature, humidity, and width) affecting the strengths, but also to develop separate regression models for each of the strengths.

Apart from the small-scale testing, the full-scale load testing was conducted with DMSs. In detail, one DMS with adhesive joints and one with welded connections were tested to examine the ultimate strength, whereas one DMS with adhesive joints and one with welded connections were utilized to perform their fatigue testing. The full-scale testing setup and instrumentation plans were developed that were identical for all the tests. A network of strain and deflection gauges was installed to record strains and displacements when loaded to ultimate load failure and under fatigue load conditions.

RESEARCH OBJECTIVES

The goal of this study is to provide comprehensive knowledge of the structural behavior of DMSs with adhesive joints and welded connections subjected to ultimate and fatigue loads. The following objectives are designed to achieve this goal as follows:

1. Study the effects of environmental and geometrical characteristics on joint performance of adhesive and welded small-scale specimens.

2. Examine the ultimate strength and fatigue performance of DMSs with adhesive connections

3. Compare the structural performance between adhesive bonded DMSs and welded DMSs.

SCOPE OF RESEARCH

To achieve the aforementioned objectives, the scope of work can be listed as follows:

- Literature review of the state of the art and practice on adhesive joints.
- Small-scale testing and data investigation for adhesive specimens.
- Comparison with small-scale testing data of welding specimens.
- Ultimate load and fatigue testing of full-scale DMS systems
- Full-scale testing data analysis.

OUTLINE OF THESIS

This thesis is divided into five different chapters, assembling five different research papers, investigating the strength of adhesive connection in DMSs and comparing the results with that of welded connections. Chapter 1 presents the tensile and shear testing results obtained from small-scale testing of the adhesive specimens that were performed incorporating three different parameters including conditioning temperature, conditioning humidity, and specimen's width. Chapter 2 details the peel and cleavage strengths of the adhesive specimens that were also tested with variation in conditioning temperature, conditioning humidity, and specimen's width. Chapter 3 provides a detail comparison of the tensile and shear strengths of the welded and adhesive specimens. Adhesive and welded specimens with different widths were also tested after conditioning at extreme high and extreme low temperature. In Chapter 4, peel and cleavage strength of the welded specimens is compared with the peel and cleavage strength of the adhesive specimens with variation in conditioning temperature and specimen's width. Chapter 5 presents the results and discussion on the ultimate strength tests and fatigue load tests conducted for full-sized adhesive and welded DMSs.

CHAPTER 1: TENSILE AND SHEAR STRENGTH TESTS WITH ADHESIVE CONNECTIONS IN DYNAMIC MESSAGE SIGNS

1.1 ABSTRACT

A Dynamic Message Sign (DMS) is made up of a display, cabinet sheet aluminum skin, and internal structure along with electrical components. The aluminum skin is connected to the internal structure usually with a welded connection; however, adhesive or chemical bonding can be used instead for the connection between these two components. The goal of this paper is to examine the tensile and shear strengths along with other mechanical properties of adhesives used in the DMS under varying environmental and geometrical conditions. Adhesive tensile and shear specimens with different widths were tested according to the American Society for Testing and Materials (ASTM) standards after conditioning them in different temperature and humidity conditions. Numerous data resulting from the tests were analyzed through graphical comparisons and statistical analysis, so as to explore the effect of the considered parameters on tensile and shear strengths. As part of the statistical analysis, Multiple Linear Regression (MLR) and Response Surface Metamodels (RSM) were utilized not only to determine statistically significant parameters affecting the strengths, but also to develop separate regression models for the tensile and shear strengths. Key findings revealed that an increase in humidity decreases the tensile strengths. The MLR and RSM model-based analysis also found humidity to be the most significant parameter negatively affecting the tensile stress. Finally, this work found adhesive or chemical bonding to be a possible substitute to welding for assembly of the DMS.

Keywords: DMS, Strength, Aluminum; Adhesive; Connection, Statistical analysis.

1.2 INTRODUCTION

A Dynamic Message Sign (DMS) is a digital sign that provides real-time traffic information to road users during traveling. The use of DMSs has been rapidly increasing since it is the most convenient way to deliver useful information to the commuters such as road closures, service stations, and rest areas. A DMS is conventionally fabricated with thin aluminum skins and internal frame structure. The most common connection used in the DMS assembly is a weld connection. However, some manufacturers have started using adhesive for the connection between the back-skin and frame of the DMS. Due to efficient applications, less labor work, and ability to join different metals, adhesives are becoming popular with these manufacturers. An adhesive is a decent alternative to join metals with different melting points (Sakiyama et al. 2013). In adhesive joints, loads are more homogeneously distributed than in welded joints (Chapman 2010). Different complexities are observed in welding in the course of manufacturing like difficulties in joining irregular seams. Further, the residual stresses and distortion are found to be higher in welded connections. Even with such high potential of adhesive joints, limited experimental studies have been carried out to study the performance of adhesive joints for DMSs.

Inconsistent research results on adhesive have restricted its potential in DMSs. The strengths of the adhesive have been investigated to a great extent to understand the effects of moisture (Colak et al. 2009, Agarwal et al. 2014, Savvilotidou et al. 2017, Kim et al. 2012). Colak et al. (2009) indicated that the strength of the adhesive was reduced the most during the formation of the bond under saturated conditions. A directly proportional

relationship was found between strength reduction and the amount of moisture absorbed. Agarwal et al. (2014) studied the effects of freeze-thaw cycles on the adhesive connection of steel-carbon fiber reinforced polymer joints. Single-lap shear specimens were tested and a reduction in shear strength between 12-18% was found after freeze-thaw cycles. The elastic modulus was decreased by 14-19% when tensile specimens entirely made of adhesive were tested; however, the tensile strength was not changed considerably. Savvilotidou et al. (2017) investigated the adhesives to observe the effects of moisture. The results found a reduction in elastic modulus and tensile strength due to humidity after saturation when submerged in water. The adhesive bonded joints were studied by Kim et al. (2012) for shear strength using double-lap joint specimens after repeated freeze-thaw cycles. A slight increase in shear strength was found due to further curing of the adhesive as a result of moisture.

Several studies (Lettieri and Frigione 2011, Goglio and Rezaei 2014, Silva et al. 2016 Sousa et al. 2018, Moussa et al. 2012, Na et al. 2017, 2016) have been performed to evaluate the combined effects of temperature and moisture on the bond strength of adhesive. Lettieri and Frigione (2011) tested three different epoxy adhesives and had varying results between them. It was observed that flexural strength and modulus were increased in one adhesive, while a decrease in strength with no change in modulus was observed in the next, and the final had a decrease in both. Goglio and Rezaei (2014) conditioned the specimens at 100% relative humidity and 50° C for five weeks to study the effects of warm temperatures and moisture on mechanical properties of epoxy adhesives. It was reported that tensile strength was reduced by 75% before failure, while the modulus of elasticity and shear modulus were reduced by 20%. Silva et al. (2016)

studied the effects of thermal cycles (-15° C to 60° C) and immersion in water on adhesives. The thermal cycles resulted in an increase in tensile strength and modulus of elasticity, but the exposure to water resulted in decreases in tensile strength and modulus of elasticity due to plasticization. Sousa et al. (2018) studied the effects of moisture and temperature on the durability of adhesives, demonstrating that the shear modulus decreased by 43%, but the shear strength increased by nearly 25% due to immersion in water. Moussa et al. (2012) subjected a structural adhesive to temperatures above the glass transition temperature and found that a slight increase in tensile stiffness and strength was observed. Na et al. (2017) tested adhesive tensile dog-bone specimens at −40° C, room temperature, and 90° C. The increment in temperature reduced the modulus of elasticity, tensile strength, and failure strain. Na et al. (2016) further investigated the effect of seven different temperatures ranging from -40° C to 90° C on the tensile and shear strength of automotive polyurethane adhesive. Increase in temperature lowered both tensile and shear strength of the adhesive joint. Da Silva et al. (2009) found that lap shear strength was improved almost linearly with the increase in overlap length contributing 45.5% of the lap shear strength, and Neto et al. (2012) demonstrated that in ductile adhesive, the increase in overlap length increased the failure load consistently for the overlap length tested between 10 mm to 80 mm. Banea et al. (2015) examined structural polyurethane adhesive to determine the influence of adhesive thickness on the mechanical behavior of adhesive. Double-cantilever beam tests were performed for adhesive layer varying between 0.2 mm to 2 mm thickness. The lap shear strength was observed to be decreased, while fracture toughness was increased with the increase in thickness of adhesive layer.

The aforementioned studies have shown that temperature and moisture can affect the strength and durability of adhesives; however, the severity of the effects due to these parameters has not been conclusive. The variance between studies can be attributed to the difference in chemical composition between adhesives. It is also important to note that many of these studies have subjected the adhesives to extreme conditions unlikely to be seen in practice. For example, most DMS applications would rarely be immersed in water, especially for extended periods, and high humidity conditions are generally intermittent. Therefore, the effects of practical exposure to moisture and temperature should be graphically and statistically researched at or slightly above expected service conditions for individual adhesives to measure its performance. In addition to the moisture and temperature conditions, adhesive joints are required to be examined with variation in geometry such as overlap length and width. The application of overlap length is not practical for tensile specimens; therefore, width of both tensile and shear specimens is consistently considered for the variation in geometry in this study.

This paper aims at establishing an experimental program to investigate the tensile and shear strengths of adhesively bonded connections along with other mechanical properties, such as modulus of elasticity and ductility. Tensile and shear specimens were tested to failure at different environmental and geometrical conditions. 64 adhesive specimens, including 32 tensile and 32 shear specimens, were tested according to the American Society for Testing and Materials (ASTM) Standards (ASTM 2014, 2010).

1.3 BACKGROUND FOR STATISTICAL ANALYSIS

Statistical analysis was performed for evaluation of tensile and shear testing data in an efficient manner. To that end, Multiple Linear Regression (MLR) and Response Surface Metamodels (RSM) were utilized in this study for the determination of significant parameters affecting tensile and shear strength. Note, MLR (Seo and Pokhrel 2019, Kokaly and Clark 1999) and RSM (Seo and Linzell 2010, 2012, 2013) models have been used in previous studies to investigate the effect of different input parameters on outputs such as structural or mechanical behaviors. A well-organized set of input parameters, temperature, humidity, and width of specimen was required in order to generate the statistical models. During the analysis, probability values were acquired for each parameter per model. Based upon the probability values, significant parameters affecting the tensile and shear strength were identified. The better fit model can be used for the prediction of response variable (tensile and shear strength) within distinct range of input parameters.

1.4 EXPERIMENTAL PROGRAM

The experimental program was designed to study the results of tensile and shear tests at different widths and temperature and humidity conditions. This section discusses the specimens, testing matrix and conditioning, manufacturing, and testing necessary for the determination of the ultimate shear and tensile strengths and other mechanical properties.

1.4.1 SPECIMENS

Tensile and shear specimens were fabricated based on ASTM D638 (ASTM 2014) and ASTM D1002 (ASTM 2010), respectively. The bone-shaped tensile specimens were entirely made up of LORD 406-19GB (LORD Corporation 2018) acrylic adhesive. The

shear specimens were built with two 5052 aluminum metal bars having 1.62 mm thickness bonded with the same LORD acrylic adhesive at the overlap in the middle of each specimen. An extra aluminum piece was added to each of the shear specimens to facilitate efficient installation of an extensometer. The specimens were left for two weeks to ensure proper curing of the adhesive after conditioning. The geometry of representative tensile specimen is shown in Figure 1.1a and Figure 1.1b, whereas geometry of representative shear specimen is shown in Figure 1.1c and Figure 1.1d, correspondingly. The width of both tensile and shear specimens is defined as W with tolerance of ± 0.5 mm for tensile and ± 0.254 mm for shear specimens. In this study, tensile and shear specimens having width (W) 13 mm, 25 mm, and 38 mm are considered.

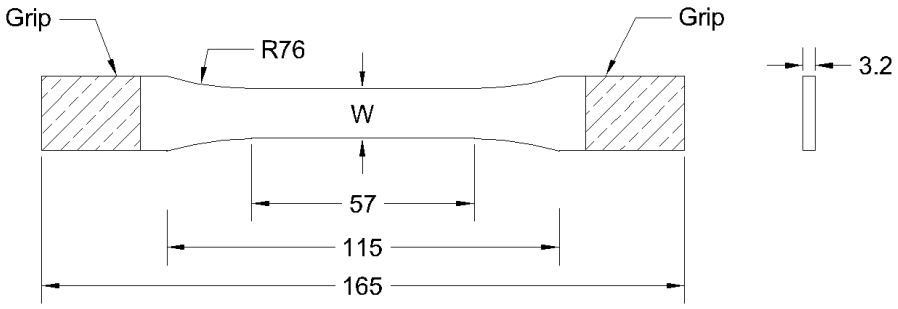

(a) (b)

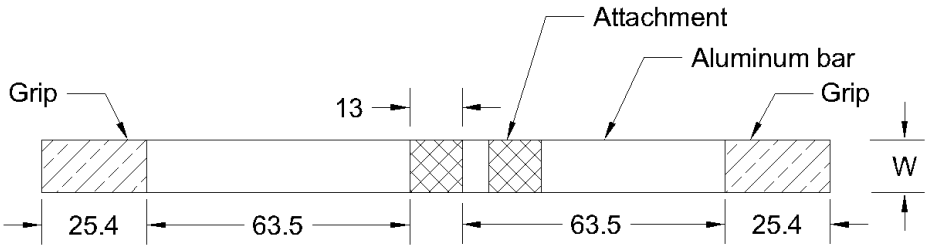

(c)

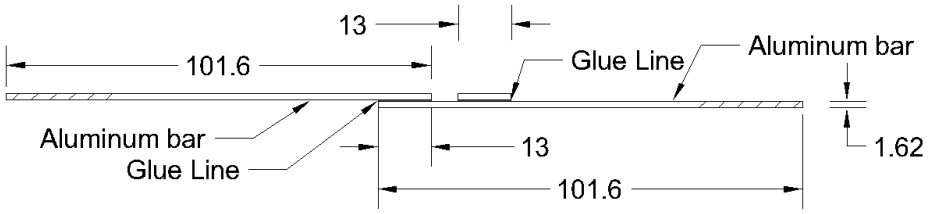

(d)

Figure 1.1: Geometry of adhesive specimens (a) top view of tensile; (b) cross-section of tensile dog bone; (c) top view of shear and (d) side view of shear (All dimensions are in mm).

1.4.2 TESTING MATRIX AND CONDITIONING

To study the performance of the adhesive connection, sixteen different combinations comprising different parameters were developed using Plackett-Burman Design (PBD) (Seo 2013, Chandorkar et al. 2008, Seo and Linzell 2013) through JMP, commercially available statistical software (SAS Institute Inc. 2008). Note, PBD was used to develop statistical models in an efficient manner. Included in the parameters were temperature, humidity, and width of the specimens. These parameters were considered inputs for statistical analysis. The combinations consisted of a low, medium, and high value for each of the considered input parameters. For example, three different widths of 13 mm, 25 mm, and 38 mm were used to account for variation in geometry of the specimens. The developed sixteen combinations with three different values for each parameter can be seen in Table 1.1. It consists of five combinations with 13 mm width, six combinations with 25 mm width, and five combinations with 38 mm width specimens. Note, each combination consisted of two tensile specimens and two shear specimens; thus, the total number of specimens was 64, including 32 tensile and 32 shear specimens.

Table 1.1 Testing specimen combinations with different temperature, humidity, and width

Combination	ID	Temperature (°C)	Humidity (%)	Width (mm)
C1	20T/48H/13W	20	48	13
C2	20T/48H/38W	20	48	38
C3	20T/71H/25W	20	71.5	25
C4	20T/95H/13W	20	95	13
C5	20T/95H/38W	20	95	38
C6	52T/48H/25W	52.5	48	25
C7	52T/71H/13W	52.5	71.5	13
C8	52T/71H/25W	52.5	71.5	25
C9	52T/71H/25W	52.5	71.5	25
C10	52T/71H/38W	52.5	71.5	38
C11	52T/95H/25W	52.5	95	25
C12	85T/48H/13W	85	48	13
C13	85T/48H/38W	85	48	38
C14	85T/71H/25W	85	71.5	25
C15	85T/95H/13W	85	95	13
C16	85T/95H/38W	85	95	38

The specimens per combination were conditioned in a temperature and humidity-controlled chamber as seen in Figure 1.2a. Specifically, the specimens grouped with the same humidity, yet different temperatures were first conditioned at the lowest temperature of the group for 96 hours for its moisture saturation. Then, the combinations conditioned at the lowest temperature among the group were first taken out of the chamber for the test, and the temperature was increased up to the next lower temperature to condition the remaining specimens for additional 24 hours. For example, the specimens for the combinations C1, C2, C6, C12 and C13 were placed inside the chamber at 20°C and 48% humidity. The specimens for combinations C1 and C2 were taken out for test after conditioning for 96 hours and the temperature of the chamber was increased to 52.5°C for the remaining specimens. The specimens for combination C6 were taken out of the chamber for testing after conditioning for additional 24 hours and

the temperature of the chamber was again increased to 85°C for the specimens with combination C12 and C13. The remaining specimens were tested after conditioning for additional 24 hours. The humidity was kept constant at 48% throughout this period. The specimens conditioned at 20°C, 52.5°C, and 85°C were conditioned for 96, 120, and 144 hours, respectively. To observe the change in moisture, the specimens were weighed prior to conditioning, after conditioning, after transporting to the lab and after testing. Mylar bags were used to minimize any loss of humidity during transportation of the specimens from the conditioning lab to the testing lab. The specimens were transported in a thick Styrofoam (see Figure 1.2b) cooler to prevent the loss of heat after taking the specimens out of the chamber. Temperatures were recorded after transporting the specimens to the lab and after the test for each of the specimens.

Change in moisture and temperature for both tensile and shear specimens were calculated. Note, changes in moisture between before and after conditioning phases, between after conditioning and after transporting phases, and after transporting and after the testing phases were calculated. The change in moisture for the tensile and shear specimens remained below 1.015% and 2.086%. It appears that there is insignificant change in moisture for the majority of the specimens during each of the three phases. Change in temperature was calculated by comparing the temperature measured after it was transported to the lab and after the test was completed. For the tensile specimens, change in temperature was observed below 9.6%, 41.5%, and 43% for specimens conditioned at 20°C, 52.5°C, and 85°C, respectively. For the shear specimens, change in temperature was observed below 12%, 30%, and 48.3% for the specimens conditioned at 20°C, 52.5°C, and 85°C, respectively. The specimens conditioned at higher temperatures

showed a greater loss in temperature than those conditioned at lower temperatures due to the difference in ambient conditions during the shear or tensile testings.

(a) (b)

Figure 1.2: Conditioning of the specimens (a) temperature-humidity controlled chamber and (b) styrofoam cooler

1.4.3 MANUFACTURING

For the fabrication of tensile specimens shown in Figure 1.1a and Figure 1.1b, moulds having appropriate dimensions were prepared from acetal material first. The moulds were filled with LORD acrylic adhesive and covered with thin metal from the top. Accurate weights were placed on the metal to acquire proper thickness of the tensile specimens. The tensile specimens were left to cure at room temperature and humidity for two weeks. Minimal voids were observed in some specimens during the fabrication, however, the tensile specimens with no external voids were only considered for the study. To make shear specimens, aluminum metal bars were cut with appropriate dimensions. LORD acrylic adhesive was spread over 13 mm length at the end of one aluminum bar and overlapped by another aluminum bar with 13 mm overlap length for each shear specimen. An average thickness of 0.385 mm was maintained for adhesive layer of shear specimens

by applying pressure after spreading the adhesive in aluminum surface. During installation of the extensometer in shear specimens in preliminary tests, the extensometer could not be installed in a vertical alignment parallel to the shear specimen. Therefore, an extra aluminum piece was added to ensure the proper installation of the extensometer. The extensometer was mounted at the overlap area of the shear specimen for the calculation of strain value.

1.4.4 TESTING

Tensile and shear tests with each specimen were performed using an MTS 370 Landmark (MTS Systems Corporation 2018) 100-kN servo-hydraulic load unit calibrated to 20% of its load capacity. Each specimen was mounted and aligned in the grips of the MTS. An MTS 634.31F-24 clip-on extensometer with a gauge length of 20 mm was mounted to each of the specimens to measure the longitudinal strains of the specimens during each test. Note, the extensometer was a class B2 calibrated with an accuracy of ±0.25% of measured strain. The tests were performed under a monotonic loading with a free crosshead speed of 5 mm/min for the tensile specimen following ASTM D638 (ASTM 2014) and 1.3 mm/min for the shear based on ASTM D1002 (ASTM 2010). The testing setups for the tensile specimen and for the shear specimen are shown in Figure 1.3a and Figure 1.3b, respectively. It should be noted that all the tests were performed at room temperature.

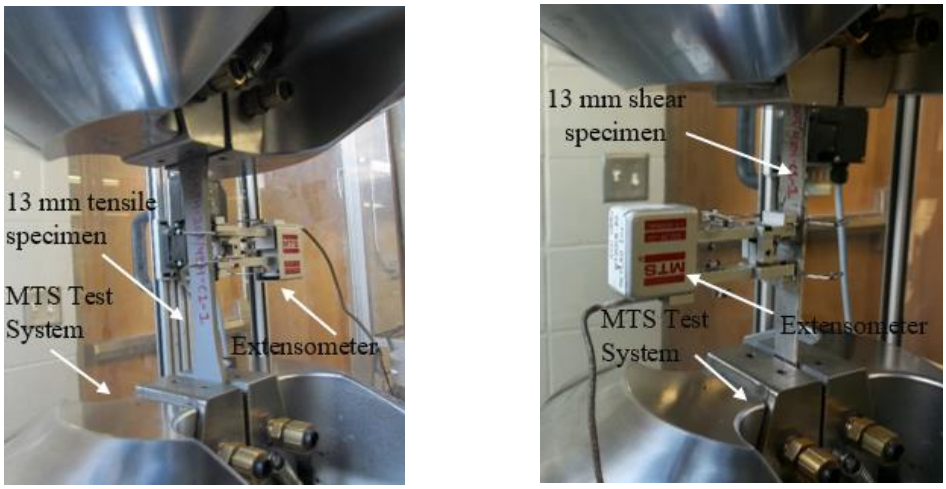

(a) (b)

Figure 1.3: Installation of the specimens in the testing machine (a) tensile and (b) single-lap shear

1.5 RESULTS AND DISCUSSION

Results from the tensile and shear tests are summarized and discussed herein. Stress-strain curves were plotted for each of the tests along with the determination of various mechanical properties such as strength.

1.5.1 TENSILE TESTING DATA

Stress-strain curves for the tensile specimens are presented in Figure 1.4. Mechanical properties encompassing ultimate stress, modulus of elasticity, and ductility are determined from the stress-strain curve. The calculated mechanical properties at varying environmental and geometrical parameters are summarized in Table 1.2. The ultimate tensile stress and tensile strain were calculated from the Equation 1.1 and Equation 1.2 presented below. Ductility is calculated as percentage of elongation of the specimen at rupture or breaking point.

$$f_u = {}^{P_u}/_{A} \qquad \text{(Equation 1.1)}$$

$$\varepsilon = {}^{\Delta l}/_{l_0} \qquad \text{(Equation 1.2)}$$

where f_u is ultimate tensile stress, P_u is ultimate tensile load, A is cross-sectional area of the tensile specimen, ε is tensile strain, Δl is change in extensometer gauge length, and l_0 is initial extensometer gauge length.

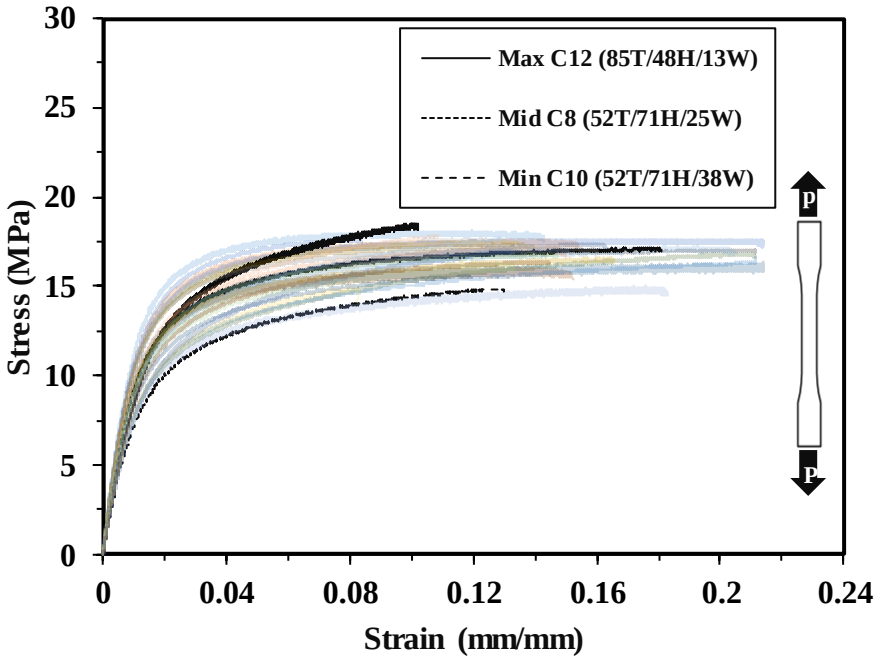

Figure 1.4: Stress-strain curves for tensile specimens

Table 1.2 Mechanical properties from the tensile tests

ID	Modulus of elasticity, E (MPa)	Ultimate tensile stress, f_u (MPa)	Ductility, e (%)
20T/48H/13W	1339.49	17.9	14.81
20T/48H/38W	1303.06	17.6	13.02
20T/71H/25W	1289.87	17.6	14.86
20T/95H/13W	1227.73	16.2	18.34
20T/95H/38W	1227.02	17.2	17.55
52T/48H/25W	1025.97	17.1	18.79
52T/71H/13W	971.62	17.3	17.74
52T/71H/25W	1075.74	17.1	16.45
52T/71H/25W	1081.75	17.0	14.91
52T/71H/38W	888.87	15.7	17.08
52T/95H/25W	1279.08	16.9	16.29
85T/48H/13W	896.23	17.8	11.75
85T/48H/38W	1261.39	17.8	11.93
85T/71H/25W	932.76	16.1	11.31
85T/95H/13W	1029.21	15.7	15.79
85T/95H/38W	1010.92	16.0	13.19

Representative failure modes of the tensile specimens are shown in Figure 1.5. During the test, all tensile specimens failed with rupture with no sign of necking. The rupture in all the tested specimens was observed to be almost perpendicular to the loading direction as depicted in Figure 1.5a and Figure 1.5b.

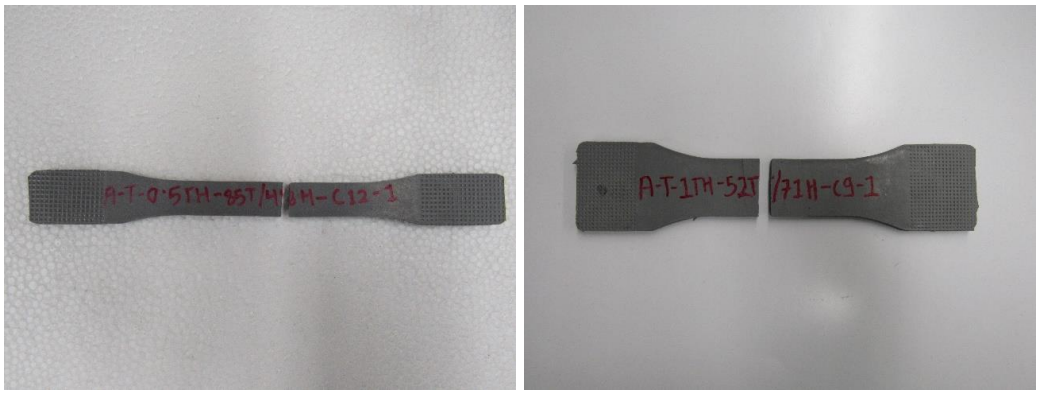

(a) (b)

Figure 1.5: Representative failure modes of tensile specimens (a) 13 mm and (b) 25 mm

1.5.1.1 EFFECT OF TEMPERATURE

An effort has been made to understand the effect of temperature on the ultimate tensile stress as shown in the graphical representation in Figure 1.6. In addition to the tensile stress examination, the other mechanical properties focusing on ductility were investigated. Ductility is a crucial property of the adhesive in the structural system of DMS. The effect of temperature on the ultimate tensile stress and ductility in terms of the percent difference between combination pairs is further examined using a bar chart as seen in Figure 1.7. For specimens of 13 mm width, the stress is reduced by 0.4% at 48% humidity and 3.3% at 95 % humidity, respectively when the temperature is increased from 20 °C to 85 °C as shown in pairs C1-C12 and C4-C15 in this figure. At 71.5 % humidity, when the temperature is increased from 20 °C to 52.5 °C, the stress declines by 2.9 % for 25 mm specimens. The stress decreases by 5.7 % after the temperature rises from 52.5 °C to 85 °C as displayed in pairs C3-C8 and C8-C14 in this figure. The stress is increased by 0.8 % at 48 % humidity, however, decreased by 7.2 % at 95 % humidity

for specimens of 38 mm width after the elevation of temperature to 85 °C from 20 °C as depicted in pairs C2-C13 and C5-C16.

For 13mm wide specimens, ductility declines by 20.7% at 48% humidity and 13.9% at 95% humidity, respectively when the temperature is increased from 20 °C to 85 °C as presented in pairs C1-C12 and C4-C15. When the temperature is increased from 20 °C to 52.5 °C, ductility increases by 10.7% for 25 mm specimens at 71.5% humidity. Ductility is reduced by 31.2 % after the temperature is elevated to 85 °C from 52.5 °C as depicted in pairs C3-C8 and C8-C14 in this figure. Ductility is decreased by 8.3% at 48% humidity and 24.8 % at 95 % humidity for 38 mm specimens when the temperature is increased from 20 °C to 85 °C as presented in pairs C2-C13 and C5-C16.

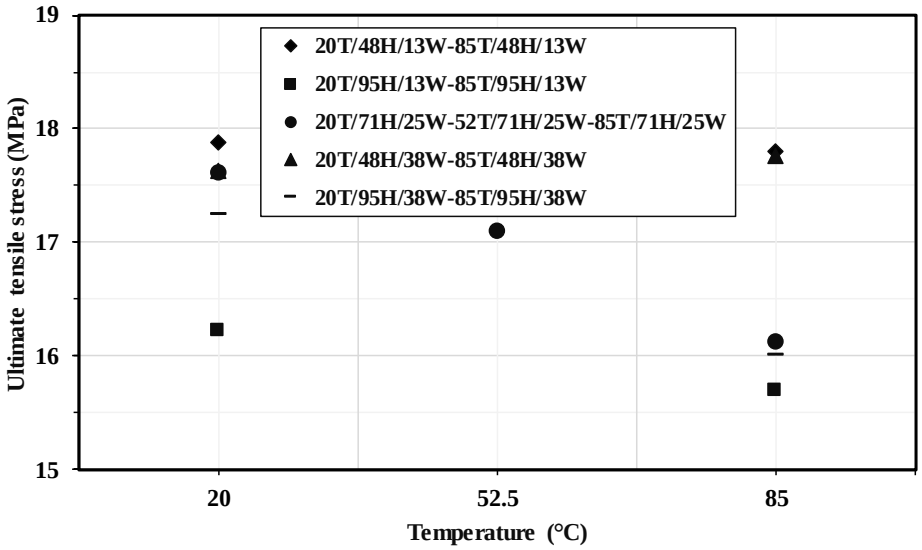

Figure 1.6: Temperature effect on ultimate stress for tensile specimens

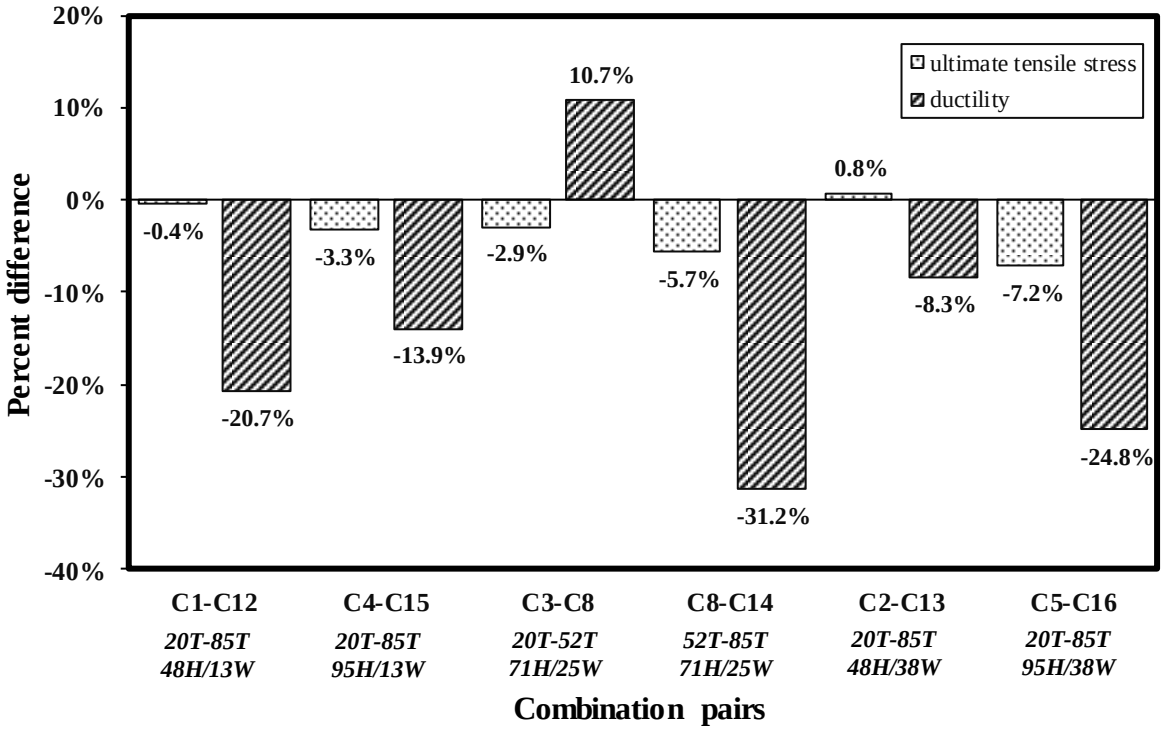

Figure 1.7: Percent difference in ultimate tensile stress and ductility due to variation in temperature with a fixed humidity and width

1.5.1.2 EFFECT OF HUMIDITY

Figure 1.8 shows the graphical representation of the effect of humidity on the ultimate tensile stress. Figure 1.9 shows a bar chart to further illustrate the humidity effect in ultimate tensile stress and ductility in terms of percent difference among combination pairs. For specimens of 13 mm width, the stress is reduced by 9.3% at 20 °C and 11.9% at 85 °C, respectively when the humidity is increased from 48% to 95 % as depicted in pairs C1-C4 and C12-C15 in this figure. At 52.5 °C, when the humidity was increased from 48% to 95 %, the stress decreases by 0.3% for 25 mm specimens. The stress is decreased by 1.2 % after the humidity is elevated to 95% from 48% as shown in pairs C6-C8 and C8-C11. The stress is decreased by 2.2% at 20 °C and 9.9 % at 95 % humidity for

specimens of 38 mm width after the humidity is increased from 48% to 95 % which is shown in pairs C2-C5 and C13-C16.

In Figure 1.9, for specimens of 13 mm width, ductility increased by 23.9% at 20 °C and 34.5% at 85 °C respectively when humidity is increased from 48% to 95 % (see comparison C1-C4 and C12-C15). At 52.5 °C temperature, when humidity was increased from 48% to 71.5 %, ductility declined by 12.5% for 25 mm specimens. Ductility was slightly decreased by 0.9 % after the elevation of humidity to 95% from 71.5% (see comparison C6-C8 and C8-C11). Ductility, however, increased by 34.8% at 20 °C with an increment of 10.6% at 85 °C for specimens of 38 mm after the elevation of humidity to 95% from 48% (see comparison C2-C5 and C13-C16).

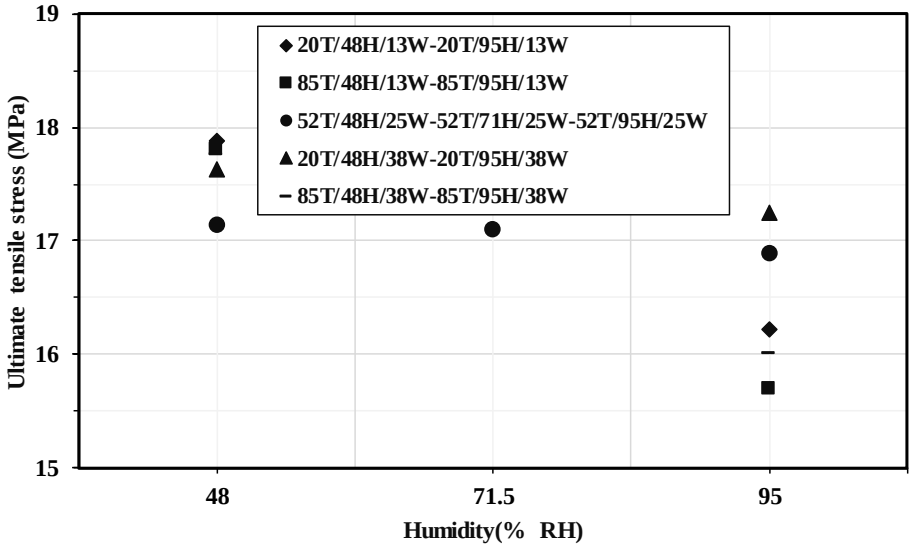

Figure 1.8: Humidity effect on ultimate stress for tensile specimens

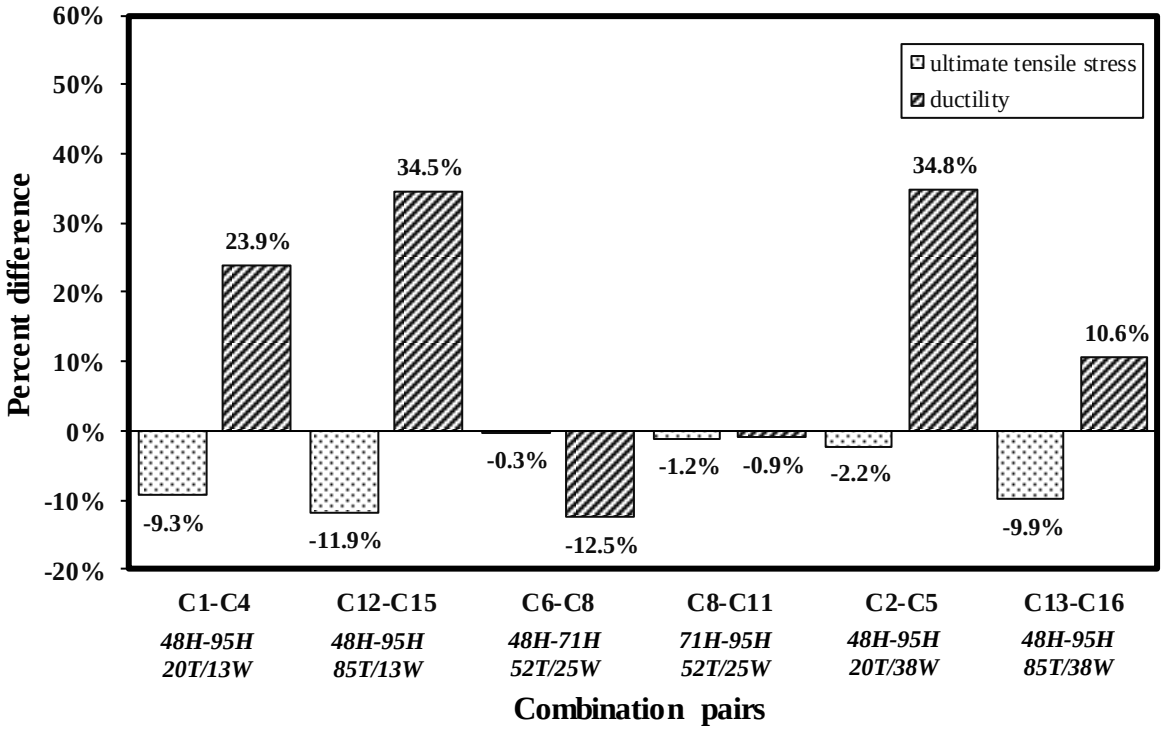

Figure 1.9: Percent difference in ultimate tensile stress and ductility due to the variation in humidity with a fixed temperature and width

1.5.1.3 EFFECT OF WIDTH

The trend of the effect of width in ultimate tensile stress can be seen in Figure 1.10. Figure 1.11 shows the bar chart depicting the percent difference in ultimate tensile stress and ductility due to the effect of width at different conditioning. For specimens at 20°C, ultimate tensile stress is reduced by 1.4% at 48% humidity and increased by 6.3% at 95% humidity respectively when the width of the specimen is increased from 13mm to 38mm (see comparison C1-C2 and C4-C5). At 52.5°C, when the specimen width was increased from 13 mm to 25 mm, stress declined by 1.2% at 71.5% humidity. The stress was further decreased by 7.9 % after the increment of width to 38 mm from 25 mm (see comparison C7-C8 and C8-C10). The stress is decreased by 0.2% at 48% humidity and increased by

2% at 95% humidity for specimens conditioned at 85°C with an increment of specimen width from 13mm to 38mm (see comparison C12-C13 and C15-C16).

In Figure 1.11, for specimens at 20 °C, ductility declined by 12.1% at 48% humidity and 4.3% at 95 % humidity respectively when specimen width is increased from 13mm to 38mm as portrayed in pairs C1-C2 and C4-C5. For specimens conditioned at 52.5 °C, when the width is increased from 13mm to 25mm, ductility is reduced by 7.2% at 71.5% humidity. Ductility, however, increased by 3.8 % with the further increment of specimens' width from 25mm to 38 mm as presented in C7-C8 and C8-C10. The ductility is increased by 1.6% at 48% humidity, though, decreased by 16.5 % at 95 % humidity for the specimens conditioned at 85 °C with the increment of width from 13mm to 38mm as shown in pairs C2-C13 and C5-C16.

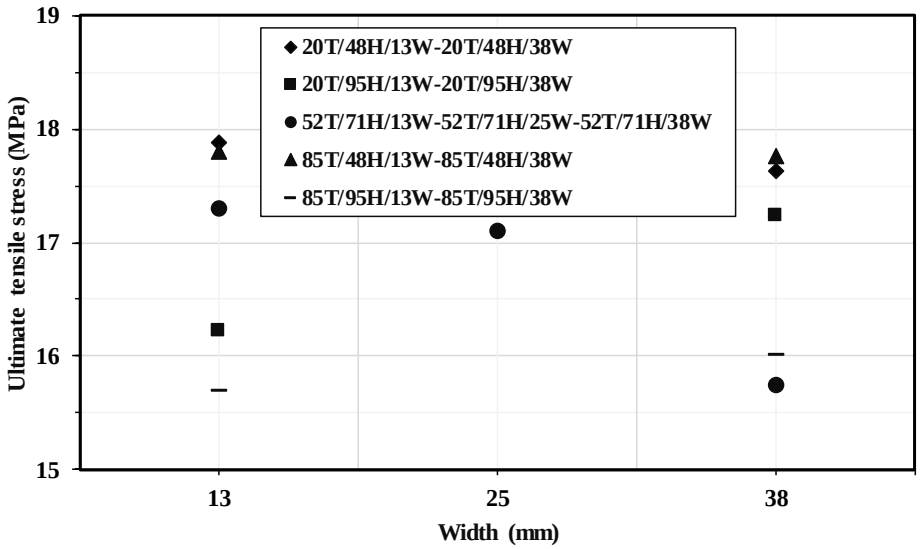

Figure 1.10: Width effect on ultimate stress for tensile specimens

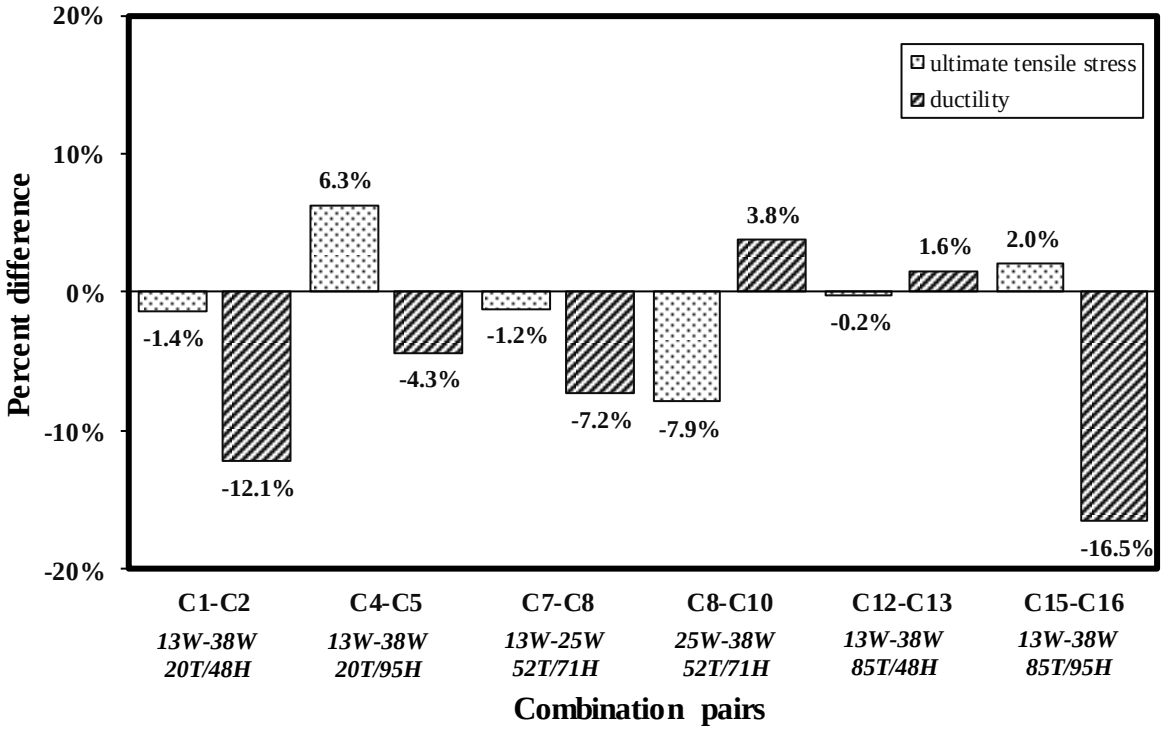

Figure 1.11: Percent difference in ultimate tensile stress and ductility due to the variation in width with a fixed temperature and humidity

1.5.2 SHEAR TEST

Stress-strain curves for the shear specimens are shown in Figure 1.12. Key mechanical properties, including ultimate stress, shear modulus and ductility, are determined from the stress-strain curve. The ultimate shear stress and other mechanical properties at different conditions are shown in Table 1.3. The shear stress and shear strain were calculated from Equation 1.3 and Equation 1.4 presented below.

$$\tau_u = {}^{V_u}/_{A_0} \qquad \text{(Equation 1.3)}$$

$$\gamma = {}^{\Delta l}/_{t_a} \qquad \text{(Equation 1.4)}$$

where τ_u is ultimate shear stress, V_u is ultimate shear load, A_0 is overlap area of the shear specimen, γ is shear strain, Δl is change in extensometer gauge length, and t_a is adhesive thickness.

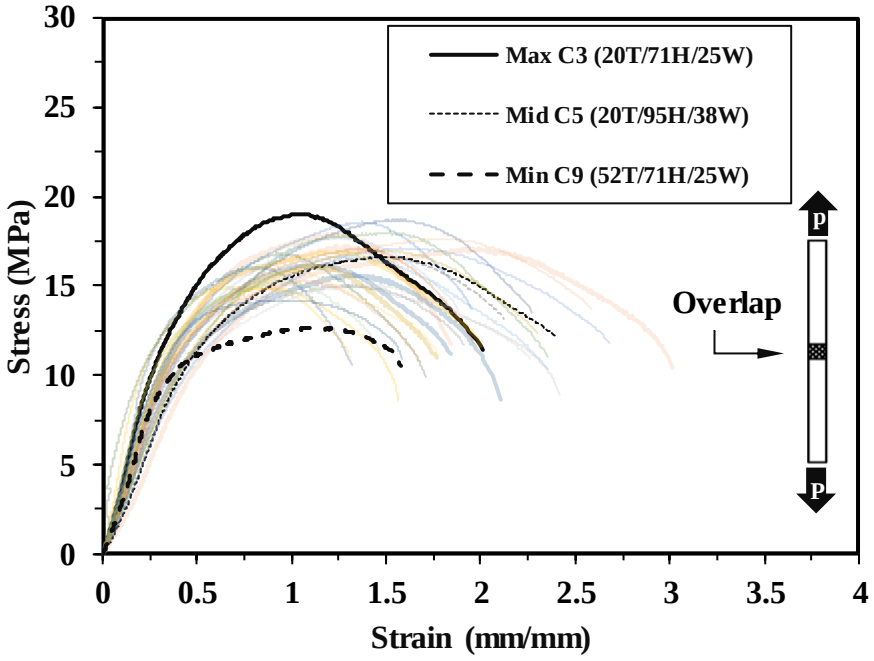

Figure 1.12: Stress-strain curves for shear specimens

Table 1.3 Mechanical properties from the shear tests

ID	Shear modulus, G (MPa)	Ultimate shear stress, τ_u (Mpa)	Ductility, e (%)
20T/48H/13W	26.1	17.5	4.17
20T/48H/38W	43.4	16.1	4.45
20T/71H/25W	35.7	18.0	4.66
20T/95H/13W	34.9	15.8	3.40
20T/95H/38W	27.3	16.4	3.49
52T/48H/25W	27.8	17.8	4.00
52T/71H/13W	32.2	16.0	3.64
52T/71H/25W	37.2	15.0	3.66
52T/71H/25W	27.3	14.9	3.20
52T/71H/38W	33.5	17.8	3.42
52T/95H/25W	26.4	16.0	3.70
85T/48H/13W	29.6	17.0	3.53
85T/48H/38W	32.7	17.7	3.20
85T/71H/25W	29.1	15.5	3.76
85T/95H/13W	34.6	15.6	3.50
85T/95H/38W	28.8	15.4	3.47

Representative failure modes of the shear specimens after the test are shown in Figure 1.12. Three different failure modes were observed during the shear test. Only one specimen from combination 13 was failed with adhesive failure mode as shown in Figure 1.13. In this type of failure mode, adhesive is observed when the adherend separates from the adhesive layer. Figure 1.13b, presents the cohesive failure mode which is the predominant failure mode in this study for shear test. A cohesive failure occurs when the failure plane is through the adhesive itself. A total of 28 specimens failed with cohesive failure. A mixture of the two failure modes named as adhesive/cohesive failure mode is also observed in this study as shown in Figure 1.13c. Two specimens from combination C2 and one specimen from combination C13 were observed to have this failure mode.

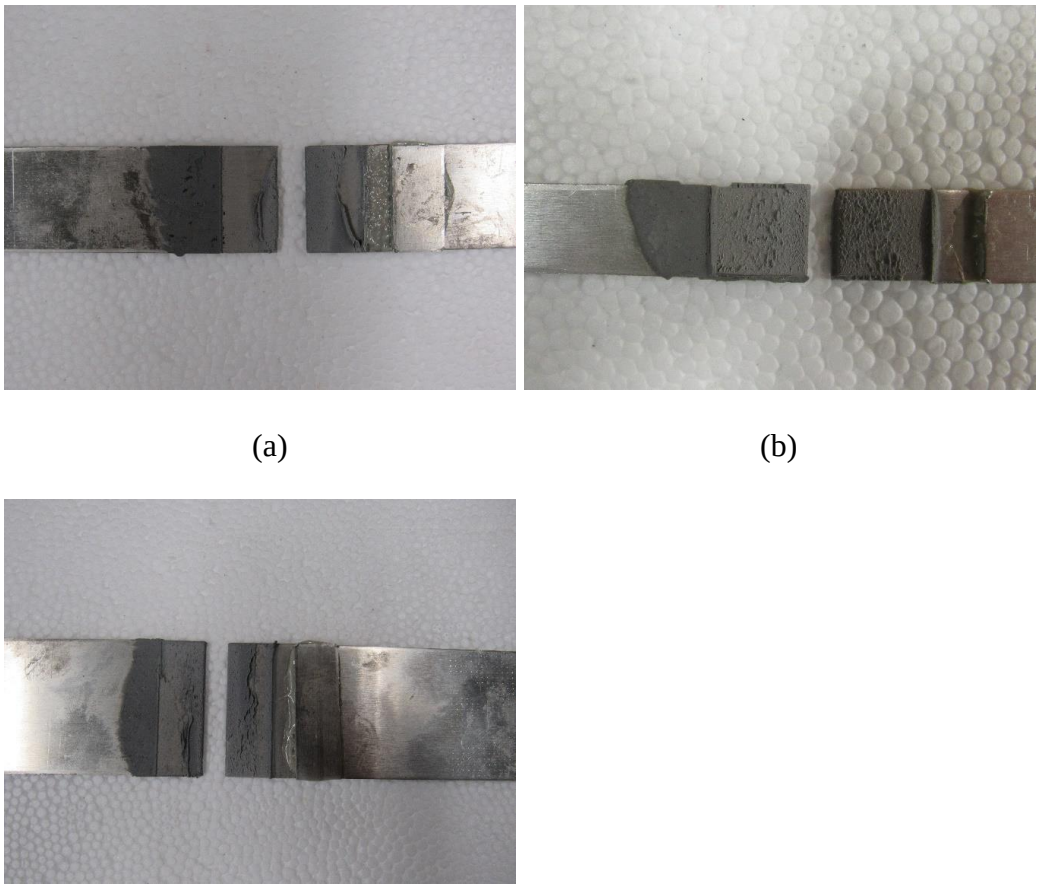

(a) (b)

(c)

Figure 1.13: Representative failure modes of shear specimens (a) adhesive failure, (b) cohesive failure and (c) adhesive/cohesive failure

1.5.2.1 EFFECT OF TEMPERATURE

Figure 1.14 shows the graphical illustration of the effect of temperature on the ultimate shear stress. A figure showing the change in ultimate shear stress and ductility in terms of percent difference due to temperature effect is further shown in Figure 1.15. For specimens of 13 mm width, the shear stress is reduced by 2.5% at 48% humidity and 1.4% at 95 % humidity, respectively when the temperature is increased from 20 °C to 85 °C as presented in pairs C1-C12 and C4-C15. At 71.5 % humidity, when the temperature

is increased from 20 °C to 52.5 °C, the shear stress is significantly declined by 16.8% for 25 mm specimens. The shear stress, on the contrary, is increased by 3.4 % after the elevation of temperature to 85 °C from 52.5 °C as displayed in pairs C3-C8 and C8-C14. The shear stress is increased by 10% at 48% humidity, however, decreased by 6% at 95 % humidity for specimens of 38 mm after the elevation of temperature to 85 °C from 20 °C as shown in pairs C2-C13 and C5-C16.

In Figure 1.15, for specimens of 13 mm width, the ductility is declined by 15.2% at 48% humidity, yet, increased by 2.8% at 95 % humidity respectively when the temperature is increased from 20 °C to 85 °C as shown in pairs C1-C12 and C4-C15. At 71.5 % humidity, when the temperature is increased from 20 °C to 52.5 °C, ductility is lowered by 21.6% for 25 mm specimens. The ductility is increased by 2.7 % after an additional increase of temperature to 85 °C from 52.5 °C as shown in pairs C3-C8 and C8-C14. The ductility is reduced by 28.1% at 48% humidity and 0.6% at 95 % humidity for specimens of 38 mm width after the elevation of temperature to 85 °C from 20 °C as presented in pairs C2-C13 and C5-C16.

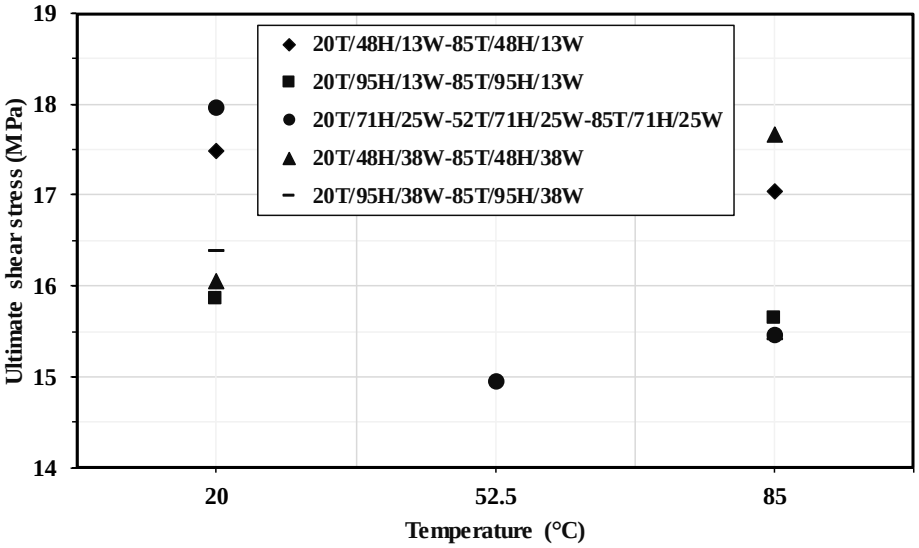

Figure 1.14: Temperature effect on ultimate stress for shear specimens

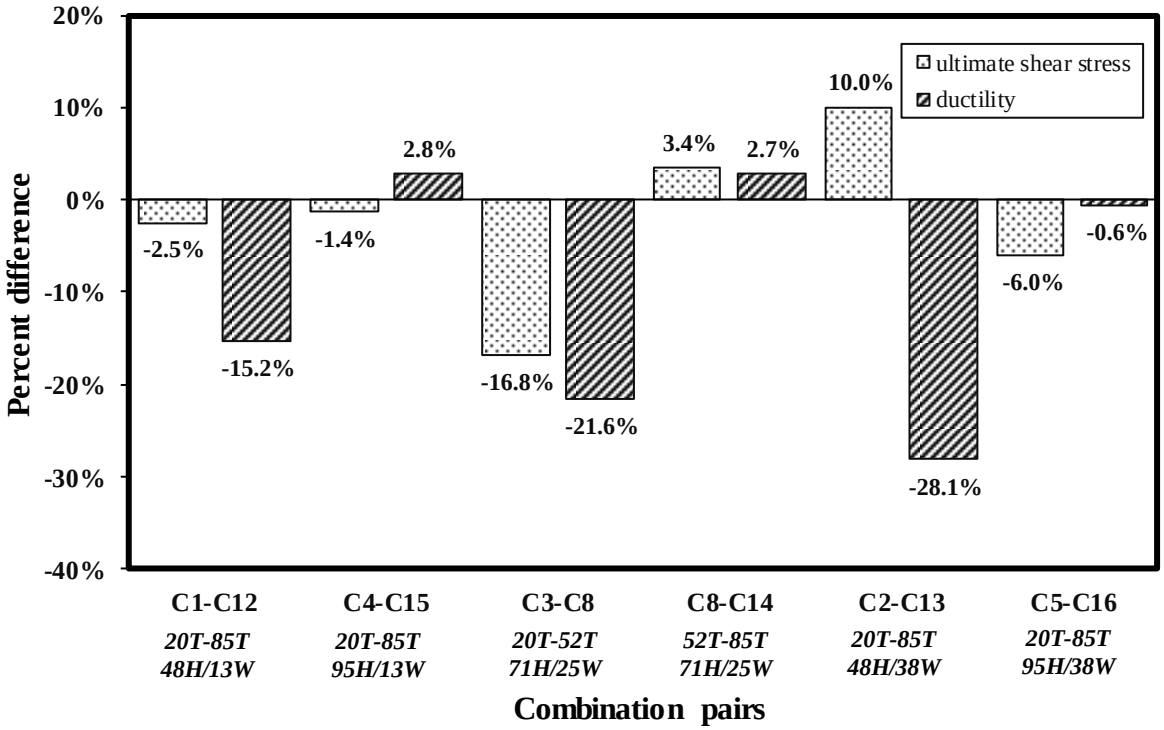

Figure 1.15: Percent difference in ultimate shear stress and ductility due to the variation in temperature with a fixed humidity and width

1.5.2.2 EFFECT OF HUMIDITY

Figure 1.16 shows the graphs representing the effect of humidity in the ultimate shear stress. The effect of humidity in ultimate shear stress and ductility is further depicted in Figure 1.17 for different conditioning. For specimens of 13 mm width, the shear stress is reduced by 9.3% at 20 °C and 8.3% at 85 °C respectively when humidity is increased from 48% to 95 % (see comparison C1-C4 and C12-C15). At 52.5 °C, when humidity is increased from 48% to 95 %, ultimate shear stress is declined by 15.7% for 25 mm specimens. The shear stress, however, increases by 7% after the elevation of humidity to 95% from 48% (see comparison C6-C8 and C8-C11). The shear stress is increased by 2.1% at 20 °C but decreased by 12.7 % at 95 % humidity for specimens of 38 mm after the elevation of humidity from 48% to 95 % (see comparison C2-C5 and C13-C16).

In Figure 1.17, for specimens of 13 mm width, ductility is declined by 18.3% at 20 °C and 0.9% at 85 °C respectively when the humidity is increased from 48% to 95 % as illustrated in pairs C1-C4 and C12-C15. At 52.5 °C, when the humidity is increased from 48% to 71.5 %, the ductility reduces by 8.6% for 25 mm specimens (see pair C6-C8). The ductility, however, increases by 1.3 % after the elevation of humidity from 71.5% to 95% as shown in pair C8-C11 in this figure. The ductility decreases by 21.5% at 20 °C and increases by 8.6% at 85 °C for specimens of 38 mm humidity is increased from 48% to 95% as presented in pairs C2-C5 and C13-C16 in this figure.

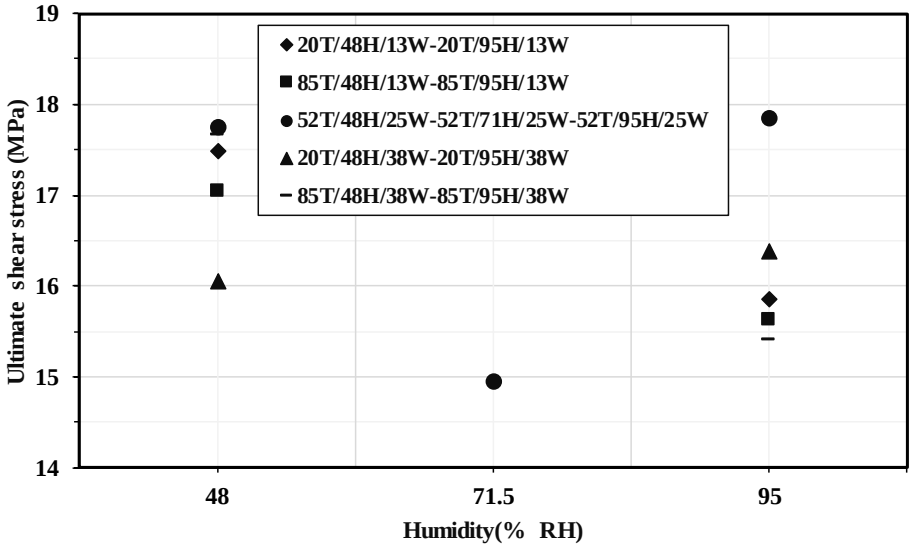

Figure 1.16: Humidity effect on ultimate stress for shear specimens with different widths

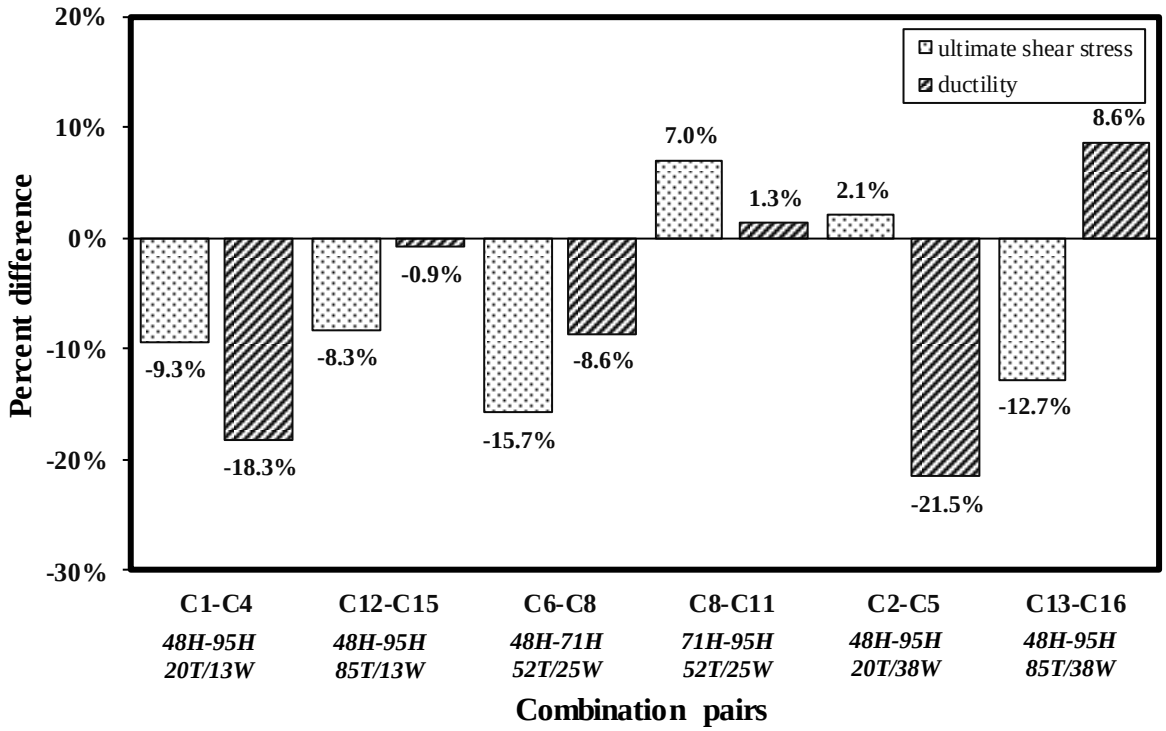

Figure 1.17: Percent difference in ultimate shear stress and ductility due to the variation in humidity with a fixed temperature and width

1.5.2.3 EFFECT OF WIDTH

The effect of width on the ultimate shear stress is graphically explored in Figure 1.18. The effect of width on the ultimate shear stress and ductility in percentage is further illustrated in a bar chart as shown in Figure 1.19. For specimens at 20°C, the shear stress is reduced by 8.1% at 48% humidity and increased by 3.4% at 95% humidity respectively when the width of the specimens is increased from 13mm to 38mm as shown in pairs C1-C2 and C4-C5. At 52.5°C, when the specimen width is increased from 13 mm to 25 mm, the shear stress declines by 6.5% at 71.5% humidity. The shear stress, however, increases by 19.3% after the increment of width to 38 mm from 25 mm as presented in pairs C7-C8 and C8-C10. The shear stress increases by 3.6% at 48% humidity and decreases by 1.4% at 95% humidity for specimens at 85°C when the specimen width is increased from 13mm to 38mm as displayed in pairs C12-C13 and C15-C16.

In Figure 1.19 for specimens at 20 °C, the ductility is increased by 6.7% at 48% humidity and 2.5% at 95 % humidity while at an increase in width from 13mm to 38mm as displayed in pairs C1-C2 and C4-C5 in this figure. For specimens conditioned at 52.5 °C, when the width changes from 13mm to 25mm, ductility increases by 0.4% at 71.5% humidity (see pair C7-C8). Ductility, however, dropped off by 6.4 % with a further increment of specimen width from 25mm to 38mm as depicted in pair C8-C10. As shown in pairs C12-C13 and C15-C16, the ductility decreases by 9.5% at 48% humidity and 0.8 % at 95 % humidity for the specimens conditioned at 85 °C with the increase of specimen width from 13mm to 38mm.

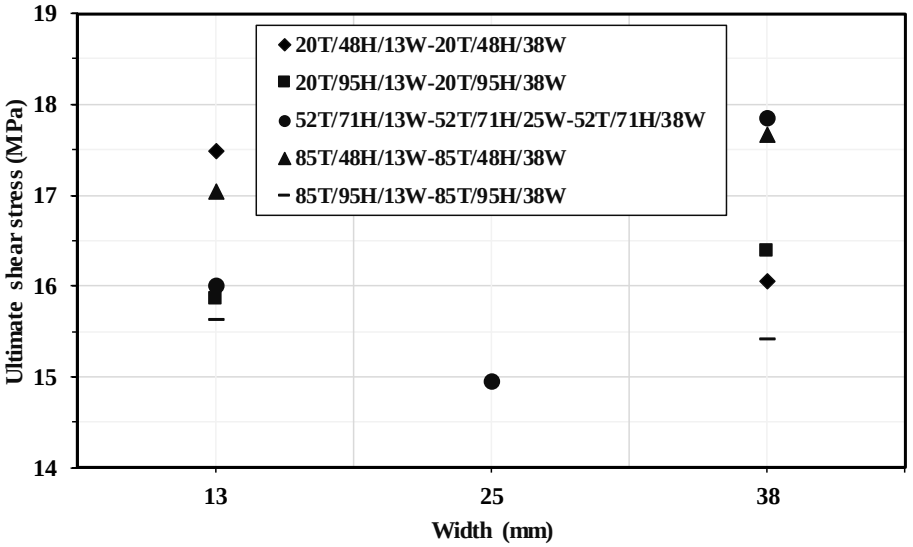

Figure 1.18: Width effect on ultimate stress for shear specimens at different temperatures

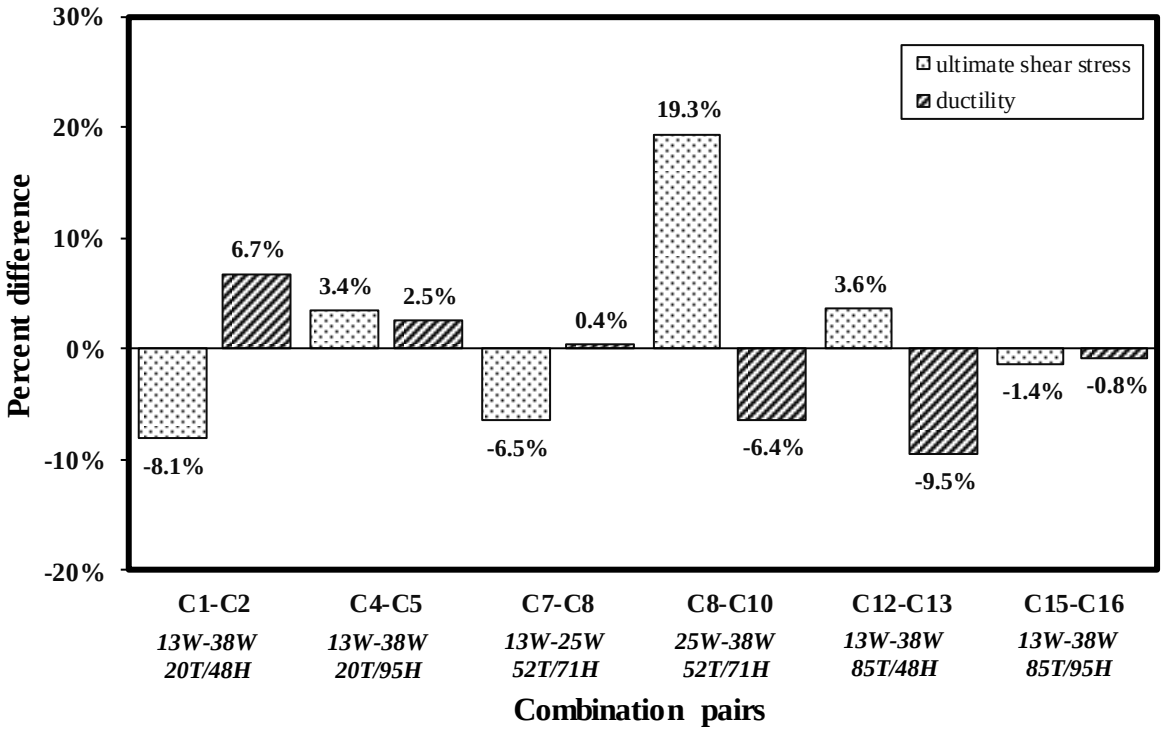

Figure 1.19: Percent difference in ultimate shear stress and ductility due to the variation in width with a fixed temperature and humidity

1.6 STATISTICAL ANALYSIS ON TESTING DATA

This section discusses findings gained through statistical analysis of the testing data. The following subsection focuses on sensitivity analysis necessary for the determination of statistically significant parameters on each of the strengths and statistical model selection required for the prediction of the respective strengths in an efficient and accurate manner.

1.6.1 REGRESSION MODEL DEVELOPMENT

Multiple Linear Regression (MLR) and Response Surface Metamodels (RSM) models were created only for the ultimate tensile and shear stresses from the testing, which are the most critical to design the adhesive connection for DMSs. The testing data at each input parameter were modeled to generate both MLR and RSM models using R, a commercially available statistical software. Three parameters were considered in each of the statistical models, including temperature, humidity, and width of the specimens. The MLR and RSM models for prediction of the ultimate tensile stress are shown in Equation 1.5 and Equation 1.6, respectively.

$$f_u(MLR) = 19.4329 - 0.0098T - 0.0263H - 0.0378W \quad \text{(Equation 1.5)}$$

$$f_u(\text{RSM}) = 21.104 + 0.004\,T - 0.096\,H + 0.026W - 0.0003TH - 0.0002TW + 0.0007\text{H}W + 0.0001T^2 + 0.0005H^2 - 0.0014W^2 \quad \text{(Equation 1.6)}$$

where f_u is ultimate tensile stress, T is conditioning temperature, H is conditioning humidity, and W is width of the specimen.

The MLR and RSM models for prediction of the ultimate shear stress are provided in Equation 1.7 and Equation 1.8, correspondingly.

$$\tau_u(\text{MLR}) = 18.583 - 0.008T - 0.029\,H + 0.011W \quad \text{(Equation 1.7)}$$

$$\tau_u(\text{RSM}) = 21.161 + 0.006\,T - 0.072\,H - 0.122W - 0.0004TH + 0.0004TW + 0.0005\text{H}W + 0.00004T^2 + 0.0004H^2 + 0.0015W^2 \quad \text{(Equation 1.8)}$$

where τ_u is ultimate shear stress

1.6.2 SENSITIVITY ANALYSIS

To determine significant parameters on both ultimate tensile and shear stress data, probability values for the developed MLR and RSM models were calculated through statistical analysis. The standard level of significance was set at 5% for the analysis where a probability value less than 0.05 was considered significant. Table 1.4 shows the resulting probability value of each parameter with regard to tensile and shear stress. By analyzing the probability values from the MLR and RSM models, humidity was found to be the most significant parameter for the tensile stress. Meanwhile, the shear stress didn't show any parameters to be significant in any of the models created.

Table 1.4 Probability values from the statistical analysis on the tensile and shear stress data

Parameter	MLR		RSM	
	Tensile stress	Shear stress	Tensile stress	Shear stress
T	0.09473	0.435	0.17736	0.5596
H	**0.00427**	0.053	**0.02529**	0.1518
W	0.78412	0.671	0.82129	0.7503
T:H	-	-	0.36704	0.5429
T:W	-	-	0.80011	0.7386
H:W	-	-	0.41685	0.7685
T^2	-	-	0.77909	0.9565
H^2	-	-	0.53467	0.8070
W^2	-	-	0.59727	0.7655

Note: T, H, and W represent temperature, humidity, and the width of the specimens, respectively.

1.6.3 COMPARISON BETWEEN MLR AND RSM

To better predict the ultimate tensile and shear stress for the adhesive connection with respect to different parameters taken for this study, the most reliable model between MLR and RSM models was determined by comparing coefficient of determination acquired from each (see Table 1.5). The coefficient of determination values of the RSM model on the tensile and shear stress are higher than those from the MLR model. It turns out that the predicted ultimate tensile and shear stress from the RSM model were more accurate than the MLR-derived values; thus, the RSM model was chosen for predicting the tensile and shear stress at different conditions of temperature, humidity, and width. To graphically evaluate the accuracy of RSM and MLR models, the testing data versus predicted ultimate tensile and shear stress from each are compared as seen in Figure 1.20. Based on the statistical and graphical comparisons with the experimental data, it was proven that the RSM model was a better fit for the tensile and shear testing data.

Table 1.5 Coefficient of determination values for MLR and RSM models

MLR		RSM	
Tensile stress	Shear stress	Tensile stress	Shear stress
0.5670	0.3123	0.6949	0.412

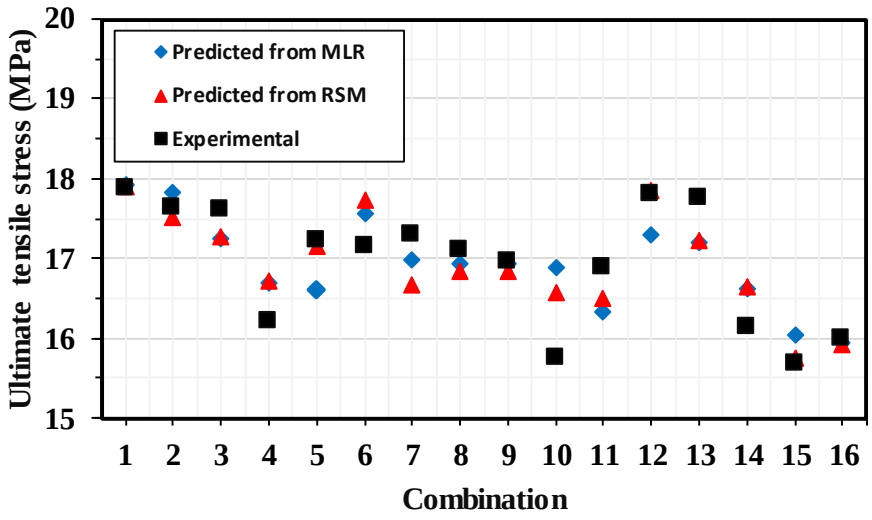

(a)

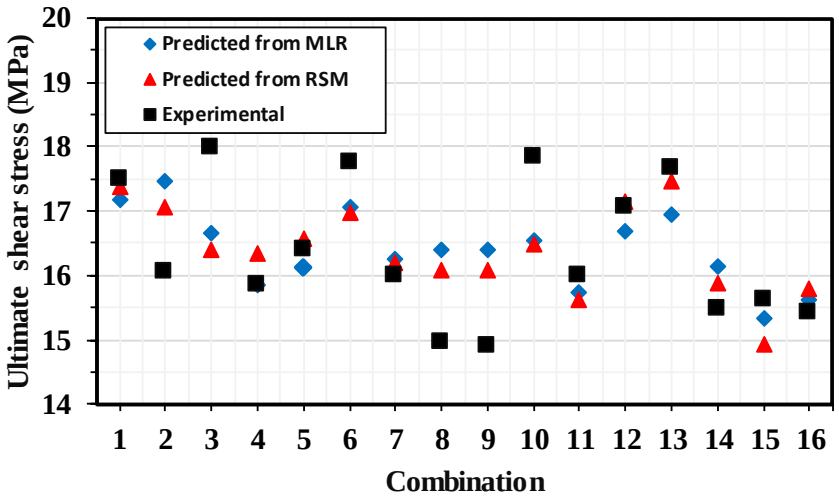

(b)

Figure 1.20: Experimental stress versus predicted stress from the MLR and RSM model: (a) tensile data and (b) shear data

1.6.4 RSM SURFACES

The RSM model was used to create three-dimensional (3D) surface plots for ultimate tensile stress with respect to different parameters. The tensile stress was plotted against two parameters at a time, while the remaining parameter was considered a fixed value; thus, three separate figures (see Figure 1.21a, b, and c) showing the effects of two parameters were developed. Specifically, an average value of the remaining parameter is taken for developing the plots between the two input parameters deemed as variables. For instance, an average value of width (25 mm) is taken for the RSM model to explore the effect of temperature and humidity on tensile stress and to develop the corresponding plot as shown in Figure 1.21a. Figure 1.21b shows the plot for width and temperature variation with the constant of humidity, while Figure 1.21c displays the plot regarding different values of width versus humidity with the fixed value of temperature.

In Figure 1.21a, at lower humidity (48%), increase in temperature (20 °C to 85 °C) decreased the ultimate tensile stress slightly by 1.12%. At higher humidity (95%), the tensile stress is reduced by 6.41% when the temperature is increased (20 °C to 85 °C). When the ultimate tensile stress is observed at higher temperature (85 °C), there is a significant drop of 9.52% with the increase in humidity (48% to 95%). At lower temperature (20 °C), when the humidity is increased (48% to 95%), ultimate tensile stress is dropped by 4.40%. The tensile stress for different width and temperature is shown in Figure 1.21b. The increase in width from 13 mm to 38 mm is observed to increase the tensile stress with a slight reduction up to 1.39%. The increased temperature (20 °C to 85 °C) resulted in a significant decrease in tensile stress by 3.00% at smaller width (13 mm) and by 4.45% at larger width (38 mm) specimens. It can be observed in Figure 1.21c that

humidity plays a vital role in tensile stress. The tensile stress is dropped considerably by 9.34% at smaller width (13 mm) and by 4.81% at larger width (38 mm) when the humidity is increased from 48% to 95%. Only a slight increase of 1.92% in tensile stress is observed at high humidity of 95% when the width is increased (13 mm to 38 mm). The tensile stress, however, is reduced by 2.81% at low humidity (48%) when the specimen width is increased from 13 mm to 38 mm.

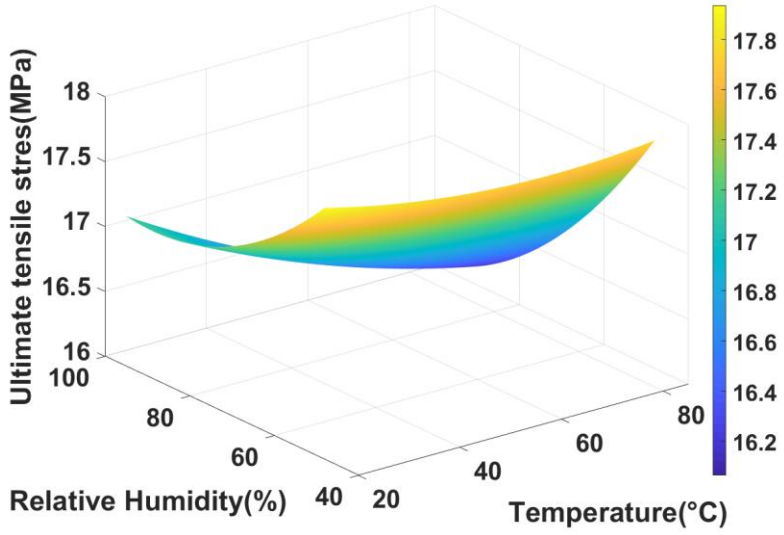

(a)

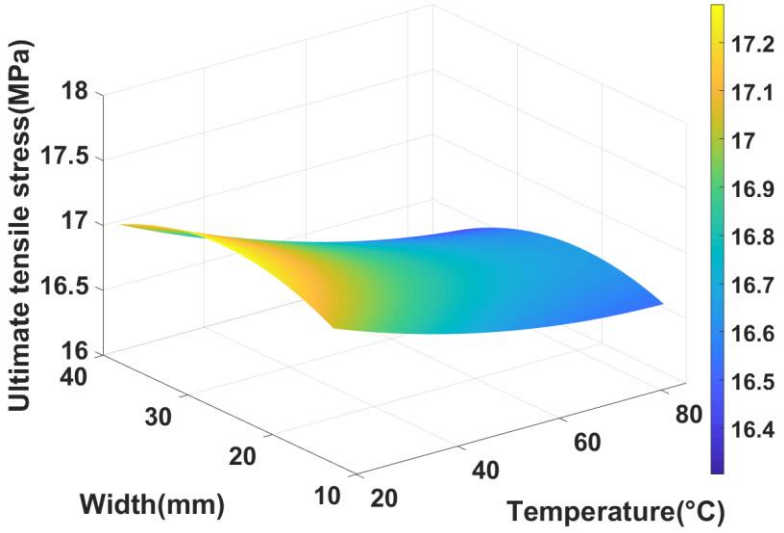

(b)

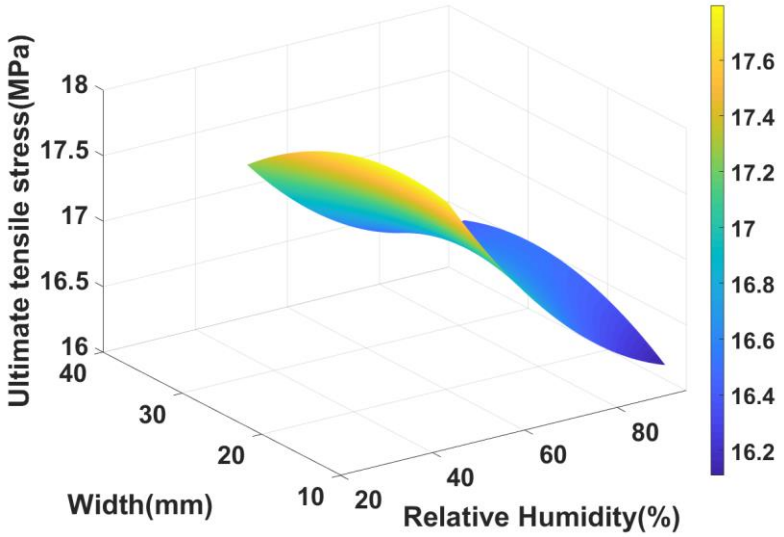

(c)

Figure 1.21: 3D RSM surfaces of ultimate tensile stress showing effects of (a) temperature and humidity (b) temperature and width and (c) humidity and width

3D surface plots for ultimate shear stress were also developed using the RSM function presented in Equation 1.8. 3D plots of the ultimate shear stress are shown in

Figure 1.22. The plots show the behavior of shear stress with respect to two different parameters. In Figure 1.22a, the increase in temperature (20 °C to 85 °C) at lower humidity (48%) increased the ultimate shear stress by 0.47%, however, at higher humidity (95%), the ultimate shear stress is reduced by 6.72%. The increase in humidity (48% to 95%) is observed to decrease the ultimate shear stress by 4.47% at lower temperature (20 °C) and by 11.31% at the higher temperature (85 °C). When the width is plotted with respect to temperature in Figure 1.22b, an increase in width (13 mm to 38 mm) decreased the shear stress by 0.30% at a lower temperature (20 °C), however, the shear stress is increased by 3.72% at the higher temperature (85 °C). When the temperature is increased (20 °C to 85 °C), the shear stress is decreased rapidly at smaller width (13 mm) by 4.98%, however, the effects seem to be minimal at wider specimen (38 mm) with 1.08% reduction in the shear stress. The shear stress for width and humidity is plotted in Figure 1.22c. At lower humidity (48%), with the increase in width (13 mm to 38 mm), the shear stress is reduced only by 0.05%, however, increased by 3.59% at higher humidity (95%). The increase in humidity (48% to 95%) decreased the shear stress by 9.47% at smaller width (13 mm) and 6.16% at larger width (38 mm).

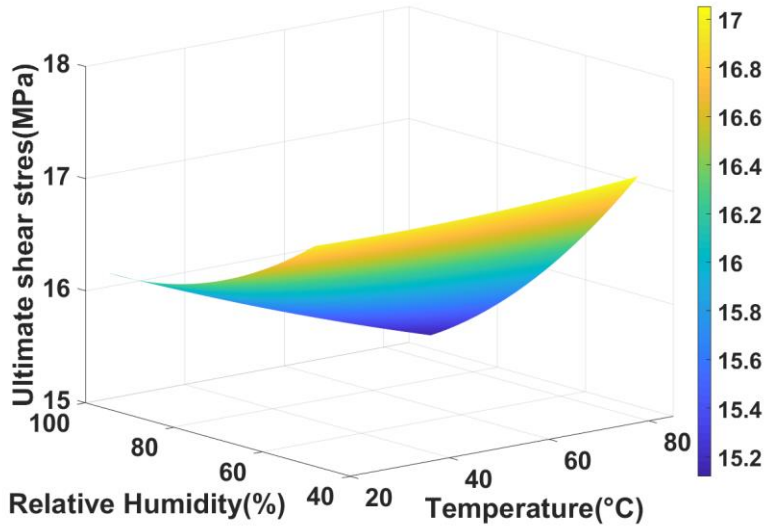
Ultimate shear stres(MPa)
18
17
16
15
100
80
60
40
Relative Humidity(%)
20
40
60
80
Temperature(°C)
17
16.8
16.6
16.4
16.2
16
15.8
15.6
15.4
15.2

(a)

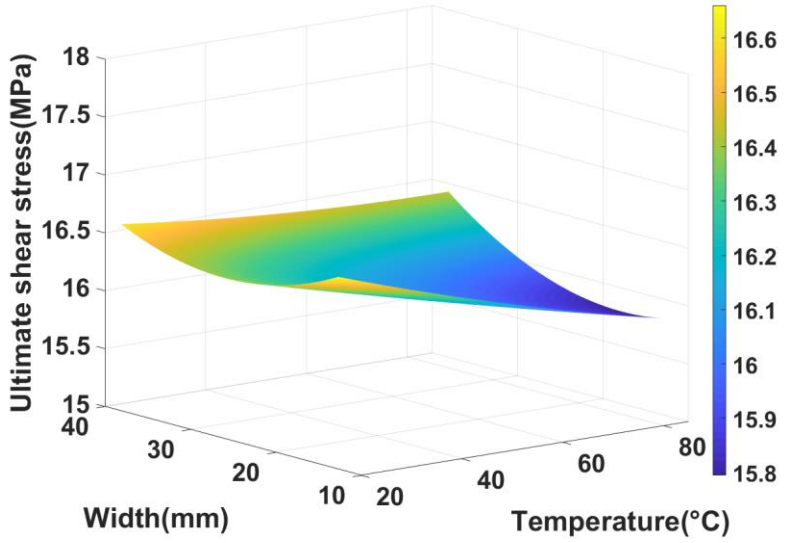
Ultimate shear stress(MPa)
18
17.5
17
16.5
16
15.5
15
40
30
20
10
Width(mm)
20
40
60
80
Temperature(°C)
16.6
16.5
16.4
16.3
16.2
16.1
16
15.9
15.8

(b)

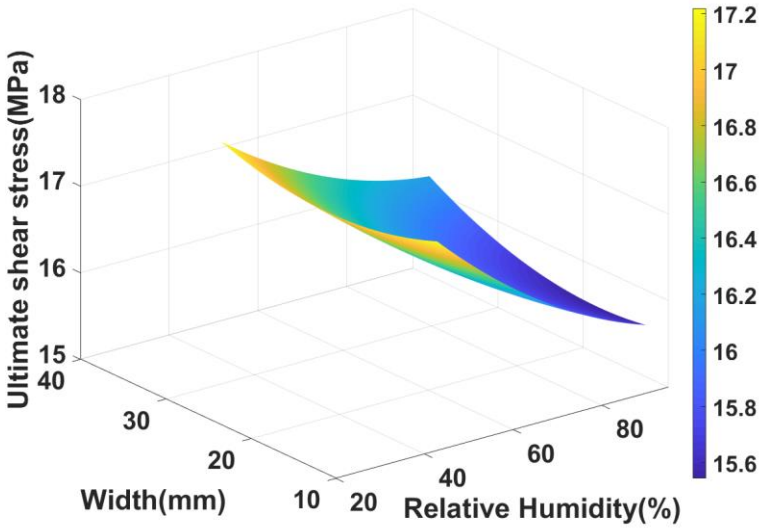

(c)

Figure 1.22: 3D RSM surfaces of ultimate shear stress showing effects of (a) temperature and humidity (b) temperature and width and (c) humidity and width

From the above discussion, it was found that humidity plays a significant role in determining both the ultimate tensile and shear stress in adhesive connection. Increase in humidity changed the ultimate tensile stress up to 9.52% and ultimate shear stress up to 11.31%. A maximum percentage change of 6.41% and 6.72% is observed for ultimate tensile and shear stress respectively with the increase in temperature, but the effect of width while predicting ultimate stress cannot be neglected either. The ultimate tensile stress is found to be changed up to 2.81% and the ultimate shear stress is changed up to 3.72% when the width of the specimens is increased. It should be noted that the developed RSM functions can be used for a certain range of input parameters only to predict the ultimate tensile and shear stress at low uncertainties. The temperature should be in the range of 20°C to 85°C, humidity should be limited to 48% to 95% and the width

of the adhesive joints should be within 12.7 to 38.1 mm only. Beyond that range, significant uncertainties can be expected for the outputs from the RSM functions.

1.7 CONCLUSIONS

The effects of tensile and shear loads were investigated on the mechanical properties of adhesive specimens that serve as the basis to examine structural behaviors of main connections in Dynamic Message Sign (DMS). To that end, tensile and shear tests were carried out with 16 different combinations created with variations in temperature, humidity, and width of the adhesive specimens. Effects of temperature, humidity, and width of the specimens on their mechanical properties were graphically and statistically examined for tensile and shear tests separately. As part of the statistical examination, Multiple Linear Regression (MLR) and Response Surface Metamodels (RSM) functions were generated, and the most accurate function was selected for forecasting the ultimate tensile and shear stresses. Then, three-dimensional RSM surfaces were created to visually examine the effects of each parameter on the tensile and shear properties. The following major conclusions can be derived from the experimental and statistical results:

1. In the tensile test, when the temperature was increased, the ultimate tensile stress reduced for all the tested combination pairs excepted for one pair (20T/48H/38W-85T/48H/38W). With the increase in humidity, the ultimate tensile stress showed a decreasing trend for all the combination pairs examined. When the width of the specimens was increased in the tensile test, ultimate tensile stress reduced for four combination pairs with increment in other two pairs (20T/95H/13W-20T/95H/38W and 85T/95H/13W-85T/95H/38W).

2. In the shear test, when the temperature was increased, the ultimate shear stress decreased for four combination pairs and increased for two pairs (52T/71H/25W-85T/71H/25W and 20T/48H/38W-85T/48H/38W). With the increase in the humidity during the shear tests, the ultimate shear stress dropped for four combination pairs with increment in two combination pairs (52T/71H/25W-52T/95H/25W and 20T/48H/38W-20T/95H/38W). With the increment in width, the ultimate shear stress reduced for three combination pairs with highest reduction (8.1%) in the pair (20T/48H/13W-20T/48H/38W) and increased for three combination pairs.

3. Two statistical models (MLR and RSM) were created for the prediction of ultimate tensile and shear stress. It was found that the RSM model was more accurate than MLR with a comparison of the coefficient of determination and visual inspection values.

4. A significant effect of humidity was identified for the ultimate tensile stress from the statistical analysis. Probability values obtained from the statistical analysis indicates that humidity is the decisive parameter causing the most significant effect on ultimate tensile stress. A probability value of 0.427% and 2.529% was observed for MLR and RSM model of ultimate tensile stress.

1.8 REFERENCES

Agarwal, A., Foster, S. J., Hamed, E., and Ng, T. S. 2014. “Influence of freeze–thaw cycling on the bond strength of steel–FRP lap joints.” *Composites Part B: Engineering, 60,* 178-185. http://dx.doi.org/10.1016/j.compositesb.2013.12.024.

ASTM (American Society for Testing and Materials). 2010. *Standard test method for apparent shear strength of single-lap-joint adhesively bonded metal specimens by tension loading (metal-to-metal)*. ASTM international. West Conshohocken, PA.

ASTM (American Society for Testing and Materials). 2014. *Standard test method for tensile properties of plastics*. ASTM International. West Conshohocken, PA.

Banea, M. D., da Silva, L. F. M., and Campilho, R. D. 2015. “The effect of adhesive thickness on the mechanical behavior of a structural polyurethane adhesive.” *The Journal of Adhesion, 91*(5), 331-346. http://dx.doi.org/10.1080/00218464.2014.903802.

Chandorkar, A. N., Mande, S., and Iwai, H. 2008. “Estimation of process variation impact on DG-FinFET device performance using Plackett-Burman design of experiment method.” In *Proc 9th International Conference on Solid-State and Integrated-Circuit Technology* (pp. 215-218). IEEE.

Chapman, J. 2010. “Bonding with adhesives.” Accessed October 04, 2019, https://www.compositesone.com/wp-content/uploads/2013/07/RE3043-LORD-Case-Study.pdf.

Çolak, A., Çoşgun, T., and Bakırcı, A. E. 2009. “Effects of environmental factors on the adhesion and durability characteristics of epoxy-bonded concrete

prisms." *Construction and Building materials, 23*(2), 758-767. doi:10.1016/j.conbuildmat.2008.02.013.

Da Silva, L. F., Carbas, R. J. C., Critchlow, G. W., Figueiredo, M. A. V., and Brown, K. 2009. "Effect of material, geometry, surface treatment and environment on the shear strength of single lap joints." *International Journal of Adhesion and Adhesives, 29*(6), 621-632. doi:10.1016/j.ijadhadh.2009.02.012.

Goglio, L., and Rezaei, M. 2014. "Variations in mechanical properties of an epoxy adhesive on exposure to warm moisture." *Journal of Adhesion Science and Technology, 28*(14-15), 1394-1404. http://dx.doi.org/10.1080/01694243.2012.697392.

Kim, Y. J., Hossain, M., and Yoshitake, I. 2012. "Cold region durability of a two-part epoxy adhesive in double-lap shear joints: Experiment and model development." *Construction and Building Materials, 36*, 295-304. http://dx.doi.org/10.1016/j.conbuildmat.2012.04.026.

Kokaly, R. F., and Clark, R. N. 1999. "Spectroscopic determination of leaf biochemistry using band-depth analysis of absorption features and stepwise multiple linear regression." *Remote sensing of environment, 67*(3), 267-287. doi:10.1016/s0034-4257(98)00084-4.

Lettieri, M., and Frigione, M. 2011. "Natural and artificial weathering effects on cold-cured epoxy resins." *Journal of Applied Polymer Science, 119*(3), 1635-1645. DOI 10.1002/app.32835.

LORD Corporation. 2018. "LORD® 406 Acrylic Adhesive." Accessed November 29, 2018, https://www.lord.com/products-and-solutions/adhesives/lord-406-acrylic-adhesive.

Moussa, O., Vassilopoulos, A. P., de Castro, J., and Keller, T. 2012. "Time–temperature dependence of thermomechanical recovery of cold-curing structural adhesives." *International Journal of Adhesion and Adhesives, 35,* 94-101. doi:10.1016/j.ijadhadh.2012.02.005

MTS Systems Corporation. 2018. "MTS Landmark® Servohydraulic Test Systems." Accessed November 29, 2018, http://www.mts.com/en/products/producttype/test-systems/load-frames-uniaxial/servohydraulic/standard/index.htm.

Na, J., Liu, Y., Fan, Y., Mu, W., Chen, X., and Yan, Y. 2017. "Effect of temperature on the joint strength of a silyl-modified polymer-based adhesive." *The Journal of Adhesion, 93*(8), 626-639. http://dx.doi.org/10.1080/00218464.2015.1128330.

Na, J., Liu, Y., Wang, Y., Pan, L., and Yan, Y. 2016. "Effect of temperature on the joints strength of an automotive polyurethane adhesive." *The Journal of Adhesion, 92*(1), 52-64. http://dx.doi.org/10.1080/00218464.2014.996634.

Neto, J. A. B. P., Campilho, R. D., and Da Silva, L. F. M. 2012. "Parametric study of adhesive joints with composites." *International Journal of Adhesion and Adhesives, 37,* 96-101. doi:10.1016/j.ijadhadh.2012.01.019

Sakiyama, T., Murayama, G., Naito, Y., Saita, K., Oikawa, Y. M. H., and Nose, T. 2013. "Dissimilar metal joining technologies for steel sheet and aluminum alloy sheet in auto body." *Nippon steel technical report, 103,* 91-98.

SAS Institute Inc. 2008. *JMP statistics and graphics guide, version 5.1.2*, Cary, NC

Savvilotidou, M., Vassilopoulos, A. P., Frigione, M., and Keller, T. 2017. "Development of physical and mechanical properties of a cold-curing structural adhesive

in a wet bridge environment." *Construction and Building Materials, 144*, 115-124. http://dx.doi.org/10.1016/j.conbuildmat.2017.03.145.

Seo, J. 2013. "Statistical determination of significant curved I-girder bridge seismic response parameters." *Earthquake Engineering and Engineering Vibration, 12*(2), 251-260. DOI: 10.1007/s11803-013-0168-y.

Seo, J., and Linzell, D. G. 2010. "Probabilistic Vulnerability Scenarios for Horizontally Curved Steel I-Girder Bridges Under Earthquake Loads." *Transportation Research Record, 2202*(1), 206-211. DOI: 10.3141/2202-24.

Seo, J., and Linzell, D. G. 2012. "Horizontally curved steel bridge seismic vulnerability assessment." *Engineering Structures, 34*, 21-32. doi:10.1016/j.engstruct.2011.09.008.

Seo, J., and Linzell, D. G. 2013. "Influential Curved Steel Bridge Fragility Analysis Parameters." *Forensic Engineering 2012: Gateway to a Safer Tomorrow* (pp. 84-92).

Seo, J., and Linzell, D. G. 2013. "Use of response surface metamodels to generate system level fragilities for existing curved steel bridges." *Engineering Structures, 52*, 642-653. http://dx.doi.org/10.1016/j.engstruct.2013.03.023.

Seo, J., and Pokhrel, J. 2019. "Surrogate Modeling for Self-Consolidating Concrete Characteristics Estimation for Efficient Prestressed Bridge Construction." *American Concrete Institute Special Publication.*

Silva, P., Fernandes, P., Sena-Cruz, J., Xavier, J., Castro, F., Soares, D., and Carneiro, V. 2016. "Effects of different environmental conditions on the mechanical characteristics

of a structural epoxy." *Composites Part B: Engineering*, *88*, 55-63. doi: 10.1016/j.compositesb.2015.10.036.

Sousa, J. M., Correia, J. R., and Cabral-Fonseca, S. 2018. "Durability of an epoxy adhesive used in civil structural applications." *Construction and Building Materials*, *161*, 618-633. https://doi.org/10.1016/j.conbuildmat.2017.11.168 0950-0618.

CHAPTER 2: PEEL AND CLEAVAGE STRENGTH TESTS WITH ADHESIVE CONNECTIONS IN DYNAMIC MESSAGE SIGNS

2.1 ABSTRACT

This paper aims to examine the mechanical properties of the adhesive focusing on peel strength and cleavage strength for varying environmental and geometrical conditions. To that end, peel and cleavage specimens with variations in width were fabricated and examined according to American Society for Testing and Materials (ASTM) after conditioning them in different environmental conditions, including temperature and humidity. The effect of temperature, humidity, and width on peel and cleavage strengths were graphically and statistically examined by analyzing the testing data. As part of the statistical analysis, regression models, encompassing multiple linear regression (MLR) and response surface metamodels (RSM), were established to predict the peel and cleavage strengths. Through evaluation of R-squared values and graphs of the predicted values against the testing data, it was found that the RSM was more accurate than MLR. Key results indicated that the peel strength of tested adhesive specimens was increased with the increment in humidity up to 30.1% and was decreased by the maximum reduction of 28.2% with increment in specimen's width, while the cleavage strength of the tested specimens improved with the peak increment of 27.4% and 28.5% when the temperature and specimen's width was increased, respectively. The cleavage strength, however, was decreased up to 13.7% with the increment in humidity. Findings from 3-D surfaces generated from the RSM to observe the effect of different parameters on the peel and cleavage strength of adhesive joints were in agreement to the

testing results. The statistical analysis indicated that the width was a significant parameter affecting the peel strength.

Keywords: Dynamic message sign; Peel; Cleavage; Strength; Adhesive.

2.2 INTRODUCTION

A dynamic message sign (DMS) is a digital message board that displays vital traffic information to commuters while traveling through highways for the convenience and safety of travelers. The DMS comprises a cabinet sheet aluminum skin, internal aluminum frame, sign controller, interconnect cable, and a traffic cabinet enclosure. The aluminum back-skin needs to be connected to the aluminum frame. The majority of the clients such as State Departments of Transportation prefer welded connections for connecting the aluminum back-skin with the frame of the DMS. However, an adhesive can be an appropriate substitute for these connections to be used in the DMS. The manufacture of various structures for automobile and aircraft is performed by bonding with adhesive. Higgins (2000) has stated that adhesive has been used for the fabrication of wing structures in aerospace from 1945. Some DMS producers have started using adhesives due to their advantages such as efficient fabrications and manufacturing labor reduction. Further, the adhesive can be a suitable replacement due to its ability to join metals with different melting points. More uniformly distributed loads can be observed in the connections bonded with adhesive than the welded connections. During the welding process, welders frequently find it difficult to join asymmetrical connections due to high residual stresses and distortion.

If adhesives have the potential to replace welding in DMS, there is a need to investigate cleavage and peel strength of adhesively bonded joints. Adhesives have been studied to

explore their mechanical properties resulting from tensile and shear tests by Seo and Lim (2005), Ferreira et al (2002), He et al. (2013), and recently the tensile and shear strength of the adhesive in DMS has been investigated considering varying environmental and geometrical parameters by Amatya et al. (2020). However, there are rarely studies pertaining to investigation of the effects of environmental and geometrical factors on the cleavage and peel strengths of the adhesive used for DMSs. Meanwhile, some studies performed by Shahid and Hashim (2000, 2002), You et al. (2008), and Cognard (1988) have been investigated to better understand the cleavage strength of small-scale adhesive specimens. Shahid and Hashim (2000) tested adhesively bonded cleavage specimens to determine their cleavage strengths with different adhesive thickness. The adhesive thickness was found to be highly insignificant to the measured cleavage strengths. Shahid and Hashim (2002) further investigated the effect of surface roughness on the cleavage strength of specimens through experimental testing. It was observed that the increase in roughness and surface area of adherend increased the cleavage strength. You et al. (2008) conducted laboratory testing of the cleavage joints to analyze the effect of recessing and/or gap length and reported slight decrement in the failure load of cleavage joints due to the gap length lower than 10 mm. Cognard (1988) investigated the cleavage of adhesive joints for the effect of water and indicated humidity beyond 70% increased the progression of crack in the adhesive joints.

Several studies (Kim and Aravas(1988, De Freitas and Sinke 2014, Broughton et al. 1999, Noori et al. 2016, Arouche 2018, Price and Sargent 1997) on peel strength tests have been also conducted for adhesively bonded substrates to understand the properties of the adhesive when subjected to peel loadings. For peel strength, previous research

accomplished by Kim and Aravas (1988), showed that peel strength was significant to the yield strength, Young's modulus, ductility and thickness of flexible adherend. De Freitas and Sinke (2014) determined the properties of adhesive using peel tests for bonded composite-to-aluminum joints, demonstrating that the peel load decreased when composite adherend was used instead of the flexible adherend. Broughton et al. (1999) conducted T-peel tests of the adhesively bonded specimens subjected to temperature, humidity, and load to determine their peel strength. It was reported that average peeling force was observed to be higher for smaller specimens due to higher and more uniform clamping forces being applied during curing. Noori et al. (2016) conducted the peel test of polymer laminated sheet metal specimens. It was found that the interfacial peel strength was greatly influenced by residual stress in the polymer adherend. Arouche (2018) delved into the effect of moisture on the peel strength of adhesive joints by immersing the specimens in salt water through floating roller peel tests and found decrease in peel strength due to the higher moisture uptake. Price and Sargent (1997) tested peel specimens to measure the fracture energy of adhesive with aluminum adherends, revealing that there was no significant change in peeling strength for the large width specimens.

The goal of this paper is to determine the peel and cleavage strength of the adhesive in use for DMS under various environmental and geometrical conditions. To pursue this goal, 64 adhesive specimens, including 32 peel and 32 cleavage specimens, were tested according to American Society for Testing and Materials (ASTM) to determine the peel and cleavage strength. The resulting strength quantities were graphically and statistically analyzed for the examination of the effect of temperature, humidity, and specimen width

on each of the strengths. Then, two regression models were further developed not only to predict the peel and cleavage strength, but also to better understand mechanical behaviors at different parametric conditions. Excluding this section, this paper deals with an overview of the experimental program, testing data and discussion, and statistical analysis along with data-driven conclusions.

2.3 EXPERIMENTAL PROGRAM

The experimental program involves the study of peel and cleavage tests with a variety of width, temperature and humidity conditions to determine the peel strength and cleavage strengths of respective specimens. This section explains the details of the experimental program used for testing the specimens. This includes the testing matrix and conditioning, description of the specimens, and testing.

2.3.1 TESTING MATRIX AND CONDITIONING

As shown in Table 2.1, sixteen different combinations considering three levels of temperature, humidity, and width were created to study the peel strength and cleavage strengths of adhesive connections in the use of DMS. It should be noted that each combination was comprised of two peel strength specimens and two cleavage specimens; thus, the total number of specimens was 64, including 32 peel and 32 cleavage specimens. A commercially available statistical software, JMP, was used based on to develop these combinations that served as a basis for efficient data analysis, according to Plackett-Burman Design (PDB) which was also used by Seo (2013). PDB allows an effective range of the critical parameters and development of statistical models that are

discussed in a later section of the paper. Temperature, humidity, and width of the specimens were used as inputs for statistical analysis. The experiment was designed for low, medium and high values for each of the input parameters studied (i.e., temperature, humidity, and width). Temperature values of 20°C, 52.5°C, and 85°C, humidity values of 48%, 71.5%, and 95%, and width values of 13 mm, 25 mm, and 38 mm were considered for variation in temperature, humidity, and width of specimens. The range of temperature and humidity were selected considering the capacity of the conditioning chamber where both temperature and humidity in the chamber can be achieved safely and efficiently. The recommended width of the peel and cleavage specimens as per ASTM D1876 (2008) and ASTM D1062 (2008) was 25 mm, however, specimen widths of 13 mm and 38 mm are also taken into account to explore the effect of width on the peel and cleavage strength.

Table 2.1 Combination table for the experimental program

Combination	Humidity (%)	Width (mm)	Temperature (°C)
C1	48.0	13.0	20.0
C2	48.0	38.0	20.0
C3	71.5	25.0	20.0
C4	95.0	13.0	20.0
C5	95.0	38.0	20.0
C6	48.0	25.0	52.5
C7	71.5	13.0	52.5
C8	71.5	25.0	52.5
C9	71.5	25.0	52.5
C10	71.5	38.0	52.5
C11	95.0	25.0	52.5
C12	48.0	13.0	85.0
C13	48.0	38.0	85.0
C14	71.5	25.0	85.0
C15	95.0	13.0	85.0
C16	95.0	38.0	85.0

All the specimens were conditioned in a temperature and humidity-controlled chamber in the Daktronics reliability lab (see Figure 2.1). For complete moisture saturation, all the specimens with the same humidity were grouped and conditioned in the chamber for 96 hours at the lowermost temperature. The specimens from the combination with the lowest temperature from the group were taken out of the chamber initially for the test. To condition the remaining specimens, the temperature was increased to the next lower temperature for an extra 24 hours. For instance, the specimens from the combinations C3, C7, C8, C9, C10, and C14 were left inside the chamber at 20°C and 71.5% humidity. The specimens from combination C3 were removed from the chamber and transported to the lab for testing after 96 hours of conditioning. The chamber temperature was increased to 52.5°C and conditioned for an additional 24 hours at the

same humidity. The specimens from the combinations C7, C8, C9, and C10 were taken to the lab for testing and the temperature of the chamber was further increased to 85°C at 71.5% humidity for the specimens with combination C14. The remaining specimens were tested after conditioning 24 hours. A graphical representation of the conditioning time for specimens at different temperatures and humidity are shown in Figure 2.2a and Figure 2.2b, respectively. The specimens were weighed prior conditioning, after conditioning, after transporting to the lab and after the test to observe the moisture absorption. Specimens were weighed at regular intervals. Moisture saturation was considered when no or minimum change in weight of the specimens were observed. Mylar bags were used to prevent the loss of moisture during transportation of the specimens from conditioning lab to the testing lab. A thick Styrofoam cooler was used to transport the specimens to avoid heat loss. Temperatures of the specimens were recorded after the specimens were brought to the lab and after the testing.

Figure 2.1: Temperature-humidity controlled chamber for conditioning of the specimens

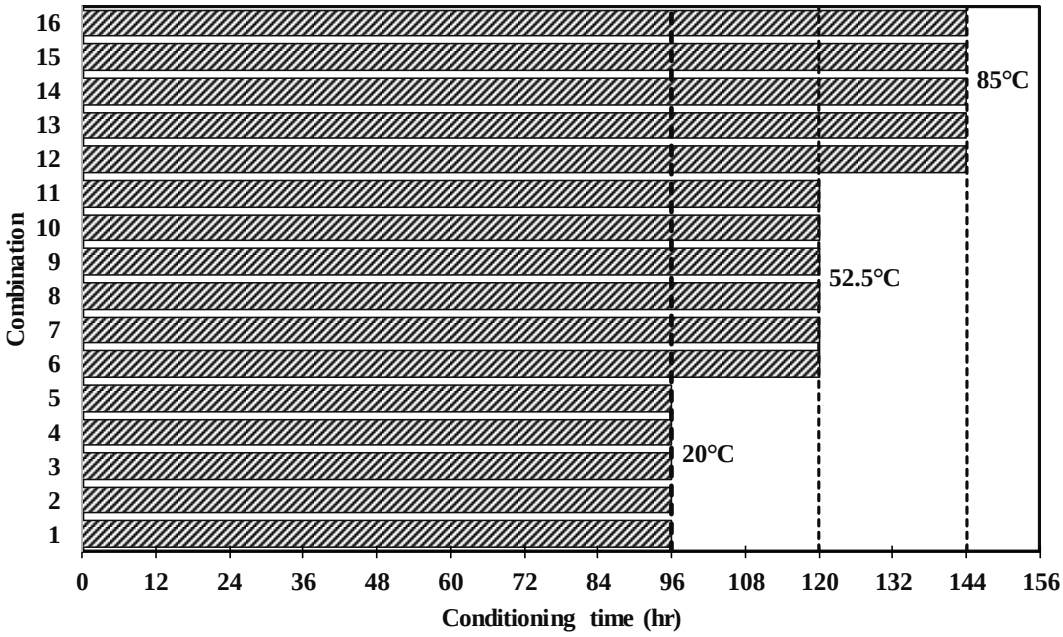

(a)

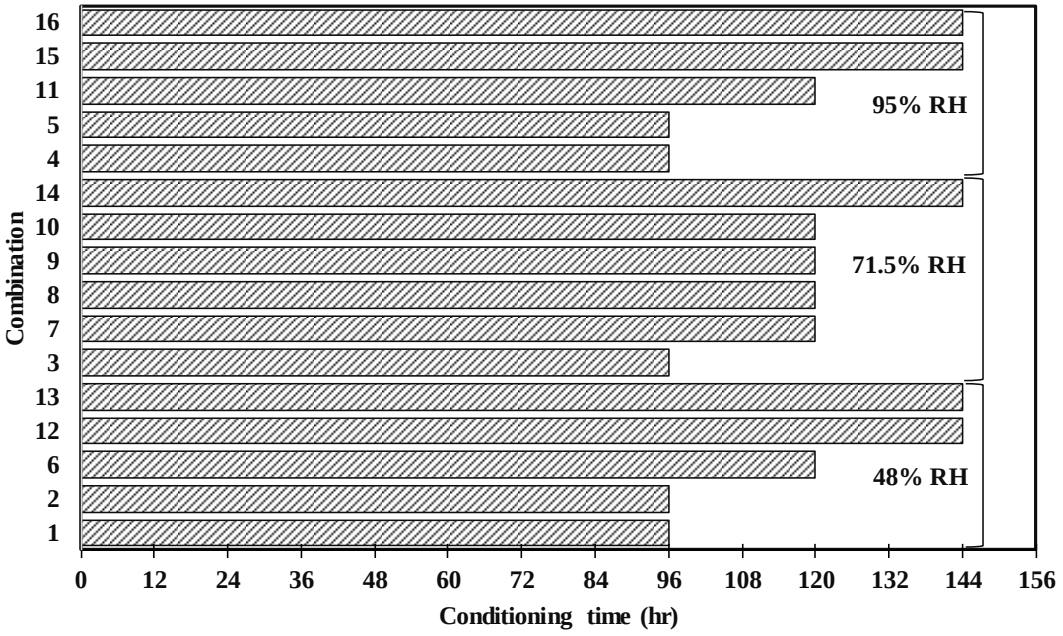

(b)

Figure 2.2: Conditioning period of the specimens for (a) temperature and (b) humidity

Each specimen was labeled with a specimen ID for efficient conditioning and testing. An example of the specimen ID is A-P-25TH-20T/71H-C3. The first letter represents the type of the specimens (A-adhesive), and the second letter denotes the type of test (P-peel/S-cleavage). The third letter (13TH, 25TH, and 38TH) stands for whether the width of the specimen is 13 mm, 25 mm or 38 mm. T/H indicates the temperature (20°C, 52.5°C, and 85°C) and humidity (48%, 71.5%, and 95%) of the conditioning chamber and C is the combination number from the testing matrix shown in Table 2.1. Table 2.2 presents the moisture and temperature change in the peel and cleavage specimens. The change in moisture and temperature presented in Table 2.2 represents the average value calculated from each of the two specimens for each combination. Note that in Table 2.2 change in moisture of the specimens before and after conditioning intervals is termed "moisture change after chamber (%)", between after conditioning and after transporting intervals is called "moisture change after transportation (%)", and between after transporting and after the testing intervals is called "moisture change after testing (%)." Absorption in moisture is specified by the positive change in moisture and loss in moisture is suggested by a negative change in moisture. At each interval, the majority of the specimens noticed an insignificant change in moisture. The temperature was measured after transporting the specimens to the testing lab and compared with the temperature measured after the test to evaluate the temperature change. This is termed "temperature change after testing (%)" in Table 2.2. The rise in temperature is denoted by a positive temperature change, whereas the loss in temperature is shown by a negative temperature change. It was revealed that the specimens conditioned at lower temperatures observed smaller temperature loss than the specimens conditioned at higher temperatures.

Table 2.2 Moisture and temperature change in peel and cleavage specimens

Test type	Combination	Specimen ID	Moisture change after chamber (%)	Moisture change after transportation (%)	Moisture change after testing (%)	Temperature change after testing (%)
Peel	C1	A-P-13TH-20T/48H-C1	-0.013	0.000	-0.011	+9.1
	C2	A-P-38TH-20T/48H-C2	+0.003	-0.011	-0.005	+9.1
	C3	A-P-25TH-20T/71H-C3	-0.001	-0.003	-0.007	+6.8
	C4	A-P-13TH-20T/95H-C4	+0.001	-0.003	-0.015	0.0
	C5	A-P-38TH-20T/95H-C5	+0.011	+0.009	-0.023	+9.1
	C6	A-P-25TH-52T/48H-C6	-0.011	-0.001	-0.004	-23.8
	C7	A-P-13TH-52T/71H-C7	-0.009	-0.003	-0.009	-26.5
	C8	A-P-25TH-52T/71H-C8	-0.006	-0.002	-0.004	-10.7
	C9	A-P-25TH-52T/71H-C9	-0.006	-0.003	-0.004	-10.7
	C10	A-P-38TH-52T/71H-C10	+0.007	-0.012	0.000	-9.1
	C11	A-P-25TH-52T/95H-C11	0.000	-0.004	-0.008	-25.0
	C12	A-P-13TH-85T/48H-C12	-0.029	-0.001	-0.006	0.0
	C13	A-P-38TH-85T/48H-C13	-0.002	-0.013	0.000	-35.8
	C14	A-P-25TH-85T/71H-C14	-0.011	0.000	-0.004	-26.7
	C15	A-P-13TH-85T/95H-C15	-0.001	-0.005	-0.013	-20.0
	C16	A-P-38TH-85T/95H-C16	+0.015	-0.015	0.000	-12.1
Cleavage	C1	A-C-13TH-20T/48H-C1	-0.001	0.000	+1.566	+4.5
	C2	A-C-38TH-20T/48H-C2	-0.002	+0.001	-0.003	+4.5
	C3	A-C-25TH-20T/71H-C3	+0.001	0.000	-0.001	0.0
	C4	A-C-13TH-20T/95H-C4	+0.003	-0.004	-0.003	6.4
	C5	A-C-38TH-20T/95H-C5	+0.001	-0.002	-0.003	+4.3
	C6	A-C-25TH-52T/48H-C6	-0.007	+0.002	-0.001	-27.0
	C7	A-C-13TH-52T/71H-C7	-0.002	0.000	0.000	-8.9
	C8	A-C-25TH-52T/71H-C8	-0.003	0.000	-0.001	-10.7
	C9	A-C-25TH-52T/71H-C9	-0.001	0.000	0.000	-12.5
	C10	A-C-38TH-52T/71H-C10	-0.002	0.000	0.000	-12.5
	C11	A-C-25TH-52T/95H-C11	0.000	-0.002	-0.002	-28.1
	C12	A-C-13TH-85T/48H-C12	-0.007	0.000	+0.002	-43.3
	C13	A-C-38TH-85T/48H-C13	-0.006	-0.001	+0.001	-40.5
	C14	A-C-25TH-85T/71H-C14	-0.002	-0.001	0.000	-37.7
	C15	A-C-13TH-85T/95H-C15	+0.004	-0.003	-0.003	-21.8
	C16	A-C-38TH-85T/95H-C16	0.000	-0.002	-0.003	-24.2

2.3.2 SPECIMENS

The peel and cleavage specimens were fabricated based on ASTM D1876 (2008) and ASTM D1062 (2008), respectively. For the fabrication of peel specimens, two 5052 aluminum metal bars were bent 90° to 76 mm from the end. The bent aluminum bars are adhesively bonded with LORD 406-19GB acrylic adhesive with a glass transition temperature of 72 °C. Cleavage specimens were fabricated with two metal blocks adhesively bonded with LORD 406-19GB acrylic adhesive in the middle of each specimen. Specimens were set aside for two weeks to allow for effective curing of the adhesive. The geometry of the representative peel and cleavage specimens with a width of 13 mm is shown in Figure 2.3.

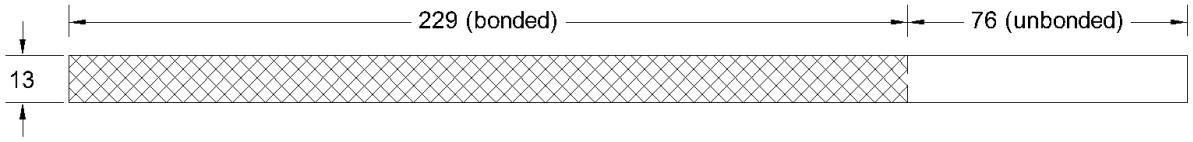

(a)

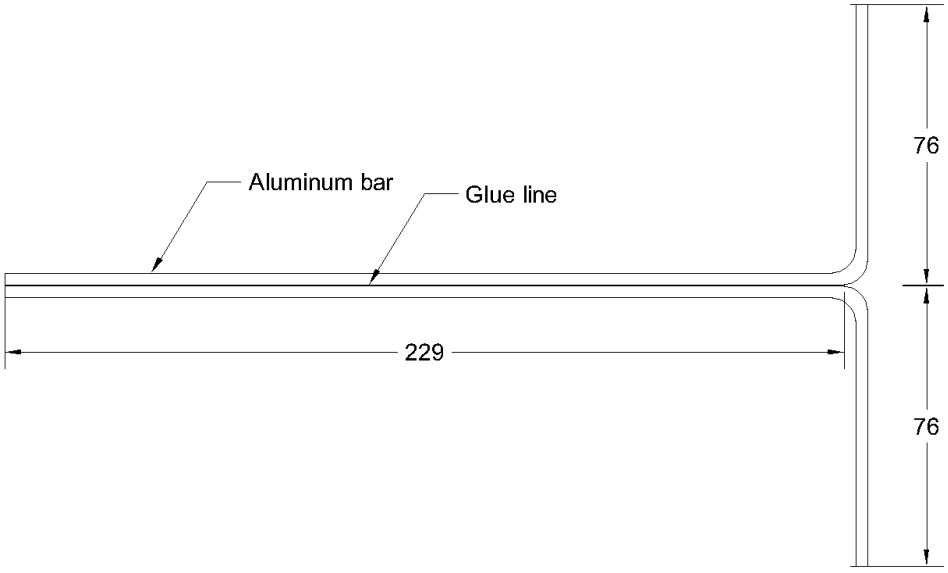

(b)

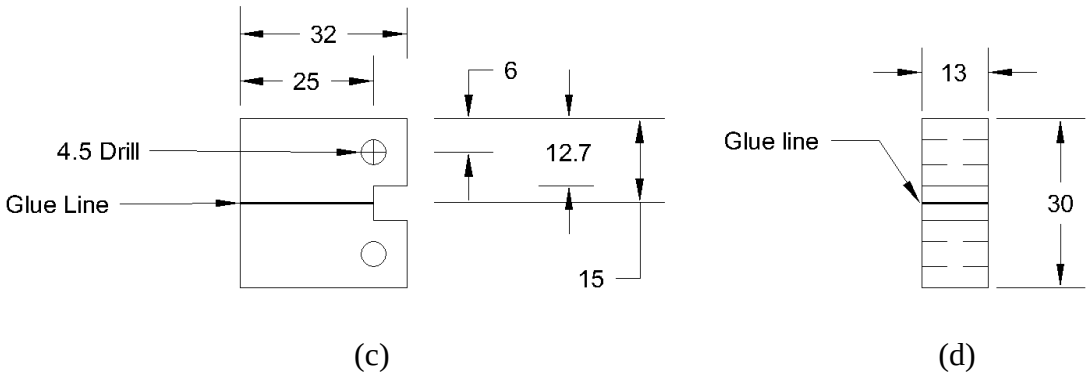

(c) (d)

Figure 2.3: Geometry of adhesive test specimens (a) top view of peel; (b) side view of peel; (c) side view of cleavage and (d) front view of cleavage (All dimensions are in mm).

2.3.3 TESTING

Peel tests were performed using an MTS Insight 5 whereas cleavage tests were performed using an MTS 370 Landmark 100-kN servo-hydraulic load unit calibrated to 20% of its load capacity. Each specimen was mounted and aligned in the grips of the testing machine. Tests were performed under a monotonic loading with a free crosshead speed of 254 mm/min for the peel specimens and 1.27 mm/min for the cleavage specimens. The load rating for the peel and cleavage tests are specified by ASTM D1876 and ASTM D1062, respectively. The testing setups for the peel specimen and for the cleavage specimen are shown in Figure 2.4a, and Figure 2.4Figure 1.4b, respectively. All the experiments were performed at room temperature.

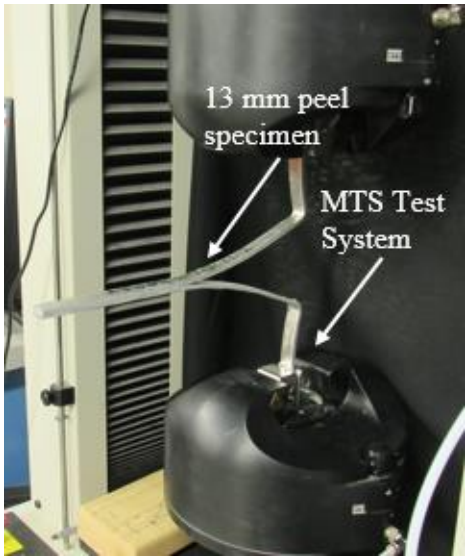

(a)

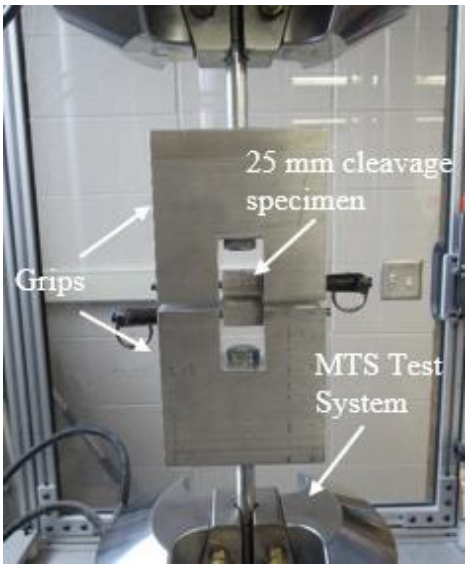

(b)

Figure 2.4: Installation of the specimens in the testing machine (a) peel and (b) cleavage

2.4 RESULTS AND DISCUSSION

Experimental results from the peel and cleavage tests are analyzed herein for the investigation of the effects of temperature, humidity, and specimen width on each strength. The results are, in detail, summarized and discussed in the following subsections.

2.4.1 PEEL STRENGTH

Load-displacement curves for all the tested peel specimens is presented in Figure 2.5. The peel strength (f_{ap}) of the first and second specimens is calculated by evaluating the average load per unit width for the first 127 mm of peeling after the initial peak from the load-displacement curve. This process was repeated to determine the first and second specimens under each combination, and the average and standard deviation of both the specimens' peel strengths per combination were calculated. The resulting peel strengths

with the standard deviations for all the combinations and corresponding failure modes are summarized in Table 2.3. Note, the peel strength (ASTM D1876 2008) was calculated from the Equation 2.1.

$$f_{ap} = Average\left({}^{P}/_{W}\right) \quad \text{(Equation 2.1)}$$

where f_{ap} is the peel strength, P is the load recorded during the test, and W is the width of the peel specimen.

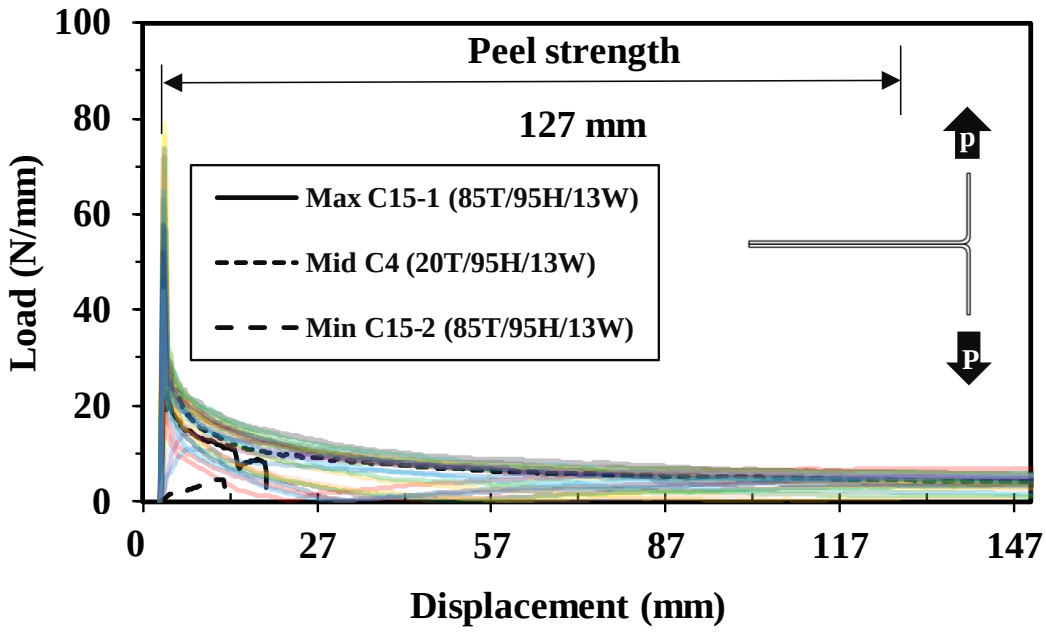

Figure 2.5: Load-displacement curves for all the tested peel specimens

Table 2.3 Mechanical properties from all the peel tests

Combination	Specimen	Peel strength, f_{ap}(N/mm)	Failure mode
C1	A-P-13TH-20T/48H-C1	8.10 ± 0.10	Cohesive
C2	A-P-38TH-20T/48H-C2	5.82 ± 2.13	Cohesive
C3	A-P-25TH-20T/71H-C3	4.41 ± 0.62	Cohesive
C4	A-P-13TH-20T/95H-C4	8.28 ± 0.80	Cohesive
C5	A-P-38TH-20T/95H-C5	6.55 ± 2.46	Cohesive
C6	A-P-25TH-52T/48H-C6	5.77 ± 2.35	Cohesive
C7	A-P-13TH-52T/71H-C7	7.73 ± 0.77	Cohesive
C8	A-P-25TH-52T/71H-C8	7.51 ± 2.27	Cohesive
C9	A-P-25TH-52T/71H-C9	6.54 ± 3.33	Cohesive
C10	A-P-38TH-52T/71H-C10	6.10 ± 2.95	Cohesive
C11	A-P-25TH-52T/95H-C11	5.03 ± 0.96	Cohesive
C12	A-P-13TH-85T/48H-C12	6.79 ± 1.08	Cohesive
C13	A-P-38TH-85T/48H-C13	5.84 ± 1.96	Cohesive
C14	A-P-25TH-85T/71H-C14	7.63 ± 0.56	Cohesive
C15	A-P-13TH-85T/95H-C15	7.75 ± 5.05	Adhesive
C16	A-P-38TH-85T/95H-C16	6.16 ± 2.38	Cohesive

Figure 2.6 presents the representative failure modes of the tested peel specimens. The peel specimens failed with two different types of failure modes, which encompass cohesive or adhesive failure. The fracture surfaces of the tested specimens were analyzed to determine the failure mode of each of the tested specimens. Only combination 15 specimens were failed with an adhesive failure mode as shown in Figure 2.6a. Adherend was separated from the adhesive layer when the specimens failed with the adhesive failure mode. In this figure, adhesive appears to be completely detached from one surface of the aluminum. A cohesive failure mode is observed in all the other combination specimens. Figure 2.6b displays a representative picture for the cohesive failure mode. In this figure, the adhesive is observed in both surfaces of the failed peel specimen.

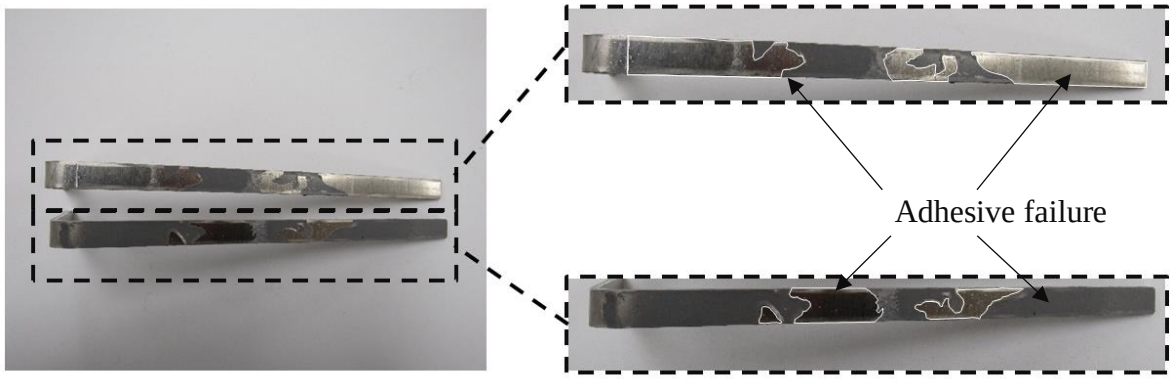

(a)

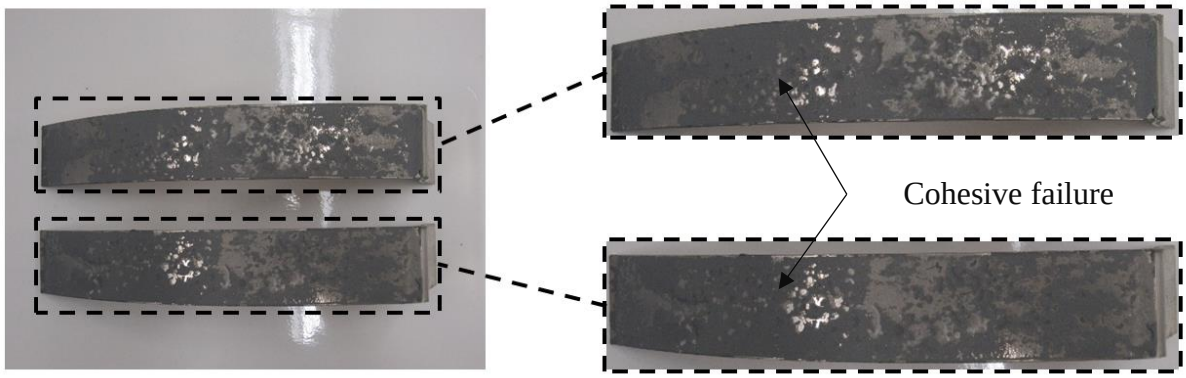

(b)

Figure 2.6: Representative failure modes of peel specimens (a) adhesive failure and (b) cohesive failure

2.4.1.1 EFFECT OF TEMPERATURE

To investigate the influence of temperature on the peel strength of adhesive, the specimens conditioned at different temperatures were compared. Figure 2.7 depicts the temperature effect on the average peel strength in the bar graph with the percent difference. For specimens of 13 mm width, the peel strength is reduced by 16.3% at 48% humidity and by 6.4% at 95% humidity when the temperature is increased from 20 °C to

85 °C as illustrated in pairs C1-C12 and C4-C15 in this figure. At 71.5% humidity, when the temperature elevates from 20 °C to 52.5 °C, the peel strength is increased by 70.4% for 25 mm width specimens as depicted in C3-C8 pair. The peel strength further increases by 1.6% after the elevation of temperature to 85 °C from 52.5 °C as shown in C8-C14 pair. As presented in a pair of C2-C13, the peel strength is increased by 0.4% at 48% humidity after the elevation of temperature to 85 °C from 20 °C, however, it is decreased by 5.9 % at 95 % humidity for specimens with 38 mm width from 20 °C to 85 °C (see C5-C16 in Figure 2.7). Other than a significant increase of 70.4% in the peel strength with the increment of temperature from 20 °C to 52.5 °C, the peel strength is not found to be significantly affected by temperature of the conditioning environment. Figure 2.8 also shows a representative, graphical representation of the effect of temperature on the peel strength based on the average value and standard deviation of peel strengths acquired from the tested peel specimens with 38 mm width. When the temperature of 38 mm width specimens is increased to 85 °C from 20 °C, the peel strength increases at 48% humidity, however, it decreases at 95% humidity.

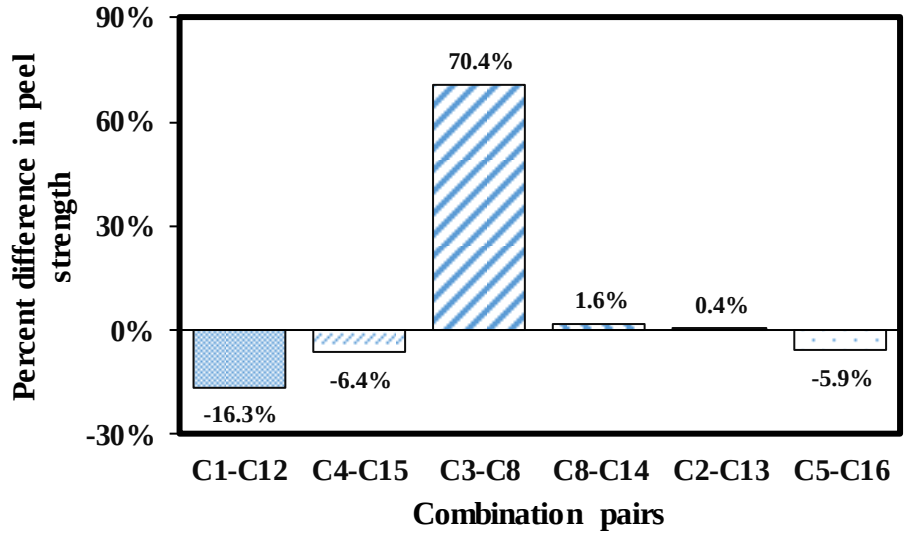

Figure 2.7: Percent difference in peel strength due to the variation in temperature with a fixed humidity and width.

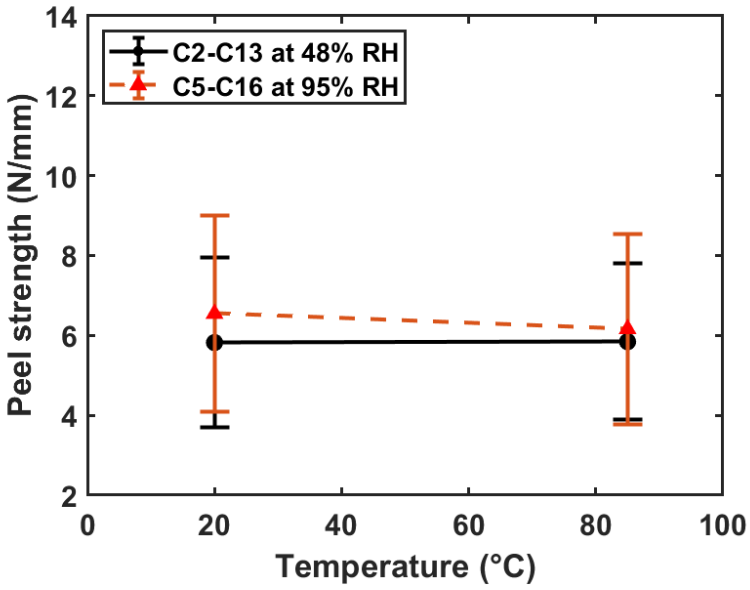

Figure 2.8: Temperature effect on the representative peel strength for the specimens with 38 mm width

2.4.1.2 EFFECT OF HUMIDITY

The effect of humidity on the peel strength in terms of percent difference among different combination pairs is explored as shown in Figure 2.9. In this figure, for

specimens with 13 mm width, the peel strength is raised by 2.2% at 20 °C (see a pair of C1-C4) and 14.3% at 85 °C (see a pair of C12-C15), respectively, when the humidity is increased from 48% to 95%. At 52.5 °C, when humidity is elevated from 48% to 71.5%, the peel strength is increased by 30.1% for 25 mm width specimens as shown in C6-C8 pair. The peel strength is, however, decreased by 33% after the elevation of humidity from 71.5% to 95% as shown in C8-C11. The peel strength is increased by 12.5% at 20 °C as shown in pair C2-C5 and by 5.5% at 85 °C as displayed in pair C13-C16 for specimens of 38 mm width after the elevation of humidity from 48% to 95 %. The trend of the testing results indicated improvement in the peel strength of the specimens with increment in humidity, although a peak reduction of 33% in the peel strength of 25 mm specimens is observed when humidity is increased from 71.5% to 95%. The effect of humidity on the average peel strength with the standard deviations is also graphically examined as shown in Figure 2.10 for an example for the peel specimen pairs with 38 mm width. In this figure, as the humidity of 38 mm width specimens is increased from 48% to 95%, the peel strength is observed to be improved at both 20 °C and 85 °C.

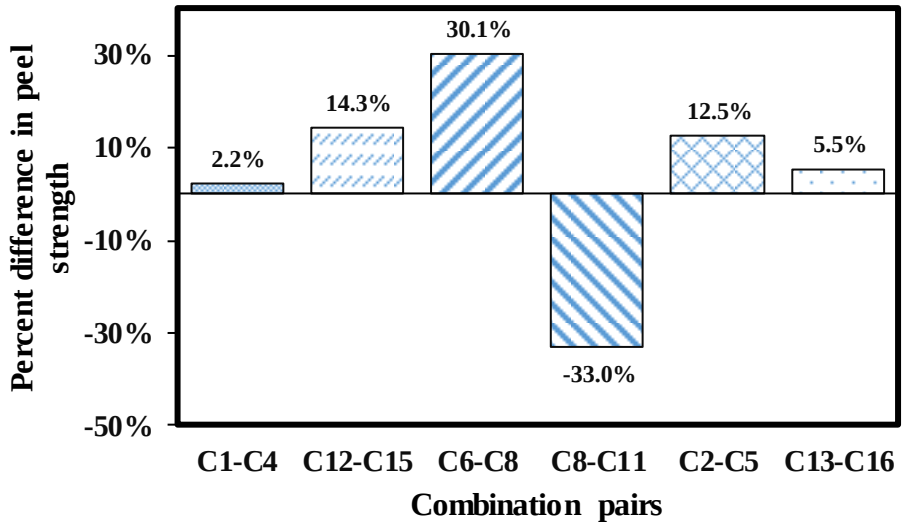

Figure 2.9: Percent difference in peel strength due to the variation in humidity with a fixed temperature and width

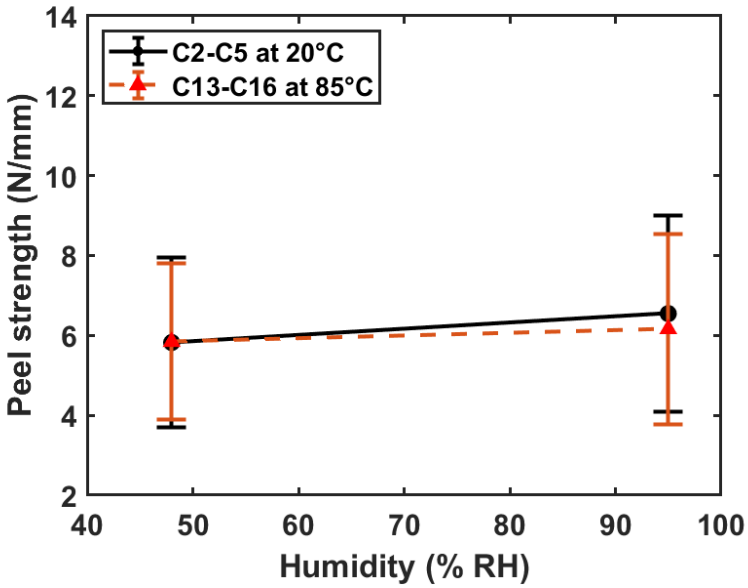

Figure 2.10: Humidity effect on peel strength for specimens with for 38 mm width

2.4.1.3 EFFECT OF WIDTH

Figure 2.11 portrays the percent difference of peel strength in a bar graph due to the effect of width. For specimens at 20°C, the peel strength is reduced by 28.2% at 48% humidity (see a pair of C1-C2) and by 20.9% at 95% humidity (see a pair of C4-C5), when the width of the specimen is increased from 13mm to 38mm. At 52.5°C, when the specimen width is increased from 13 mm to 25 mm, peel strength declines by 2.8% at 71.5% humidity as seen in C7-C8. At the same humidity as in C7-C8, the peel strength further decreases by 18.8 % after the increment of width to 38 mm from 25 mm (refer to C8-C10). The peel strength is dropped by 13.9% at 48% humidity (see C12-C13) and 20.5% at 95% humidity (see C15-C16) for the four specimens conditioned at 85°C with the increment of specimen width from 13mm to 38mm. Based on these results, it can be concluded that the width of specimen is inversely proportional to its peel strength, which can explain the negative effect of the specimen's width on the peel strength. This trend occurs because increase in the adherend surfaces of each of the specimens that were predominantly failed with cohesive failure, which means low adhesion between the surfaces, was caused by the increment in the specimen width. As an example of the investigation of the width effect on the average peel strengths and corresponding standard deviations, Figure 2.12 shows the tested specimens at 20°C among the considered specimen pairs. It appears that the peel strength reduces at both 48% and 95% humidity due to the increase in width from 13 mm to 38 mm.

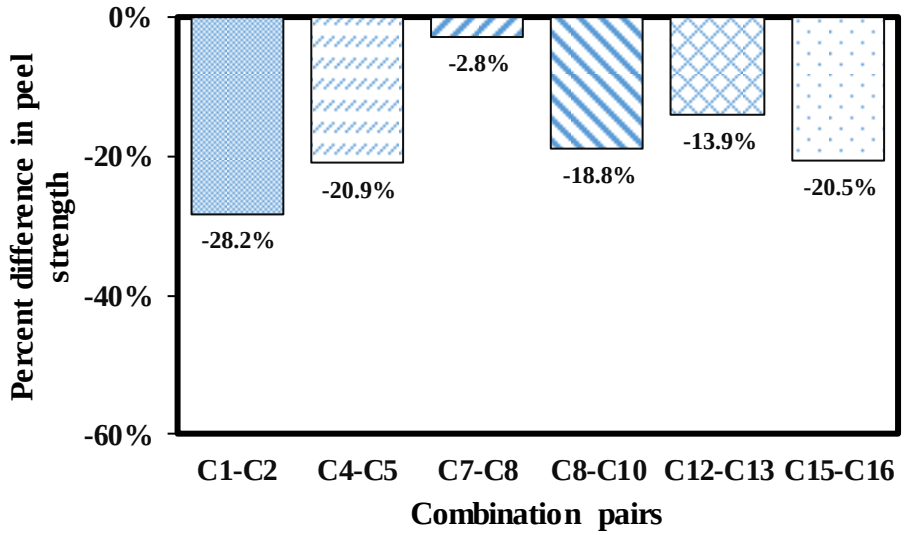

Figure 2.11: Percent difference in peel strength due to the variation in width with a fixed temperature and humidity

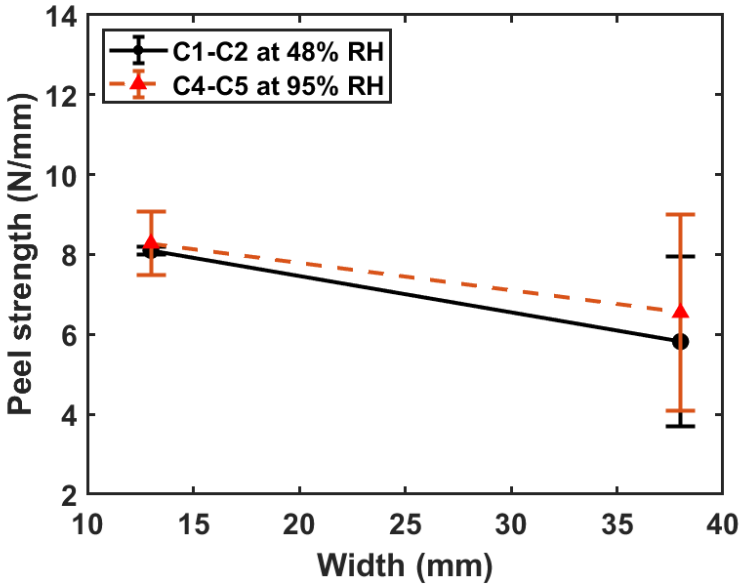

Figure 2.12: Width effect on peel strength for specimens at 20°C

2.4.2 CLEAVAGE TEST

Load-displacement curves encompassing the behavior of all the cleavage specimens is shown in Figure 2.13. The cleavage strength of the specimens was calculated by taking the maximum load from the load-displacement curve and dividing that load by respective specimen width. Then, the average of both the specimens was determined for this combination. This was applied to specimens conditioned at each of the remaining combinations to determine the average cleavage strengths. All the results of cleavage tests with failure modes are summarized in Table 2.4. The cleavage strength was calculated from Equation 2.2.

$$f_c = {}^{P_{cu}}/_{W} \qquad \text{(Equation 2.2)}$$

where f_c is the cleavage strength, Pc_u is the maximum load, and W is the width of the cleavage specimen.

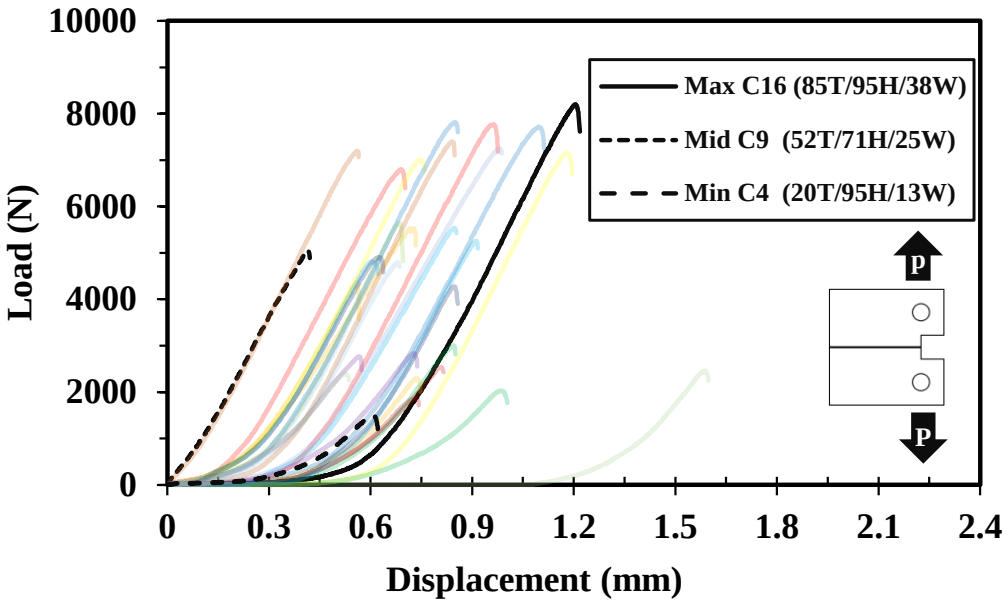

Figure 2.13: Load-displacement curves for cleavage specimens

Table 2.4 Mechanical properties from the cleavage tests

Combination	Specimen	Cleavage strength, (N/mm)	Failure mode
C1	A-C-13TH-20T/48H-C1	173.52 ± 25.90	Cohesive
C2	A-C-38TH-20T/48H-C2	191.19 ± 12.67	Cohesive
C3	A-C-25TH-20T/71H-C3	195.01 ± 22.86	Cohesive
C4	A-C-13TH-20T/95H-C4	149.75 ± 31.15	Cohesive
C5	A-C-38TH-20T/95H-C5	185.77 ± 1.72	Cohesive
C6	A-C-25TH-52T/48H-C6	216.15 ± 6.10	Cohesive
C7	A-C-13TH-52T/71H-C7	198.32 ± 38.41	Cohesive
C8	A-C-25TH-52T/71H-C8	198.11 ± 8.73	Cohesive
C9	A-C-25TH-52T/71H-C9	208.16 ± 10.00	Cohesive
C10	A-C-38TH-52T/71H-C10	254.55 ± 49.38	Cohesive
C11	A-C-25TH-52T/95H-C11	180.67 ± 12.43	Cohesive
C12	A-C-13TH-85T/48H-C12	220.62 ± 2.85	Cohesive
C13	A-C-38TH-85T/48H-C13	191.54 ± 2.65	Cohesive
C14	A-C-25TH-85T/71H-C14	188.74 ± 0.11	Cohesive
C15	A-C-13TH-85T/95H-C15	190.76 ± 2.70	Cohesive
C16	A-C-38TH-85T/95H-C16	202.82 ± 12.46	Cohesive

Failure modes of the cleavage specimens are shown in Figure 2.14. The failure modes of the cleavage specimens were categorized by observing the fracture surfaces of the tested cleavage specimens. As shown in Figure 2.14, adhesive was found on the both aluminum surfaces of specimens after failure. All cleavage specimens are found to be failed with the cohesive failure mode. Adhesive layer of the representative cleavage specimens after the test is shown in Figure 2.14a for 13 mm width and Figure 2.14b for 38 mm width, respectively.

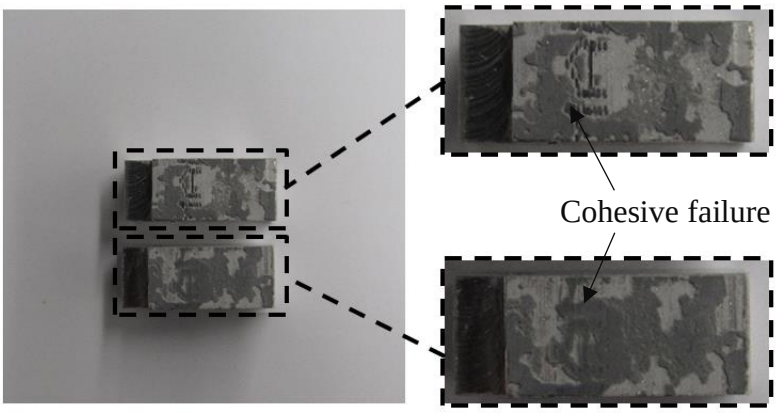

(a)

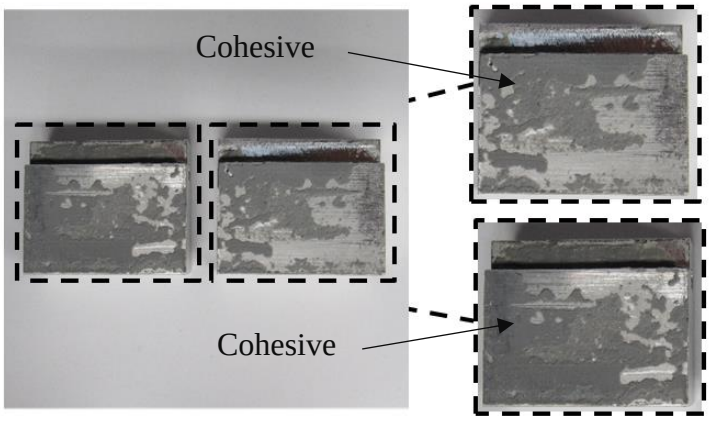

(b)

Figure 2.14: Representative failure modes of cleavage specimens (a) 13 mm and (b) 38 mm

2.4.2.1 EFFECT OF TEMPERATURE

Figure 2.15 demonstrates the bar graph depicting the temperature effect in cleavage strength. For specimens of 13 mm width, cleavage strength is increased by 27.1% at 48% humidity as shown in pairs C1-C12 and by 27.4% at 95% humidity as shown in pairs C4-C15 when the temperature is increased from 20 °C to 85 °C. At 71.5% humidity, when the temperature increases from 20 °C to 52.5 °C, cleavage strength is slightly improved by 1.6% for 25 mm width specimens (see a pair of C3-C8). The cleavage strength, on the contrary, is decreased by 4.7% after the elevation of temperature to 85 °C from 52.5 °C as depicted in pair C8-C14. The cleavage strength is only increased by 0.2% at 48% humidity as depicted in pair C2-C13 and by 9.2% at 95 % humidity as displayed in pair C5-C16 for specimens of 38 mm width after the elevation of temperature from 20 °C to 85 °C. While a slight decrement of 4.7% in the cleavage strength of 25 mm specimens is observed with increment of temperature from 52.5 °C to 85 °C, the general trend of the cleavage testing results suggests rise in the cleavage strength with increment in the conditioning temperature. In addition to the bar graph, the effect of temperature on the average cleavage strength with the standard deviations is shown diagrammatically in Figure 2.16 for the specimens with 38mm width in particular. This indicates that the cleavage strength is slightly increased at 48% humidity, and is moderately increased at 95% humidity as a result of increase of temperature from 20°C to 85°C.

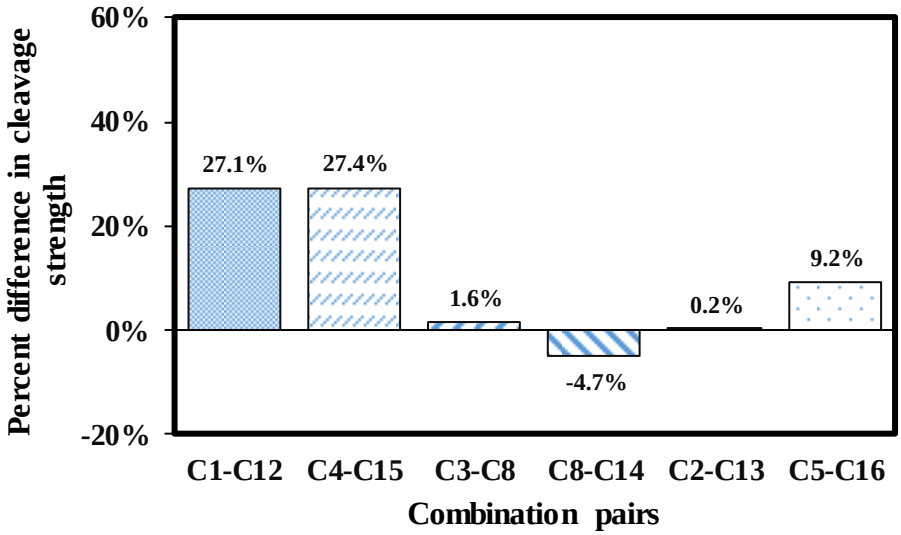

Figure 2.15: Percent difference in cleavage strength due to the variation in temperature with a fixed humidity and width

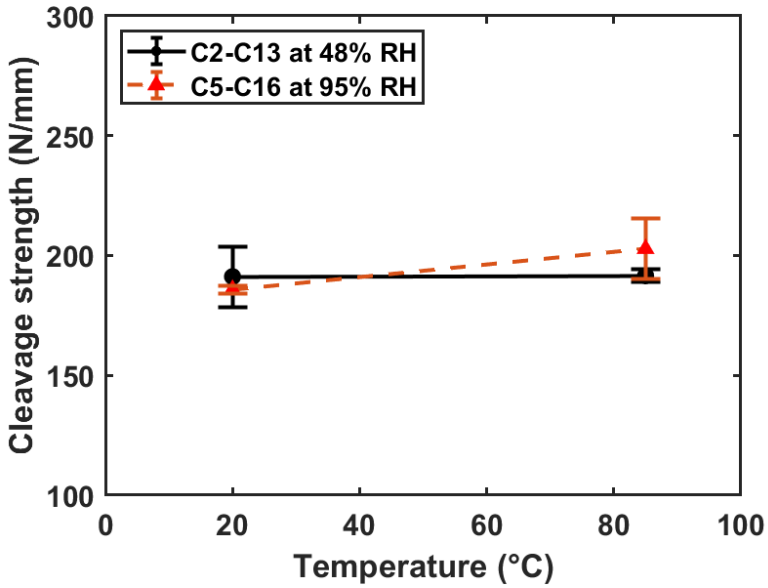

Figure 2.16: Temperature effect on cleavage strength for specimens with 38 mm width

2.4.2.2 EFFECT OF HUMIDITY

Figure 2.17 shows the effect of humidity on cleavage strength in terms of percent difference among combination pairs. For specimens of 13 mm width, the cleavage strength is reduced by 13.7% at 20 °C (see a pair of C1-C4) and by 13.5% at 85 °C (see a pair of C12-C15), respectively, when humidity is increased from 48% to 95%. At 52.5 °C, when humidity is increased from 48% to 71.5%, the cleavage strength declines by 8.3% for 25 mm width specimens as displayed in pair C6-C8. The cleavage strength of 25 mm width specimens is further decreased by 8.8% after the elevation of humidity to 95% from 71.5% as depicted in pair C8-C11. The cleavage strength decreases by 2.8% at 20 °C (see a pair of C2-C5) but is increased by 5.9 % at 85 °C for 38 mm specimens after the elevation of humidity from 48% to 95% as shown in pair C13-C16. Following the general trend of the test results, increase in the conditioning humidity is found to have negative effect with reduction in the cleavage strength. Increase in humidity increased the moisture penetrations, which in turn decreased the cleavage strength of the tested specimens. A representative comparison of the effect of humidity in the average cleavage strength with corresponding standard deviations for the specimens with 38mm width is shown in Figure 2.18. In this figure, the cleavage strength of 38 mm width specimens decreases at 20 °C, however, cleavage strength increases at 85 °C due to the increase in humidity from 48% to 95%.

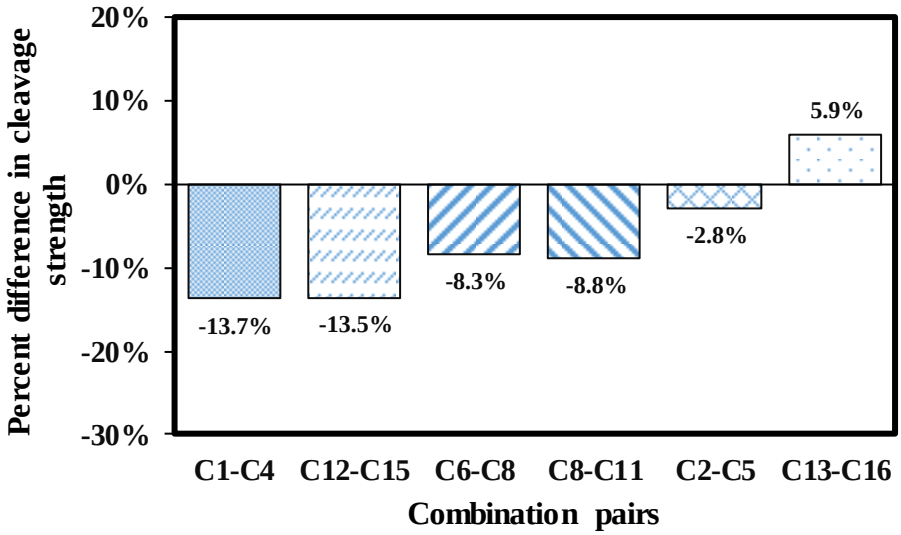

Figure 2.17: Percent difference in cleavage strength due to the variation in humidity with a fixed temperature and width

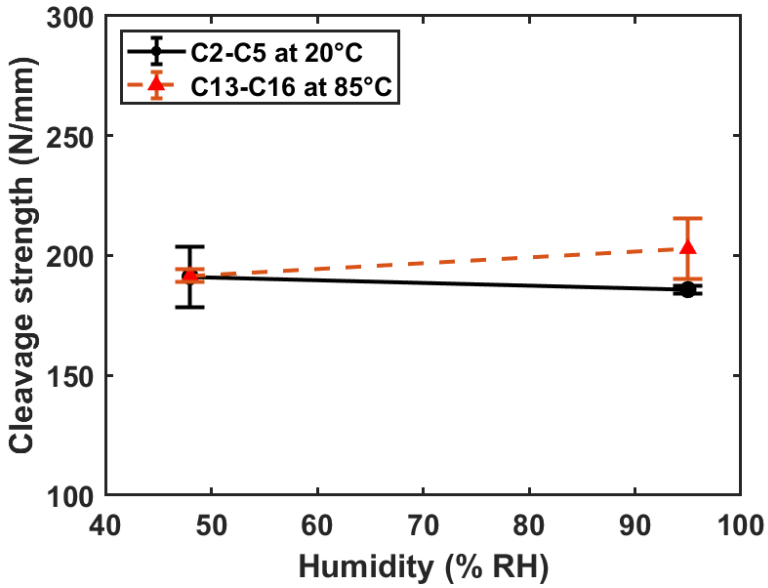

Figure 2.18: Humidity effect on cleavage strength for specimens with 38mm width

2.4.2.3 EFFECT OF WIDTH

Figure 2.19 illustrates the percent difference of cleavage strength due to the effect of width in a bar graph. For specimens at 20°C, the cleavage strength is increased by 10.2% at 48% humidity as shown in pair C1-C2 and by 24.1% at 95% humidity as shown in pair C4-C5 when the width of the specimen increases from 13mm to 38mm. At 52.5°C, when the specimen width increases from 13 mm to 25 mm, cleavage strength declines by 0.1% at 71.5% humidity (C7-C8). At the same temperature and humidity, the cleavage strength, however, increases by 28.5% after the increment of width to 38 mm from 25 mm as displayed in pair C8-C10. The cleavage strength decreases by 13.2% at 48% humidity (C12-C13), however, the cleavage strength increases by 6.3% at 95% humidity (C15-C16) for specimens at 85°C with the increment of specimen width from 13mm to 38mm. Even though decrement of 0.1% and 13.2% is found in the cleavage strength for two combination pairs, increment in specimen's width is observed to have positive influence in the cleavage strength while examining the overall trend. This is understandable as increase in width increases the area of adhesive region, which ultimately increases the load resisting capacity of the cleavage specimens. This result is in agreement with the findings from the literature of Shahid and Hashim (2002), where cleavage strength was increased with the increase in surface area of the adherend. Figure 2.20 shows the effect of width on the average cleavage strength and standard deviations for the specimens at 85°C particularly. This reveals that the cleavage strength decreases at 48% humidity, but it increases at 95% humidity for specimens at 85°C with the increment of specimen width from 13mm to 38mm.

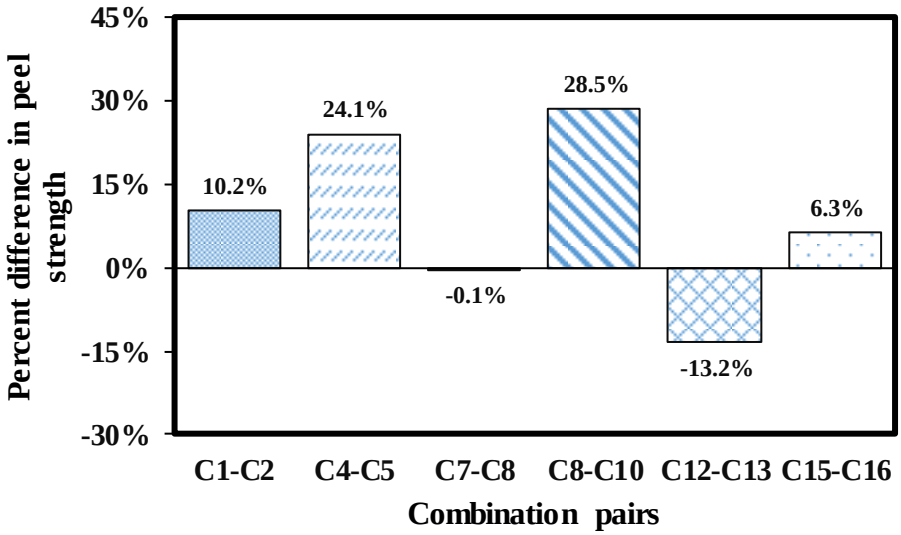

Figure 2.19: Percent difference in cleavage strength due to the variation in width with a fixed temperature and humidity

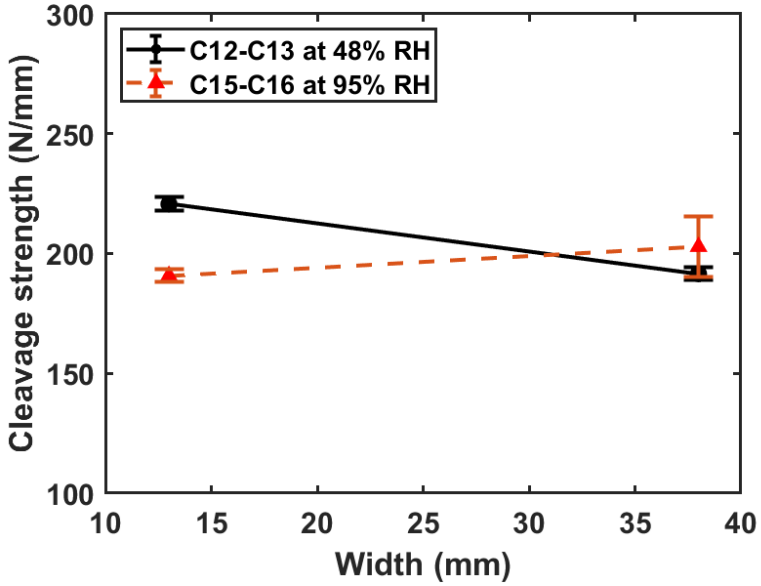

Figure 2.20: Width effect on cleavage strength for specimens at 85°C

2.5 STATISTICAL ANALYSIS ON TESTING DATA

The results obtained from the testing is further investigated through statistical analysis. The following sections attempt to find the significant parameters affecting the peel and cleavage strength and generate a statistical model for the prediction of respective peel and cleavage strength at various geometrical and environmental conditions.

2.5.1 REGRESSION MODEL

To explore the significance of each parameter on the peel and cleavage strength of specimens in a efficient manner, multiple linear regression (MLR) model and response surface metamodels (RSM) were developed. Note, Kokaly and Clark (1999) has used MLR model, whereas RSM model has been applied by Seo and Linzell (2010, 2012, 2013) to evaluate the effect of various input factors on outcomes of respective research. A statistical software R was employed to generate both MLR and RSM models using the data resulting from the experimental program. Three input parameters, including temperature and humidity of the conditioning environment and width of the specimens, were considered in the statistical model. Equation 2.3 and Equation 2.4 present the MLR and RSM models, respectively for the prediction of the peel strength.

$$f_{ap}(MLR) = 7.6609 + 0.0031 * T + 0.0061 * H - 0.0644 * W \quad \text{(Equation 2.3)}$$

$$f_{ap}(RSM) = 11.4711 - 0.2503 * T + 0.1656 * H - 0.1796 * W + 0.0462 * T * H + 0.0072 * T * W - 0.0004 * H * W + 0.0796 * T^2 - 0.5353 * H^2 + 0.0015 * W^2 \quad \text{(Equation 2.4)}$$

where f_{ap} = the peel strength, T = the conditioning temperature, H = the conditioning humidity, and W = the specimen width.

The equations for the prediction of the cleavage strength from the MLR and RSM models are shown in Equation 2.5 and Equation 2.6, respectively.

$$f_c(MLR) = 187.3232 + 0.3054 * T - 0.3543 * H + 0.7315 * W \quad \text{(Equation 2.5)}$$

$$f_c(RSM) = 243.5033 + 26.9055 * T - 22.6119 * H - 1.7691 * W + 1.3262 * T * H - 0.3479 * T * W + 0.2927 * H * W - 20.4477 * T^2 - 13.9127 * H^2 + 0.0218 * W^2 \quad \text{(Equation 2.6)}$$

where f_c = the cleavage strength, T = the conditioning temperature, H = the conditioning humidity, and W = the specimen width.

2.5.2 SIGNIFICANT PARAMETERS

To determine the significant parameters affecting each of the peel and cleavage strengths, P-values from both MLR and RSM models were examined. The P-values were acquired from each model during the creation of individual MLR and RSM models. The standard level of significance was set at 5% for the analysis where P-value less than 0.05 was considered significant. The P-value for each parameter subjected to the peel and cleavage strength is presented in Table 2.5. The width was found to be the most significant parameter for the peel strength as the P-value of the MLR model for the peel strength is less than 0.05. The significance of the specimen's width on the peel strength observed from the statistical analysis is also analogous to the results acquired from the experimental testing. A substantial effect of width was observed for the peel strength of

the tested specimens. Both MLR and RSM models did not found input parameters (temperature, humidity, and width) significant as the P-values for each parameter were observed to be greater than 0.05.

Table 2.5 P-values acquired from the statistical analysis to evaluate peel and cleavage strength

Parameter	MLR		RSM	
	Peel strength	Cleavage strength	Peel strength	Cleavage strength
T	0.75540	0.1580	0.80105	0.1188
H	0.65950	0.2300	0.72175	0.1778
W	**0.02480**	0.1840	0.07834	0.1394
T:H	-	-	0.91470	0.8351
T:W	-	-	0.68182	0.1974
H:W	-	-	0.97824	0.2685
T^2	-	-	0.91737	0.1026
H^2	-	-	0.50150	0.2383
W^2	-	-	0.24176	0.2324

Note: T, H, and W represent temperature, humidity, and the width of the specimens, respectively.

2.5.3 MLR AND RSM MODEL COMPARISON

The aim of this section is to present a reliable model that can predict the peel and cleavage strength for the adhesive connection with respect to different parameters taken for the study. The coefficient of determination (R^2 value) of the RSM models for the peel and cleavage strength is higher than the MLR model as presented in Table 2.6. The higher R^2 value of the model indicates better reliability of the model for the prediction of peel and cleavage strength. The predicted peel and cleavage strength from the RSM models were observed to be more accurate than the strength values predicted from MLR

models; thus, the RSM models were considered for predicting the peel and cleavage strengths with various environmental and geometrical parameters.

The experimental versus predicted strengths from the MLR and RSM models are also shown in Figure 2.21 to compare the precision of the models graphically. The comparison of MLR and RSM models for the peel strength is presented in Figure 2.21a. In this figure, the lowest variation of peel strength found between the RSM values and experimental data is only 0.07%, however, the MLR values and experimental data are differed by 0.82%. As shown in Figure 2.21b, the cleavage strengths predicted from the MLR and RSM models are compared against the corresponding experimental values. It should be noted that the lowest variations between the predicted values from each of the MLR and RSM models and experimental cleavage strength were calculated. The cleavage strength from the RSM model varies by only 0.53%, while that from the MLR model is differed by 1.51%. Based on the graphical comparisons, it was confirmed that the RSM models better predicted both the strengths than the MLR models.

Table 2.6 Multiple R-squared values for MLR and RSM models

Multiple linear regression (MLR)		Response surface metamodels (RSM)	
Peel strength	Cleavage strength	Peel strength	Cleavage strength
0.3646	0.328	0.5346	0.7695

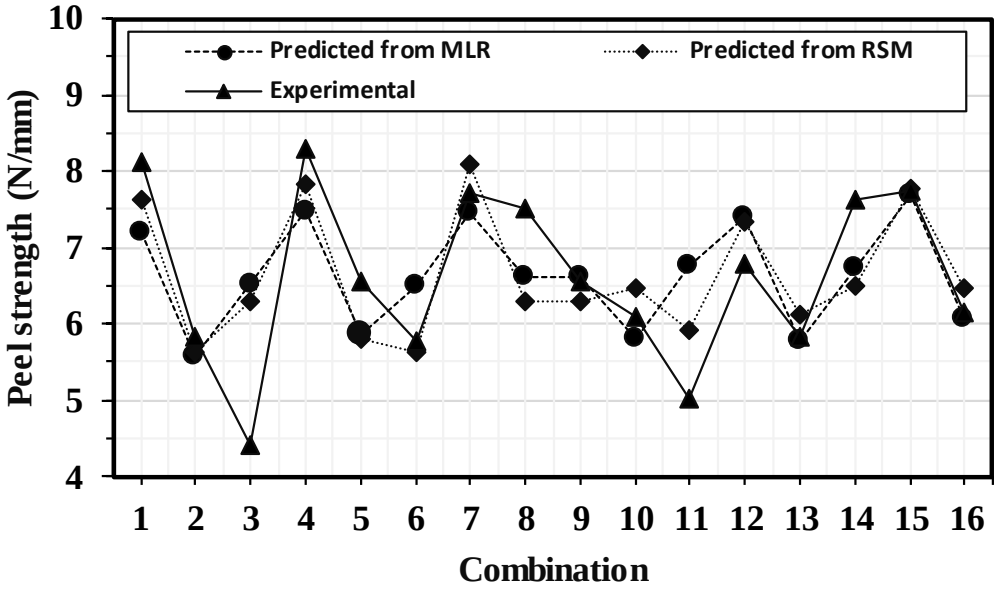

(a)

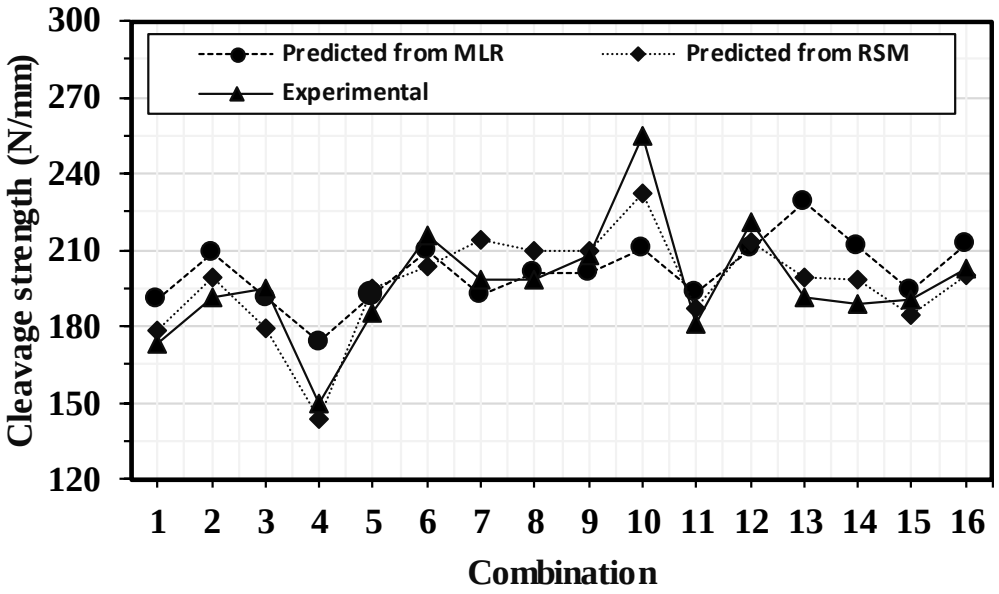

(b)

Figure 2.21: Experimental strength versus predicted strength from the MLR and RSM model (a) peel strength and (b) cleavage strength

2.5.4 RSM SURFACES

This section presents the use of an RSM model to determine the effects of temperature, humidity, and width on the peel and cleavage strength. The RSM model, Equation 2.4, was used to create a three-dimensional (3-D) surface for the peel strength to explore the RSM responses with respect to variation in a pair of different considered parameters. Specifically, the peel strength was plotted for two input parameters at a time with a fixed average value for the third parameter as shown in Figure 2.22a through Figure 2.22c. For example, an average value of humidity is considered for the RSM model to examine the effects of temperature and width on the peel strength and to develop the corresponding surface plot as displayed in Figure 2.22b.

In Figure 2.22a, an increase in temperature decreased the peel strength by 5.06% at lower humidity and 1.77% at higher humidity. The peel strength is observed to increase at first reaching a maximum and then dropping to a minimum when humidity is increased without regard to temperature. The peel strength is ultimately increased by 3.33% at a lower temperature and 6.91% at a higher temperature after dropping from the highest value. The peel strength for different width and temperature is shown in Figure 2.22b. The increase in width is observed to decrease the peel strength with a slight increment at the end. At a lower temperature, the increase in width decreased the peel strength significantly by 24.29% and the peel strength is reduced by 15.66% at a higher temperature with the increase in specimen width. At smaller widths, an increase in temperature resulted in the reduction of peel strength by 2.05%, however, the peel strength is increased by 9.11% at larger widths when the temperature is increased. Figure 2.22c shows the plot of peel strength against humidity and width. The increase in width

decreased the peel strength considerably by 21.59% at lower humidity and 21.51% at higher humidity. The increase in humidity but increased the peel strength by 4.44% at a smaller width and by 4.56% at a larger width.

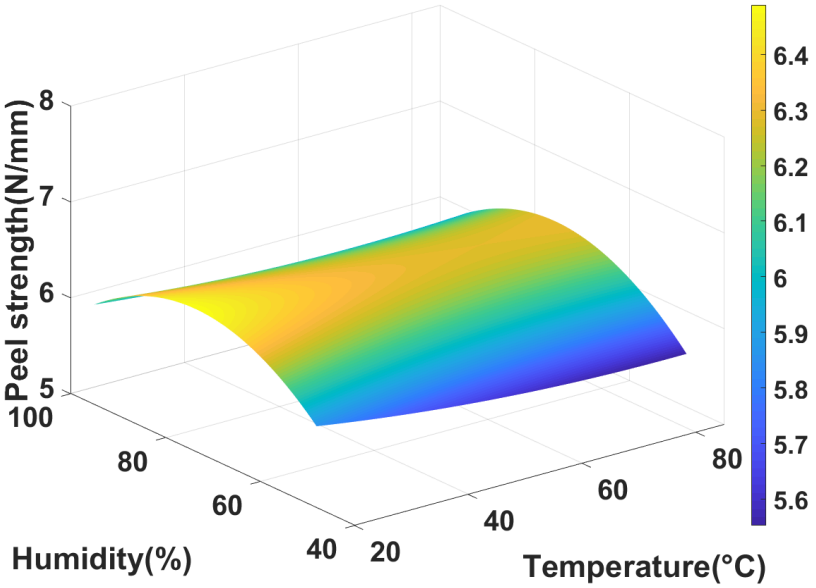

(a)

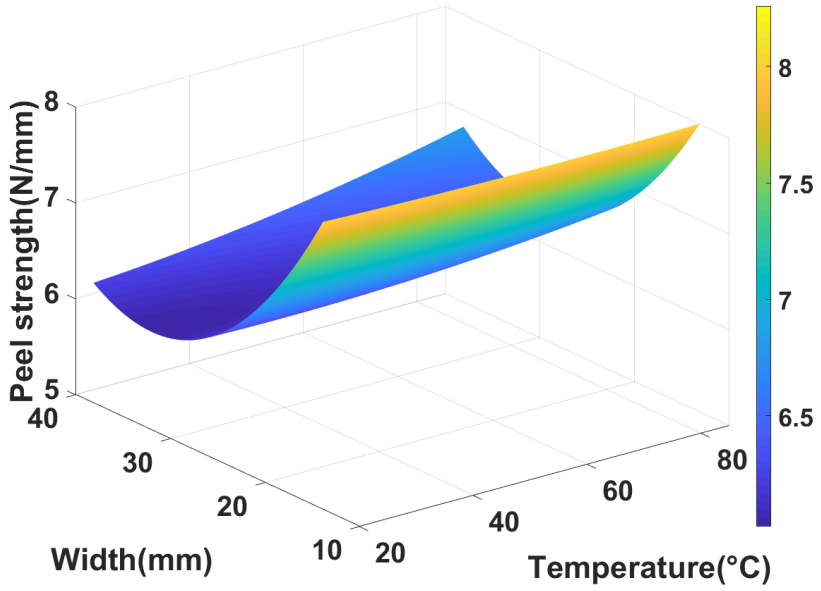

(b)

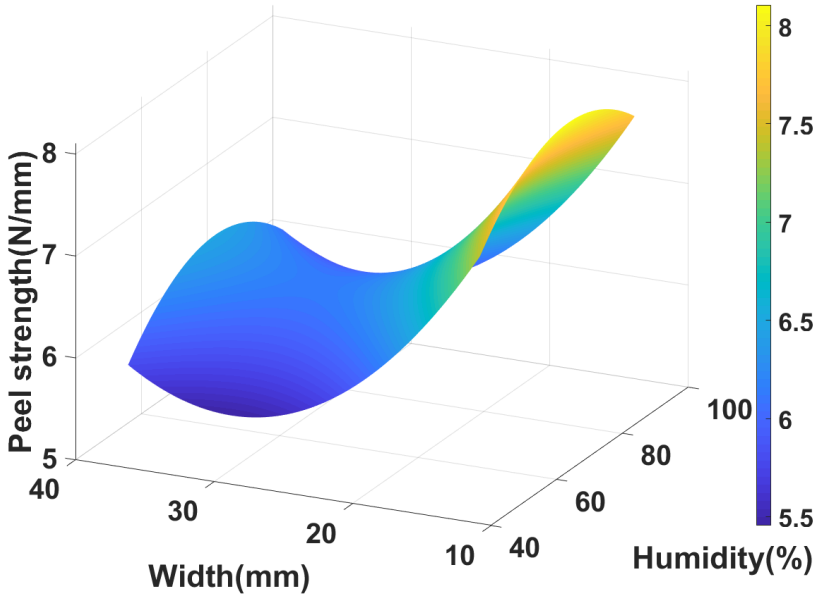

(c)

Figure 2.22: 3-D surface plots of peel strength showing effects of (a) temperature and humidity (b) temperature and width and (c) humidity and width

The RSM model, Equation 2.6, is utilized to create the 3-D surface plots for the cleavage strength. The 3D plots of the cleavage strength are shown in Figure 2.23. In Figure 2.23a, the cleavage strength is increased by 9.85% at lower humidity and by 14.19% at higher humidity, when the temperature is increased. The cleavage strength is reduced by 10.82% at lower a temperature and by 7.30% at higher temperature with the increment in humidity. In Figure 2.23b, at a lower temperature, an increase in width improved the cleavage strength significantly by 20.70% and at a higher temperature, the cleavage strength increased slightly by 0.57%. Increase in temperature increased the cleavage strength by 21.27% at lower width and by 1.04% at higher width. In Figure 2.23c, at lower humidity, the cleavage strength is increased by 1.71% with the increase in specimen width. The cleavage strength is raised significantly by 18.17% at higher humidity when the specimen width is increased. An increase in humidity decreased the cleavage strength by 14.59% at smaller width and by 0.77% at larger width specimens.

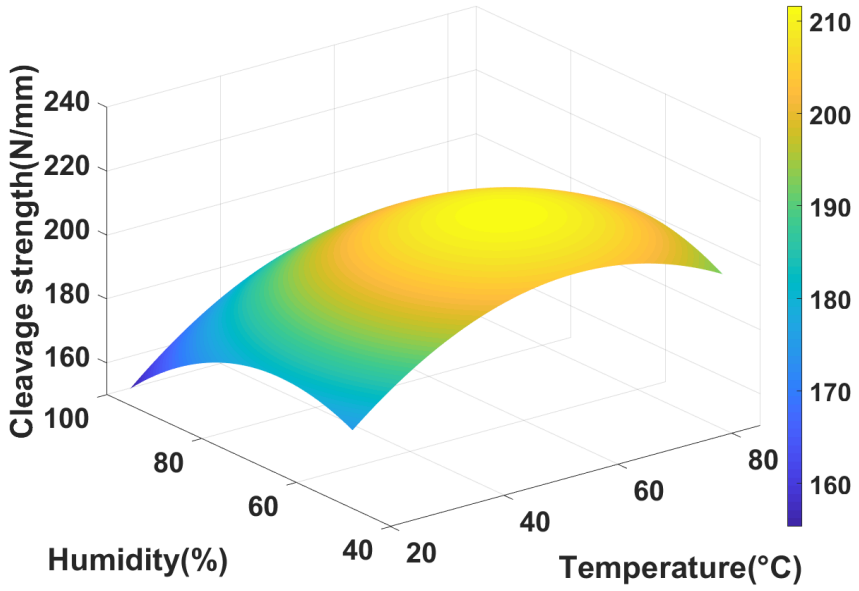
Cleavage strength(N/mm)
240
220
200
180
160
100
80
60
40
Humidity(%)
20
40
60
80
Temperature(°C)
210
200
190
180
170
160

(a)

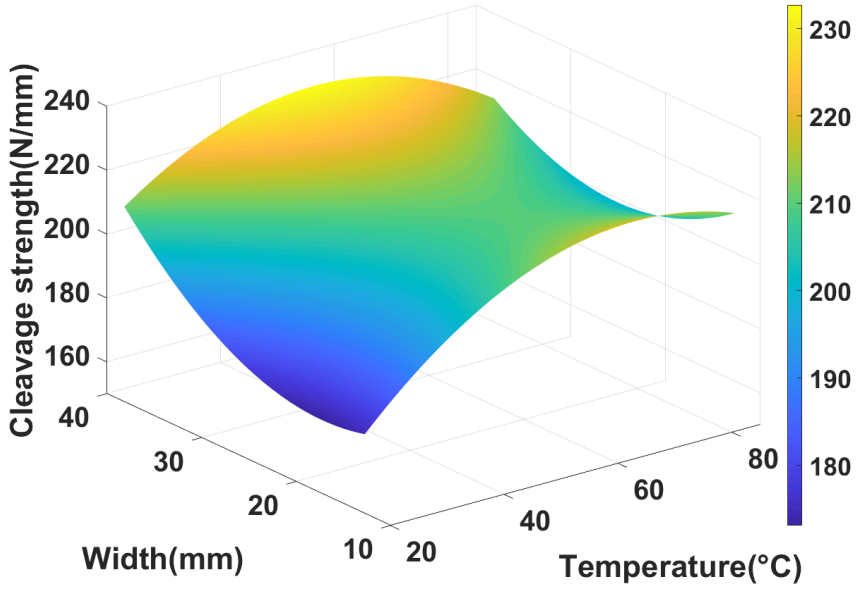
Cleavage strength(N/mm)
240
220
200
180
160
40
30
20
10
Width(mm)
20
40
60
80
Temperature(°C)
230
220
210
200
190
180

(b)

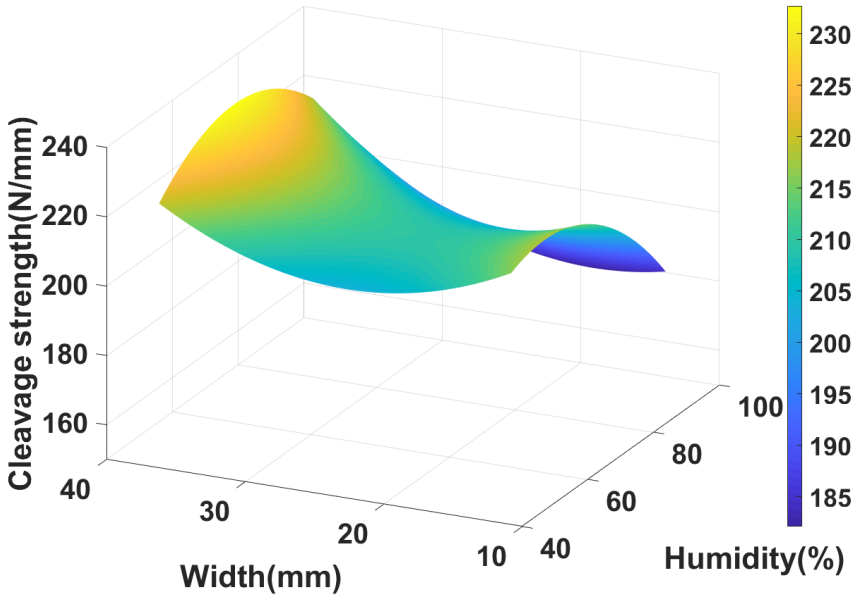

(c)

Figure 2.23: 3-D surface plots of cleavage strength showing effects of (a) temperature and humidity (b) temperature and width and (c) humidity and width

In Figure 2.22a and Figure 2.22c, increase in humidity amplified the peel strength, which is similar to the peel testing results. Increase in width is observed to decrease the peel strength in Figure 2.22b and Figure 2.22c, which validates the results obtained from the experimental testing of peel specimens. In Figure 2.23a and Figure 2.23b, the effect of increasing temperature increased the cleavage strength, which follows the trend of the results obtained from cleavage testing. The cleavage strength is decreased with the increase humidity as presented in Figure 2.23a and Figure 2.23c, whereas in Figure 2.23b and Figure 2.23c, cleavage strength is increased with the increment in specimen's width. Results acquired from these 3-D surface plots follows the trend of the cleavage strength determined from the cleavage tests. The RSM models presented in this work, however, can be efficiently yet reliably used for a certain range of input parameters only to predict

the peel and cleavage strength: the temperature, humidity, and width should be in the range of 20°C to 85°C, within 48% to 95%, and between 12.7 mm to 38.1 mm, respectively.

2.6 CONCLUSIONS

Peel and cleavage strengths of the adhesive connection to be used in dynamic message signs (DMS) were studied herein. According to American Society for Testing and Materials (ASTM), 64 adhesive specimens, including 32 peel and 32 cleavage specimens, were tested under 16 different variations of temperature, humidity, and specimen width to study the effect of each parameter on the peel and cleavage strength. Experimental and statistical comparisons of the peel and cleavage loadings were performed. Two separate regression models, encompassing multiple linear regression (MLR) and response surface metamodels (RSM), were developed, and statistically and graphically compared with testing data. Then, the RSM models for both strengths, which was more accurate than the MLR models, were used to efficiently explore the effects of different parameters on the peel and cleavage strengths. The following conclusions can be derived from the experimental and statistical studies:

1. No significant effect of the conditioning temperature was observed for the peel strength, whereas increase in conditioning humidity was found to improve the peel strength up to 30.1%. The peel strength of the tested specimens was revealed to be decreased up to 28.2% with the increase in the specimen’s width. Cohesive failure was also observed to be the predominant failure mode for the peel specimens that were tested.

2. Increment in conditioning temperature had positive effects on the cleavage strength with increase in cleavage strength by 27.4%, however, cleavage strength was observed to be decreasing up to 13.7% with the rise in humidity. Increase in the cleavage strength by 28.5% with the increase in the specimen's width is understandable as increase in width increases the area of adhesive region. This result was supported by the conclusion from Shahid and Hashim (2002). All the tested cleavage specimens were observed to be failed in cohesive failure mode indicating high cohesion of the adhesive.

3. The RSM models were found to be more reliable for the prediction of both the peel and cleavage strength than the MLR model by evaluating the coefficient of determination (R^2) of the models and comparison of peel and cleavage strength predicted from the model with experimental data. The MLR-based statistical analysis indicated that the specimen width was the most significant parameter for the peel strength as the P-value of 0.00248 was less than 0.05. Results obtained from the experimental tests were in agreement with the observations from the 3-D surface plots created using the RSM models.

2.7 REFERENCES

Higgins, A. (2000). Adhesive bonding of aircraft structures. *International Journal of Adhesion and Adhesives*, *20*(5), 367-376.

Seo, D. W., & Lim, J. K. (2005). Tensile, bending and shear strength distributions of adhesive-bonded butt joint specimens. *Composites science and technology*, *65*(9), 1421-1427.

Ferreira, J. A. M., Reis, P. N., Costa, J. D. M., & Richardson, M. O. W. (2002). Fatigue behaviour of composite adhesive lap joints. *Composites science and technology*, *62*(10-11), 1373-1379.

He, P., Chen, K., Yu, B., Yue, C. Y., & Yang, J. (2013). Surface microstructures and epoxy bonded shear strength of Ti6Al4V alloy anodized at various temperatures. *Composites Science and Technology*, *82*, 15-22.

Amatya, I., Seo, J., Letcher, T., & Bierschbach, D. (2020). Tensile and shear strength tests with adhesive connections in dynamic message signs. *Mechanics of Materials*.

Shahid, M., & Hashim, S. A. (2000). Cleavage strength of steel/composite joints. *The Journal of Adhesion*, *73*(4), 365-384.

Shahid, M., & Hashim, S. A. (2002). Effect of surface roughness on the strength of cleavage joints. *International Journal of Adhesion and Adhesives*, *22*(3), 235-244.

You, M., Li, Z., Zheng, X. L., & Yan, Z. M. (2008). Effect of Recessing Length in Adhesive Layer on the Cleavage Joints. In *Key Engineering Materials* (Vol. 385, pp. 225-228). Trans Tech Publications Ltd.

Cognard, J. (1988). Influence of water on the cleavage of adhesive joints. *International Journal of Adhesion and Adhesives*, *8*(2), 93-99.

Kim, K. S., & Aravas, N. (1988). Elastoplastic analysis of the peel test. *International Journal of Solids and Structures*, *24*(4), 417-435.

De Freitas, S. T., & Sinke, J. (2014). Adhesion properties of bonded composite-to-aluminium joints using peel tests. *The Journal of Adhesion*, *90*(5-6), 511-525.

Broughton, W. R., Mera, R. D., & Hinopoulos, G. Project PAJ3—Combined Cyclic Loading and Hostile Environments 1996-1999: Report No. 13—Creeping Testing of Adhesive Joints T-Peel Test, Oct. 1999. *NPL Report CMMT (A)*, *193*, 4-5.

Noori, H., Jain, M., Nielsen, K., & Brandys, F. (2016). Effect of Deformation-induced Residual Stress on Peel Strength of Polymer Laminated Sheet Metal. *The Journal of Adhesion*, *92*(10), 862-876.

Arouche, M. M., Budhe, S., Alves, L. A., de Freitas, S. T., Banea, M. D., & de Barros, S. (2018). Effect of moisture on the adhesion of CFRP-to-steel bonded joints using peel tests. *Journal of the Brazilian Society of Mechanical Sciences and Engineering*, *40*(1), 10.

Price, A. J., & Sargent, J. P. (1997). Small scale aluminium/epoxy peel test specimens and measurement of adhesive fracture energy. *International journal of adhesion and adhesives*, *17*(1), 27-32.

Seo, J. (2013). Statistical determination of significant curved I-girder bridge seismic response parameters. *Earthquake Engineering and Engineering Vibration*, *12*(2), 251-260.

ASTM D1876-08. (2008). Standard test method for peel resistance of adhesives (T-peel test). West Conshohocken: American Society of Testing and Materials.

ASTM D1062-08. (2008). Standard test method for cleavage strength of metal-to-metal adhesive bonds. West Conshohocken: American Society of Testing and Materials.

Kokaly, R. F., & Clark, R. N. (1999). Spectroscopic determination of leaf biochemistry using band-depth analysis of absorption features and stepwise multiple linear regression. *Remote sensing of environment*, *67*(3), 267-287.

Seo, J., & Linzell, D. G. (2010). Probabilistic Vulnerability Scenarios for Horizontally Curved Steel I-Girder Bridges Under Earthquake Loads. *Transportation Research Record*, *2202*(1), 206-211.

Seo, J., & Linzell, D. G. (2013). Use of response surface metamodels to generate system level fragilities for existing curved steel bridges. *Engineering Structures*, *52*, 642-653.

Seo, J., & Linzell, D. G. (2012). Horizontally curved steel bridge seismic vulnerability assessment. *Engineering Structures*, *34*, 21-32.

CHAPTER 3: TENSILE AND SHEAR BEHAVIOR FOR ADHESIVE AND WELDED THIN-WALLED CONNECTIONS IN DYNAMIC MESSAGE SIGNS

3.1 ABSTRACT

This paper was intended to investigate the strength of adhesive and welded thin-walled connections to be used in a dynamic message sign (DMS). The tensile strength and shear strength were studied for both of the adhesive and welded specimens. A number of tensile specimens and shear specimens with variations in width and temperature were tested until failure according to the ASTM D638 and ASTM D1002, respectively. The specimens with a range of width from 13 mm to 38 mm were conditioned with temperatures between -56.67 °C and 93.33 °C. The effects of temperature and width on each of the strengths were evaluated by analysing the testing data in a graphical and statistical manner. As expected, all the tests revealed that the welded specimens have significantly higher strength compared to the adhesive specimens in tensile and shear loadings. For the adhesive specimens, due to the increment of temperature, the highest increments were found to be 31.9% and 30.4%. In addition to the tests, Response Surface Metamodels (RSMs) and practical design equations were developed with regression analysis of the testing data, so as to predict tensile and shear stresses of both adhesive and welded specimens in an efficient way. 3D plots generated from the RSMs showed a higher effect of the temperature and width on the ultimate tensile and shear strength for both adhesive and welded specimens, and the practical

design equations were founded to be more reliable for the overall tensile and shear stress prediction compared to the RSMs.

Keywords: Dynamic message sign; Tensile; Shear; Strength; Adhesive; Weld.

3.2 INTRODUCTION

Structural components in Dynamic Message Sign (DMS) primarily comprising aluminum frames and thin aluminum sheets are required to be connected properly to assure structural integrity and public safety. Adhesives can be a good alternative to conventional welded connections for use in DMS due to several benefits, including low labor cost, faster manufacturing, uniform load distribution, and the ability to join dissimilar metals Lee et al. (2006). With these benefits, adhesives are burgeoning in its use among many DMS producers (Higgins 2000, Hill 2003). However, there are limited studies attempted in the strength of adhesive connections and its comparison with welded connections. To shed light on the possibility of adhesives as a substitute for welded thin-walled connections in DMS, a detailed experimental and statistical study to compare the strength of adhesive and welded thin-walled connections is required. Strictly speaking, tensile and shear tests need to be completed to provide an insight for the prospect of the use of adhesive in DMS connections.

Adhesives have not been used to their full potential albeit its excellence as a bonding agent. The strength of adhesive connections has been investigated under various loading conditions (Colak et al. 2009, Savvilotidou et al. 2017, Goglio and Rezaei 2014, Silva et al. 2016). Colak et al. (2009) observed that adhesives with high glass transition temperatures performed adequately at high temperatures, whereas adhesives having lower

glass transition temperatures were inappropriate to be used at high temperatures. Savvilotidou et al. (2017) found the tensile strength of adhesive was decreased after reaching saturation point. Goglio and Rezaei (2014) revealed a reduction in tensile strength of adhesive when tested after conditioning the specimens at 50 °C with 100% relative humidity. Silva et al. (2016) determined the effects of thermal cycles ranging from -15 °C to 60 °C that increased the tensile strength of adhesives. Zhang et al. (2010) studied the effects of temperature ranging between -35 °C and 60 °C on the tensile strength of adhesive connecting pultruded glass fiber-reinforced polymer laminates. It was found that the tensile strength and stiffness of the adhesive connection was decreased when the temperature was increased above the glass transition temperature range from 40 °C to 50 °C. Hu et al. (2019) tested tensile specimens cured at various temperatures for different time duration to determine the mechanical properties of adhesive for analyzing the performance of adhesively bonded corrugated sandwich structures. Both length of curing and temperature were observed to have considerable effect on the strength properties. Fernando et al. (2009) studied five different adhesives to determine their tensile properties to investigate the strength of rectangular hollow section steel tube adhesively bonded with carbon fiber reinforced polymer plates and found that adhesive with higher ultimate strain provided better strength for the bonded tube.

Shear strength of the adhesives have also been studied (Agarwal et al. 2014, Kim et al. 2012, Ferreira et al. 2002, Sugiman et al. 2013, Sousa et al. 2018) to some extent. Agarwal et al. (2014) examined the adhesive connection in steel-carbon fiber reinforced polymer to delve into the effects of freeze-thaw cycles. It was reported that shear strength declined by 12-18% after freeze-thaw cycles in single-lap shear specimens. Kim et al.

(2012) tested double-lap shear specimens and observed a slight increase in shear strength after the repeated freeze-thaw cycles. Ferreira et al. (2002) studied the effects of immersion of water, elevated temperatures, and joint length on the static and fatigue shear strength of adhesive. Results indicated that shorter bond lengths had higher static and fatigue strength, while the effects of water were dependent on the water temperature. Sugiman et al. (2013a, b) tested single-lap joints specimens at a temperature of 50 °C. The exposure to the temperature decreased the number of cycles for the failure of the lap-joints. Sousa et al. (2018) investigated the shear strength of adhesives due to the effects of temperature ranging from 20 °C to 40 °C and found an increment of nearly 25% in the shear strength of the adhesive.

Although some of the aforementioned past studies have reported that temperature can affect the strength and durability of adhesives, a comprehensive experimental study to examine tensile and shear strength is necessary for demonstrating the use of adhesive bonded DMSs exposed to varying temperatures and other geometric factors is needed. To that end, this study experimentally determined the effect of temperatures and width of thin-walled specimens on the tensile and shear strength and compare with respective strength of weld to use in the design of DMSs. This paper is structured into six sections, including this section, laboratory testing, results and discussion, statistical analysis for Response Surface Metamodels (RSMs), design equations, and conclusions.

3.3 LABORATORY TESTING

The testing involves the study of tensile and shear tests in variation with width and temperature conditions. This section discusses the testing combinations, tested specimens, and testing procedures.

3.3.1 TESTING COMBINATIONS

To investigate the tensile and shear strength for the adhesive and welded thin-walled specimens, 15 and 9 combinations were considered, respectively, as shown in Table 3.1. Note, each combination consisted of two specimens for tensile and shear specimens individually. The adhesive specimen combinations (A1-A6) and welded specimen combinations (W1-W9) were tested for each strength type for this work. In addition to A1-A6 and W1-W9, data presented for adhesive specimen combinations C1, C2, C3, C7, C8, C10, C12, C14, and C16 were recycled from the previous work (Amatya et al. 2020) to facilitate examination of the effects of temperature and width over a broader range on each strength. Note, the previous work (Amatya et al. 2020) initially generated 16 different combinations created based on Plackett-Burman Design (Seo 2013, Chandorkar et al. 2008, Seo and Linzell 2010, 2012, 2013) incorporating temperature, humidity, and width parameters with help of commercially available statistical software JMP (SAS Institute Inc. 2008). Further information on the recycled combinations can be found elsewhere (Amatya et al. 2020). Table 3.1 presents all the combinations along with the respective temperature and width.

The specimens per combination were conditioned in a temperature and humidity-controlled chamber. Each specimen was assigned an ID;, for example, W-T-25TH-93.3T-

A2, where the first character is the specimen type (A-adhesive/W-welded), and the following character represents the test type (T-tensile/S-shear). The width of the specimens is denoted by 13TH, 25TH, and 38TH for 13 mm, 25 mm, and 38 mm specimen width. The temperature of the conditioning chamber is represented by T, and the last character symbolizes the combination number shown in Table 3.1. The specimens having the same conditioning temperatures were placed collectively in the chamber for at least 24 hours to be conditioned before testing them. For instance, the specimens under the combinations A1, A2, A3, W1, W2, and W3 were conditioned in the chamber at 93.3 ℃ together.

Table 3.1 Combinations for the experimental program

Specimen type	Combination	Specimen ID	Temperature (°C)	Width (mm)
Adhesive	A1	A-T/S-13TH-93.3T-A1	93.3	13
	A2	A-T/S-25TH-93.3T-A2	93.3	25
	A3	A-T/S-38TH-93.3T-A3	93.3	38
	A4	A-T/S-13TH-(-56.7)T-A4	-56.7	13
	A5	A-T/S-25TH-(-56.7)T-A5	-56.7	25
	A6	A-T/S-38TH-(-56.7)T-A6	-56.7	38
	C1 [20-21]	A-T/S-13TH-20.0T-C1	20.0	13
	C2 [20-21]	A-T/S-38TH-20.0T-C2	20.0	38
	C3 [20-21]	A-T/S-25TH-20.0T-C3	20.0	25
	C7 [20-21]	A-T/S-13TH-52.5T-C7	52.5	13
	C8 [20-21]	A-T/S-25TH-52.5T-C8	52.5	25
	C10 [20-21]	A-T/S-38TH-52.5T-C10	52.5	38
	C12 [20-21]	A-T/S-13TH-85.0T-C12	85.0	13
	C14 [20-21]	A-T/S-25TH-85.0T-C14	85.0	25
	C16 [20-21]	A-T/S-38TH-85.0T-C16	85.0	38
Welded	W1	W-T/S-13TH-93.3T-W1	93.3	13
	W2	W-T/S-25TH-93.3T-W2	93.3	25
	W3	W-T/S-38TH-93.3T-W3	93.3	38
	W4	W-T/S-13TH-(-56.7)T-W4	-56.7	13
	W5	W-T/S-25TH-(-56.7)T-W5	-56.7	25
	W6	W-T/S-38TH-(-56.7)T-W6	-56.7	38
	W7	W-T/S-13TH-20.0T-W7	20.0	13
	W8	W-T/S-25TH-52.5T-W8	52.5	25
	W9	W-T/S-38TH-85.0T-W9	85.0	38

3.3.2 TESTED SPECIMENS

Two different types of strength tests were performed for both adhesive and welded specimens. This section focuses on the fabrication and geometry of the tensile and shear specimens.

3.3.2.1 ADHESIVE SPECIMENS

The adhesive tensile and shear specimens were fabricated based on ASTM D638 (ASTM D638 2010) and ASTM D1002 (ASTM D1002 2010), respectively. The

representative tensile and shear specimens with a width of 13 mm is shown in Figure 3.1 and Figure 3.2, respectively. The tensile specimens were completely made from LORD 406-19GB (LORD Corporation 2018) acrylic adhesive in a standard dog-bone geometry. 5052 aluminum metal bars having 3.2 mm thickness were used to prepare the shear specimens. To install the extensometer on the shear specimens fabricated following ASTM D1002, a small piece of 5052 aluminum with 3.2mm thick and 13mm wide was glued with the acrylic adhesive to each of the shear specimens. The specimens were cured for at least two weeks after their fabrication and all the specimens were prepared and distributed by a local DMS producer in the United States.

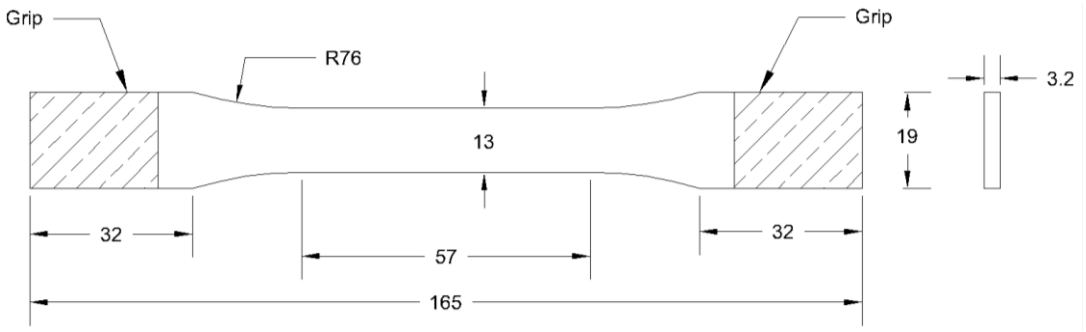

(a) (b)

Figure 3.1: Geometry of adhesive tensile specimens (a) top view and (b) cross-section (All dimensions are in mm).

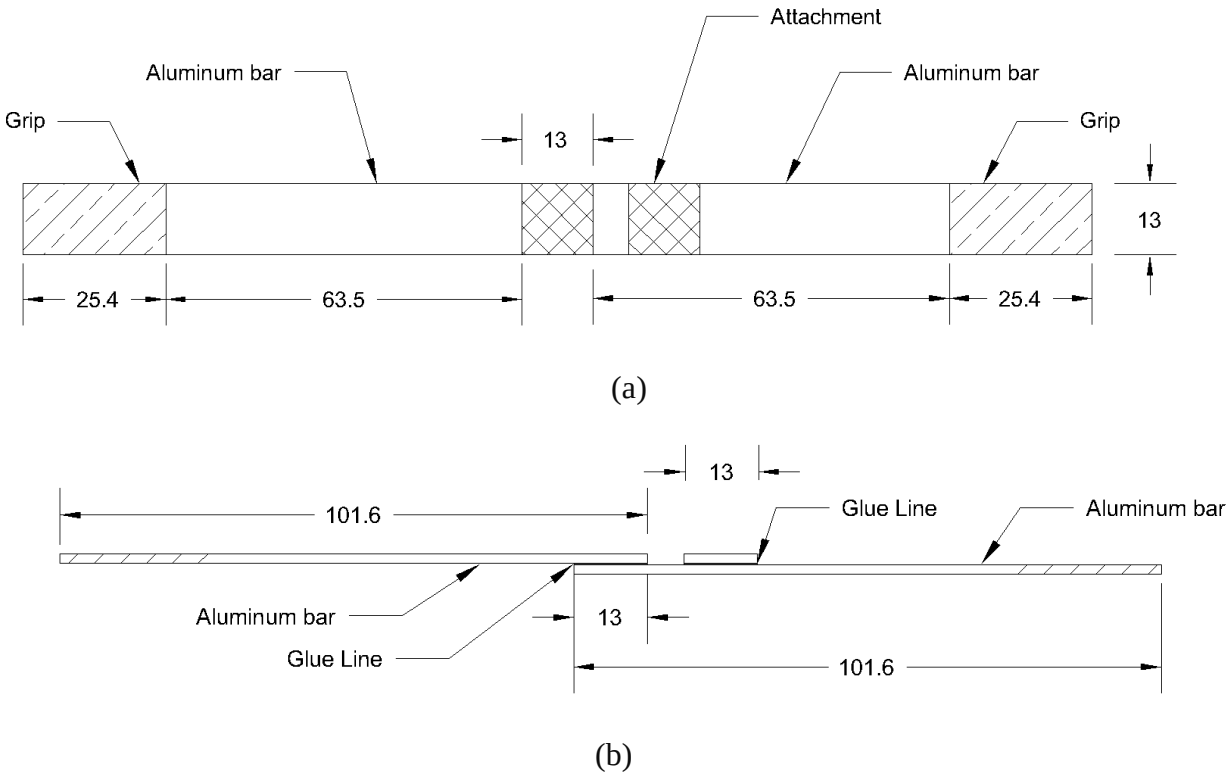

Figure 3.2: Geometry of adhesive shear specimens (a) top view and (b) side view (All dimensions are in mm).

3.3.2.2 WELDED SPECIMENS

The welded tensile and shear specimens were designed according to ASTM D638 (ASTM D638 2010) and ASTM D1002 (ASTM D1002 2010), respectively following the guidelines of American Welding Society (American Welding Society 2015). All the specimens were manufactured by the local DMS producer using weld of 4043 aluminum alloy. The entirety of the dimensions was kept as close as possible to the adhesive specimens. The sample welded tensile and shear specimens with a width of 13 mm is shown in Figure 3.3 and Figure 3.4, correspondingly. As in the adhesive specimens, the 5052 aluminum was used to fabricate all types of the specimens. Specifically, the tensile

specimens were fabricated by joining two aluminum bars with 3.2 mm square groove welds in dogbone shape. Two 5052 aluminum metal bars with 6.4 mm thickness were overlapped and bonded by transverse fillet welds in the middle to build the shear specimens. To install the extensometer, a small piece of additional aluminum piece was glued to each of the welded shear specimens.

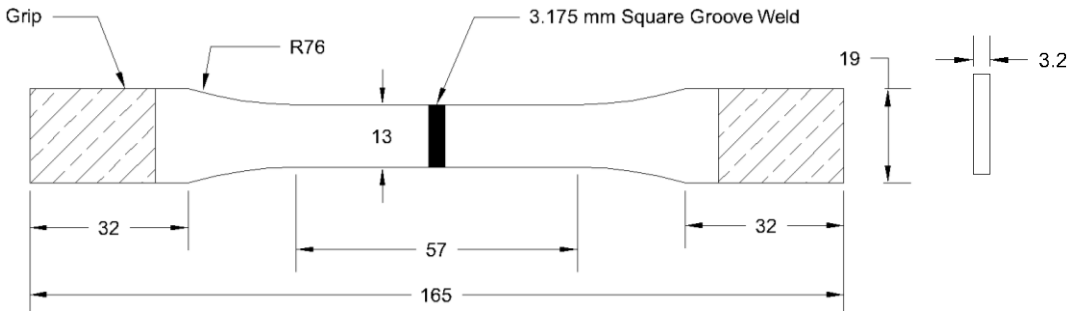

(a) (b)

Figure 3.3: Geometry of welded tensile specimens (a) top view and (b) cross-section view (all dimensions are in mm).

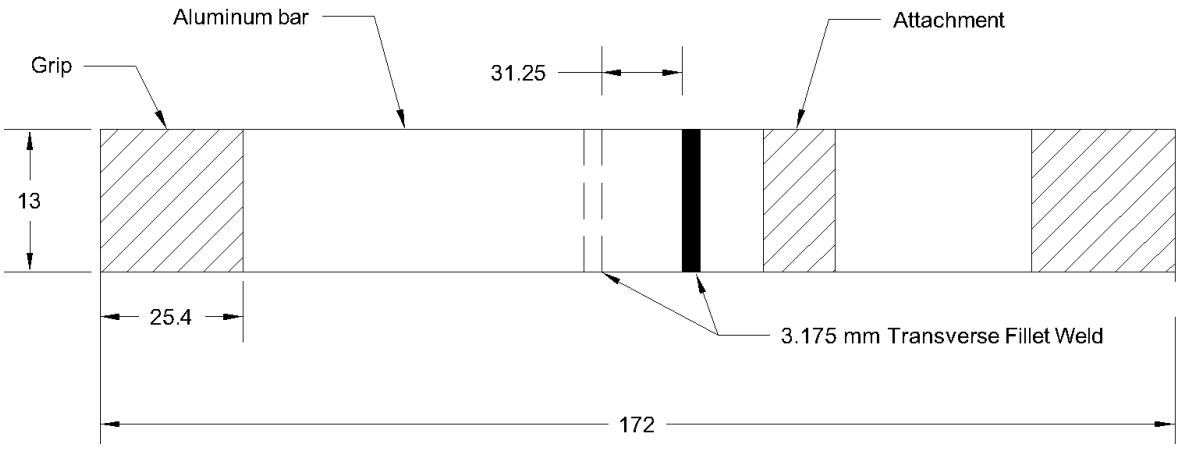

(a)

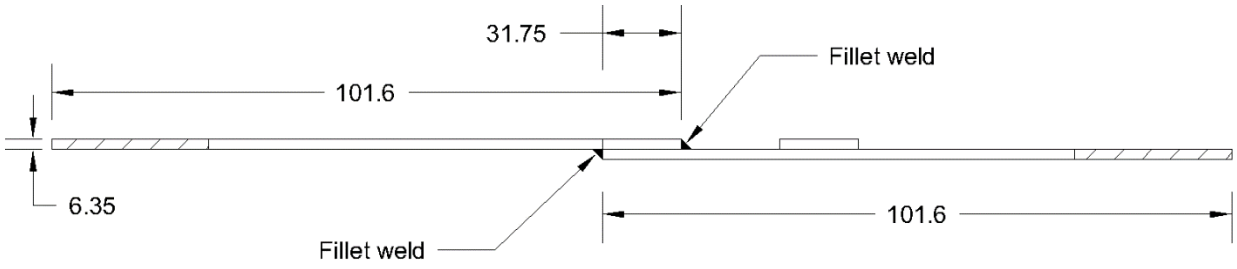

(b)

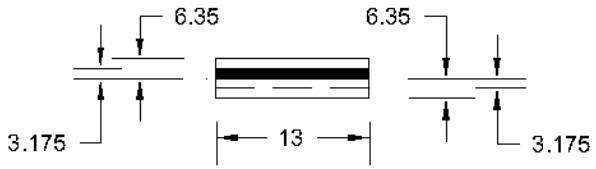

(c)

Figure 3.4: Geometry of welded shear specimens (a) top view, (b) side view and (c) front view (All dimensions are in mm).

3.3.3 TESTING PROCEDURE

All the specimens were tested to failure using MTS (Material Testing System) Universal Testing System. Note that all the tests were performed at room temperature and each specimen was mounted and aligned in the grips of the MTS. In detail, the tensile and shear specimens were tested using an MTS 370 Landmark (MTS Systems Corporation 2018) 100-kN servo-hydraulic load unit calibrated to 20% of its load capacity. The longitudinal strains of the tensile and shear specimens were calculated by measuring the extension recorded from a MTS 634.31F-24 clip-on extensometer with a gauge length of 20 mm mounted to each specimen during the test. The extensometer was a class B2 calibrated with an accuracy of ±0.25% of measured strain. The tests were conducted by

applying a loading with a free crosshead speed of 5 mm/min for the tensile specimens and 1.3 mm/min for the shear specimens. The testing procedures for the tensile and shear tests are specified by ASTM D638 (ASTM D638 2010) and ASTM D1002 (ASTM D1002 2010), respectively. The testing setups for the tensile and shear specimens are shown in Figure 3.5.

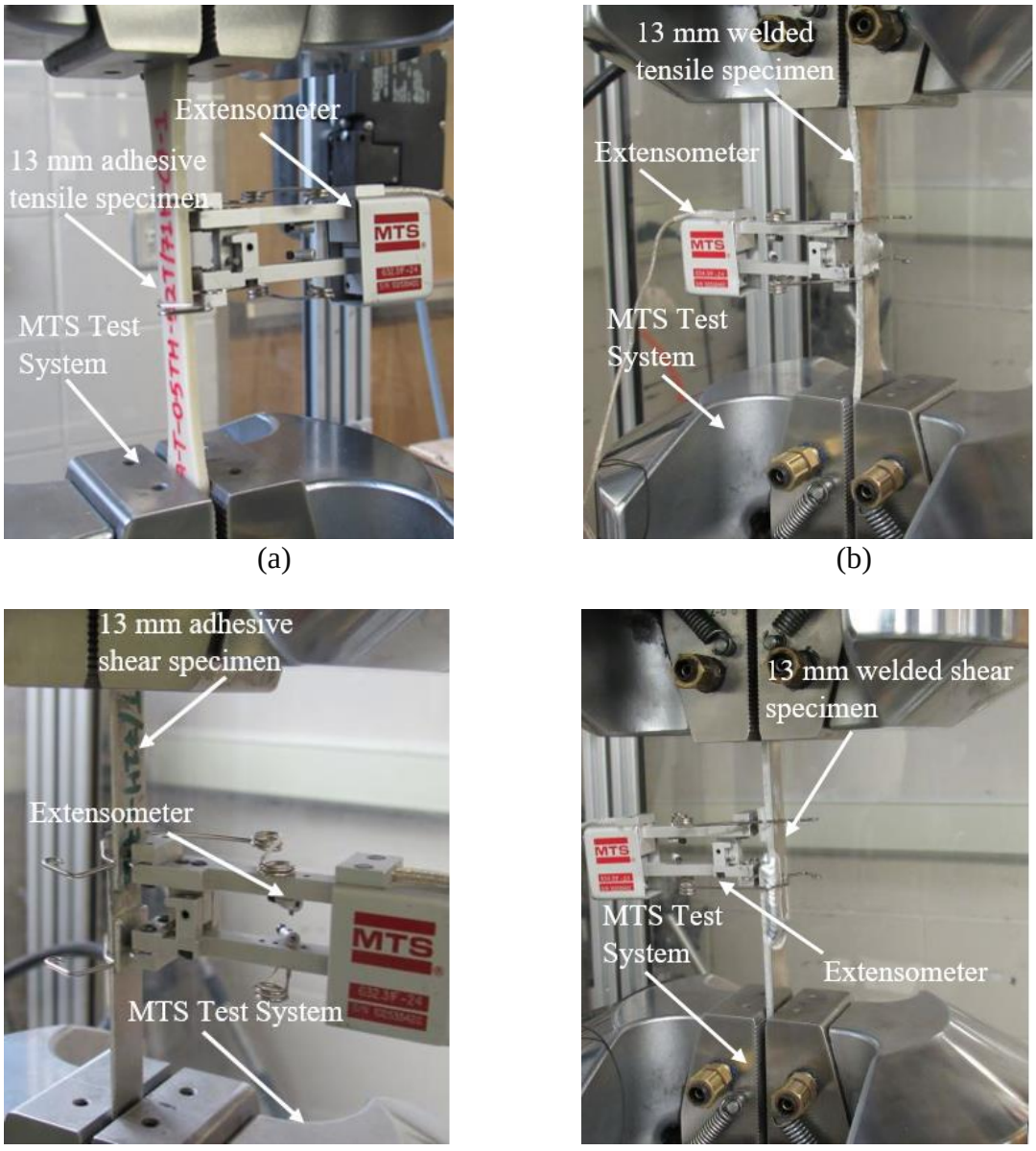

Figure 3.5: Installation of the specimens in the testing machine (a) adhesive tensile, (b) welded tensile, (c) adhesive shear and (d) welded shear

3.4 RESULTS AND DISCUSSION

Results from the tensile and shear tests are presented and discussed herein. Specifically, stress-strain curves were plotted for each of the tests to calculate the strengths, and the

influence of temperature and width on each strength of both adhesive and welded specimens is graphically explained.

3.4.1 TENSILE TEST

Figure 3.6 shows stress-strain curves generated from all the tensile tests. The stress-strain curves for the adhesive tensile specimens are shown in Figure 3.6a. The maximum ultimate tensile stress occurs for the 25 mm specimens conditioned at 93.33 °C from combination C2, while the minimum ultimate tensile stress is observed for the 38 mm specimens conditioned at 52.5 °C from combination C10. Among all the specimens, the 13 mm specimen conditioned at 20 °C showed the median ultimate tensile stress. Figure 3.6b presents the stress-strain curves for the welded tensile specimens. The 13 mm welded tensile specimen from combination W4 conditioned at -56.67 °C showed the maximum ultimate tensile stress, whereas the 25 mm welded tensile specimen from combination W8 conditioned at 52.5 °C exhibited the minimum tensile stress. The 13 mm tensile specimens showed the median ultimate tensile stress between all the welded tensile specimens tested. The ultimate tensile stresses at varying temperature and width considered in this study are tabulated in

Table 3.2. Note, the ultimate tensile stress per combination shown in this table represents the ultimate tensile stress averaged from the two specimens' data for each combination. It appears that all the adhesive specimens fail with rupture failure and all the welded specimens are broken at weld throat failure.

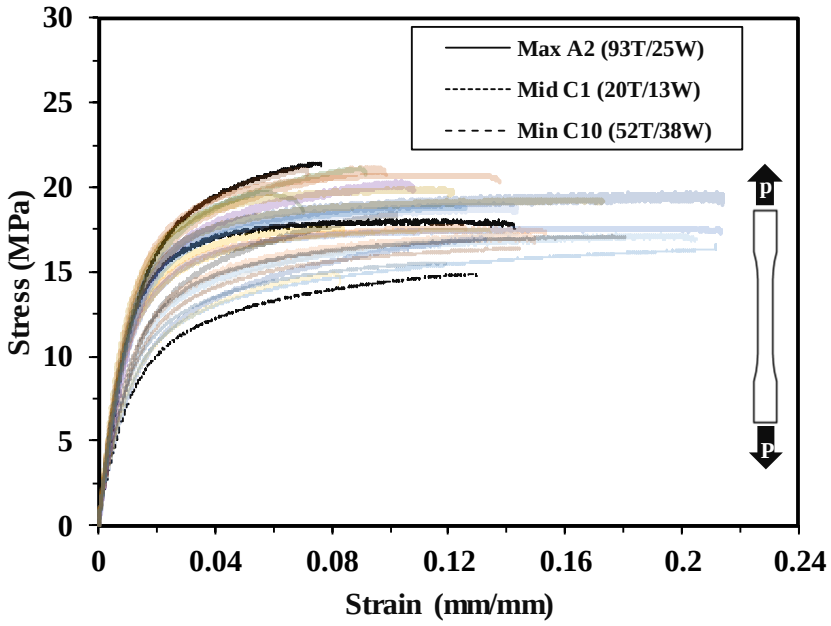

(a)

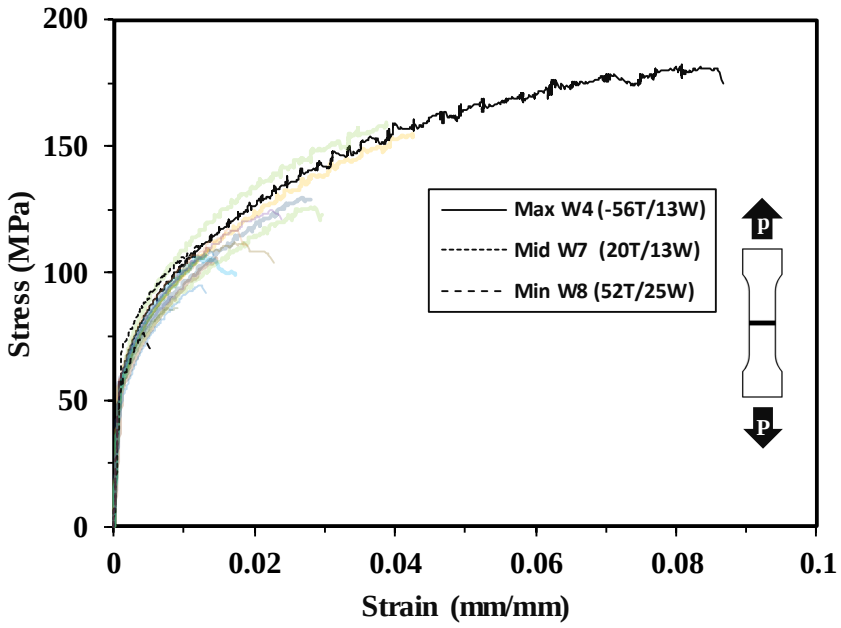

(b)

Figure 3.6: Representative stress-strain curves for tensile specimens (a) adhesive and (b) welded

Table 3.2 Ultimate tensile strength from the tensile test

Specimen ID	Ultimate tensile stress, f_u(MPa)	Failure mode
A-T-13TH-93.3T-A1	20.76	Rupture failure
A-T-25TH-93.3T-A2	21.28	Rupture failure
A-T-38TH-93.3T-A3	20.40	Rupture failure
A-T-13TH-(-56.7)T-A4	19.37	Rupture failure
A-T-25TH-(-56.7)T-A5	19.62	Rupture failure
A-T-38TH-(-56.7)T-A6	19.80	Rupture failure
A-T-13TH-20.0T-C1	17.87	Rupture failure
A-T-38TH-20.0T-C2	17.63	Rupture failure
A-T-25TH-20.0T-C3	17.61	Rupture failure
A-T-13TH-52.5T-C7	17.30	Rupture failure
A-T-25TH-52.5T-C8	17.10	Rupture failure
A-T-38TH-52.5T-C10	15.75	Rupture failure
A-T-13TH-85.0T-C12	17.80	Rupture failure
A-T-25TH-85.0T-C14	16.13	Rupture failure
A-T-38TH-85.0T-C16	16.00	Rupture failure
W-T-13TH-93.3T-W1	117.74	Weld throat failure
W-T-25TH-93.3T-W2	110.84	Weld throat failure
W-T-38TH-93.3T-W3	122.77	Weld throat failure
W-T-13TH-(-56.7)T-W4	170.99	Weld throat failure
W-T-25TH-(-56.7)T-W5	116.45	Weld throat failure
W-T-38TH-(-56.7)T-W6	107.78	Weld throat failure
W-T-13TH-20.0T-W7	103.05	Weld throat failure
W-T-25TH-52.5T-W8	81.36	Weld throat failure
W-T-38TH-85.0T-W9	121.23	Weld throat failure

Figure 3.7a and Figure 3.7b show the failure modes of the adhesive tensile specimens with 13 mm width and 38 mm width, respectively. During the testing, all the adhesive specimens were observed to be failed due to rupture at a proximity to center of the specimens as the width near the middle section of the specimens is narrow compared to width at the edges. The line of rupture after failure was observed to be approximately perpendicular to the direction of load applied to the specimens. All the tested adhesive specimens did not show any indication of necking as presented in the figures. Figure 3.7c

and Figure 3.7d show the representative failure modes of the welded tensile specimens with 13 mm width and 38 mm width. All welded tensile specimens were observed to fail at the weld metal, and the failure modes are designated as weld throat failure as the strength of base metal was higher compared to the strength of weld metal at the center of specimens.

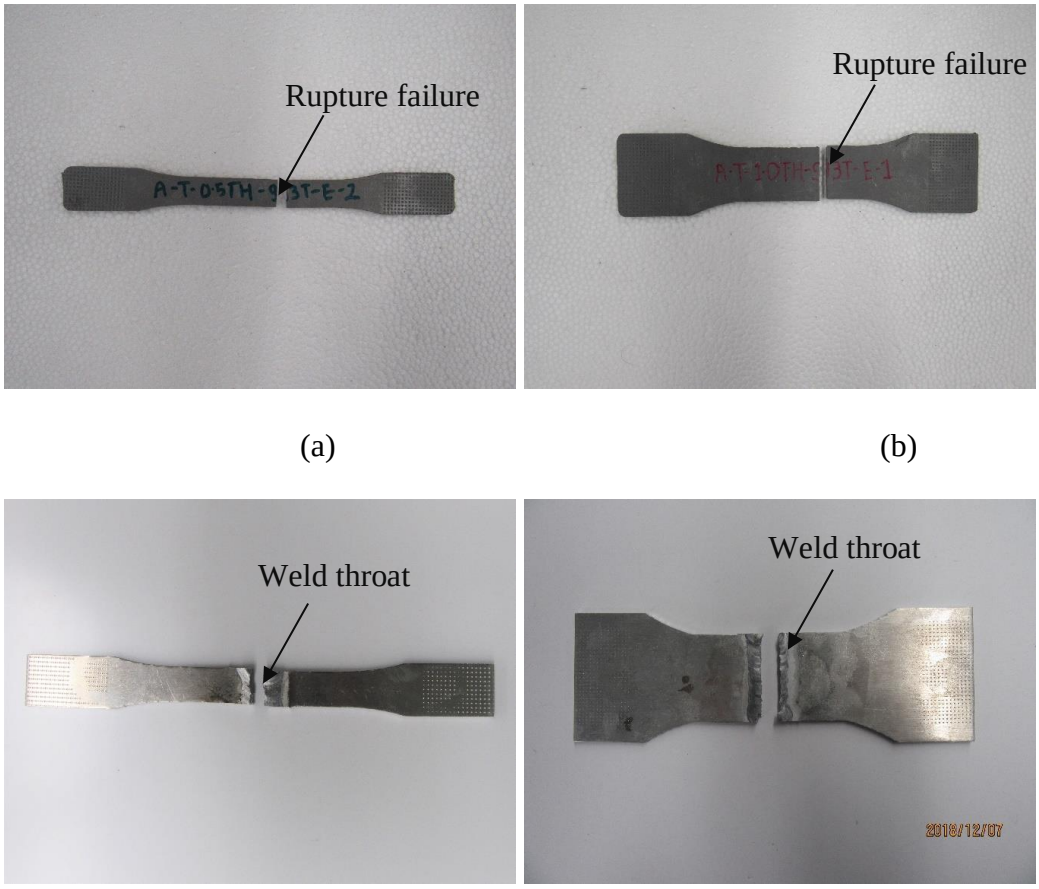

Figure 3.7: Representative failure modes of tensile specimens (a) adhesive with 13 mm width, (b) adhesive with 38 mm width, (c) welded with 13 mm width, and (d) welded with 38 mm width

3.4.1.1 EFFECT OF TEMPERATURE

The effect of temperature on the ultimate tensile stress at different temperatures is shown in Figure 3.8. In Figure 3.8a, the ultimate stress for the adhesive tensile specimens with different widths is plotted against temperature. For 13 mm specimens, the ultimate stress decreases by 7.7% and 3.2% when the temperature increases from -56.67 °C to 20 °C and 20 °C to 52.5 °C, respectively. The ultimate stress, however, is increased by 2.9% and 16.7% when the temperature elevates from 52.5 °C to 85 °C and 85 °C to 93.33 °C as shown in A4-C1-C7-C12-A1. For 25 mm specimens, the ultimate stress declines by 10.3% and 2.9% when the temperature rises from -56.67 °C to 20 °C and 20 °C to 52.5 °C. The ultimate stress of the 25 mm specimens is further reduced by 5.7% when the temperature increases from 52.5 °C to 85 °C. When the temperature was increased from 85 °C to 93.33 °C, the ultimate stress is increased significantly by 31.9% as displayed in A5-C3-C8-C14-A2. The ultimate stress of 38 mm specimens is decreased by 11% and 10.7% with an increment of temperature from -56.67 °C to 20 °C and 20 °C to 52.5 °C, simultaneously. The ultimate stress is increased by 1.6% and 27.5% when the temperature was elevated from 52.5 °C to 85 °C and 85 °C to 93.33 °C, respectively as illustrated in A6-C2-C10-C16-A3. Interestingly, the ultimate tensile stress is observed to be decreasing with the increase in temperature from 20 °C to 52.5 °C which is below the glass transition temperature of adhesive (75 °C). The ultimate tensile stress, however, is found to be increasing when the temperature was increased from 52.5 °C to 93.33 °C which is above glass transition temperature (75 °C). When the adhesive is conditioned at a temperature above glass transition temperature, adhesive initiates to transform from hard glassy surface to soft rubbery surface. As the flexibility of the adhesive is increased,

cohesion within the adhesive is increased, which increased the load resisting capacity of the adhesive joint.

In Figure 3.8b, the effect of temperature on the ultimate tensile stress for the welded tensile specimens with different widths is presented. The ultimate stress of 13 mm specimens is decreased by 39.7% when the temperature is raised from -56.67 °C to 20 °C whereas the ultimate stress is increased by 14.3% with a further elevation of temperature from 20 °C to 93.33 °C (see W4-W7-W1). The rise in temperature from -56.67°C to 52.5°C declined the ultimate stress of 25 mm specimens by 30.1%. The ultimate stress, however, increases by 36.2% when temperature is further elevated to 93.33 °C from 52.5 °C as shown in W5-W8-W2. For 38 mm specimens, the ultimate stress rises slightly by 12.5% when temperature was increased from -56.67 °C to 85 °C. The increment of temperature from 85 °C to 93.33 °C increased the ultimate stress by 1.3% as portrayed in W6-W9-W3. In this figure, the design tensile strength of the 4043 aluminum filler weld (165 MPa) acquired from Aluminum Design Manual (Aluminum Association 2010) is observed to be higher for all the welded tensile specimens tested, except for the 13 mm welded specimens conditioned at -56.67 °C from combination W4.

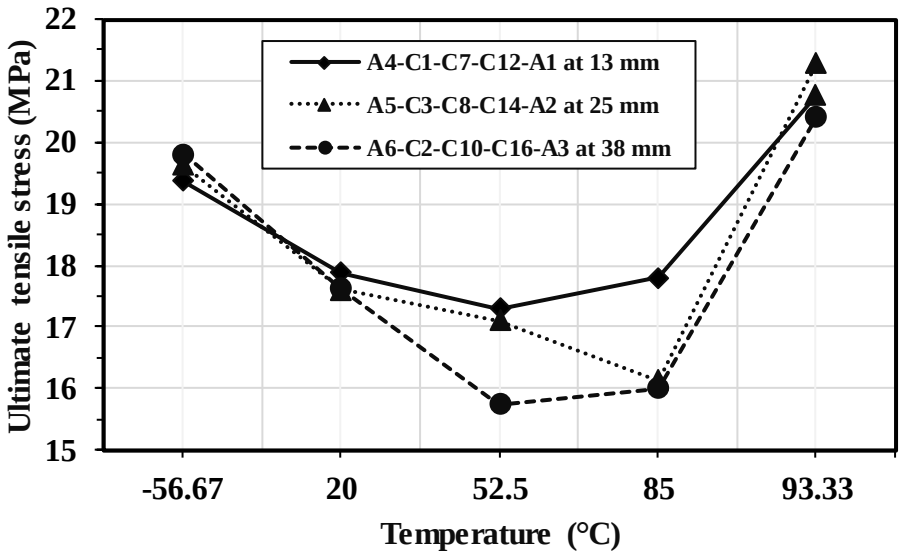

(a)

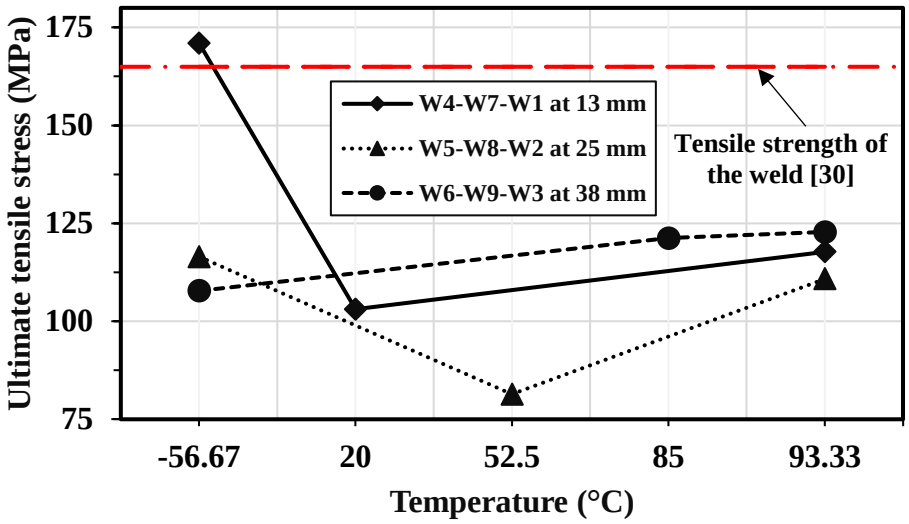

(b)

Figure 3.8: Temperature effect on ultimate stress for tensile specimens (a) adhesive and (b) weld

3.4.1.2 EFFECT OF WIDTH

The effect of the specimen width on the ultimate tensile stress is shown in Figure 3.9. The ultimate stress for the adhesive tensile specimens having different widths at various

temperatures is plotted in a bar chart in Figure 3.9a. At -56.67 °C, the ultimate stress is increased by 1.3% and 0.9% when the specimen width increases from 13 mm to 25 mm and 25 mm to 38 mm, respectively as shown in A4-A5-A6. The ultimate stress is decreased by 1.5% and increased by 0.1% with increment of specimen width from 13 mm to 25 mm and 25 mm to 38 mm at 20 °C as shown in C1-C3-C2. For specimens at 52.5 °C, the ultimate stress declines by 1.2% and 7.9% when width of specimen increases from 13 mm to 25 mm and 25 mm to 38 mm as displayed in C7-C8-C10. The ultimate stress of specimens at 85 °C is reduced by 9.4% and 0.8% as depicted in C12-C14-C16 with increment of specimen width from 13 mm to 25 mm and 25 mm to 38 mm. When the width of the specimens at 93.33 °C is increased from 13 mm to 25 mm, the ultimate stress is increased by 2.5%, whereas the ultimate stress decreases by 4.1% when the specimen width is increased from 25 mm to 38 mm as displayed in A1-A2-A3. There is no doubt that insignificant effect of width was observed for the ultimate tensile stress when tensile stress at different conditioning temperatures were considered.

In Figure 3.9b, the effect of width on the ultimate stress for the welded tensile specimens at different temperatures is shown. The ultimate stress at -56.67 °C is decreased by 31.9% and 7.4% with an increment of specimen width from 13 mm to 25 mm and 25 mm to 38 mm as displayed in W4-W5-W6. As shown in W1-W2-W3 at 93.33 °C, the ultimate stress is decreased by 5.9% with increment of specimen width from 13 mm to 25 mm, however, the ultimate stress is increased by 10.8% with further increment of specimen width from 25 mm to 38 mm. The ultimate stress is decreased by 21.1% when the stress of 25 mm specimens at 52.5 °C is compared with that of 13 mm specimens at 20 °C (see W7 and W8). The comparison between 38 mm specimens at 85 °C and 25 mm specimens at

52.5 °C shows 49% increment in ultimate tensile stress (see W8 and W9). As shown in the figure, the design tensile strength of the welded specimens (165 MPa) is observed to be significantly higher than the tensile strength obtained from testing, excluding 13 mm welded specimens conditioned at -56.67 °C from combination W4.

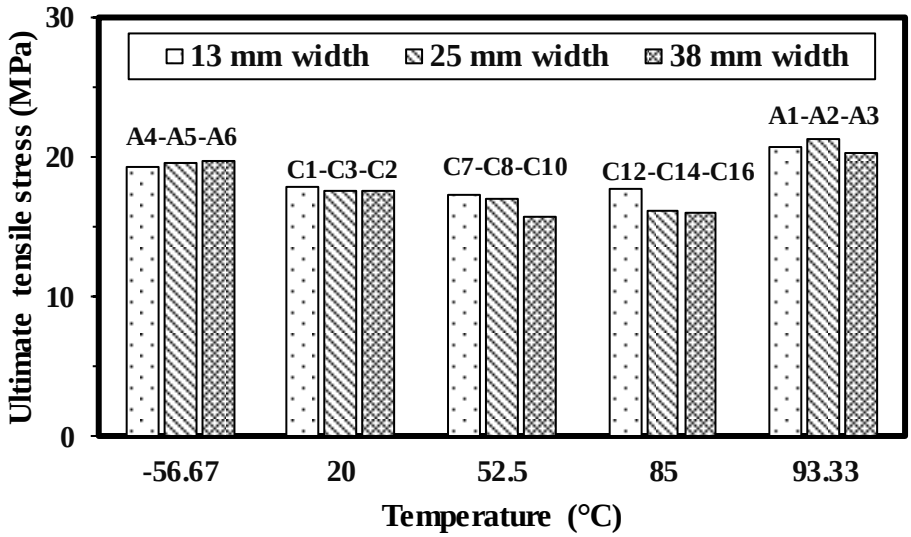

(a)

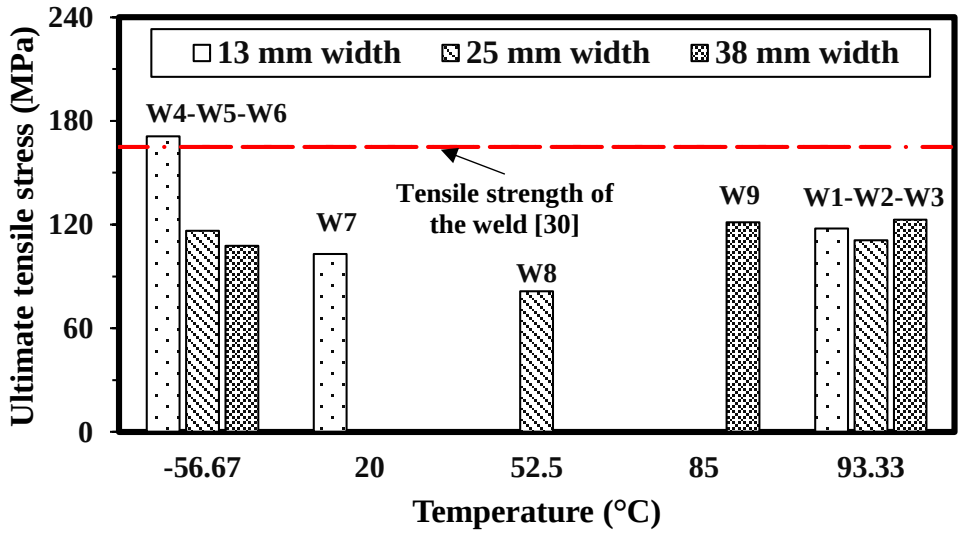

(b)

Figure 3.9: Width effect on ultimate stress for tensile specimens (a) adhesive and (b) weld

3.4.1.3 COMPARISON BETWEEN ADHESIVE AND WELDED SPECIMENS

Figure 3.10 shows a comparative representation of ultimate tensile stress between the adhesive and welded specimens. For 13 mm specimens, the welded specimens have more the ultimate stress than the adhesive specimens by 467%, 783%, and 477% at 93.33 °C, -56.67 °C, and 20 °C, respectively as displayed in pairs A1-W1, A4-W4, and C1-W7. The welded specimens with 25 mm width at 93.33 °C, -56.67 °C, and 52.5 °C are observed to have 421%, 493%, and 376% higher ultimate tensile stress compared to the adhesive specimens as shown in pairs A2-W2, A5-W5, and C8-W8. For specimens at 93.33 °C, -56.67 °C, and 85 °C, the welded specimens are found to have 502%, 444%, and 658% higher ultimate tensile stress relative to the adhesive specimens (see pairs A3-W3, A6-W6, and C16-W9). The highest difference in ultimate tensile stress between the adhesive and welded specimens were observed for the 13 mm specimens at -56.67 °C for pair A4-W4 as welded tensile specimens from combination W4 possessed the maximum tensile strength. Variation in ultimate tensile stress was observed to be minimum for pair C8-W8 (25 mm specimens at 52.5 °C) welded tensile specimens from combination W8 exhibited the least tensile strength during the test.

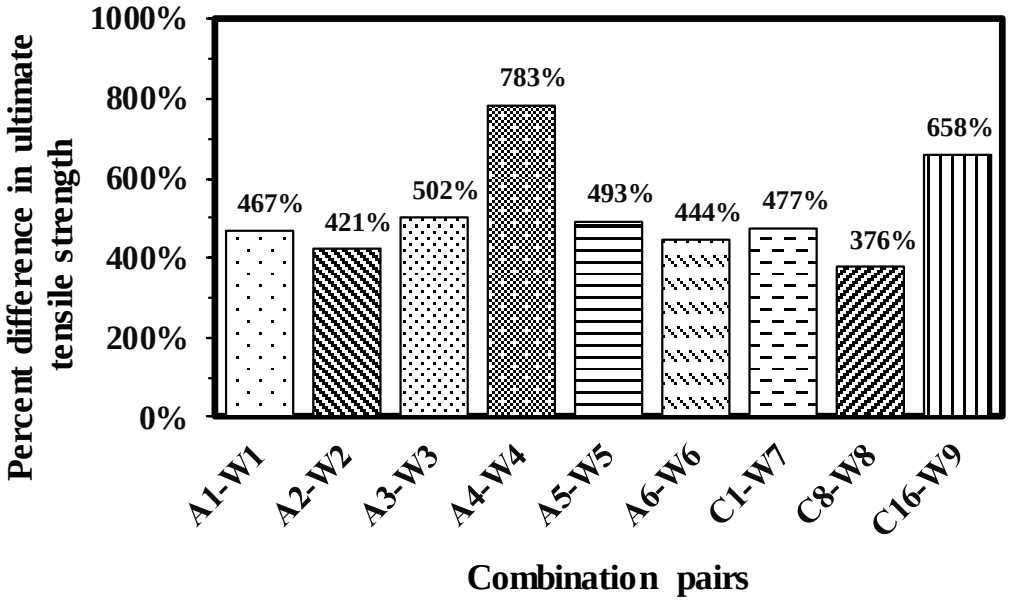

Figure 3.10: Percent difference in ultimate tensile stress between adhesive and welded specimens

3.4.2 SHEAR TEST

Stress-strain curves generated from the testing result of shear specimens are depicted in Figure 3.11. Figure 3.11a shows the stress-strain curves of adhesive shear specimens. It is apparent that the 25 mm specimens conditioned at 93.33 °C exhibit the peak shear stress, the 13 mm specimen conditioned at 20 °C showed the median shear stress, and the 38 mm specimen conditioned at 85 °C showed the minimum shear stress. The stress-strain curves of the welded shear specimens are presented in Figure 3.11b. The 38 mm specimens conditioned at 93.33 °C provide the highest shear stress, while the 38 mm specimen conditioned at 85 °C displayed the lowest shear stress. The median shear stress is observed in the 38 mm specimen conditioned at 85 °C. The ultimate shear stress values acquired from shear tests at different combinations along with failure modes are presented in Table 3.3. In this table, cohesive failure is observed to the major failure

mode for the adhesive shear specimens, whereas all the welded shear specimens are found to be failed with weld throat failure mode.

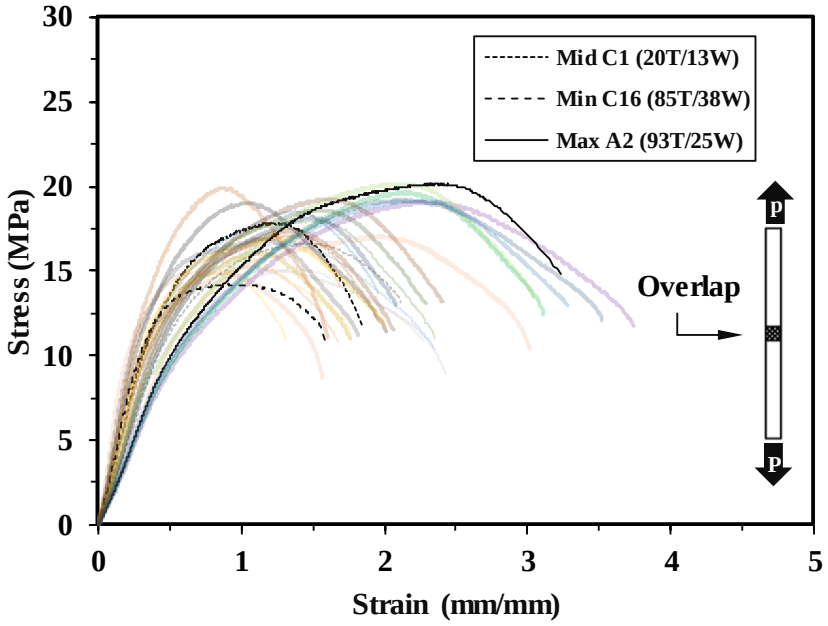

(a)

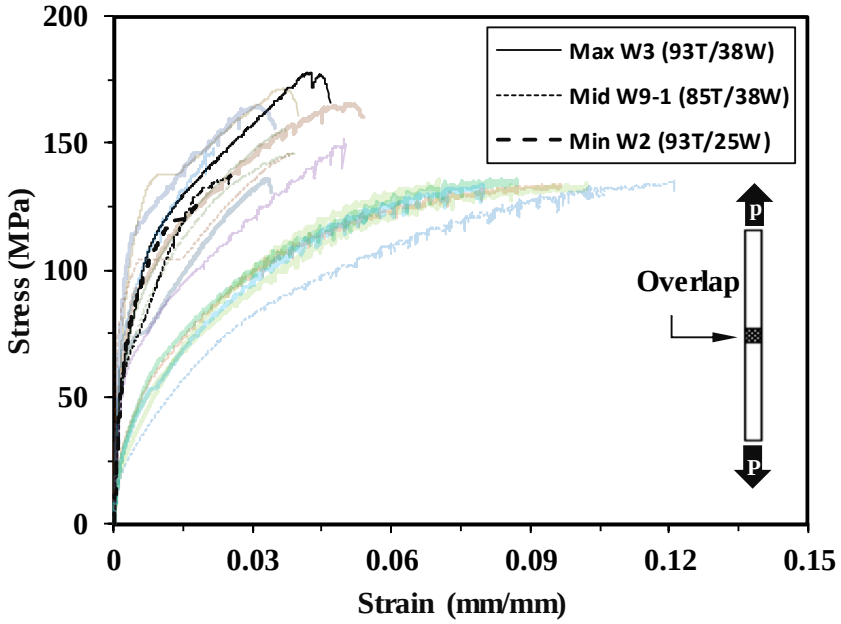

(b)

Figure 3.11: Representative stress-strain curves for shear specimens (a) adhesive and (b) welded

Table 3.3 Ultimate shear strength from the shear test

Specimen ID	Ultimate shear stress, τ_u (MPa)	Failure mode
A-S-13TH-93.3T-A1	19.38	cohesive failure
A-S-25TH-93.3T-A2	20.17	cohesive failure
A-S-38TH-93.3T-A3	19.18	cohesive failure
A-S-13TH-(-56.7)T-A4	18.68	cohesive failure
A-S-25TH-(-56.7)T-A5	18.10	cohesive failure
A-S-38TH-(-56.7)T-A6	18.39	cohesive failure
A-S-13TH-20.0T-C1	17.48	cohesive failure
A-S-38TH-20.0T-C2	16.06	Adhesive/cohesive failure
A-S-25TH-20.0T-C3	17.97	cohesive failure
A-S-13TH-52.5T-C7	16.00	cohesive failure
A-S-25TH-52.5T-C8	14.96	cohesive failure
A-S-38TH-52.5T-C10	17.84	cohesive failure
A-S-13TH-85.0T-C12	17.05	cohesive failure
A-S-25TH-85.0T-C14	15.47	cohesive failure
A-S-38TH-85.0T-C16	15.41	cohesive failure
W-S-13TH-93.3T-W1	150.86	Weld throat failure
W-S-25TH-93.3T-W2	149.07	Weld throat failure
W-S-38TH-93.3T-W3	171.21	Weld throat failure
W-S-13TH-(-56.7)T-W4	134.16	Weld throat failure
W-S-25TH-(-56.7)T-W5	135.72	Weld throat failure
W-S-38TH-(-56.7)T-W6	134.79	Weld throat failure
W-S-13TH-20.0T-W7	147.21	Weld throat failure
W-S-25TH-52.5T-W8	150.76	Weld throat failure
W-S-38TH-85.0T-W9	144.56	Weld throat failure

Figure 3.12a and Figure 3.12b present the sample failure modes of adhesive shear specimens having a width of 13 mm and 38 mm, respectively. Cohesive failure is observed to be the predominant failure mode. In this failure mode, adhesive can be observed in both surfaces of aluminum that represents high adhesion between the surfaces in the adhesive joint. As there is high adhesion between the surfaces in the adhesive joint, failure occurs within the interface of adhesive, resulting in the cohesive failure in the shear specimens. Remarkably, two adhesive specimens of combination C2

failed in adhesive/cohesive failure mode. In this failure mode, only certain part of adhesive joint in the shear specimens is observed to fail in cohesive failure mode. This type of failure mode is observed when the adhesion between the aluminum surfaces is not uniform throughout the adhesive joint. Representative failure modes of the welded shear specimens are also shown in Figure 3.12c and Figure 3.12d. All welded specimens appeared to fail in weld throat failure mode as in the welded tensile specimens. In each specimen, failure was detected at the weld between the connections of thin-walled aluminum specimens. As the base aluminum of the welded shear specimens possess higher shear strength than the shear strength of the weld throat at welded section, weld throat failure is observed.

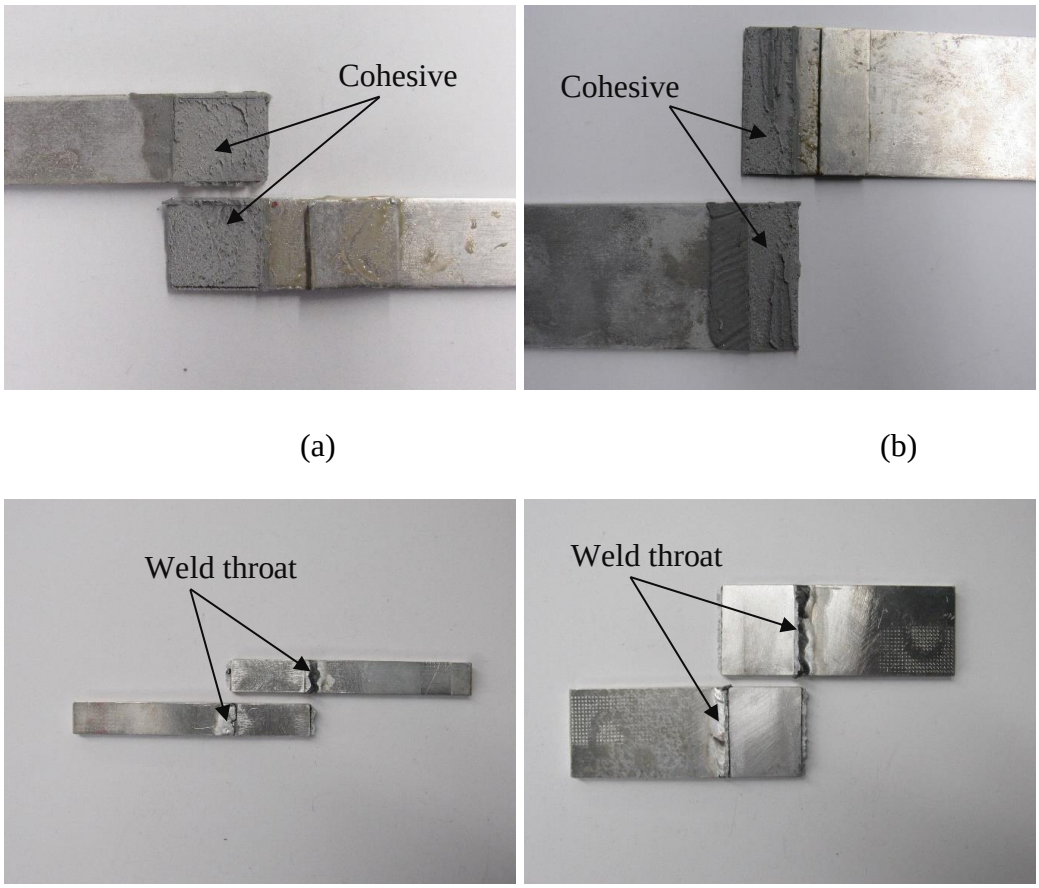

Figure 3.12: Representative failure modes of shear specimens (a) adhesive with 13 mm width, (b) adhesive with 38 mm width, (a) welded with 13 mm width, and (d) welded with 38 mm width

3.4.2.1 EFFECT OF TEMPERATURE

Figure 3.13 illustrates the effect of temperature on the ultimate shear stress at several temperature conditions considered in this study. The temperature effect on the ultimate stress of the adhesive shear specimens is shown in Figure 3.13a. The ultimate stress of 13 mm shear specimens is decreased by 6.4% and 8.5% when the temperature is increased from -56.67 °C to 20 °C and 20 °C to 52.5 °C subsequently. When the temperature increases from 52.5 °C to 85 °C and 85 °C to 93.33 °C successively, the ultimate stress is

increased by 6.5% and 13.7%, as shown in A4-C1-C7-C12-A1. For 25 mm specimens, the ultimate stress is decreased by 0.7% and 16.8% with an increment of temperature from -56.67 °C to 20 °C and 20 °C to 52.5 °C. The ultimate stress of the 25 mm specimens increases by 3.4% and 30.4% when the temperature is increased from 52.5 °C to 85 °C and 85 °C to 93.33 °C (see A5-C3-C8-C14-A2). For 38 mm shear specimens, the ultimate stress reduces by 12.7% and increases by 11.1% when the temperature increases from -56.67 °C to 20 °C and 20 °C to 52.5 °C. The ultimate stress is reduced by 13.6% when the temperature further increases from 52.5 °C to 85 °C, whereas the ultimate stress is increased by 24.5% with an increment of temperature from 85 °C to 93.33 °C as shown in A6-C2-C10-C16-A3. Although 38 mm specimens between the temperatures of 20 °C to 85 °C are observed to have a different trend, the ultimate shear stress is appeared to decrease from 20 °C to 52.5 °C and increase from 52.5 °C to 93.33 °C. Again, the glass transition temperature of the adhesive is 75 °C. The shear stress is observed to decrease below the glass transition temperature, whereas the shear stress is observed to increase when the temperature is increased beyond the glass transition temperature. This increase in shear stress can be attributed to the fact that above glass transition temperature, adhesive begins to transition from hard to soft, rubbery substance which increases the cohesive nature of the adhesive. This increases the shear stress of the adhesive when specimens are conditioned beyond glass transition temperature.

Figure 3.13b presents the temperature effect on the ultimate shear stress for the welded shear specimens. As shown in W4-W7-W1, the ultimate stress of 13 mm specimens is increased by 9.7% and 2.5% with the increment of temperature from -56.67 °C to 20 °C and 20 °C to 93.33 °C successively. The ultimate stress of 25 mm specimens

increases by 11.1% when temperature is increased from -56.67 °C to 52.5 °C but decreases by 1.1% with further increment in temperature from 52.5 °C to 93.33 °C (see W5-W8-W2). For 38 mm specimens, when the temperature was increased from -56.67 °C to 85 °C, the ultimate stress is surged by 7.3%. The ultimate stress is increased by 18.4% when the temperature further increases from 85 °C to 93.33 °C as displayed in W6-W9-W3. Observing the general trend of tested welded shear specimens, increase in temperature is found to have positive effects in the ultimate shear stress. Further, the shear stress of the welded shear specimens is found to be substantially higher than the design shear stress of the 4043 aluminum filler weld (80 MPa) calculated according to Aluminum Design Manual (Aluminum Association 2010).

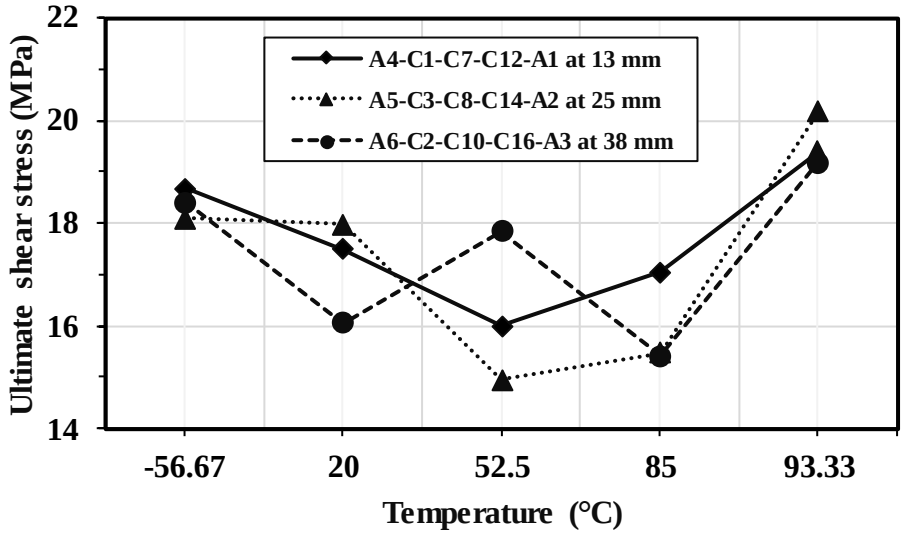

(a)

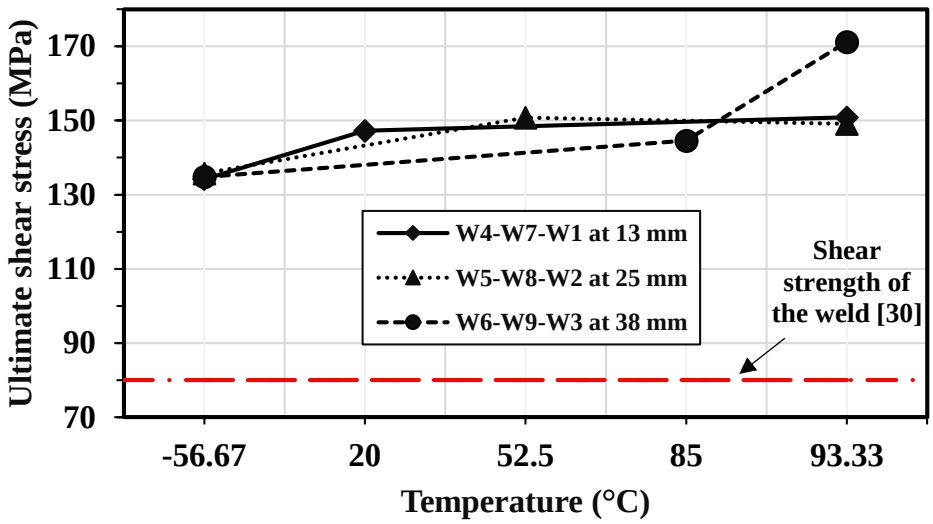

(b)

Figure 3.13: Temperature effect on ultimate stress for shear specimens (a) adhesive and (b) weld

3.4.2.2 EFFECT OF WIDTH

The effect of specimen's width on the ultimate shear stress is shown in Figure 3.14 in a bar graph. Figure 3.14a shows the effect of width on the ultimate stress of the adhesive specimens at five distinct temperatures. The ultimate stress at -56.67 °C reduces by 3.1% with an increment of specimen width from 13 mm to 25 mm. When the specimen width is increased from 25 mm to 38 mm the ultimate stress is increased by 1.6% at -56.67 °C as presented in A4-A5-A6. At 20 °C, the ultimate stress is improved by 2.8% and decreased by 10.6% with the increment of specimen width from 13 mm to 25 mm and 25 mm to 38 mm as shown in C1-C3-C2. The ultimate stress of the specimens at 52.5 °C is decreased by 6.5% and increased by 19.3% with the increment of specimen width from 13 mm to 25 mm and 25 mm to 38 mm as depicted in C7-C8-C10. At 85 °C, when the specimen width is increased from 13 mm to 25 mm and 25 mm to 38 mm, the ultimate

stress is decreased by 9.3% and 0.3%, respectively (see C12-C14-C16). The ultimate stress of specimens at 93.33 °C increases by 4% when the specimen width is increased from 13 mm to 25 mm. The ultimate stress, however, decreases by 4.9% when the width of the specimen is increased from 25 mm to 38 mm as shown in A1-A2-A3.

In Figure 3.14b, the effect of width on the ultimate shear stress for the welded shear specimens at different temperatures is illustrated. The ultimate stress at -56.67 °C is increased by 1.2% when width of welded shear specimen is increased from 13 mm to 25 mm and is decreased by 0.7% with increment of specimen width from 25 mm to 38 mm as shown in W4-W5-W6. At 93.33 °C, the ultimate stress of welded specimens is decreased by 1.2% with the increment of specimen width from 13 mm to 25 mm, however, the ultimate stress increases by 14.9% with further increment of specimen width from 25 mm to 38 mm as shown in W1-W2-W3. The 25 mm welded shear specimens at 52.5 °C observed to have 2.4% higher ultimate stress than 13 mm welded shear specimens at 20 °C (see W7 and W8). The 38 mm welded shear specimens at 85 °C is observed to have 4.1% lower ultimate stress than the 25 mm specimens at 52.5 °C (see W8 and W9). The shear stress of the welded specimens was observed to be significantly greater compared to the shear stress of 4043 aluminum filler weld (80 MPa) obtained from according to Aluminum Design Manual (Aluminum Association 2010).

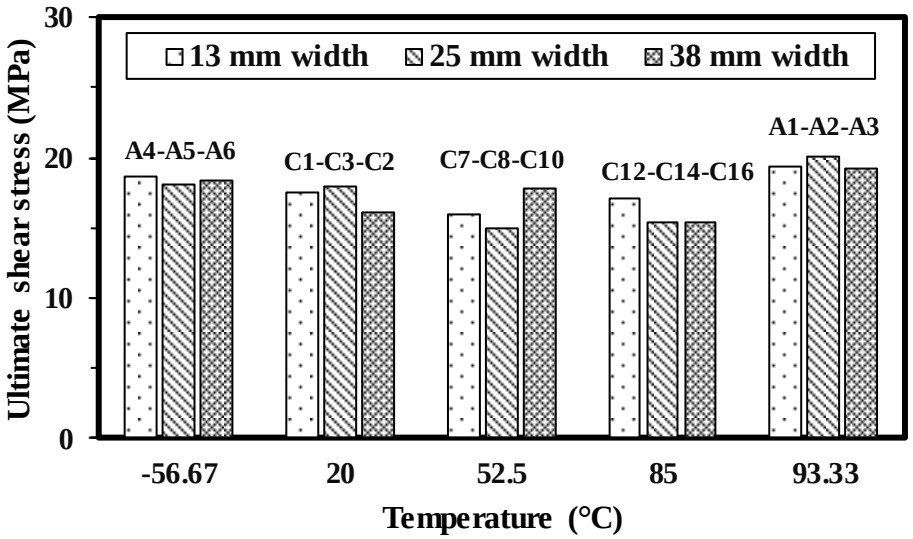

(a)

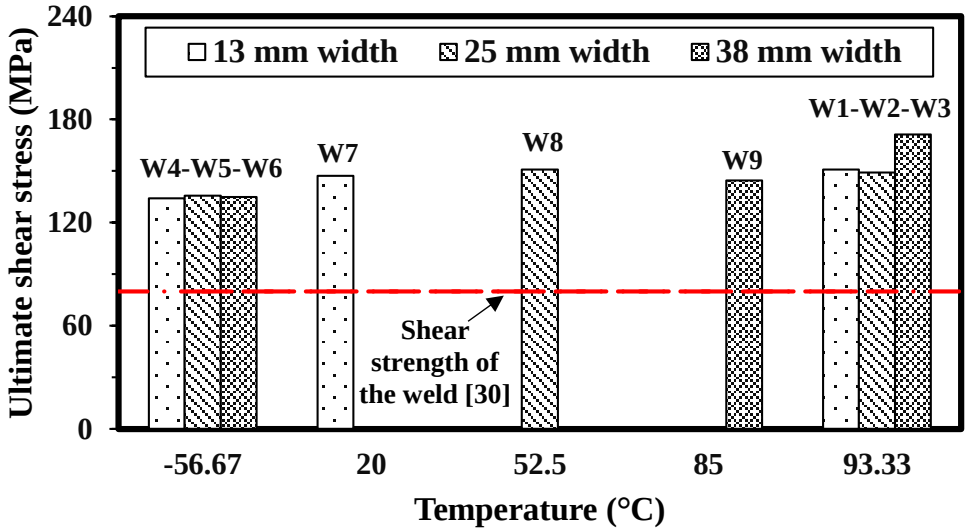

(b)

Figure 3.14: Width effect on ultimate stress for shear specimens (a) adhesive and (b) weld

3.4.2.3 COMPARISON BETWEEN ADHESIVE AND WELDED SPECIMENS

A graphical comparison of the ultimate shear stress between each combination of the adhesive and welded shear specimens is shown in Figure 3.15. The 13 mm welded shear

specimens are observed to have 678% higher shear stress than the adhesive specimens at 93.33 °C as shown in pair A1-W1. At -56.67 °C and 20 °C, the 13 mm welded specimens are found to be stronger than the adhesive specimens by 618% and 742%, respectively, as shown in pairs A4-W4 and C1-W7. The 25 mm welded specimens at 93.33 °C, -56.67 °C, and 52.5 °C observed 639%, 650%, and 908% higher ultimate shear stress in comparison to the adhesive specimens as displayed in pairs A2-W2, A5-W5, and C8-W8. For 38 mm specimens at 93.33 °C, -56.67 °C, and 85 °C, the welded specimens are found to have 792%, 633%, and 838% higher ultimate shear stress compared to the adhesive specimens (see pairs A3-W3, A6-W6, and C16-W9).

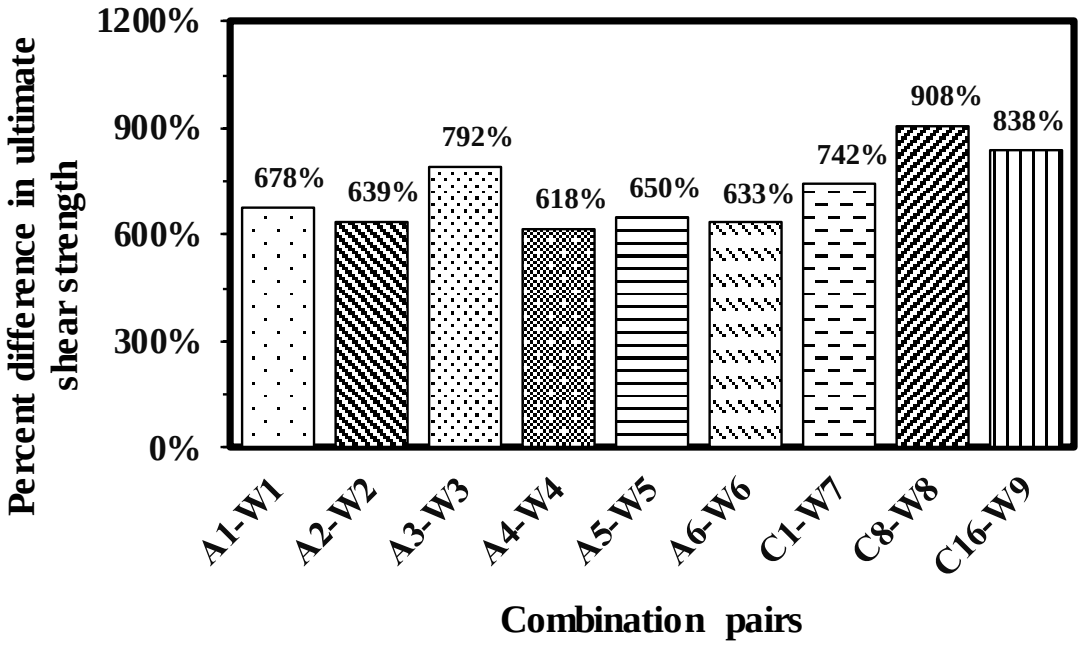

Figure 3.15: Percent difference in ultimate shear stress between adhesive and welded specimens

3.5 STATISTICAL ANALYSIS FOR RSMS

RSMs that can be used to efficiently explore the effects of temperature and width on each strength were created through regression analysis of the tensile and shear stress data acquired from the testings of both adhesive and welded specimens. Note, RSMs have been successfully used to replicate the structural and mechanical characteristics of various engineering structures (Seo, and Pokhrel 2019, Seo et al. 2012, Seo and Park 2017). A commercially available statistical software, R (Team 2015), was used to develop the RSMs through least squares regression of each set of the tensile and shear stress data corresponding to individual input parameters. The temperature and width of the specimens were deemed as the input parameters. The RSMs created for the prediction of the ultimate tensile stress of adhesive and welded specimens are presented in Equation 3.1 and Equation 3.2, respectively.

$$f_{ua} = 16.9452 - 0.3531\,T - 0.2429\,W - 0.4066TW + 2.5069T^2 - 0.0860W^2$$

(Equation 3.1)

$$f_{uw} = 75.4433 - 6.8095\,T - 13.4666W + 17.7163TW + 38.6953T^2 + 16.0623W^2$$

(Equation 3.2)

where f_{ua} is the ultimate tensile stress for adhesive specimens (MPa), f_{uw} is the ultimate tensile stress for welded specimens (MPa), T is the conditioning temperature (°C), and W is the width of the specimen (mm).

The RSMs for the prediction of the ultimate shear stress of adhesive and welded specimens are shown in Equation 3.3 and Equation 3.4.

$$\tau_{ua} = 15.9363 - 0.2526T + 0.0499W - 0.1092TW + 1.8089T^2 + 0.786W^2$$

(Equation 3.3)

$$\tau_{uw} = 145.4880 + 9.3148\,T + 1.6987W + 2.0960TH - 2.3364T^2 + 1.7918W^2$$

(Equation 3.4)

where τ_{ua} is the ultimate shear stress of adhesive specimens (MPa) and τ_{uw} is the ultimate shear stress of welded specimens (MPa).

3D surface plots were also generated for the ultimate tensile stress of adhesive and welded specimens utilizing the RSMs presented in Equation 3.1 and Equation 3.2. These plots present the trend of the ultimate tensile stress with respect to both temperature and width of the specimens as shown in Figure 3.16.

The effect of temperature and width on ultimate tensile stress of adhesive specimens is observed closely to be of concave shape as displayed in Figure 3.16a. It appears that with the increase in width from 13 mm to 38 mm at lower temperature (-56.67 °C), the ultimate tensile stress is increased by 1.67%. The increment of width at higher temperature of 93.33 °C decreased the ultimate tensile stress by 6.61%. With the increase in temperature, the ultimate tensile stress is observed to be decreasing initially with significant rise after reaching the minimum value. At lower width of 13 mm, the ultimate tensile stress is increased by 0.55% with the increase in temperature (-56.67 °C to 93.33 °C), however, at higher width of 38 mm, the tensile stress decreases by 7.64% with the increase in temperature (-56.67 °C to 93.33 °C).

The plot of ultimate tensile stress for welded specimens in terms of temperature and width is observed to be of concave shape as presented in Figure 3.16b. In this figure, the tensile stress is decreased significantly by 37.08% with increment of width (13 mm to 38 mm) at lower temperature of -56.67 °C. At higher temperature (93.33 °C), with the increase in width (13 mm to 38 mm), the tensile stress is increased by 7.13%. The ultimate tensile stress is decreased by 29.16% with the increase in temperature (-56.67 °C to 93.33 °C) at lower width of 13 mm, whereas, at higher width (38 mm), the tensile stress is raised by 20.61% with the increase in temperature from -56.67 °C to 93.33 °C.

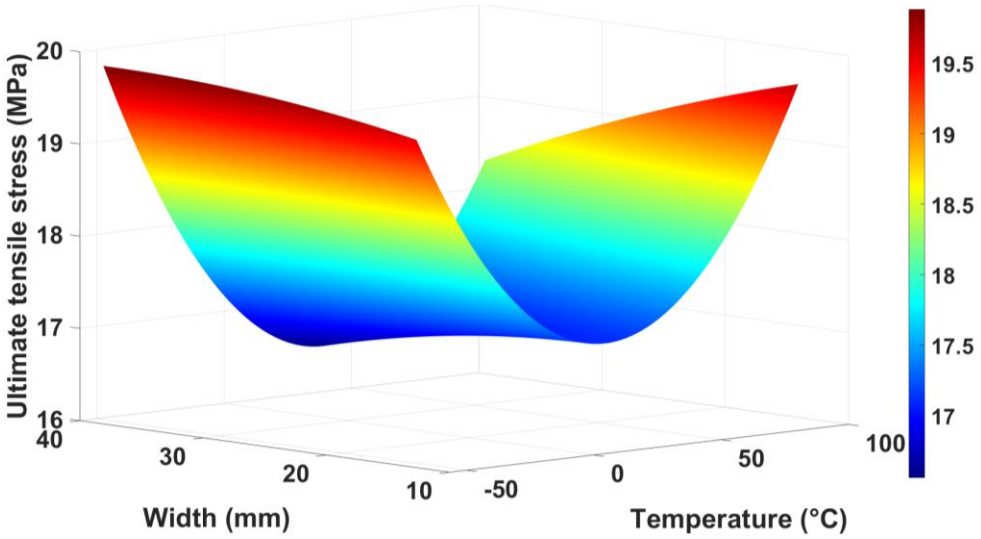

(a)

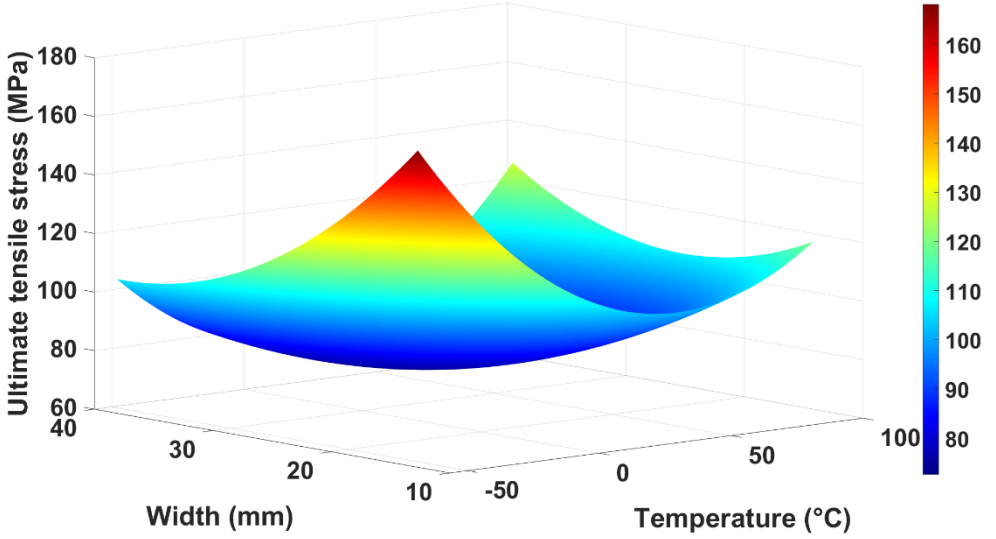

(b)

Figure 3.16: RSM plots of ultimate tensile stress showing effects of temperature and width for (a) adhesive specimens and (b) welded specimens

The RSMs presented in Equation 3.3 and Equation 3.4 were also used to develop 3D surface plots for the ultimate shear stress of adhesive and welded specimens as shown in Figure 3.17. A concave shape of the plot can be observed due to the effect of temperature

and width on the ultimate shear stress of adhesive specimens as shown in Figure 3.17a. In Figure 3.17a, the increment of width from 13 mm to 38 mm at lower temperature of -56.67 °C increased the ultimate shear stress by 1.71%, whereas, the ultimate shear stress decreased by 0.65% at higher temperature (93.33 °C) due to the increment of width (13 mm to 38 mm). The increase in temperature decreased the ultimate shear stress at first, however, the ultimate shear stress is improved significantly after a minimum value. The ultimate shear stress is dropped by 1.54% at lower width of 13 mm and by 3.82% at higher width of 38 mm with the increase in temperature (-56.67 °C to 93.33 °C).

The plot of ultimate shear stress for welded specimens showing the effect of temperature and width is found to be of planar shape as presented in Figure 3.17b. In this Figure, the shear stress is decreased by 0.58% with increment of width (13 mm to 38 mm) at lower temperature of -56.67 °C. At higher temperature of 93.33 °C, the ultimate shear stress is increased by 5.04% with the increase in width (13 mm to 38 mm). The increment of temperature from-56.67 °C to 93.33 °C increased the ultimate shear stress by 10.61% at lower width of 13 mm and by 16.88% at higher width of 38 mm.

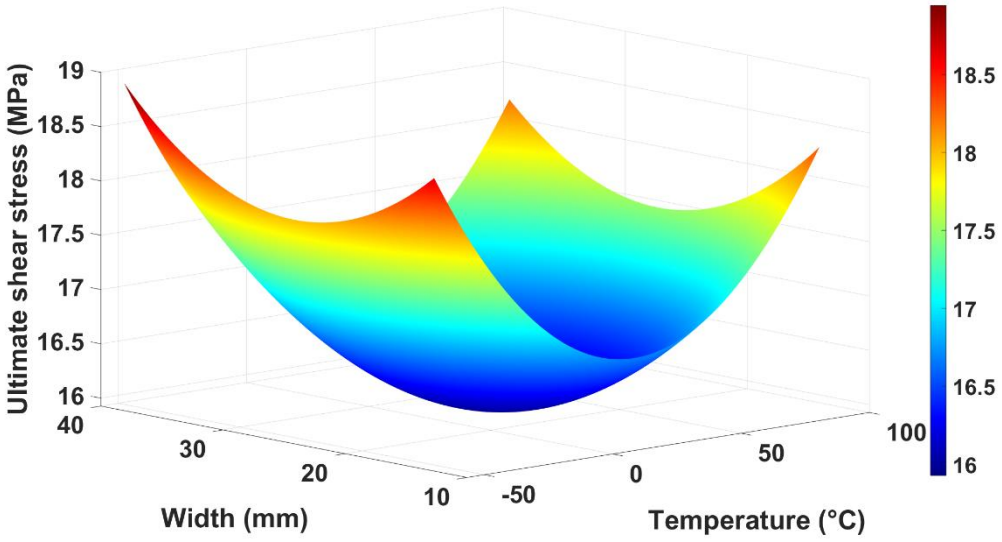

(a)

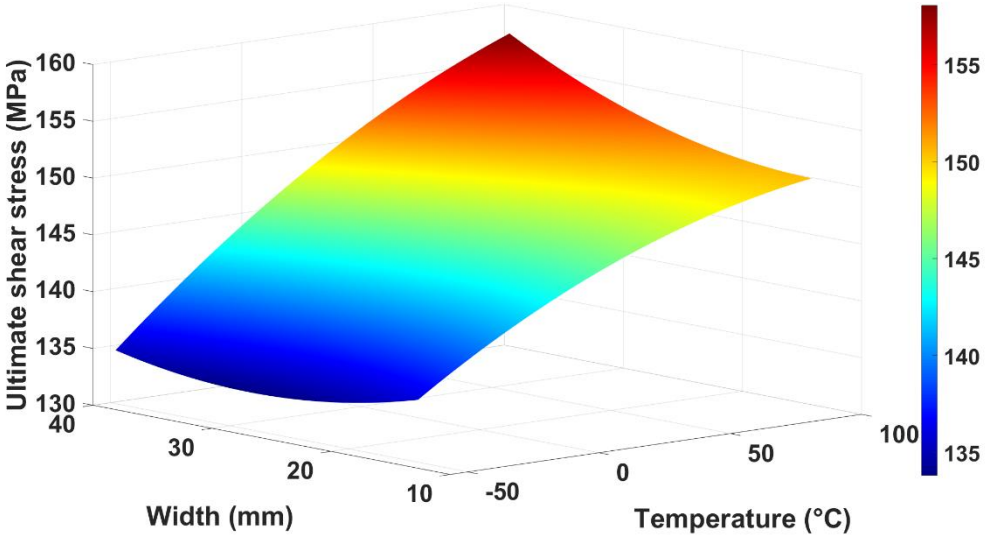

(b)

Figure 3.17: RSM plots of ultimate shear stress showing effects of temperature and width for (a) adhesive specimens and (b) welded specimens

From the study of 3D surface plots, conditioning temperature was found to affect the tensile and shear stress of welded specimens significantly. The width of specimens was observed to have a substantial influence on the tensile stress of welded specimens.

3.6 DESIGN EQUATIONS

Practical design equations were further proposed for the better prediction of ultimate tensile and shear stress of adhesive and welded specimens. As in the testing program, conditioning temperature and width of specimens were considered parameters for the development of design equations. The design equations were developed in Microsoft excel solver following the generalized reduced gradient method (Sharma and Glemmestad 2013, Lasdon et al. 1974). This method utilizes an algorithm that solves the nonlinear problem by computing reduced gradient. The developed equations for the ultimate tensile stress of adhesive and welded specimens are presented in Equation 3.5 and Equation 3.6, correspondingly.

$$f_{ua} = C_A^{P_A}(2.2939(T + 273.15)^{0.2348}) \times C_A^{P_A}(1.7390 \times W^{0.1}) \quad \text{(Equation 3.5)}$$

$$f_{uw} = C_W^{P_W}(2.2939(T + 273.15)^{0.2348}) \times C_W^{P_W}(1.7390 \times W^{0.1}) \quad \text{(Equation 3.6)}$$

where f_{ua}, f_{uw}, T, W, C_A, C_W, P_A, *and* P_W represent the ultimate tensile stress for adhesive specimens (MPa), ultimate tensile stress for welded specimens (MPa), the conditioning temperature (°C), specimen's width (mm), coefficient value for adhesive tensile specimens, coefficient value for welded tensile specimens, variable value for adhesive tensile specimens, and variable value for welded tensile specimens. Values of C_A, C_W, P_A, *and* P_W calculated for the Equation 3.5 and Equation 3.6 are 0.4830, 4.4415, 0.1000, and 0.5599, respectively.

The equations have an average error of 10.64% for the adhesive tensile specimens and 12.09% for the welded tensile specimens. Figure 3.18 presents a scatter plot of the

ultimate tensile stress developed to check the precision of the equations for the ultimate tensile stress. The ultimate tensile stress obtained from the tests is plotted against those computed from the equations. The residuals of the measured ultimate tensile stress with those calculated by the equations are represented by the identity line shown in this figure. The coefficient of determination for the proposed equations for the ultimate tensile stress was found to be 0.8864 and except for few outliers, most data lie close to the identity line, indicating high accuracy for the equations for the prediction of ultimate tensile stress of adhesive and welded specimens.

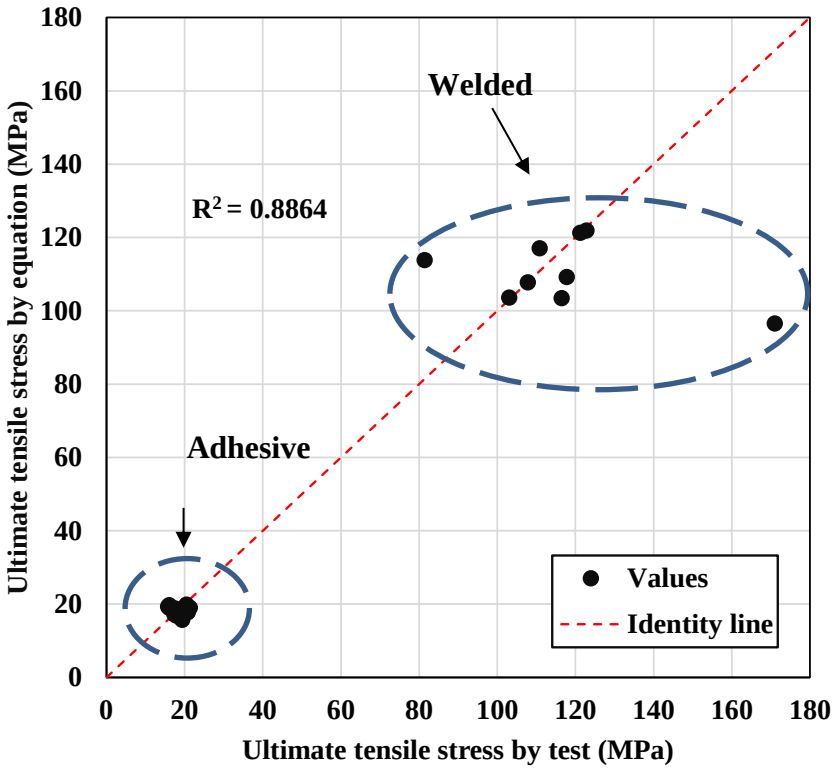

Figure 3.18: Scatter plot of ultimate tensile stress to observe proposed equation's accuracy

Equation 3.7 and Equation 3.8 present the developed equations for the prediction of ultimate shear stress for adhesive and welded specimens, respectively.

$$\tau_{ua} = C_A^{P_A}(2.8778(T + 273.15)^{0.1460}) \times C_A^{P_A}(2.1817 \times W^{0.1}) \quad \text{(Equation 3.7)}$$

$$\tau_{uw} = C_W^{P_W}(2.8778(T + 273.15)^{0.1460}) \times C_W^{P_W}(2.1817 \times W^{0.1}) \quad \text{(Equation 3.8)}$$

where τ_{ua}, τ_{uw}, *T, W,* C_A, C_W, P_A, *and* P_W denotes ultimate shear stress for adhesive specimens , ultimate shear stress for welded specimens, the conditioning temperature (°C), specimen's width (mm), coefficient value for adhesive shear specimens, coefficient value for welded shear specimens, variable value for adhesive shear specimens, and variable value for welded shear specimens. Values of C_A, C_W, P_A, *and* P_W calculated for the Equation 3.7 and Equation 3.8 are 0.5648, 4.8203, 0.1000, and 0.6301, respectively.

The equations for the prediction of ultimate shear stress for the adhesive and welded specimens are observed to have an average percentage error of 9.37% and 5.32%, respectively. A scatter plot is also created to investigate the accuracy of the equations as shown in Figure 3.19. The plot shows the shear stress quantities obtained from the shear testing and equations. The identity line displayed in this figure denotes the residuals of the predicted shear stress with the equation from the measured results. As in the trend of tensile stress data, the majority of data points were found at a proximity to the identity line. Further, the coefficient of determination for the equation was determined to be 0.9920. Discussion above implies that the equations generated for the prediction of ultimate shear stress of adhesive and welded specimens exhibit high precision.

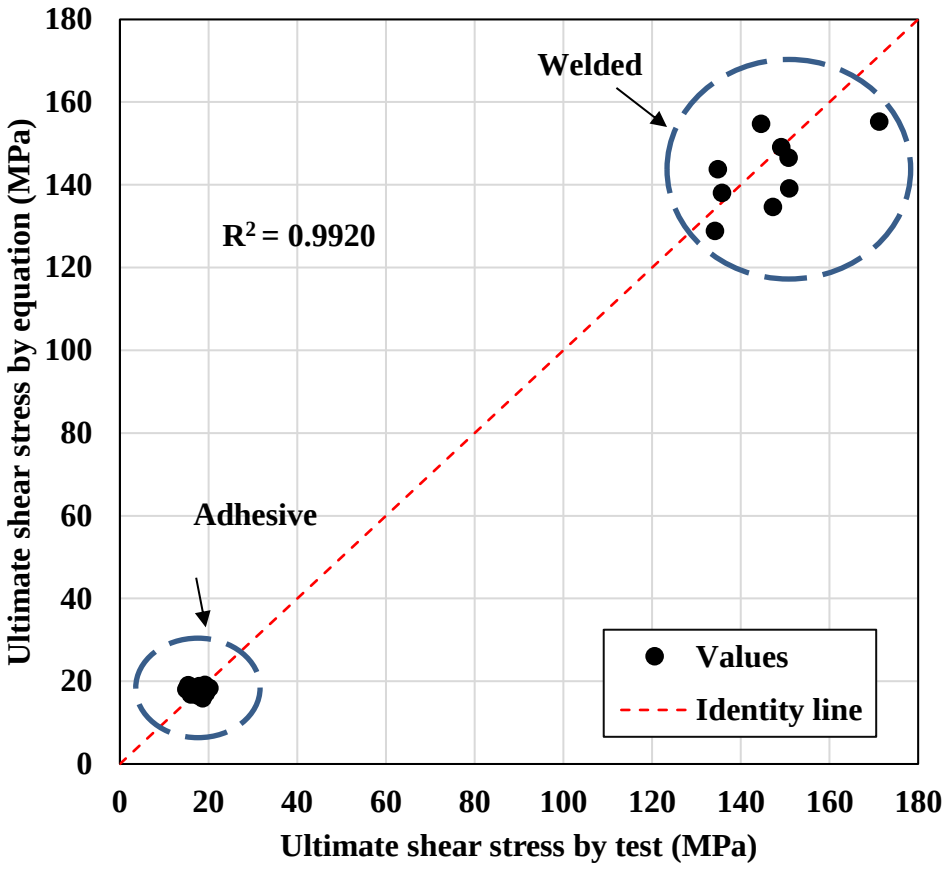

Figure 3.19: Scatter plot of ultimate shear stress to observe proposed equation's accuracy

Furthermore, the coefficient of determination of the RSMs and the design equations were compared as listed in Table 3.4 to determine the most reliable equations for the prediction of ultimate tensile and shear stress. Observation of the coefficient of determination suggests higher reliability of the design equations for the prediction of ultimate stresses except for the ultimate tensile stress of the welded specimens. It is recommended to utilize the design equations for the prediction of ultimate tensile and shear stress of adhesive and welded specimens in general. The RSM, however, would be more precise for the prediction of ultimate tensile stress of the welded specimens.

Table 3.4 Coefficient of determination values for RSMs and proposed equations

Strength type	RSM		Design equation	
	Adhesive	Welded	Adhesive	Welded
Tensile stress	0.4386	0.9821	0.8864	0.8864
Shear stress	0.3134	0.6635	0.9920	0.9920

3.7 CONCLUSIONS

In this study, the tensile and shear strength testings with the adhesive and weld specimens were conducted not only to study the effect of temperature and width on each strength, but also to help better understand the mechanical behavior of adhesive and welded connections used in dynamic message signs (DMSs). For the testings, the single set of 30 combinations was tested per strength under nine different variations of temperature and width. Each combination comprised two specimens for each strength. The effect of temperature and width on each strength for both adhesive and welded specimens was studied with the established experimental program in associated with American Society of Testing and Materials (ASTM) and American Welding Society (AWS). Each strength of adhesive specimens was also compared with that of welded specimens. The tensile and shear testing data were analyzed statistically to generate Response Surface Metamodels (RSMs) and 3D surface plots to observe the effect of temperature and specimen's width on the both stresses. The following conclusions can be derived from experimental testing and evaluation:

1. Due to the effect of temperature, in the tensile strength test of adhesive specimens, the highest increment and decrement in the tensile stress were 31.9% and

11%. For the welded specimens, the highest increment and decrement were 36.2% and 39.7%. Owing to the effect of width, for the tensile adhesive strength testing, the peak increment and decrement in the tensile stress were 2.5% and 9.4%. With the welded specimens, the peak increment and decrement in the tensile stress were 49% and 31.9%. All the adhesive tensile specimens failed with rupture failure, whereas all the welded tensile specimens failed with weld throat failure.

2. For the adhesive tensile specimens, tensile stress was observed to be decreasing when temperature was increased below glass transition temperature of the adhesive, whereas tensile stress was found to be increasing with the increment of temperature above adhesive's glass transition temperature. This can be attributed to the increase in adhesive's flexibility which improved the cohesive behavior of the adhesive in the joint when temperature was increased above adhesive's glass transition temperature. For the welded tensile specimens, tensile stress of the majority of the tested specimens was found to be lower than the design tensile stress of the weld acquired from Aluminum Design Manual (Aluminum Association 2010).

3. With the effect of temperature, in the shear strength test of adhesive specimens, the maximum increment and decrement in the shear stress were 30.4% and 16.8%. For the welded specimens, the maximum increment and decrement were 18.4% and 1.1%. Along with the effect of width, in the shear strength test of adhesive specimens, the highest increment and decrement in the shear stress were 19.3% and 10.6%. For the welded specimens, the highest increment and decrement were 14.9% and 4.1%. All the adhesive shear specimens failed with cohesive failure mode except for two specimens, whereas weld throat failure was observed in all welded shear specimens.

4. For the adhesive shear specimens, increment of temperature below adhesive's glass transition temperature observed decreasing trend in the shear stress, while increment of temperature beyond adhesive's glass transition temperature followed increasing trend in the shear stress. For the welded shear specimens, shear stress of all the tested specimens was observed to be significantly higher compared to the design shear stress of the weld obtained from Aluminum Design Manual (Aluminum Association 2010).

5. The tensile stress of welded specimens was found to be significantly higher than the adhesive specimen with the maximum difference of 783% for 13 mm width at -56.67 °C and the minimum difference of 376% for 25 mm width at 52.5 °C. In the shear test, each of the welded specimens was observed to have higher shear strength than adhesive specimens with the maximum difference of 908% for 25 mm width at 52.5 °C and minimum difference of 618% for 13 mm width at -56.67 °C.

6. The RSMs that were developed were used to efficiently predict the ultimate tensile and shear stresses of both adhesive and welded specimens and to visibly observe the effect of temperature and width on both stresses. A significant effect of temperature was observed for the tensile and shear stress of welded specimens, whereas the effect of width was found to be substantial for the tensile stress of welded specimens. The practical design equations were also developed for the prediction of both ultimate tensile and shear stresses of the tested specimens. Overall, the developed design equations were able to better predict the measured ultimate tensile stress of adhesive specimens and shear stress of both adhesive and welded specimens than the RSMs. The RSM, however, was

more reliable for forecasting the ultimate tensile stress of welded specimens relative to the corresponding design equation.

3.8 REFERENCES

Lee, M. H., Kim, H. Y., & Oh, S. I. (2006). Crushing test of double hat-shaped members of dissimilar materials with adhesively bonded and self-piercing riveted joining methods. *Thin-Walled Structures*, *44*(4), 381-386.

Higgins, A. (2000). Adhesive bonding of aircraft structures. *International Journal of Adhesion and Adhesives*, *20*(5), 367-376.

Hill, J. (2003). Adhesively Bonded Structural Composites for Aston Martin Vehicles. *Ford Motor Company Research and Advanced Engineering*.

Çolak, A., Çoşgun, T., & Bakırcı, A. E. (2009). Effects of environmental factors on the adhesion and durability characteristics of epoxy-bonded concrete prisms. *Construction and Building materials*, *23*(2), 758-767.

Savvilotidou, M., Vassilopoulos, A. P., Frigione, M., & Keller, T. (2017). Development of physical and mechanical properties of a cold-curing structural adhesive in a wet bridge environment. *Construction and Building Materials*, *144*, 115-124.

Goglio, L., & Rezaei, M. (2014). Variations in mechanical properties of an epoxy adhesive on exposure to warm moisture. *Journal of Adhesion Science and Technology*, *28*(14-15), 1394-1404.

Silva, P., Fernandes, P., Sena-Cruz, J., Xavier, J., Castro, F., Soares, D., & Carneiro, V. (2016). Effects of different environmental conditions on the mechanical characteristics of a structural epoxy. *Composites Part B: Engineering*, *88*, 55-63.

Zhang, Y., Vassilopoulos, A. P., & Keller, T. (2010). Effects of low and high temperatures on tensile behavior of adhesively-bonded GFRP joints. *Composite Structures*, *92*(7), 1631-1639.

Hu, P., Akhmet, G., Wu, C. W., Han, X., Chao, Y. X., Yu, Y., & Orazbayeva, A. (2019). Characterisation on the influence of curing history on the mechanical performance of adhesively bonded corrugated sandwich structures. *Thin-Walled Structures*, *142*, 37-51.

Fernando, D., Yu, T., Teng, J. G., & Zhao, X. L. (2009). CFRP strengthening of rectangular steel tubes subjected to end bearing loads: Effect of adhesive properties and finite element modelling. *Thin-Walled Structures*, *47*(10), 1020-1028.

Agarwal, A., Foster, S. J., Hamed, E., & Ng, T. S. (2014). Influence of freeze–thaw cycling on the bond strength of steel–FRP lap joints. *Composites Part B: Engineering*, *60*, 178-185.

Kim, Y. J., Hossain, M., & Yoshitake, I. (2012). Cold region durability of a two-part epoxy adhesive in double-lap shear joints: Experiment and model development. *Construction and Building Materials*, *36*, 295-304.

Ferreira, J. A. M., Reis, P. N., Costa, J. D. M., & Richardson, M. O. W. (2002). Fatigue behaviour of composite adhesive lap joints. *Composites science and technology*, *62*(10-11), 1373-1379.

Sugiman, S., Crocombe, A. D., & Aschroft, I. A. (2013a). The fatigue response of environmentally degraded adhesively bonded aluminium structures. *International Journal of Adhesion and Adhesives*, *41*, 80-91.

Sugiman, S., Crocombe, A. D., & Aschroft, I. A. (2013b). Experimental and numerical investigation of the static response of environmentally aged adhesively bonded joints. *International Journal of Adhesion and Adhesives*, *40*, 224-237.

Sousa, J. M., Correia, J. R., & Cabral-Fonseca, S. (2018). Durability of an epoxy adhesive used in civil structural applications. *Construction and Building Materials*, *161*, 618-633.

Amatya, I., Seo, J., Letcher, T., & Bierschbach, D. (2020). Tensile and shear strength tests with adhesive connections in dynamic message signs. *Mechanics of Materials, under review*.

Seo, J. (2013). Statistical determination of significant curved I-girder bridge seismic response parameters. *Earthquake Engineering and Engineering Vibration*, *12*(2), 251-260.

Chandorkar, A. N., Mande, S., & Iwai, H. (2008, October). Estimation of process variation impact on DG-FinFET device performance using Plackett-Burman design of experiment method. In *2008 9th International Conference on Solid-State and Integrated-Circuit Technology* (pp. 215-218). IEEE.

Seo, J., & Linzell, D. G. (2013). Influential Curved Steel Bridge Fragility Analysis Parameters. In *Forensic Engineering 2012: Gateway to a Safer Tomorrow* (pp. 84-92).

Seo, J., & Linzell, D. G. (2012). Horizontally curved steel bridge seismic vulnerability assessment. *Engineering Structures, 34*, 21-32.

Seo, J., & Linzell, D. G. (2010). Probabilistic Vulnerability Scenarios for Horizontally Curved Steel I-Girder Bridges Under Earthquake Loads. *Transportation Research Record*, *2202*(1), 206-211.

Seo, J., & Linzell, D. G. (2013). Use of response surface metamodels to generate system level fragilities for existing curved steel bridges. *Engineering Structures*, *52*, 642-653.

SAS Institute Inc. (2008). *JMP statistics and graphics guide, version 5.1.2*, Cary, NC

ASTM D638-14. (2010). *Standard test method for tensile properties of plastics*. West Conshohocken: American Society of Testing and Materials.

ASTM D1002-10. (2010). *Standard test method for apparent shear strength of single-lap-joint adhesively bonded metal specimens by tension loading (metal-to-metal)*. West Conshohocken: American Society of Testing and Materials.

LORD Corporation. (2018). LORD® 406 Acrylic Adhesive. Retrieved November 29, 2018, from https://www.lord.com/products-and-solutions/adhesives/lord-406-acrylic-adhesive

American Welding Society. (2015). AWS D1. 1: structural welding code–steel.

MTS Systems Corporation. (2018). MTS Landmark® Servohydraulic Test Systems. Retrieved November 29, 2018, from http://www.mts.com/en/products/producttype/test-systems/load-frames-uniaxial/servohydraulic/standard/index.htm

Aluminum Association. (2010). *2010 Edition of Aluminum Design Manual*. Washington, D.C.

Seo, J., & Pokhrel, J. (2019). Surrogate Modeling for Self-Consolidating Concrete Characteristics Estimation for Efficient Prestressed Bridge Construction. *ACI Special Publication*, *333*, 19-39.

Seo, J., Dueñas-Osorio, L., Craig, J. I., & Goodno, B. J. (2012). Metamodel-based regional vulnerability estimate of irregular steel moment-frame structures subjected to earthquake events. *Engineering Structures*, *45*, 585-597.

Seo, J., & Park, H. (2017). Probabilistic seismic restoration cost estimation for transportation infrastructure portfolios with an emphasis on curved steel I-girder bridges. *Structural safety*, *65*, 27-34.

Team, R. (2015). RStudio: integrated development for R. RStudio, Inc., Boston, MA URL http://www. rstudio. com.

Sharma, R., & Glemmestad, B. (2013). On generalized reduced gradient method with multi-start and self-optimizing control structure for gas lift allocation optimization. *Journal of Process Control*, *23*(8), 1129-1140.

Lasdon, L. S., Fox, R. L., & Ratner, M. W. (1974). Nonlinear optimization using the generalized reduced gradient method. *Revue française d'automatique, informatique, recherche opérationnelle. Recherche opérationnelle*, *8*(V3), 73-103.

CHAPTER 4: PEEL AND CLEAVAGE CHARACTERISTICS OF ADHESIVE AND WELDED JOINTS IN DYNAMIC MESSAGE SIGNS

4.1 ABSTRACT

This paper was intended to examine the peel and cleavage strength of adhesive and welded connections in a dynamic message sign (DMS). For this study, 30 peel specimens and 30 cleavage specimens were fabricated with different widths, conditioned with various extreme temperatures, and tested to determine their peel and cleavage strengths following the guidelines of ASTM D1876 and ASTM D1062, respectively. Effects of temperature and width on the peel and cleavage strength were evaluated by interpreting the test data in a graphical and statistical manner. For the adhesive specimens, due to the increment of temperature, the maximum increments were found to be 70.4% and 37.8%, and the maximum increments owing to the increment of width were 32% and 28.5% for the respective peel and cleavage strength. The welded specimens were found to be more resilient than the adhesive specimens in terms of peel strength, but to have lower cleavage strength up to 31% compared to the adhesive specimens. Response Surface Metamodels (RSMs) acquired from the statistical analysis of testing data was employed to create 3D surface plots that served as the basis to efficiently explore the effects of temperature and width on each strength.

Keywords: Dynamic message sign; Peel; Cleavage; Strength, Adhesive; Weld.

4.2 INTRODUCTION

The major structural components, frames and aluminium back skin in a Dynamic Message Sign (DMS), are typically bonded with welded connections. Adhesives are being popular among DMS industrialists (Higgins 2000, Hill 2003) with its numerous advantages such as workability with dissimilar metals and efficient manufacturing. Further, loads are distributed homogeneously in adhesive connections compared to welded connections, where high residual stresses and distortion are often observed during the welding process. Therefore, adhesives can be a good alternative to conventional welded connections for use in DMSs. To increase the possible use of adhesives, a comprehensive experimental program is required for comparison of adhesive and welded connections, and their peel and cleavage tests need to be performed.

Most of the studies (Amatya et al. 2020a, 2020b, Savvilotidou et al. 2017, Goglio and Rezaei 2014, Silva et al. 2016, Zhang et al. 2010, Agarwal et al. 2014, Kim et al. 2012, Ferreira et al. 2002, Sugiman et al. 2013a, 2013b, Sousa et al. 2018) have focused on determining the tensile and shear strength of adhesive, but adhesives have been rarely examined for peel (Amatya et al. 2020b, Kim and Aravas (1988, De Freitas and Sinke 2014, Broughton et al. 1999) and cleavage strength (Amatya et al. 2020b, Shahid and Hashim 2000, 2002, Zheng et al. 2007). Kim and Aravas (1988) concluded that peel strength was significant to the yield strength, Young's modulus, ductility and thickness of flexible adherend. De Freitas and Sinke (2014) performed the roller peel tests for bonded composite-to aluminum joints to examine the properties of adhesive. A lower peel strength was observed for the specimens with composite adherend rather than the flexible adherend. Adhesively bonded T-peel specimens exposed to temperature were tested by

Broughton et al. (1999), indicating that higher static strength and average peeling were observed for smaller specimens due to greater application of uniform clamping forces in the course of curing process. Regarding the investigation of cleavage strength, Shahid and Hashim (2000) investigated the cleavage strength of adhesively bonded specimens, which observed adhesive thickness insignificant to the cleavage strength. Shahid and Hashim (2002) also studied the effect of surface roughness in the cleavage strength of standard steel/steel specimens and found that cleavage strength was increased with the increment in surface area and roughness of adherend. Zheng et al. (2007) demonstrated that the hardness of the adhesively bonded area increased the cleavage strength slightly.

Studies have shown that strength and durability of adhesives are affected by temperature, however, many studies have been performed for tensile and shear tests while peel and cleavage strengths have been scarcely examined. A detail study to investigate peel and cleavage strength of adhesives and welded connections for varying temperatures is required to be used in DMSs. In this study, peel and cleavage strength of adhesive was investigated for the effect of temperatures, comprising extreme high and low temperature surroundings and compared with strength of weld connections. Excluding this section, this paper covers laboratory strength testing, results and discussion, statistical analysis, and conclusions.

4.3 LABORATORY STRENGTH TESTING

The testing details the study of peel and cleavage tests in variation with width and temperature conditions. This section provides information about the testing combinations, tested specimens, and testing procedures.

4.3.1 TESTING COMBINATIONS

30 peel specimens and 30 cleavage specimens were tested to study the strength of adhesive and welded connections. Note, each combination consisted of two specimens for peel and cleavage strengths individually. 12 adhesive specimens (A1-A6) and 18 welded specimens (W1-W9) were tested for both peel and cleavage strength evaluation. The combination table comprising respective temperature and width is presented in Table 4.1. Data provided in combinations C1, C2, C3, C7, C8, C10, C12, C14, and C16 for adhesive specimens were recycled from (Amatya et al. 2020c) to investigate the effects of temperature and width for a wide range on each strength. The different combinations were generated by Amatya et al. (2020c) with Plackett-Burman Design (Seo 2013, Chandorkar et al. 2008, Seo and Linzell 2010, 2012, 2013a, 2013b) using commercially available statistical software JMP (SAS Institute Inc. 2008). Additional details for the combinations can be obtained elsewhere (Amatya et al. 2020c).

A temperature-controlled chamber was utilized for conditioning the specimens per combination. An ID was provided for each specimen, for instance, W-T-13TH-20T-W7, where the first character is the specimen type (A-adhesive/W-welded), and the following character is to identify the test type (P-peel/C-cleavage). The width of the specimens is characterized by 13TH, 25TH, and 38TH for 13 mm, 25 mm, and 38 mm specimen width. T represents the temperature of the conditioning environment, and the last character denotes the combination number depicted in Table 1. The specimens with identical conditioning temperatures were deposited in a group and conditioned for at least

24 hours before testing. For example, the specimens for combinations A4, A5, A6, W4, W5, and W6 were placed in the chamber at -56.67 ℃ collectively before testing them.

Table 4.1 Combinations for the experimental program

Specimen type	Combination	Specimen ID	Temperature (°C)	Width (mm)
Adhesive	A1	A-P/C-13TH-93.3T-A1	93.3	13
	A2	A-P/C-25TH-93.3T-A2	93.3	25
	A3	A-P/C-38TH-93.3T-A3	93.3	38
	A4	A-P/C-13TH-(-56.7)T-A4	-56.7	13
	A5	A-P/C-25TH-(-56.7)T-A5	-56.7	25
	A6	A-P/C-38TH-(-56.7)T-A6	-56.7	38
	C1	A-P/C-13TH-20.0T-C1	20	13
	C2	A-P/C-38TH-20.0T-C2	20	38
	C3	A-P/C-25TH-20.0T-C3	20	25
	C7	A-P/C-13TH-52.5T-C7	52.5	13
	C8	A-P/C-25TH-52.5T-C8	52.5	25
	C10	A-P/C-38TH-52.5T-C10	52.5	38
	C12	A-P/C-13TH-85.0T-C12	85	13
	C14	A-P/C-25TH-85.0T-C14	85	25
	C16	A-P/C-38TH-85.0T-C16	85	38
Welded	W1	W-P/C-13TH-93.3T-W1	93.3	13
	W2	W-P/C-25TH-93.3T-W2	93.3	25
	W3	W-P/C-38TH-93.3T-W3	93.3	38
	W4	W-P/C-13TH-(-56.7)T-W4	-56.7	13
	W5	W-P/C-25TH-(-56.7)T-W5	-56.7	25
	W6	W-P/C-38TH-(-56.7)T-W6	-56.7	38
	W7	W-P/C-13TH-20.0T-W7	20	13
	W8	W-P/C-25TH-52.5T-W8	52.5	25
	W9	W-P/C-38TH-85.0T-W9	85	38

4.3.2 TESTED SPECIMENS

This section discusses the geometry and fabrication of adhesive and welded specimens for peel and cleavage tests.

4.3.2.1 ADHESIVE SPECIMENS

The adhesive peel and cleavage specimens were fabricated based on ASTM D1876 (ASTM D1876 2008) and ASTM D1062 (ASTM D1062 2008), respectively. The representative peel and cleavage specimens with a width of 13 mm is shown in Figure 4.1 and Figure 4.2. The peel specimens were fabricated by bending two 5052 aluminum metal bars 90°, leaving 76 mm from the tail of the specimen unbent. The bent aluminum bars were uniformly bonded with the LORD 406-19GB (LORD Corporation 2018) acrylic adhesive to the length of 229 mm. The cleavage specimens were manufactured by attaching two 5052 aluminum blocks with the acrylic adhesive. The specimens were cured for at least two weeks after their fabrication and all the specimens were prepared and distributed by a local DMS producer in South Dakota in the United States.

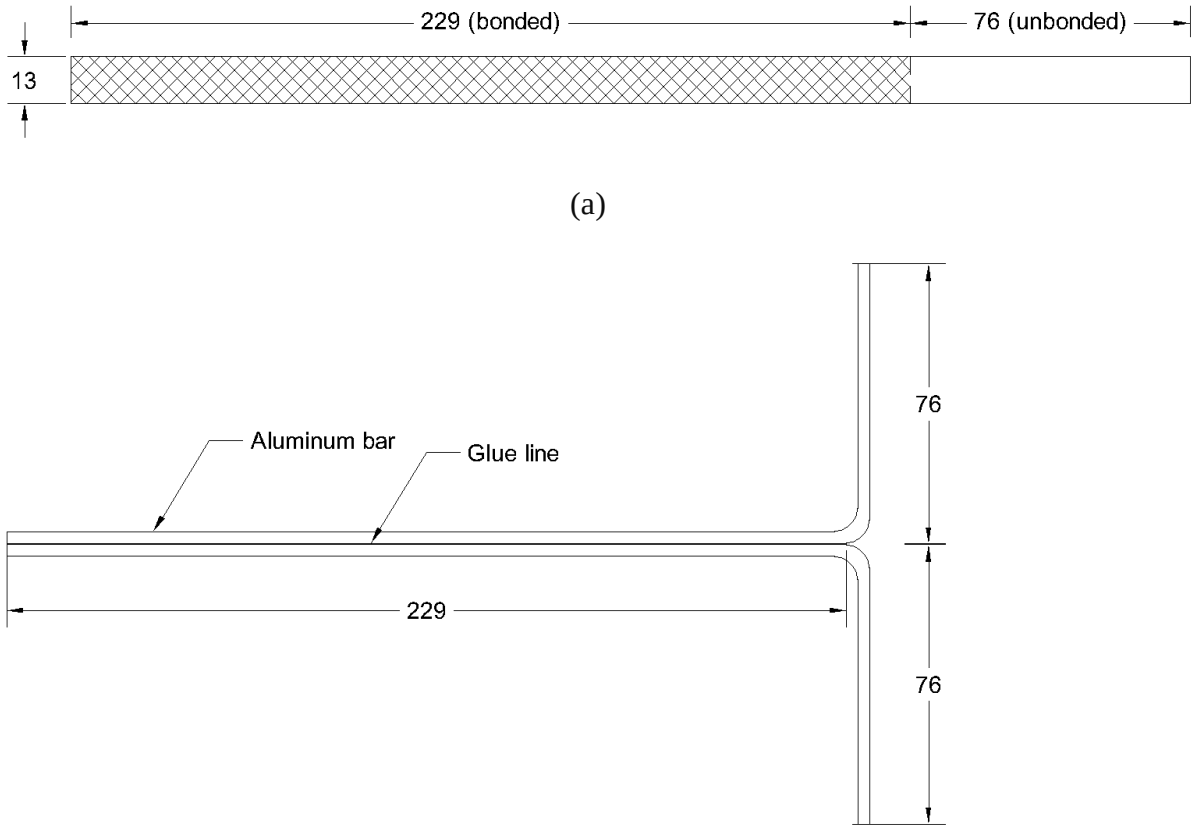

Figure 4.1: Geometry of adhesive peel specimens (a) top view and (b) side view (All dimensions are in mm).

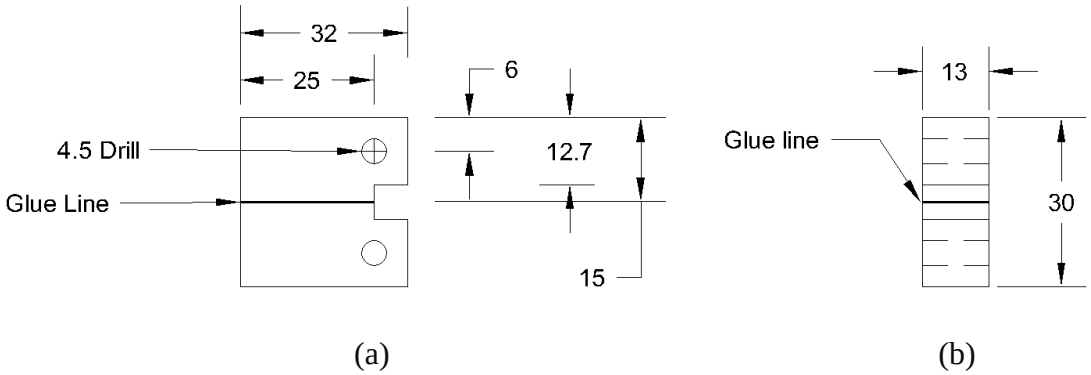

Figure 4.2: Geometry of adhesive cleavage specimens (a) side view and (b) front view (All dimensions are in mm).

4.3.2.2 WELDED SPECIMENS

The welded peel and cleavage specimens were manufactured following ASTM D1876 (ASTM D1876 2008) and ASTM D1062 (ASTM D1062 2008) standards, respectively following the guidelines of American Welding Society (American Welding Society 2015). The local DMS producer used 4043 aluminum alloy for welding in order to fabricate the welded specimens. The dimension of the welded specimens was maintained closely to that of adhesive specimens for consistency. The sample welded peel and cleavage specimens with a width of 13 mm is shown in Figure 4.3 and Figure 4.4, correspondingly. As in the adhesive specimens, the 5052 aluminum was used to fabricate all types of the welded specimens. The peel specimens were fabricated by bending two 5052 aluminum bars 90° up to 76 mm from the tail of the specimen. The bent aluminum bars were joint by 3.2 mm fillet welds up to the length of 229 mm. The cleavage specimens were manufactured by attaching two aluminum blocks with 6.35 mm fillet welds.

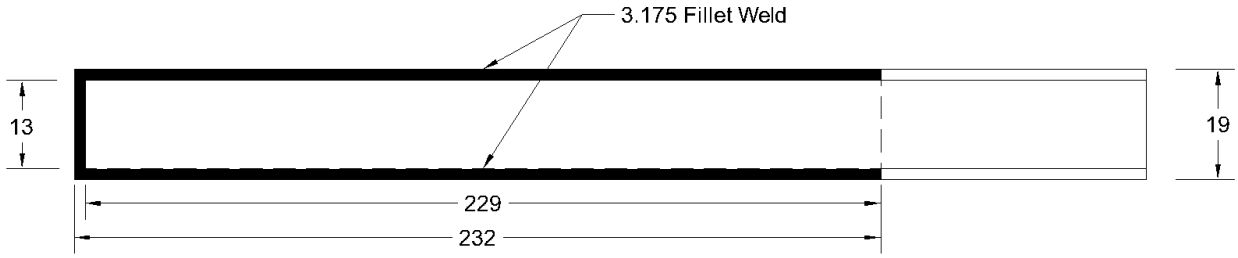

(a)

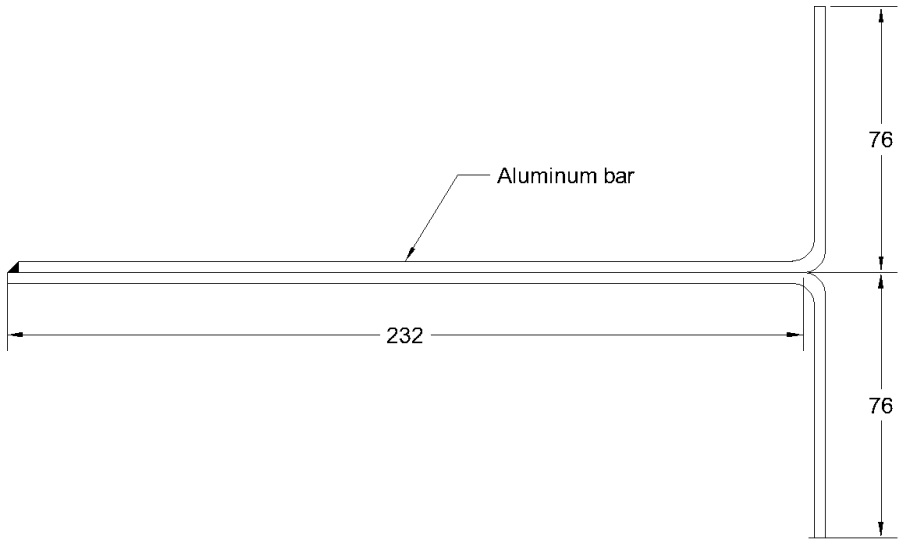

(b)

Figure 4.3: Geometry of welded peel specimens (a) top view and (b) side view (All dimensions are in mm).

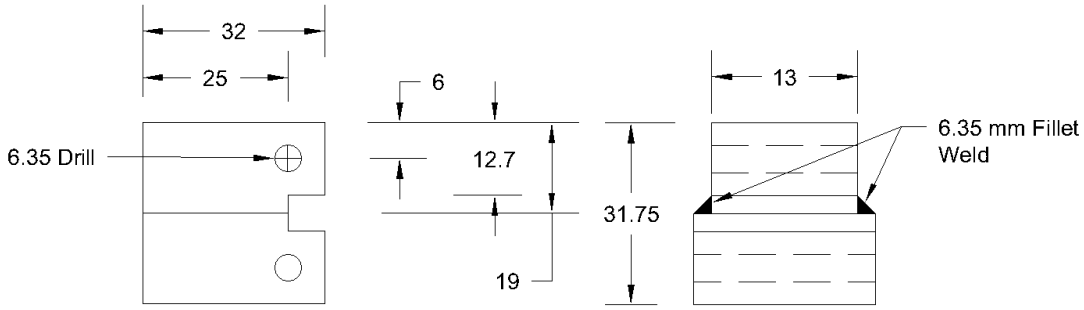

(a) (b)

Figure 4.4: Geometry of welded cleavage specimens (a) side view and (b) front view (All dimensions are in mm).

4.3.3 TESTING PROCEDURE

Two different types of MTS (Material Testing System) Universal Testing Systems were utilized for the testing of peel and cleavage specimens. Each specimen was mounted in MTS grips before the tests, and all specimens were tested to failure at room

temperature. Cleavage specimens were tested using an MTS 370 Landmark (MTS Systems Corporation 2018) 100-kN servo-hydraulic load unit calibrated to 20% of its load capacity whereas the peel tests were performed using MTS Insight 5 (MTS Systems Corporation 2019). The tests were performed with the application of loading at a free crosshead speed of 254 mm/min for the peel specimens and 1.27 mm/min for the cleavage specimens. The testing procedures for peel and cleavage tests are provided in ASTM D1876 (ASTM D1876 2008) and ASTM D1062 (ASTM D1062 2008) standards. The testing setups for the peel and cleavage specimens are presented in Figure 4.5.

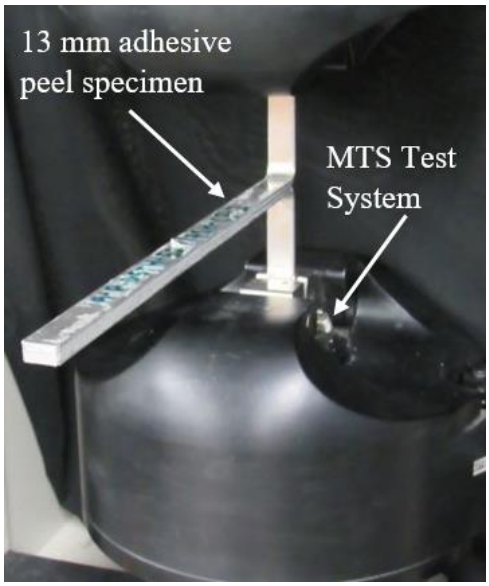

(a)

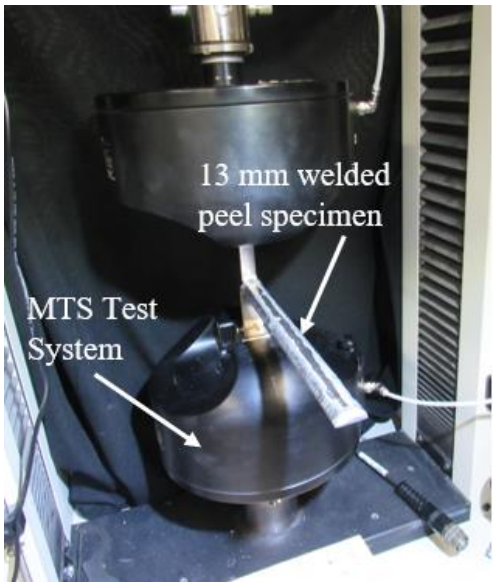

(b)

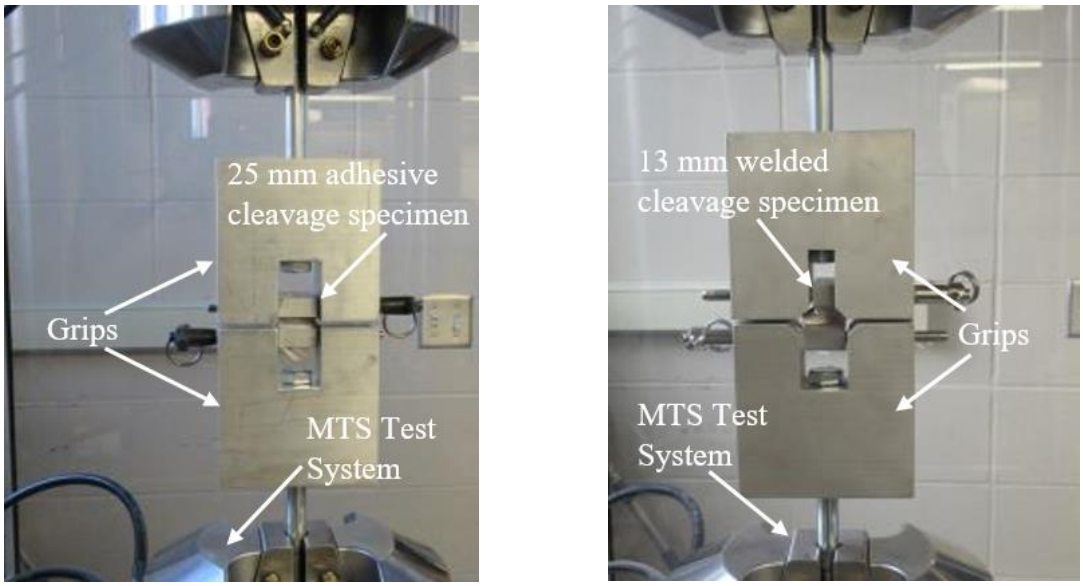

(c) (d)

Figure 4.5: Installation of the specimens in the testing machine (a) adhesive peel, (b) welded peel, (c) adhesive cleavage and (d) welded cleavage.

4.4 RESULTS AND DISCUSSION

Peel and cleavage strength tests along with their results are discussed here. Load-displacement relationships were examined for all the tested specimens to calculate the strength of each. A graphical description for the effect of temperature and width on each of both adhesive and welded specimens is provided as follows.

4.4.1 CHARACTERISTICS FOR PEEL SPECIMENS

Figure 4.6 presents the load-displacement curves for the peel specimens. The peel strength was computed as the average load per unit width of the specimens for the first 127 mm of peeling after the initial peak. As two specimens were tested for each combination generated in Table 4.1, an average peel strength value was calculated from the peel strengths obtained from the first and second tested specimens. Figure 4.6a

presents the behavior of each adhesive peel specimen with load-displacement graphs. 25 mm adhesive peel specimen from combination C8 conditioned at 52.5 °C displayed the maximum peel strength, whereas 38 mm adhesive peel specimen from combination C10 conditioned at 52.5 °C exhibited the minimum peel strength. The load-displacement curves of welded peel specimens is shown in Figure 4.6b. For welded peel specimens, the specimen from combination W7 having 13 mm width conditioned at 20 °C and the specimen from combination W3 having 38 mm width conditioned at 93.33 °C were found to have maximum and minimum peel strengths, respectively. The peel strengths and failure modes of the adhesive and welded peel specimens tested for all the combinations are tabulated in Table 4.2. The peel strengths presented in this table correspond to the average peel strength computed from two peel specimens tested per combination. The equation for the computation of peel strength is provided in Equation 4.1.

$$f_{ap} = Average\left(P/W\right) \quad \text{(Equation 4.1)}$$

where f_{ap} denotes the peel strength, P represents the load observed during the test, and W is the width of the peel specimen.

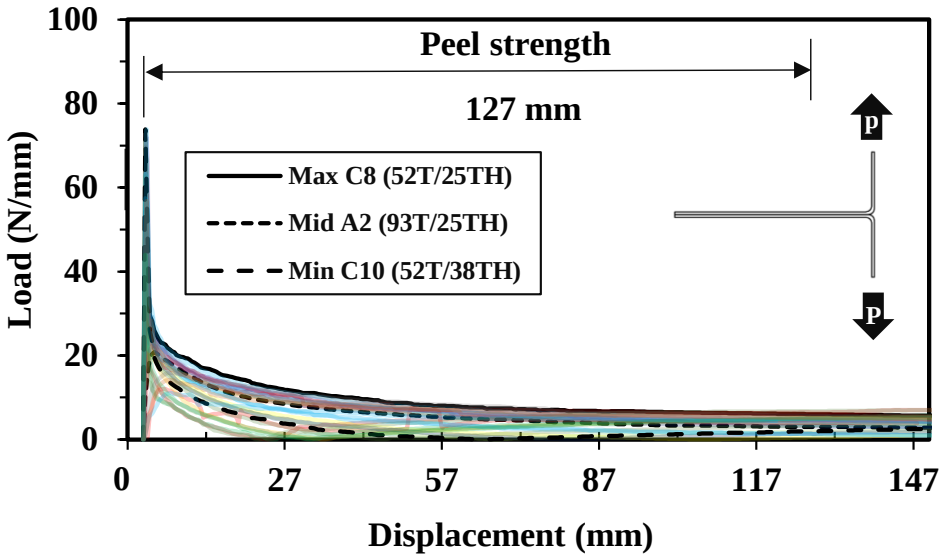

(a)

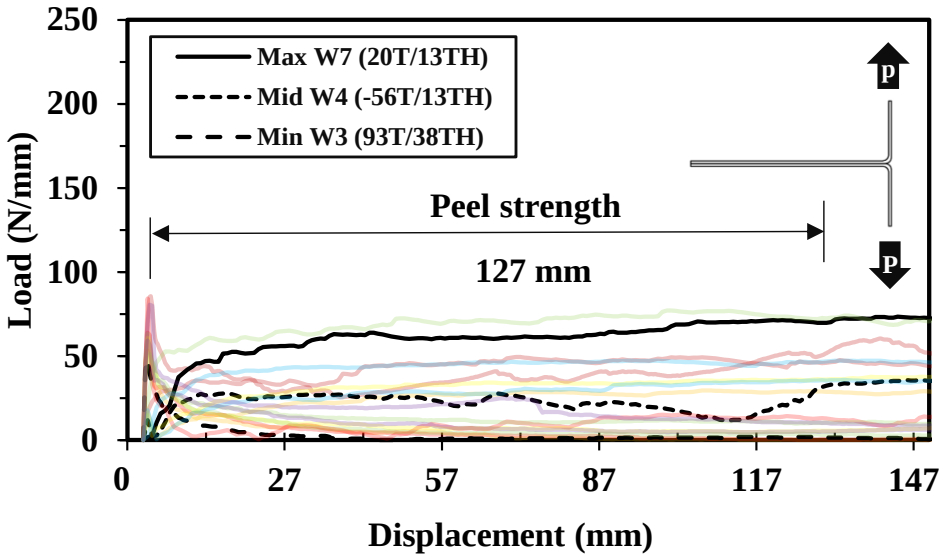

(b)

Figure 4.6: Representative load-displacement curves: (a) adhesive peel specimens and (b) welded peel specimens

Table 4.2 Peel strength from the peel test

Specimen type	Combination	Specimen ID	Peel strength, f_{ap}(N/mm)	Failure mode
Adhesive	A1	A-P-13TH-93.3T-A1	5.06	cohesive
	A2	A-P-25TH-93.3T-A2	5.26	cohesive
	A3	A-P-38TH-93.3T-A3	3.47	cohesive
	A4	A-P-13TH-(-56.7)T-A4	5.42	cohesive
	A5	A-P-25TH-(-56.7)T-A5	6.61	cohesive
	A6	A-P-38TH-(-56.7)T-A6	5.34	cohesive
	C1	A-P-13TH-20.0T-C1	8.10	cohesive
	C2	A-P-38TH-20.0T-C2	5.82	cohesive
	C3	A-P-25TH-20.0T-C3	4.41	cohesive
	C7	A-P-13TH-52.5T-C7	7.73	cohesive
	C8	A-P-25TH-52.5T-C8	7.51	cohesive
	C10	A-P-38TH-52.5T-C10	6.10	cohesive
	C12	A-P-13TH-85.0T-C12	6.79	cohesive
	C14	A-P-25TH-85.0T-C14	7.63	cohesive
	C16	A-P-38TH-85.0T-C16	6.16	cohesive
Welded	W1	W-P-13TH-93.3T-W1	40.42	Weld throat failure
	W2	W-P-25TH-93.3T-W2	14.67	Weld throat failure
	W3	W-P-38TH-93.3T-W3	4.52	Weld throat failure
	W4	W-P-13TH-(-56.7)T-W4	16.06	Weld throat failure
	W5	W-P-25TH-(-56.7)T-W5	19.98	Weld throat failure
	W6	W-P-38TH-(-56.7)T-W6	10.74	Weld throat failure
	W7	W-P-13TH-20.0T-W7	65.88	Weld throat failure
	W8	W-P-25TH-52.5T-W8	35.80	Weld throat failure
	W9	W-P-38TH-85.0T-W9	14.81	Weld throat failure

Representative failure modes of the peel specimens are shown in Figure 4.7. During the test, cohesive failure was observed in all the adhesive peel specimens, indicating good adhesion between the aluminum surface. Figure 4.7a and Figure 4.7b illustrates the representative failure modes of peel specimens with 13 mm and 38 mm widths. Figure 4.7c and Figure 4.7d presents the example of weld throat failure in peel specimens with

13 mm and 38 mm widths. All peel specimens were observed to have this failure mode.

In this failure mode, failure occurs at the weld throat connecting the aluminums.

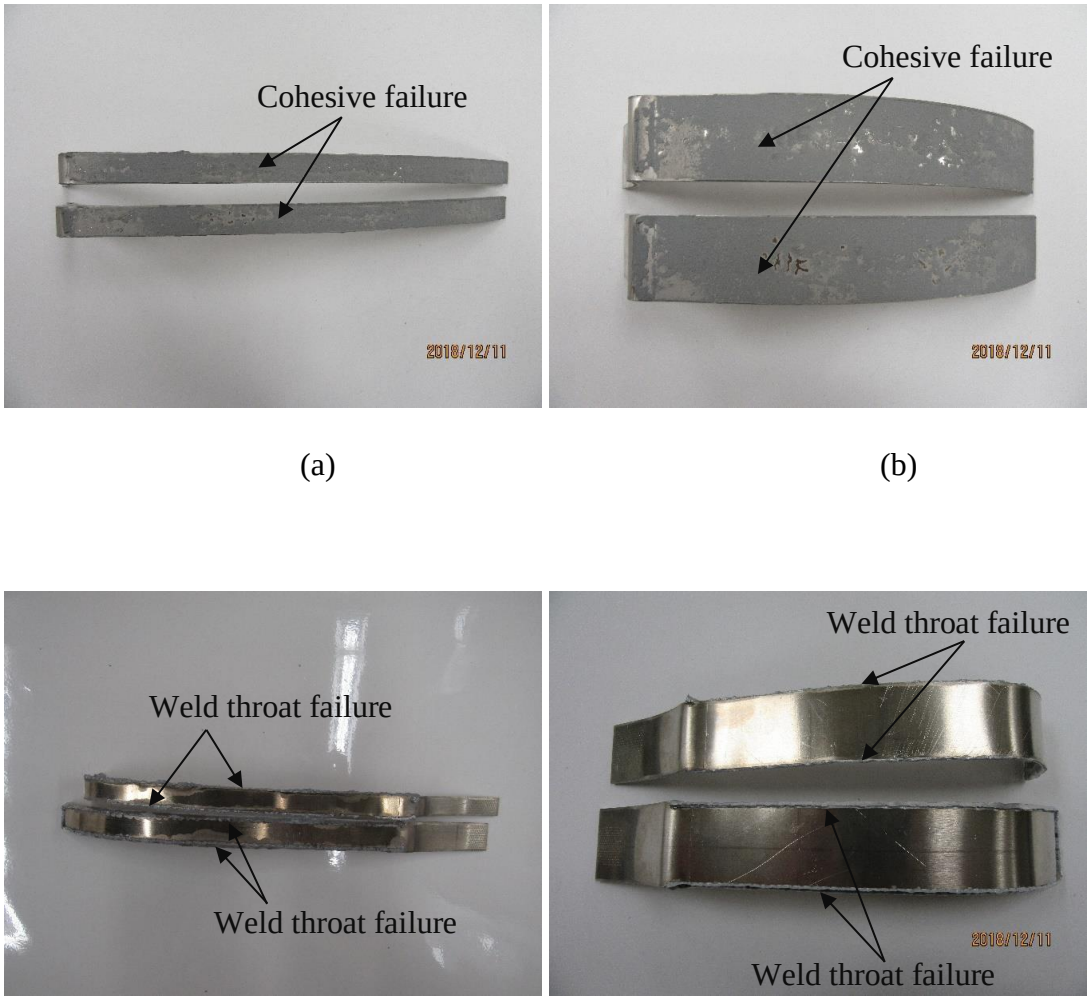

Figure 4.7: Representative failure modes of peel specimens (a) adhesive with 13 mm width, (b) adhesive with 38 mm width, (a) welded with 13 mm width, and (d) welded with 38 mm width

4.4.1.1 EFFECT OF TEMPERATURE

The effect of temperature on the peel strength of both the adhesive and welded peel specimens is shown in Figure 4.8. The behavior of adhesive specimens on the peel strength due to the temperature effect is depicted in Figure 4.8a. The peel strength of 13 mm specimens is increased by 49.7% with the increment of temperature from -56.67 °C to 20 °C. When the temperature is further increased from 20 °C to 52.5 °C, 52.5 °C to 85 °C, and 85 °C to 93.33 °C, the peel strength declines by 4.7%, 12.2%, and 25.5%, respectively as shown in A4-C1-C7-C12-A1. For 25 mm specimens, the decrement in the peel strength is 33.3% when the temperature elevates from -56.67 °C to 20 °C. The peel strength is increased by 70.4% and 1.6% with an additional increment of temperature from 20 °C to 52.5 °C and 52.5 °C to 85 °C respectively. However, the peel strength decreases significantly by 31.1% when the temperature increases by 85 °C to 93.33 °C as depicted in A5-C3-C8-C14-A2. The peel strength of 38 mm specimens improved by 8.9%, 4.8%, and 1.0% with an elevation of temperature from -56.67 °C to 20 °C, 20 °C to 52.5 °C, and 52.5 °C to 85 °C. The peel strength decreases by 43.7% when the temperature increases from 85 °C to 93.33 °C (see A6-C2-C10-C16-A3).

The influence of temperature on the peel strength of the welded specimens is presented in Figure 4.8b. For the 13 mm specimens, the peel strength is raised substantially by 310.3% with the increment of temperature from -56.67 °C to 20 °C, however, it is decreased by 38.7% when temperature is increased from 20 °C to 93.33 °C as shown in W4-W7-W1. The peel strength of 25 mm welded specimens is increased by 79.1% when temperature is increased from -56.67 °C to 52.5 °C whereas the peel strength is decreased by 59.0% with a further elevation of temperature from 52.5 °C to

93.33 °C as shown in W5-W8-W2. As shown in W6-W9-W3, the peel strength of 38 mm welded specimens is increased by 37.9% with the increase of temperature from -56.67 °C to 85 °C. The increment of temperature from 85 °C to 93.33 °C decreased the peel strength by 69.5%.

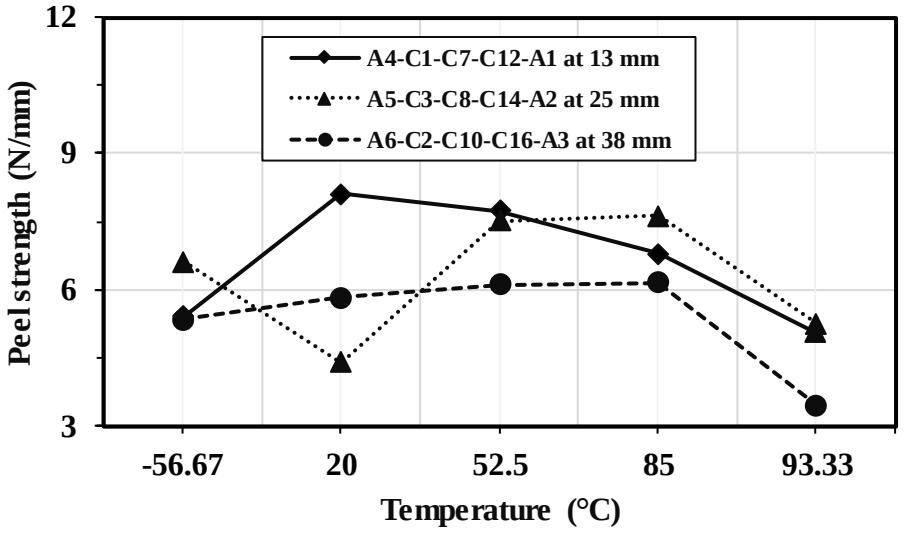

(a)

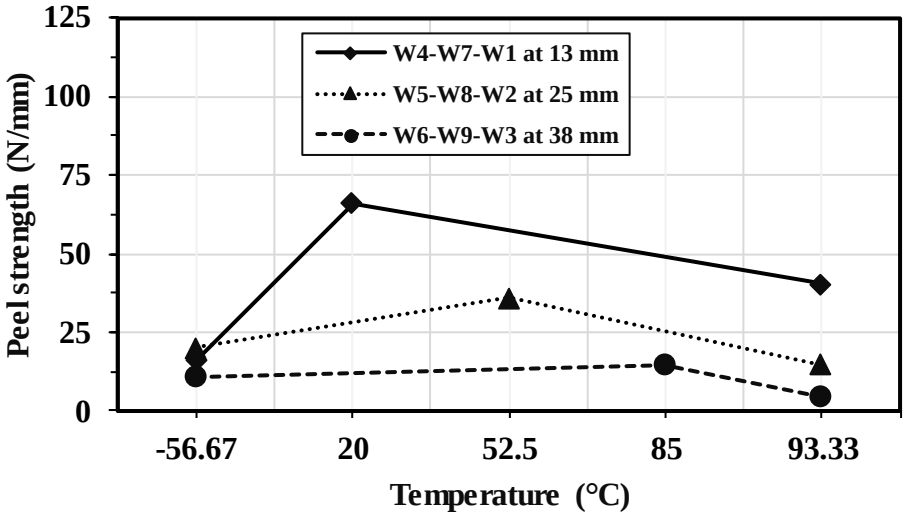

(b)

Figure 4.8: Temperature effect on peel strength: (a) adhesive and (b) weld

4.4.1.2 EFFECT OF WIDTH

The effect of width on the peel strength of the adhesive and welded specimens is shown in Figure 4.8. The peel strength for the adhesive peel specimens of different width

at various temperatures is plotted in a bar chart in Figure 4.8a. At -56.67°C, the peel strength is increased by 22.1% and decreased by 19.2% when the specimen width increases from 13 mm to 25 mm and 25 mm to 38 mm, respectively, as shown in A4-A5-A6. The peel strength is decreased by 45.6% and increased by 32% with an increment of specimen width from 13 mm to 25 mm and 25 mm to 38 mm at 20 °C as shown in C1-C3-C2. For the specimens at 52.5 °C, the peel strength declines by 2.8% and 18.8% when width of specimen increases from 13 mm to 25 mm and 25 mm to 38 mm as displayed in C7-C8-C10. The peel strength of specimens at 85 °C is improved by 12.5% but reduced by 19.2% as depicted in C12-C14-C16 with an increment of specimen width from 13 mm to 25 mm and 25 mm to 38 mm. When the width of the specimen at 93.33 °C is increased from 13 mm to 25 mm, the peel strength is increased by 4.1% only, whereas the peel strength decreases by 34.1% when the specimen width is increased from 25 mm to 38 mm as displayed in A1-A2-A3.

In Figure 4.9b, the effect of width on the peel strength for the welded specimens at different temperatures is shown. The peel strength at -56.67 °C is increased by 24.4% and decreased by 46.2% with an increment of specimen width from 13 mm to 25 mm and 25 mm to 38 mm, respectively as displayed in W4-W5-W6. As shown in W1-W2-W3 at 93.33 °C, the peel strength is decreased by 63.7% with an increment of specimen width from 13 mm to 25 mm. The peel strength is further decreased by 69.2% with an increment of specimen width from 25 mm to 38 mm. The peel strength is decreased by 45.7% when the peel strength of the 25 mm welded specimens at 52.5 °C is compared with that of the 13 mm welded specimens at 20 °C (see W7 and W8). The comparison

between the 38 mm specimens at 85 °C and 25 mm specimens at 52.5 °C shows 58.6% decrement in peel strength (see W8-W9).

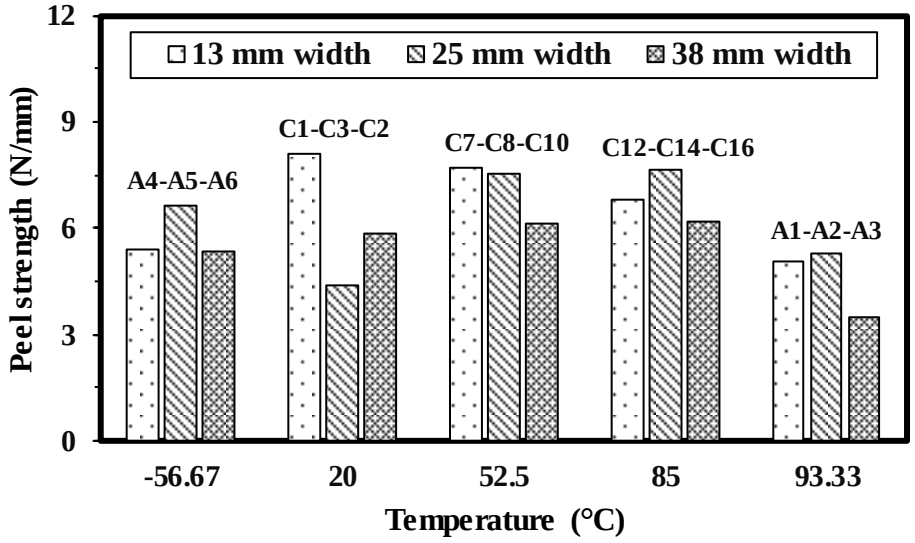

(a)

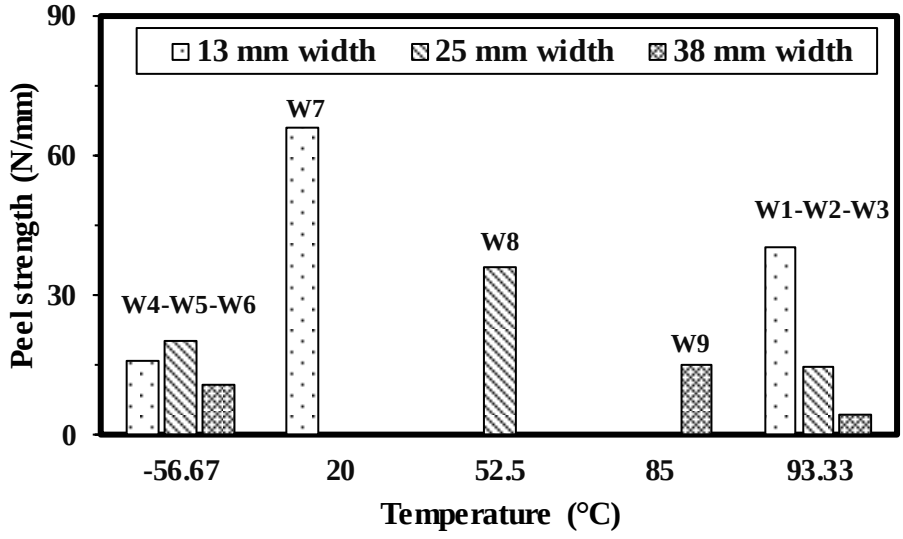

(b)

Figure 4.9: Width effect on peel strength: (a) adhesive and (b) weld

4.4.1.3 COMPARISON BETWEEN ADHESIVE AND WELDED SPECIMENS

Figure 4.10 shows a comparative representation of peel strength between the adhesive and welded peel specimens. For the 13 mm specimens, the welded specimens are more

resilient than the adhesive specimens by 699%, 197%, and 713% at 93.33 °C, -56.67 °C, and 20 °C, individually, as displayed in pairs A1-W1, A4-W4, and C1-W7. The 25 mm welded specimens at 93.33 °C, -56.67 °C, and 52.5 °C were found to have 179%, 202%, and 376% higher peel strength compared to the adhesive specimens as shown in pairs A2-W2, A5-W5, and C8-W8. For the 38 mm specimens at 93.33 °C, -56.67 °C, and 85 °C, the welded specimens are observed to have 30%, 101%, and 140% higher peel strength compared to the adhesive specimens (see pairs A3-W3, A6-W6, and C16-W9).

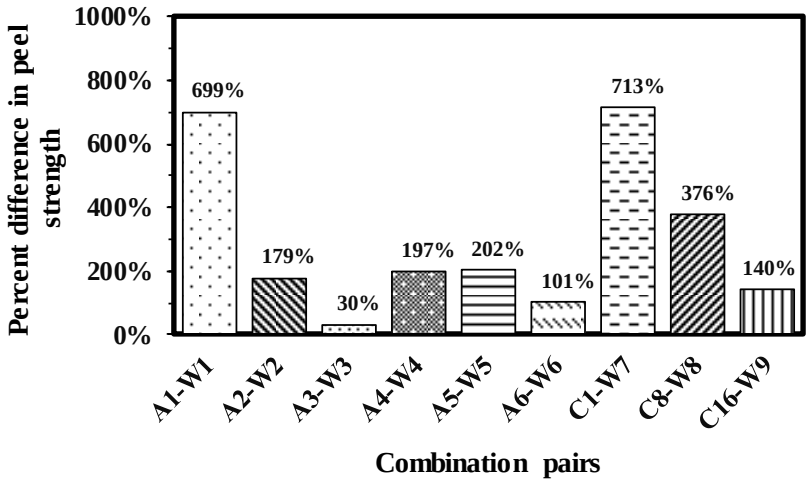

Figure 4.10: Percent difference in peel strength between adhesive and welded specimens

4.4.2 CHARACTERISTICS OF CLEAVAGE SPECIMENS

Load-displacement curves for each of the cleavage specimens tested were created through analysis of the testing data. Figure 4.11 shows load-displacement curves for all the tested cleavage specimens. Cleavage strength was computed by dividing the maximum load resisted by corresponding width of the cleavage specimen. The curves of each of the adhesive specimens are shown in Figure 4.11a. In this figure, the 38 mm

width specimen conditioned at 93.33 °C from combination A3 resists the maximum load, whereas the 13 mm width specimen conditioned at 20 °C from combination C1 produces the minimum load. The curves of each specimen are displayed in Figure 4.11b. The peak load was observed by the 38 mm cleavage specimen conditioned at 85 °C from W9, while the least load was showed by the 25 mm cleavage specimen conditioned at 52.5 °C from W8. The cleavage strength at the considered temperature and width for both adhesive and welded specimens with their respective failure modes are presented in Table 4.3. It should be noted that the cleavage strength shown in this table represents the average value of cleavage strength acquired from the first and second cleavage specimens tested for each combination. Equation 4.2 shown below was used for the calculation of cleavage strength.

$$f_c = {}^{P_{cu}}/_{W} \qquad \text{(Equation 4.2)}$$

where f_c is cleavage strength, Pc_u is the peak load recorded during the test, and W is width of the cleavage specimen.

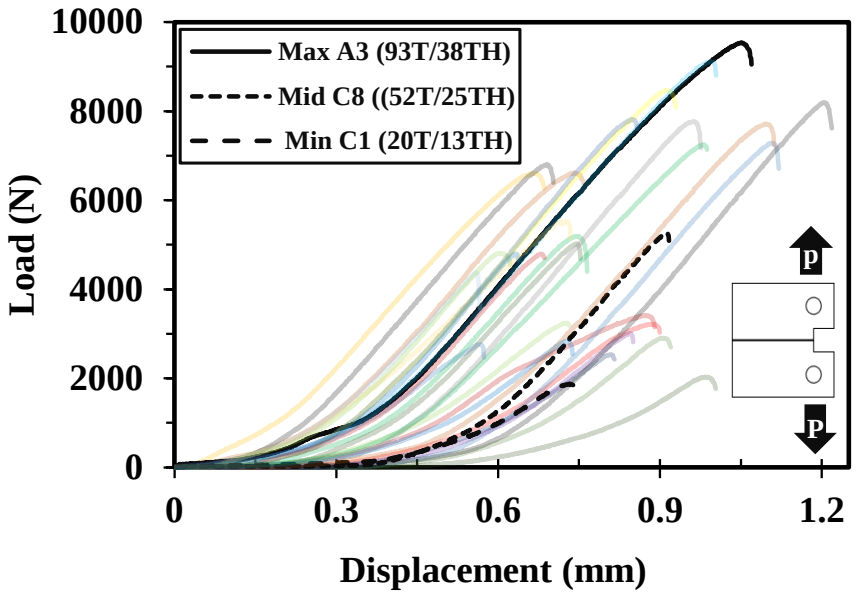

(a)

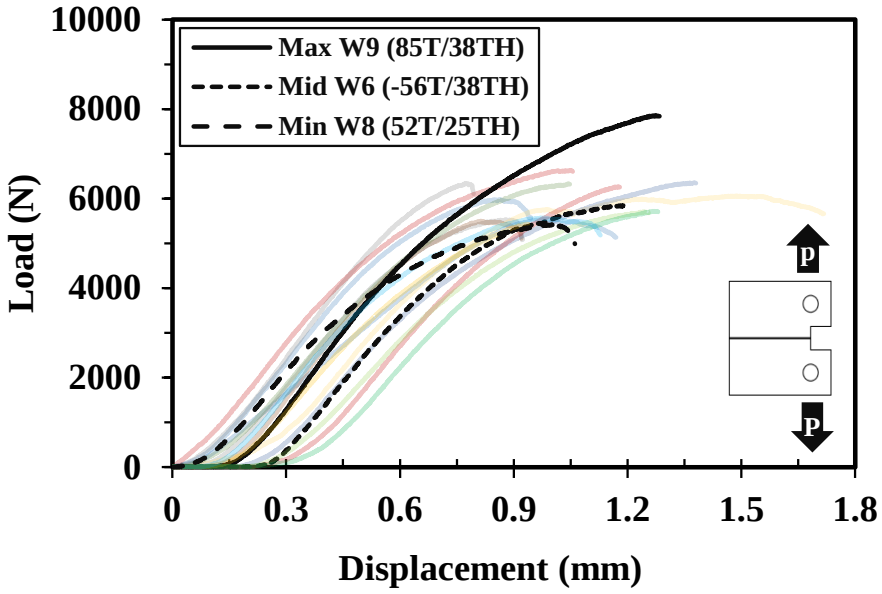

(b)

Figure 4.11: Load-displacement curve: (a) adhesive cleavage specimens and (b) welded cleavage specimens

Table 4.3 Cleavage strength from the cleavage test

Specimen type	Combination	Specimen ID	Cleavage strength (N/mm)	Failure mode
Adhesive	A1	A-C-13TH-93.3T-A1	261.19	cohesive
	A2	A-C-25TH-93.3T-A2	260.17	cohesive
	A3	A-C-38TH-93.3T-A3	236.44	cohesive
	A4	A-C-13TH-(-56.7)T-A4	242.24	cohesive
	A5	A-C-25TH-(-56.7)T-A5	201.12	cohesive
	A6	A-C-38TH-(-56.7)T-A6	215.30	cohesive
	C1	A-C-13TH-20.0T-C1	173.52	cohesive
	C2	A-C-38TH-20.0T-C2	191.19	cohesive
	C3	A-C-25TH-20.0T-C3	195.01	cohesive
	C7	A-C-13TH-52.5T-C7	198.32	cohesive
	C8	A-C-25TH-52.5T-C8	198.11	cohesive
	C10	A-C-38TH-52.5T-C10	254.55	cohesive
	C12	A-C-13TH-85.0T-C12	220.62	cohesive
	C14	A-C-25TH-85.0T-C14	188.74	cohesive
	C16	A-C-38TH-85.0T-C16	202.82	cohesive
Welded	W1	W-C-13TH-93.3T-W1	453.77	Weld throat failure
	W2	W-C-25TH-93.3T-W2	217.07	Weld throat failure
	W3	W-C-38TH-93.3T-W3	162.76	Weld throat failure
	W4	W-C-13TH-(-56.7)T-W4	499.92	Weld throat failure
	W5	W-C-25TH-(-56.7)T-W5	253.82	Weld throat failure
	W6	W-C-38TH-(-56.7)T-W6	148.23	Weld throat failure
	W7	W-C-13TH-20.0T-W7	449.88	Weld throat failure
	W8	W-C-25TH-52.5T-W8	216.42	Weld throat failure
	W9	W-C-38TH-85.0T-W9	191.13	Weld throat failure

As listed in Table 4.3, all the adhesive cleavage specimens were observed to fail with cohesive failure mode. Figure 4.12 presents the typical failure modes of the adhesive and welded cleavage specimens having a width of 13 mm and 38 mm, respectively. As shown in Figure 4.12a and Figure 4.12b, in this failure mode, adhesive can be seen on both surfaces of aluminum block after the test. For the welded specimens, weld throat failure was found to be the only failure mode as in the tested peel welded specimens. Figure 4.12c and Figure 4.12d represents the typical failure modes of the welded cleavage

specimens for specimens with 13 mm and 38 mm width. Failure is observed only on the weld throat connecting aluminum blocks.

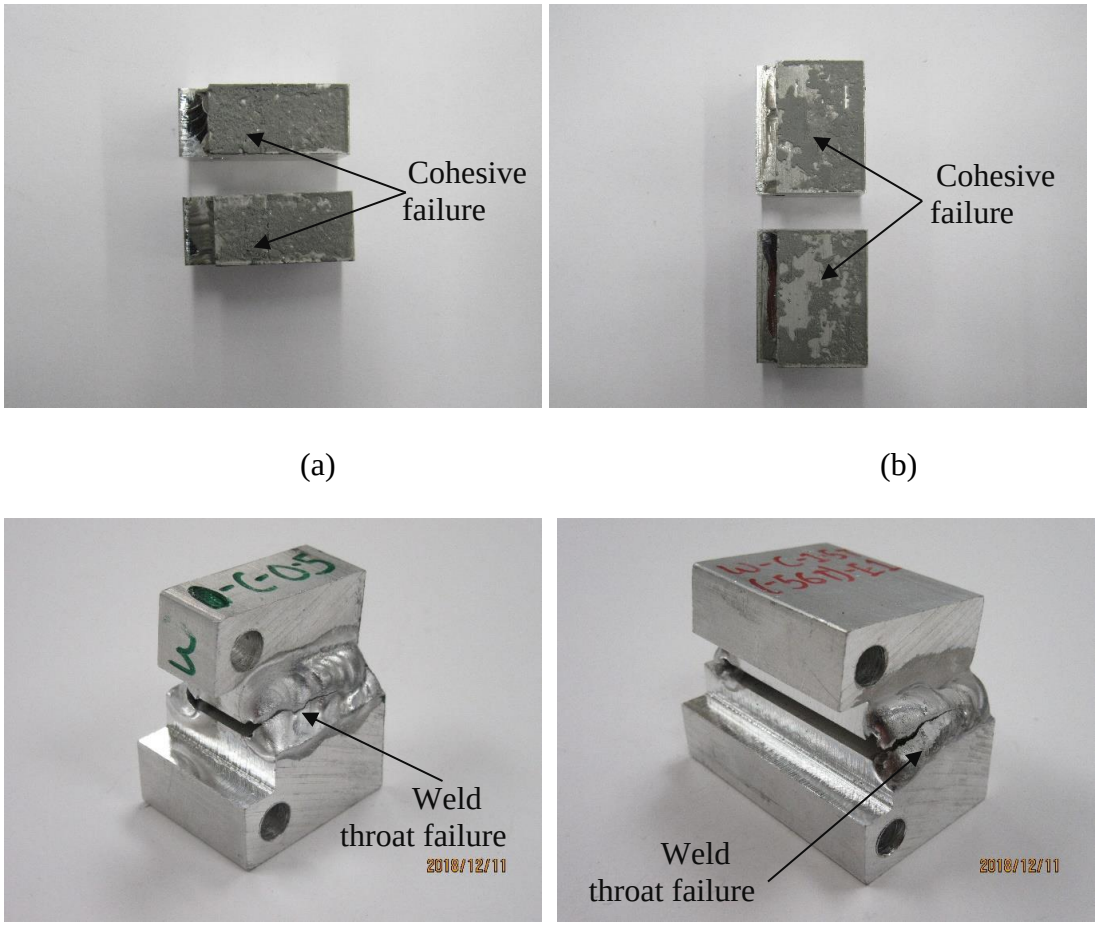

Figure 4.12: Representative failure modes of cleavage specimens (a) adhesive with 13 mm width, (b) adhesive with 38 mm width, (c) welded with 13 mm width, and (d) welded with 38 mm width

4.4.2.1 EFFECT OF TEMPERATURE

The influence of temperature on cleavage strength is illustrated in Figure 4.13. In Figure 4.13a, the effect of temperature on cleavage strength of adhesively bonded

cleavage specimens is presented. The cleavage strength of 13 mm specimens is observed to be decreased by 28.4% with the increase in temperature from -56.67 °C to 20 °C. The cleavage strength is elevated by 14.3% when the temperature increases beyond 20 °C to 52.5 °C. With further increment of temperature from 52.5 °C to 85 °C and 85 °C to 93.33 °C, the cleavage strength of adhesive specimens is increased by 11.2% and 18.4%, respectively, as depicted in A4-C1-C7-C12-A1. The cleavage strength of 25 mm specimens is declined by 3% when temperature of the specimens is increased from -56.67 °C to 20 °C and increased by 1.6% with further increment of temperature from 20 °C to 52.5 °C. The cleavage strength is decreased by 4.7% and increased by 37.8% when temperature increases from 52.5 °C to 85 °C and 85 °C to 93.33 °C (see A5-C3-C8-C14-A2). For the 38 mm cleavage specimens, the strength is decreased by 11.2% when temperature is raised from -56.67 °C to 20 °C, however, is increased by 33.1% when temperature rises from 20 °C to 52.5 °C. The cleavage strength is observed to be decreased by 20.3% and increased by 16.6% with the increment of temperature from 52.5 °C to 85 °C and 85 °C to 93.33 °C (see A6-C2-C10-C16-A3).

The temperature effect for welded specimens on cleavage strength is displayed in Figure 4.13b. When the temperature is increased from -56.67 °C to 20 °C, the strength for 13 mm welded specimens is declined by 10%, whereas additional increment of temperature from 20 °C to 93.33 °C raised the cleavage strength by 0.9% only as shown in W4-W7-W1. With the elevation of temperature from -56.67 °C to 52.5 °C for the 25 mm specimens, the strength is decreased by 14.7%, however, the strength is slightly increased by 0.3% when temperature increases from 52.5 °C to 93.33 °C as portrayed in W5-W8-W2. In W6-W9-W3 for 38 mm specimens, it is observed that the strength is

increased by 28.9% with the increment of temperature from -56.67 °C to 85 °C, whereas it is decreased by 14.8% when temperature increases from 85 °C to 93.33 °C.

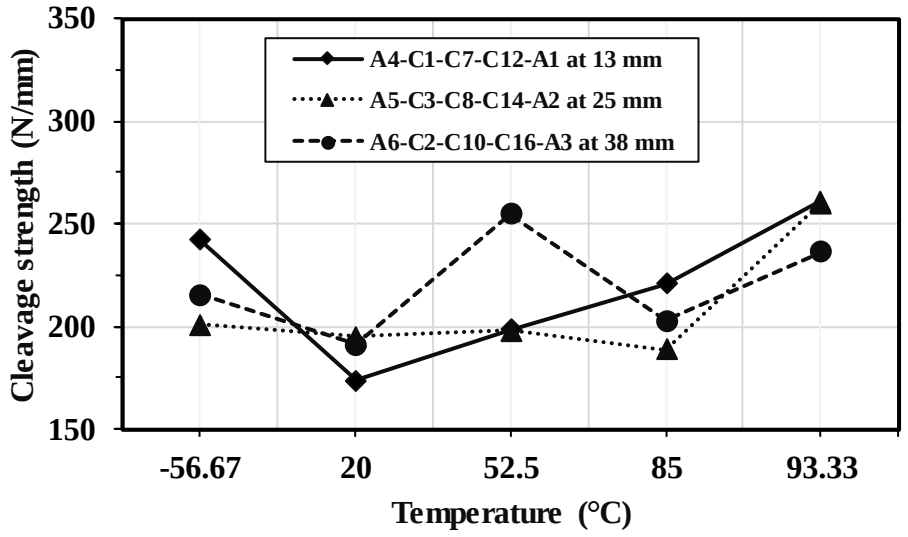

(a)

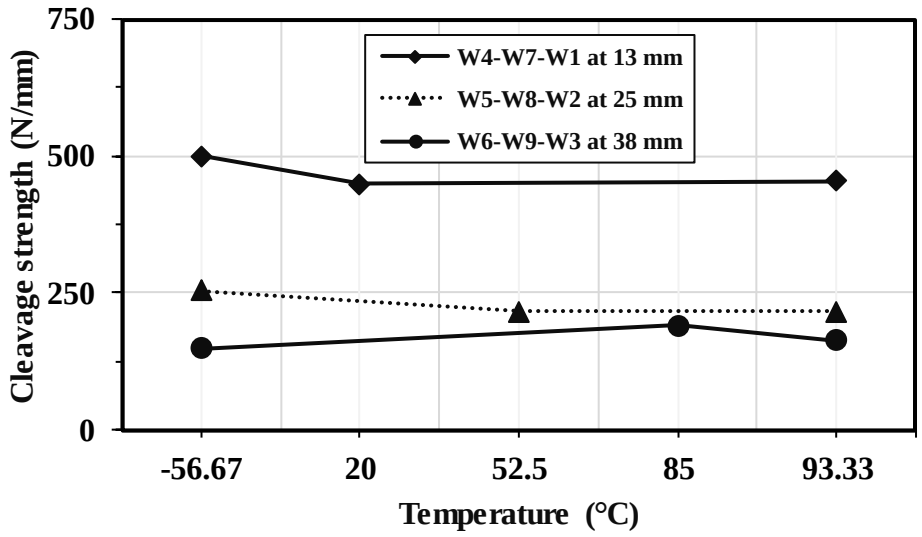

(b)

Figure 4.13: Temperature effect on cleavage strength (a) adhesive and (b) weld

4.4.2.2 EFFECT OF WIDTH

The effect of specimen's width on the cleavage strength is shown in Figure 4.14 in the form of a bar chart. Figure 4.14a shows the effect of width in the strength of adhesive specimens at different temperatures taken for study. The cleavage strength at -56.67 °C reduces by 17% with an increment of specimen width from 13 mm to 25 mm, but the strength is increased by 7.1% at -56.67 °C with the increment from 25 mm to 38 mm width as presented in A4-A5-A6. At 20 °C, the strength is improved by 12.4% and decreased by 2% with the increment of specimen width from 13 mm to 25 mm and 25 mm to 38 mm as shown in C1-C3-C2. The strength of the specimens at 52.5 °C is only decreased by 0.1% but increased by 28.5% with the increment of specimen width from 13 mm to 25 mm and 25 mm to 38 mm (see C7-C8-C10). At 85 °C, when the specimen width is increased from 13 mm to 25 mm, the strength is decreased by 14.4% and increased by 7.5% when the specimen width is increased from 25 mm to 38 mm (refer to C12-C14-C16). The strength at 93.33 °C decreases by 0.4% and 9.1% when the specimen width is increased from 13 mm to 25 mm and 25 mm to 38 mm as shown in A1-A2-A3.

In Figure 4.14b, the effect of width on cleavage strength for welded cleavage specimens is presented. The strength at -56.67 °C is decreased by 49.2% and 41.6% when the width of welded cleavage specimen is increased from 13 mm to 25 mm and 25 mm to 38 mm as shown in W4-W5-W6. At 93.33 °C, the strength of welded specimens is decreased by 52.2% and by 25.0% with the increment of specimen width from 13 mm to 25 mm and from 25 mm to 38 mm as illustrated in W1-W2-W3. The 25 mm specimens at 52.5 °C are observed to have 51.9% less strength than 13 mm welded cleavage specimens at 20 °C (see W7 and W8). The 38 mm specimens at 85 °C exhibit 11.7% reduction in

the cleavage strength compared to the 25 mm specimens at 52.5 °C as shown in W8 and W9.

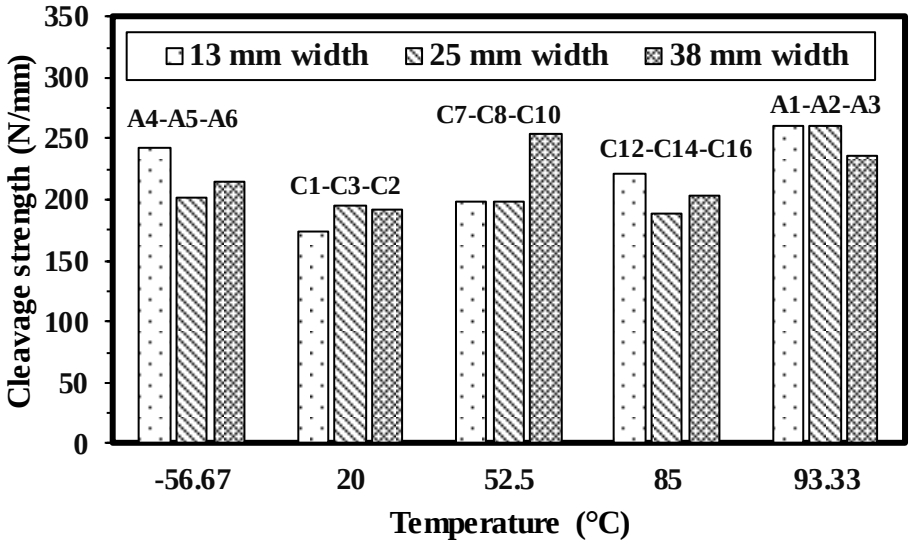

(a)

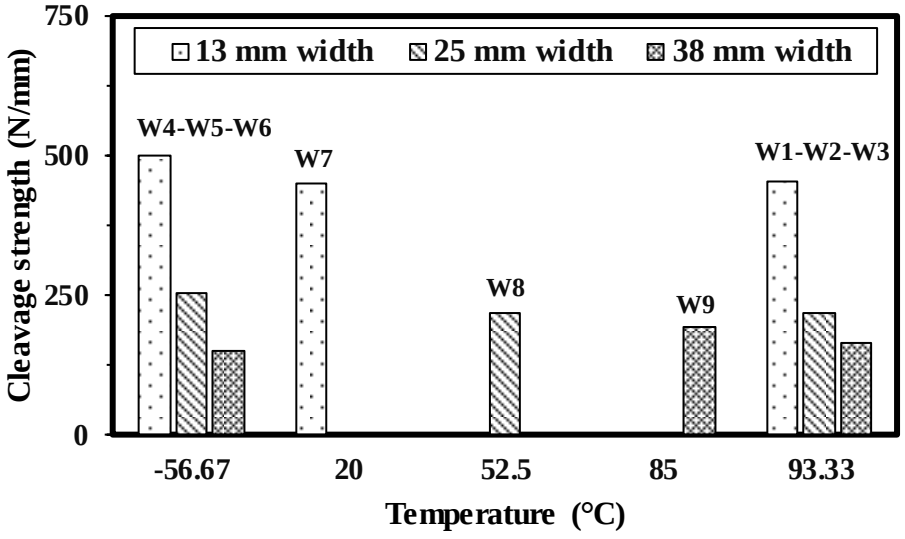

(b)

Figure 4.14: Width effect on cleavage strength for cleavage specimens (a) adhesive and (b) weld

4.4.2.3 COMPARISON BETWEEN ADHESIVE AND WELDED SPECIMENS

A comparative demonstration of cleavage strength between each combination of adhesive and welded cleavage specimens is shown in Figure 4.15. The 13 mm welded specimens are observed to have higher cleavage strength than the adhesive specimens by 74% at 93.33 °C, 106% at -56.67 °C, and 159% at 20 °C as shown in pairs A1-W1, A4-W4, and C1-W7. At 93.33 °C, the 25 mm welded specimens are found to have 17% less cleavage strength than the adhesive specimens as shown in pair A2-W2. The 25 mm welded specimens at -56.67 °C, and 52.5 °C observed 26% and 9% higher cleavage strength in comparison to the adhesive specimens as displayed in pairs A5-W5 and C8-W8. For the 38 mm width at 93.33 °C, -56.67 °C, and 85 °C, the welded specimens are shown to have 31%, 31%, and 6% lower cleavage strength compared to the adhesive specimens (see pairs A3-W3, A6-W6, and C16-W9).

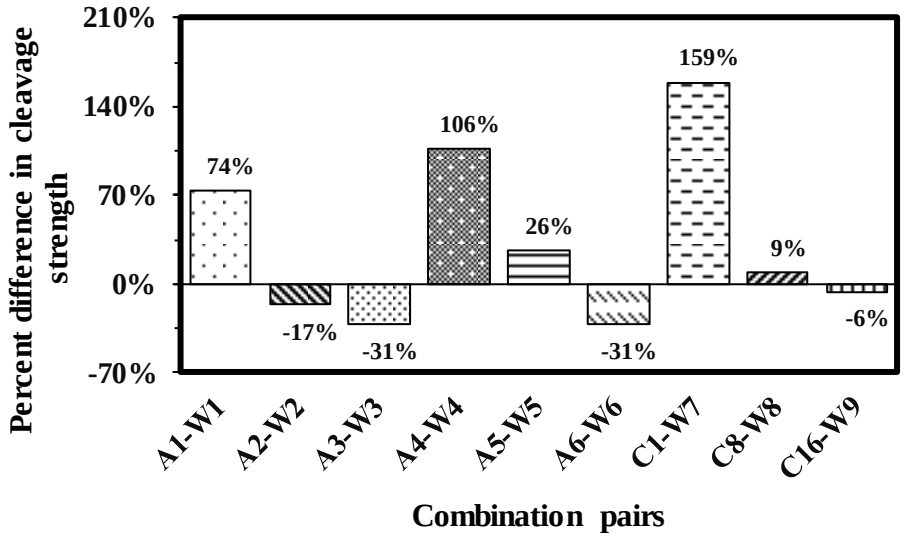

Figure 4.15: Percent difference in cleavage strength between adhesive and welded specimens

4.5 STATISTICAL ANALYSIS

Response Surface Metamodels (RSMs), which have been formerly studied by Seo and Linzell (2010, 2012, 2013) were generated for the prediction of peel and cleavage strengths with respect to temperature and width parameters and its interaction. A statistical software, R (Team 2015), was used to create a separate RSM using each of the datasets obtained from the peel and cleavage tests through regression analysis. The RSMs for the adhesive peel strength, the welded peel strength, the adhesive cleavage strength, and the welded cleavage strength are shown in Equation 4.3, Equation 4.4, Equation 4.5, and Equation 4.6, respectively.

$$f_{apa} = 7.2529 - 0.0279\,T - 0.7197\,W - 0.1547TW - 1.1328T^2 - 0.7080W^2 \quad \text{(Equation 4.3)}$$

$$f_{apw} = 46.7757 + 2.2097\,T - 10.4159W - 6.9719TW - 32.1094T^2 + 4.9385W^2 \quad \text{(Equation 4.4)}$$

$$f_{ca} = 183.9167 + 8.8019T + 0.2911W + 1.9458TW + 35.9261T^2 + 12.1350W^2 \quad \text{(Equation 4.5)}$$

$$f_{cw} = 215.8688 - 8.4411\,T - 154.5978W + 19.6156TH + 19.7272T^2 + 84.4435W^2 \quad \text{(Equation 4.6)}$$

where f_{apa} and f_{apw} are the peel strength for the adhesive and welded specimens, f_{ca} and f_{cw} are the cleavage strength of the adhesive and welded specimens, T is the conditioning temperature, and W is the specimen width.

The RSMs shown in Equation 4.3 through Equation 4.6 for the prediction of the adhesive and welded peel and cleavage strength were further analysed to develop 3D peel strength surface plots that can be used for efficient exploration of the effects of temperature and width on each strength without omission of the considered parameters between all the ranges considered in this study. Figure 4.16 presents the 3D surface plots of the predicted peel strength of adhesive and welded specimens for different values of temperature and width. The effect of these two parameters on the peel strength of adhesive specimens is shown in Figure 4.16a. The plot of peel strength for the adhesive specimens is found to be of convex shape due to the effect of temperature and specimen's width. The increase in width from 13 mm to 38 mm decreased the peel strength by 18.82% at lower temperature of -56.67 °C and by 27.94 % at higher temperature of 93.33 °C. With the increase in temperature (-56.67 °C to 93.33 °C), the peel strength is increased by 4.22% at lower width (13 mm), however, at higher width (38 mm), the peel strength is dropped by 7.49% with the increment in temperature (-56.67 °C to 93.33 °C). The 3D surface plot for the peel strength of welded specimens for various temperature and width is observed to be of tunnel shape as displayed in Figure 4.16b. With the increment in width of the specimens from 13 mm to 38 mm, significant decrements in peel strength is observed. The peel strength is reduced by 33.05% at lower temperature (-56.67 °C) and by 88.71% at higher temperature (93.33 °C). Due to increment in temperature from -56.67 °C to 93.33 °C, the peel strength is increased substantially by 88.12% at lower width (13mm) and by 68.27% at higher width (38 mm).

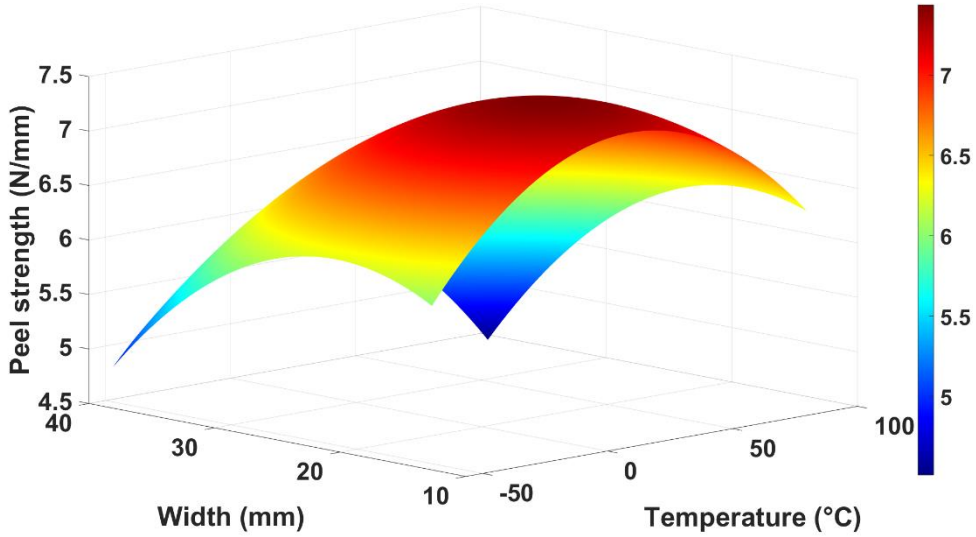

(a)

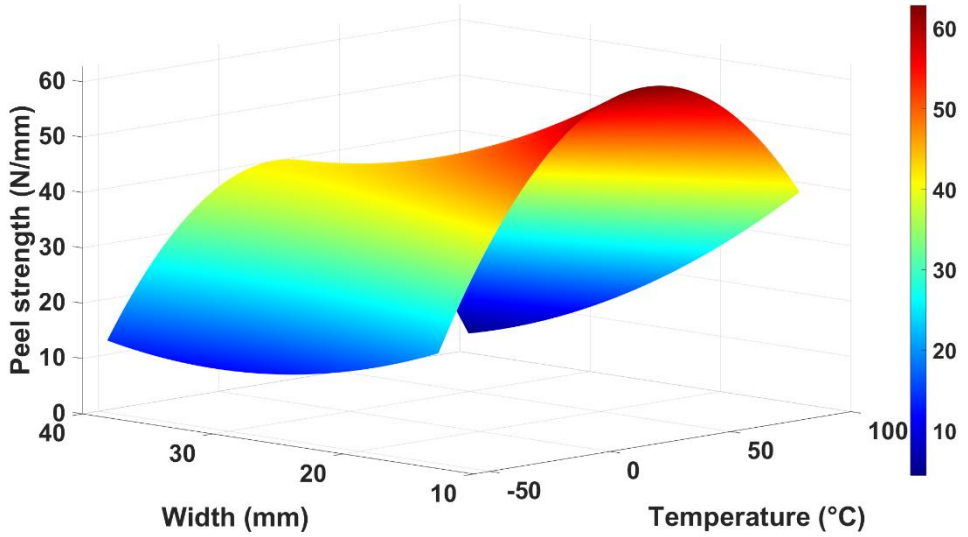

(b)

Figure 4.16: RSM surface plots of peel strength showing effects of temperature and width for (a) adhesive specimens and (b) welded specimens

Figure 4.17 presents the 3D surface plots for the cleavage strength of adhesive and welded specimens generated using the RSMs presented in Equation 4.5 and Equation 4.6. The plot of the cleavage strength for adhesive specimens is shown in Figure 4.17a. The

surface is observed to be of concave shape due to the effect of temperature and width on the cleavage strength. In Figure 4.17a, the increment of width from 13 mm to 38 mm reduced the cleavage strength of adhesive specimens by 1.47% at higher temperature (93.33 °C), whereas the cleavage strength is improved by 1.88% due to increment in the width. With the increase in temperature, the cleavage strength is dropped initially, whereas the cleavage strength increased significantly later. The cleavage strength is increased by 6.10% at smaller width (13 mm) and 9.70% at larger width (38 mm) due to increment in the temperature from -56.67 °C to 93.33 °C. Figure 4.17b presents the 3D surface plot of the cleavage strength for welded specimens at different temperature and width. The plot is observed to be approximately to that of plane surface. The increase in width of the specimen reduced the cleavage strength considerably regardless of the temperature. The cleavage strength is declined by 69.31% at lower temperature of -56.67 °C and by 60.45% at higher temperature of 93.33 °C due to increment of specimen's width (13 mm to 38 mm). At smaller width (13 mm), when temperature is increased (-56.67 °C to 93.33 °C), the cleavage is reduced by 11.16%, however with the increment in temperature from-56.67 °C to 93.33 °C at larger width (39 mm), the cleavage is improved by 14.49%.

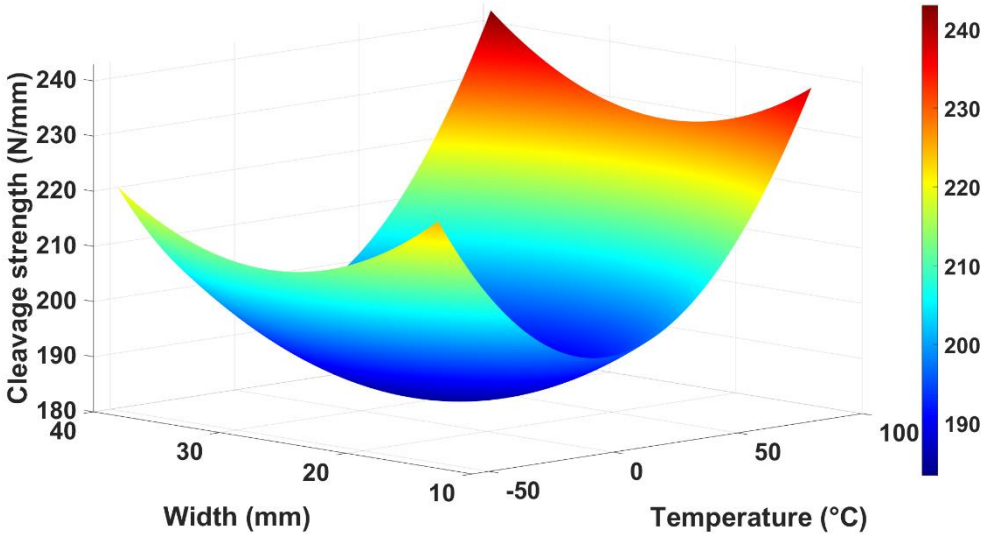

(a)

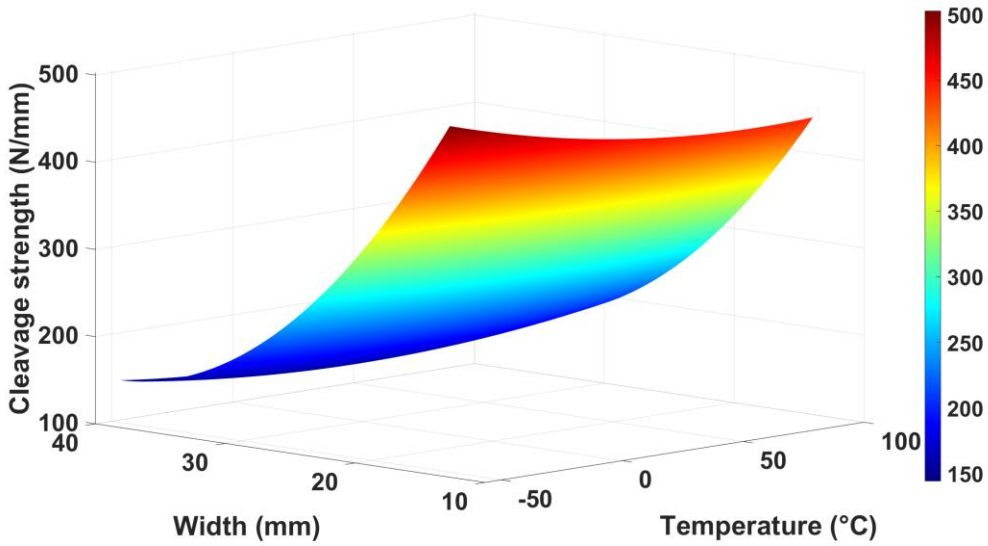

(b)

Figure 4.17: RSM surface plots of cleavage strength showing the effects of temperature and width for (a) adhesive specimens and (b) welded specimens

From the observation of the 3D surface plots, both temperature and width were found to significantly affect the peel and cleavage strength of the adhesive and welded

specimens. Peel strength of both specimen types (adhesive and welded) and cleavage strength of adhesive specimens is observed to be affected most by temperature, whereas the influence of width is observed higher for peel strength of adhesive and welded specimens along with cleavage strength of welded specimens.

4.6 CONCLUSIONS

The peel and cleavage strength of the adhesive and welded specimens were experimentally and statistically investigated to substantiate the influence of temperature and width on each strength type. 30 peel specimens and 30 cleavage specimens were tested for nine different variations of temperature and width following the guidelines of American Society of Testing and Materials (ASTM) and American Welding Society (AWS) standards with an experimental program. Further, the strength of adhesive and welded specimens was also compared to understand the difference between them in terms of peel and cleavage strength. The data obtained from the peel and cleavage strength tests were analyzed to produce Response Surface Metamodels (RSMs) and associated 3D surface plots to graphically examine the effect of the temperature and width on each strength. The following conclusions can be derived from the experimental testing and statistical evaluation:

1. On account of the effect of temperature, in the peel strength test of adhesive specimens, the peak increment and decrement in the peel strength were 70.4% and 43.7%. For the welded specimens, the peak increment and decrement were 310.3% and 69.5%. Attributable to the effect of width, in the peel strength test of adhesive specimens, the maximum increment and decrement in the peel strength were 32% and 45.6%. For the welded specimens, the maximum increment and decrement were 24.4% and 69.2%. The

peel strength of all the tested welded specimens was observed to be higher than the adhesive specimens with the highest difference of 713% for 13 mm width at 20 °C and the lowest difference of 30% for 38 mm width at 93.33 °C.

2. Owing to the effect of temperature, in the cleavage strength test of adhesive specimens, the highest increment and decrement in the cleavage strength were 37.8% and 28.4%. For the welded specimens, the highest increment and decrement were 28.9% and 14.8%. On account of the effect of width, in the cleavage strength test of adhesive specimens, the peak increment and decrement in the cleavage strength were 28.5% and 17%. For welded specimens, the peak decrement was 52.2%. The cleavage strength was not found to be increased with the increment in width. It was also found that the welded specimens (including combinations W1, W4, W5, W7, and W8) that were tested had higher cleavage strength than the adhesive specimens with the maximum difference 159%, while the remaining welded specimens possessed lower cleavage strength than the adhesive specimens with the maximum difference of 31%.

3. 3D surface plots generated by the RSMs efficiently observed the effect of both temperature and width on the peel and cleavage strength of adhesive and welded specimens. The effect of temperature was found to be most for the peel strength of both adhesive and welded specimens along with the cleavage strength of adhesive specimens. Obviously, the width had a high influence on the peel strength of adhesive and welded specimens and the cleavage strength for welded specimens.

4.7 REFERENCES

Higgins, A. (2000). Adhesive bonding of aircraft structures. *International Journal of Adhesion and Adhesives*, *20*(5), 367-376.

Hill, J. (2003). Adhesively Bonded Structural Composites for Aston Martin Vehicles. *Ford Motor Company Research and Advanced Engineering*.

Amatya, I., Seo, J., Letcher, T., & Bierschbach, D. (2020a). Tensile and shear strength tests with adhesive connections in dynamic message signs. *Journal of Materials in Civil Engineering*, *under review.*

Amatya, I., Seo, J., & Letcher, T. (2020b). Comparison of tensile and shear strengths between adhesive and welded connections in dynamic message signs. *Composite Structures, under review.*

Amatya, I., Seo, J., Letcher, T., Ahn, J. (2020c). Peel and cleavage strength tests with adhesive connections in dynamic message signs. *International Journal of Adhesion and Adhesives*, *under review.*

Savvilotidou, M., Vassilopoulos, A. P., Frigione, M., & Keller, T. (2017). Development of physical and mechanical properties of a cold-curing structural adhesive in a wet bridge environment. *Construction and Building Materials*, *144*, 115-124.

Goglio, L., & Rezaei, M. (2014). Variations in mechanical properties of an epoxy adhesive on exposure to warm moisture. *Journal of Adhesion Science and Technology*, *28*(14-15), 1394-1404.

Silva, P., Fernandes, P., Sena-Cruz, J., Xavier, J., Castro, F., Soares, D., & Carneiro, V. (2016). Effects of different environmental conditions on the mechanical characteristics of a structural epoxy. *Composites Part B: Engineering*, *88*, 55-63.

Zhang, Y., Vassilopoulos, A. P., & Keller, T. (2010). Effects of low and high temperatures on tensile behavior of adhesively-bonded GFRP joints. *Composite Structures*, *92*(7), 1631-1639.

Agarwal, A., Foster, S. J., Hamed, E., & Ng, T. S. (2014). Influence of freeze–thaw cycling on the bond strength of steel–FRP lap joints. *Composites Part B: Engineering*, *60*, 178-185.

Kim, Y. J., Hossain, M., & Yoshitake, I. (2012). Cold region durability of a two-part epoxy adhesive in double-lap shear joints: Experiment and model development. *Construction and Building Materials*, *36*, 295-304.

Ferreira, J. A. M., Reis, P. N., Costa, J. D. M., & Richardson, M. O. W. (2002). Fatigue behaviour of composite adhesive lap joints. *Composites science and technology*, *62*(10-11), 1373-1379.

Sugiman, S., Crocombe, A. D., & Aschroft, I. A. (2013a). The fatigue response of environmentally degraded adhesively bonded aluminium structures. *International Journal of Adhesion and Adhesives*, *41*, 80-91.

Sugiman, S., Crocombe, A. D., & Aschroft, I. A. (2013b). Experimental and numerical investigation of the static response of environmentally aged adhesively bonded joints. *International Journal of Adhesion and Adhesives*, *40*, 224-237.

Sousa, J. M., Correia, J. R., & Cabral-Fonseca, S. (2018). Durability of an epoxy adhesive used in civil structural applications. *Construction and Building Materials*, *161*, 618-633.

Kim, K. S., & Aravas, N. (1988). Elastoplastic analysis of the peel test. *International Journal of Solids and Structures*, *24*(4), 417-435.

De Freitas, S. T., & Sinke, J. (2014). Adhesion properties of bonded composite-to-aluminium joints using peel tests. *The Journal of Adhesion*, *90*(5-6), 511-525.

Broughton, W. R., Mera, R. D., & Hinopoulos, G. Project PAJ3—Combined Cyclic Loading and Hostile Environments 1996-1999: Report No. 13—Creeping Testing of Adhesive Joints T-Peel Test, Oct. 1999. *NPL Report CMMT (A)*, *193*, 4-5.

Shahid, M., & Hashim, S. A. (2000). Cleavage strength of steel/composite joints. *The Journal of Adhesion*, *73*(4), 365-384.

Shahid, M., & Hashim, S. A. (2002). Effect of surface roughness on the strength of cleavage joints. *International Journal of Adhesion and Adhesives*, *22*(3), 235-244.

Zheng, X. L., Zhang, M. S., You, M., Yu, H. Z., & Li, Z. (2007). A Study on Normal Stress Distribution and Failure of Adhesively Bonded Joint under Cleavage Loading. In *Key Engineering Materials* (Vol. 348, pp. 949-952). Trans Tech Publications.

Seo, J. (2013). Statistical determination of significant curved I-girder bridge seismic response parameters. *Earthquake Engineering and Engineering Vibration*, *12*(2), 251-260.

Chandorkar, A. N., Mande, S., & Iwai, H. (2008, October). Estimation of process variation impact on DG-FinFET device performance using Plackett-Burman design of experiment method. In *2008 9th International Conference on Solid-State and Integrated-Circuit Technology* (pp. 215-218). IEEE.

Seo, J., & Linzell, D. G. (2013). Influential Curved Steel Bridge Fragility Analysis Parameters. In *Forensic Engineering 2012: Gateway to a Safer Tomorrow* (pp. 84-92).

Seo, J., & Linzell, D. G. (2012). Horizontally curved steel bridge seismic vulnerability assessment. *Engineering Structures*, *34*, 21-32.

Seo, J., & Linzell, D. G. (2010). Probabilistic Vulnerability Scenarios for Horizontally Curved Steel I-Girder Bridges Under Earthquake Loads. *Transportation Research Record, 2202*(1), 206-211.

Seo, J., & Linzell, D. G. (2013). Use of response surface metamodels to generate system level fragilities for existing curved steel bridges. *Engineering Structures, 52*, 642-653.

SAS Institute Inc. (2008). *JMP statistics and graphics guide, version 5.1.2*, Cary, NC

ASTM D1876-08. (2008). Standard test method for peel resistance of adhesives (T-peel test). West Conshohocken: American Society of Testing and Materials.

ASTM D1062-08. (2008). Standard test method for cleavage strength of metal-to-metal adhesive bonds. West Conshohocken: American Society of Testing and Materials.

LORD Corporation. (2018). LORD® 406 Acrylic Adhesive. Retrieved November 29, 2018, from https://www.lord.com/products-and-solutions/adhesives/lord-406-acrylic-adhesive

American Welding Society. (2015). AWS D1. 1: structural welding code–steel.

MTS Systems Corporation. (2018). MTS Landmark® Servohydraulic Test Systems. Retrieved November 29, 2018, from http://www.mts.com/en/products/producttype/test-systems/load-frames-uniaxial/servohydraulic/standard/index.htm

MTS Systems Corporation. (2019). A complete family of quality, affordable electromechanical test systems. Retrieved March 03, 2019, from http://www.mts.com/en/forceandmotion/materialstesting/MTS_002886?article=3

Team, R. (2015). RStudio: integrated development for R. RStudio, Inc., Boston, MA URL http://www. rstudio. com.

CHAPTER 5: ULTIMATE AND FATIGUE LOAD TESTINGS OF DYNAMIC MESSAGE SIGNS WITH ADHESIVE AND WELDED CONNECTIONS

5.1 ABSTRACT

This paper discusses the results from ultimate strength and fatigue tests conducted on four full-sized dynamic message signs (DMSs) fabricated by a local producer located in South Dakota in the United States. Specifically, the ultimate strength testing was carried out on one DMS with adhesive joints and one with typical welded connections, and the fatigue testing was also conducted on one DMS with adhesive joints and one with welded connections. For the ultimate testing, monotonic loadings were applied to each of the DMSs by a hydraulic actuator under the displacement-based control until failure. For the fatigue testing, each of the DMSs was loaded up to 500,000 cycles with a constant force of 0.818 kN equivalent to design the natural wind gust pressure based on a yearly mean speed of 18.02 km/hr according to the AASHTO specifications for structural supports for highway signs, luminaires and traffic signals. During each test, strain, deflection, and load data along with visual inspection imagery were collected to gain a better understanding of structural behaviors and failure modes of each of the individually tested DMSs. The ultimate testing demonstrated that the adhesive DMS failed at 125 kN with the peak deflection of 96.14 mm, while the welded DMS failed at 146 kN with the peak deflection of 91.49 mm. During the fatigue load testing, all the stress ranges observed in each of the tested DMSs were considerably below the threshold of the DMS panel, which was determined by generating its S-N curve. It was also found that any damage was not observed in both the adhesive and welded DMSs subjected to the fatigue loading.

Keywords: DMS, Strength; Adhesive; Weld; Ultimate strength; Fatigue load.

5.2 INTRODUCTION

A dynamic message sign (DMS) is a highway electronic sign that conveys useful road and traffic information to drivers. A frame of the DMS is conventionally connected to an aluminum sheet with welded assemblies. However, high residual stresses and complications in joining irregular joints are frequently observed during welding. An adhesive can be used instead of the conventional welded connections between the frame and aluminum sheets with reduced cost and efficient fabrication. Specifically, the adhesive is capable of joining aluminium sheets with different melting points and uniform distribution of load. With these advantages, several DMS producers prefer adhesively bonded DMSs over welded DMSs, although the structural performance of the adhesive DMS has not been experimentally evaluated. Hence, the use of adhesive connections on DMSs needs to be brought to attention with a thorough study on their structural performance.

Numerous studies have been performed to investigate various mechanical characteristics such as shear and peel strengths of the small-sized adhesive specimens considering varying environmental and geometrical parameters. Stricly speaking, the majority of the studies (Amatya et al. 2020a, Da Silva et al. 2009, Silva et al. 2012, Agarwal et al. 2014, Kim et al. 2012, Silva et al. 2016, Goglio and Rezaei 2012, Sousa et al. 2018, Savvilotidou et al. 2017) have focused on the examination of the shear and tensile strength of adhesives. For example, single lap-shear joint adhesive specimens were tested by Da Silva et al. (2009), and it was found that the shear strength was

affected by the overlap length of specimens, adhesive thickness, and specimen thickness. In addition to the shear and tensile strength studies, several studies (Amatya et al. 2020b, Shahid and Hashim 2000, 2002, Zheng et al. 2007, Kim and Aravas 1988, De Freitas and Sinke 2004, Broughton et al. 1999), have been performed to examine the cleavage and peel strengths of adhesives. In particular, De Freitas and Sinke (2004) bonded composite and aluminum with adhesive to fabricate the peel specimens. Composite adherend was found to have lower resistance to peel load than flexible adherend. Recently, Amatya et al. (2020b) tested a series of small-scale tests of 64 adhesive specimens with variation in temperature, humidity, and width to examine their peel and cleavage strengths according to ASTM D1876 (2008) and ASTM D1062 (2008). It was reported that the width was the most significant parameter negatively affecting the peel strength of the adhesive.

Full-scale testing can provide a wealth of information about the behavior of the entire DMS system with adhesive connections, however, only few studies (Connor and Altstadt 2013, Huckelbridge and Metzger 2009) have been conducted on frame structures supporting DMSs using welded connections. In detail, Connor and Altstadt (2013) investigated the after-fracture reserve strength of two four-chord aluminum trusses that support the DMS with destructive testing. Truss members were cut to replicate the fractures in chords and simulated DMS dead load, and wind load were applied on the truss. It was found that the truss member possessed a significant reserve strength even in its severe condition. Huckelbridge and Metzger (2009) conducted a detailed field monitoring of an aluminum sign support truss in Ohio that was fractured in two truss members near one truss support. It was revealed that the truss failed due to excessive fatigue of the chord-web diagonal welded connection. As far as the authors are aware, the

ultimate strength test of the DMS with adhesive connections have not been conducted to date.

Several studies (Puckett et al. 2010 Arabi et al. 2018, Chang et al. 2014, Hamilton et al. 2000, Hosch and Fouad 2009, Fouad and Calvert 2005, Park and Stallings 2006) have been conducted in terms of fatigue load tests. However, all the studies have been limited to investigating the performance of structure supporting the DMS. For instance, Puckett et al. (2010) delved into the fatigue resistance of the DMS supporting structure with welded specimens in accordance with the American Association of State Highway and Transportation Officials (AASHTO) Standard Specifications for Structural Supports for Highway Signs, Luminaires and Traffic Signals (AASHTO 2001a, b). It was demonstrated that the fatigue resistance of ring-stiffened box connection was better than the standard box connection. Arabi et al. (2018) also performed a complete field test to study the damage due to fatigue loads in the DMS sign support structures during transportation, indicating that the failure damage of 0.01% in the most vital member of the support structure was observed. Chang et al. (2014) studied the overhead truss structures supporting the DMS to determine the impact of wind loads resulting from truck-induced wind gusts and thermal-induced loads, and found that the wind loads generated unnoticeable stresses and minimal damage on the DMS support structures. Park and Stallings (2006) performed field testing for fatigue evaluations of DMS support structures due to natural and truck-induced wind gusts, signifying that natural wind gusts caused highest critical stress cycles in the structures.

While all the aforementioned studies have been researched to investigate either mechanical properties of small-scale adhesive specimens or the strength and/or fatigue performace of the structure to support the DMS, the structural adequacy of any DMS with adhesive connections have not been examined in a satisfactory manner until now. Therefore, an extensive body of research on the structural performance of DMSs with adhesive connections is needed. Ultimate strength testing is required to determine the maximum load resisting capacity of the DMS. Fatigue loadings, on the other hand, are caused regularly and repeatedly due to wind. Specifically, for DMS structure, fatigue is caused due to repeatition of various wind loads. Although fatigue loads are significantly lower than the ultimate load, DMSs can be failed in fatigue due to repetition of loading. Both ultimate and fatigue load tests are essential to determine the structural adequacy of DMS. Therefore, this study is intended to perform full-scale ultimate strength and fatigue testings to determine the structural behavior of DMSs with adhesive connections and compare the results with those from the same testing of the welded DMSs. To that end, a total of four full-sized aluminium DMS specimens (including two DMSs with adhesive connections and two DMSs with welded connections) were tested for the ultimate load and fatigue load cycles following the guidelines of the AASHTO specifications (AASHTO 2015). This paper is composed of four sections encompassing the presented introduction herein followed by ultimate strength and fatigue load testing, results and discussion, and conclusions.

5.3 ULTIMATE STRENGTH AND FATIGUE LOAD TESTING

The full-scale testing was aimed to study the ultimate strength and fatigue behavior of the DMS with adhesive connections and the DMS with welded connections. Strain and displacement gauges were installed on individual DMS specimens to record two fundamental sets of physical parameters: strains and displacements, when loaded to failure and under fatigue load conditions. This section further discusses the DMS specimens and the testing setup of the ultimate strength test and fatigue load test.

5.3.1 FULL-SIZED DMS SPECIMENS

In the ultimate strength testing, two full-sized aluminium DMS specimens, which encompass one DMS specimens with adhesive connections and one DMS with welded connections, were utilized. Each DMS specimen mainly consists of aluminum back skin, aluminum internal frame structure and channels to properly function with the support structure. The back skin was fabricated with 5052-H32 aluminum alloy (Aluminum Association 2010), whereas the internal frame structure and channels were made of 6061-T6 aluminum alloy (Aluminum Association 2010). As shown in Figure 5.1, the dimension of each of the DMSs was 1.52 m in length, 1.43 m in width, and 0.28 m in depth. Each was connected with two 1.27 m long channels on the top and bottom end. The channels were connected to the frame with a bolt connection. Generally, DMSs are designed as per the requirements of each client and design are also varied on the type of connection requested by the client. All DMSs are not compatible with both adhesive and welded connections. As DMSs fabricated with this particular geometry is compatible with both adhesive and welded connections, DMS with the geometry shown in Figure 5.1

is selected. The DMS specimen with adhesive connections was bonded with 64.7 mm wide and 0.39 mm thick LORD 406-19GB (LORD 2018) acrylic adhesive on the north and south end of the DMS for the connection between the back skin and the frame. Meanwhile, an adhesive connection of 5.91 cm width was applied on the east and west end of the DMS for connecting the back skin and the frame. The geometry of the adhesive DMS with the top and the side view is also shown in Figure 5.1a and Figure 5.1b, respectively. On the other hand, the DMS specimen with weld connections was connected with 3.18 mm fillet weld to connect the back skin and the frame on the outer edge. The weld connections were completed using the 4043 aluminum filler used to fabricate the welded DMS. The geometry of the welded DMS with the top view and the side view is shown in Figure 5.1c and Figure 5.1d, respectively. For the fatigue load testing, additional two full-sized DMS specimens, including one adhesively bonded DMS specimen and one welded DMS specimen, were used. Note, each test was only once performed due to expensive cost requiring the fabrication of the four full-scale specimens, but all the tests were completed through a systematic testing protocol, so as to minimize uncertainty in the test results. It should be also noted that the adhesive and welded specimens used for the fatigue testing are identical to the respective adhesive and welded specimens used in the ultimate testing. In DMS, the frame of the DMS is required to be connected to the aluminum back skin. Loads exerted on the aluminum back skin are transferred to the frame through the adhesive or welded connection. Connection used in the DMS is also one of the major elements for the design of DMS. Therefore, the strength of each connection type should be investigated. No experimental study has been performed to determine the strength of connections in the DMS through its full-scale

tests. Therefore, the strength of DMS with respect to each connection type should be investigated and compared thoroughly for the ultimate and fatigue strengths. Figure 5.2 shows a representative photo of the DMS installed on the US highway. The mechanical properties of the adhesive and weld metal along with the aluminum materials are presented in Table 5.1.

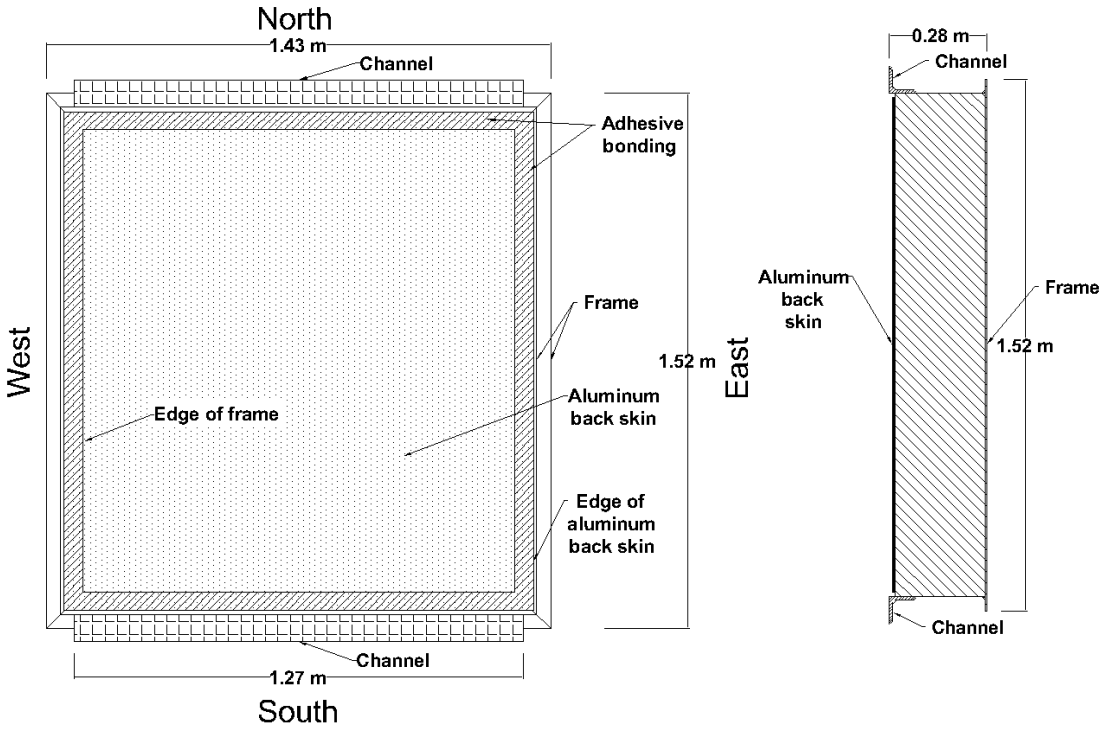

(a) (b)

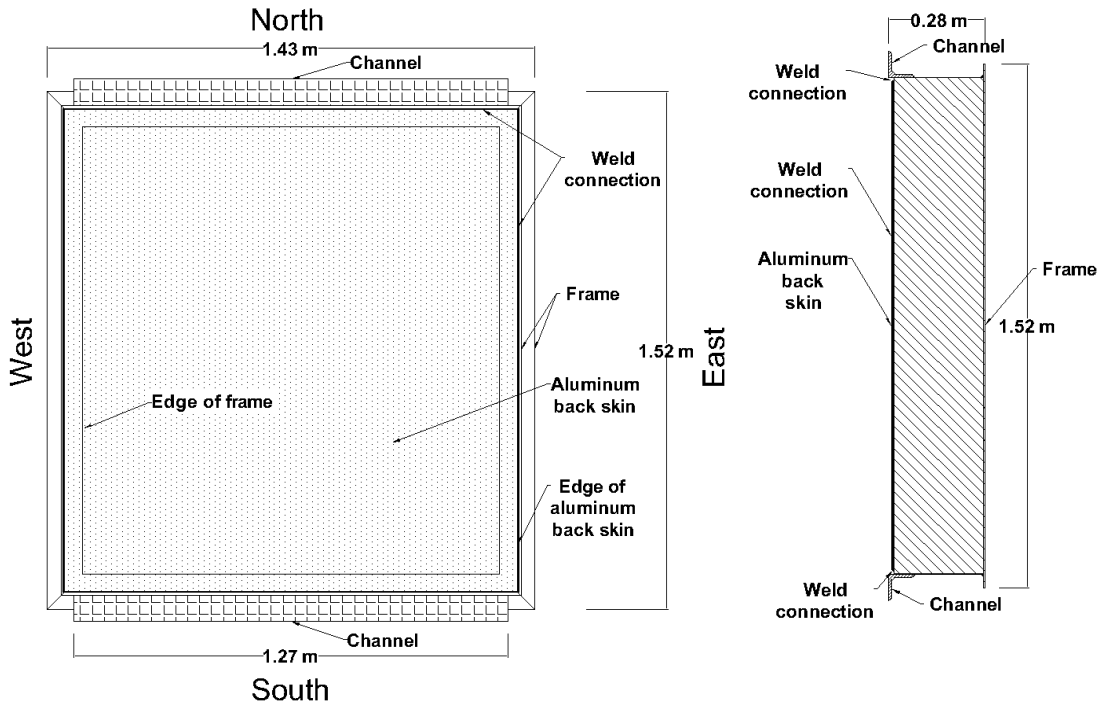

(c) (d)

Figure 5.1: Geometry of DMS specimens for ultimate strength and fatigue load testing: (a) top view of adhesive DMS, (b) side view of adhesive DMS, (c) top view of welded DMS, and (d) side view of welded DMS.

Figure 5.2: Representative picture for DMSs installed in the US highway

Table 5.1: Mechanical properties for the adhesive and weld metal and aluminum materials

Material	Tensile strength (Mpa)	Shear Strength (Mpa)
5052 aluminum	228	138
6061 aluminum	310	207
Adhesive	1307.9	53.4
4043 aluminum weld	165	80

5.3.2 TESTING SETUP

Both the ultimate strength and fatigue load tests followed an identical instrumentation plan. The instrumentation plan is made up of 24 strain-gauges installed on the surface of

the aluminum skin inside the DMS near the corners, edges, and perimeter of the loaded region near the center. 15 displacement gauges were installed at the bottom inside the DMS to record displacement data, including 14 linear variable differential transformers (LVDTs) and 1 string potentiometer. Strictly speaking, the LVDTs were installed near the corners, edges, and perimeter of the loaded region near the center and the string potentiometer was attached to the center. The strain and displacement data were obtained using a 128-channel data acquisition system. Figure 5.3 shows the details of the instrumentation plan.

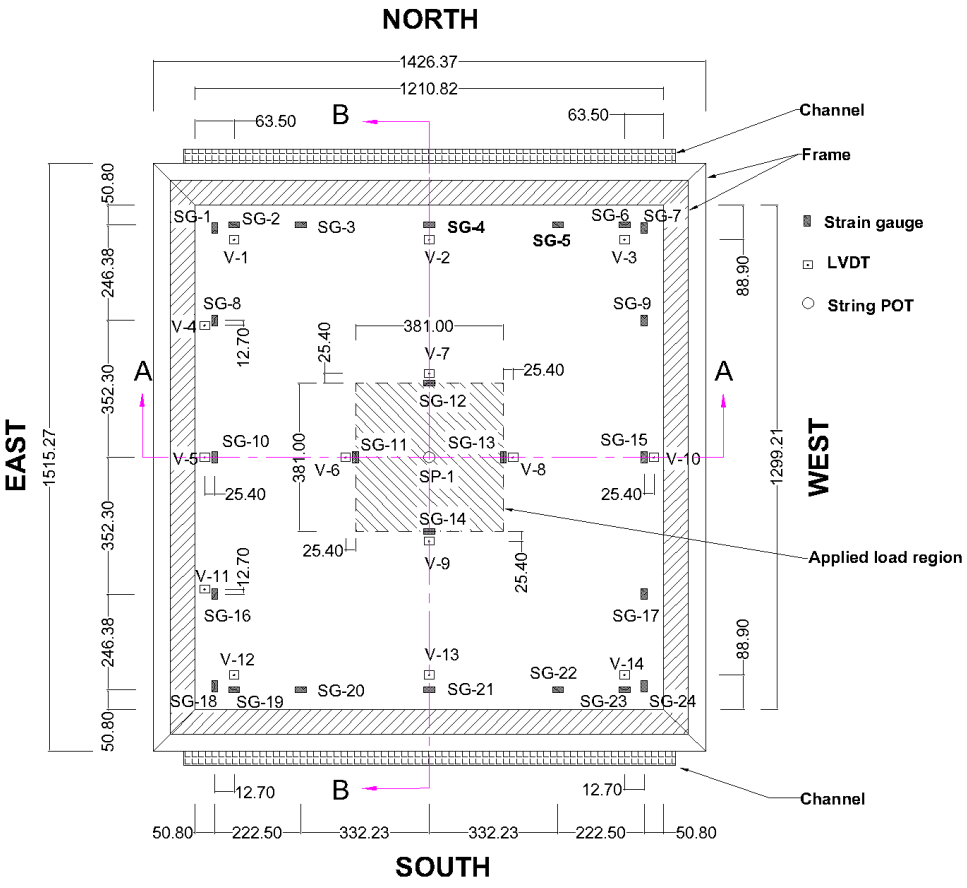

(a)

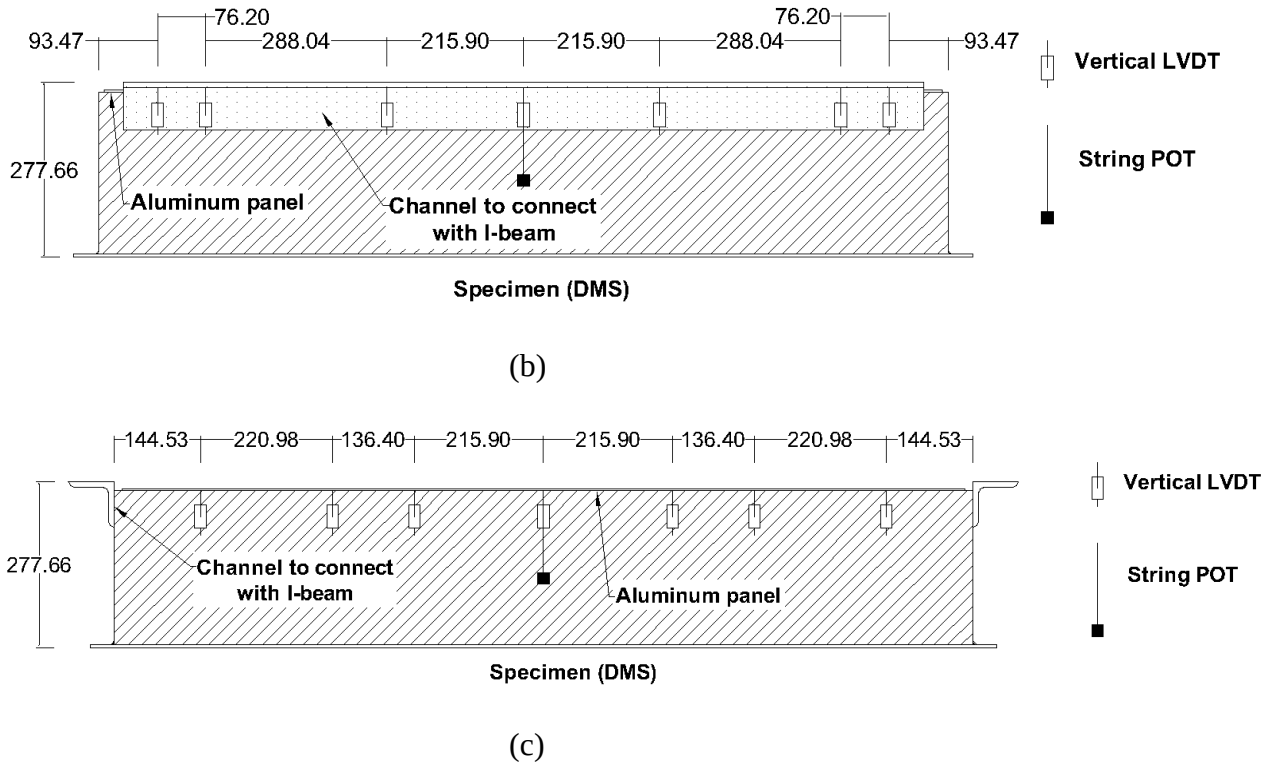

Figure 5.3: Instrumentation plan for strain and displacement gauges: (a) Bottom view, (b) Elevation view of section A-A, and (c) Elevation view of section B-B (All dimensions are in mm).

The testing setup for the ultimate strength tests and fatigue load tests is shown in Figure 5.4. An actuator of 649.44 kN capacity with 38.1 cm stroke length was used to load each of the DMS specimens at the center of the panel as shown in Figure 5.4a. Two W 6 X 12 steel I-beams were connected to the channels on the rear of the DMS. The DMS attached with the I-beams was placed on two abutments located at the north and south end of the test lab during each of the tests. Four 444.8 kN load cells (LC) were installed under the I-beams at each corner to measure the reaction forces. Rubber pads were also placed at the center of the panel followed by a 38.1 cm X 38.1 cm steel plate on the aluminum back skin to facilitate uniform load transfer from the actuator as shown in Figure 5.4b. All the tests including the ultimate and fatigue load tests were performed at a

room temperature of approximately 23 °C in Structure lab at South Dakota State University.

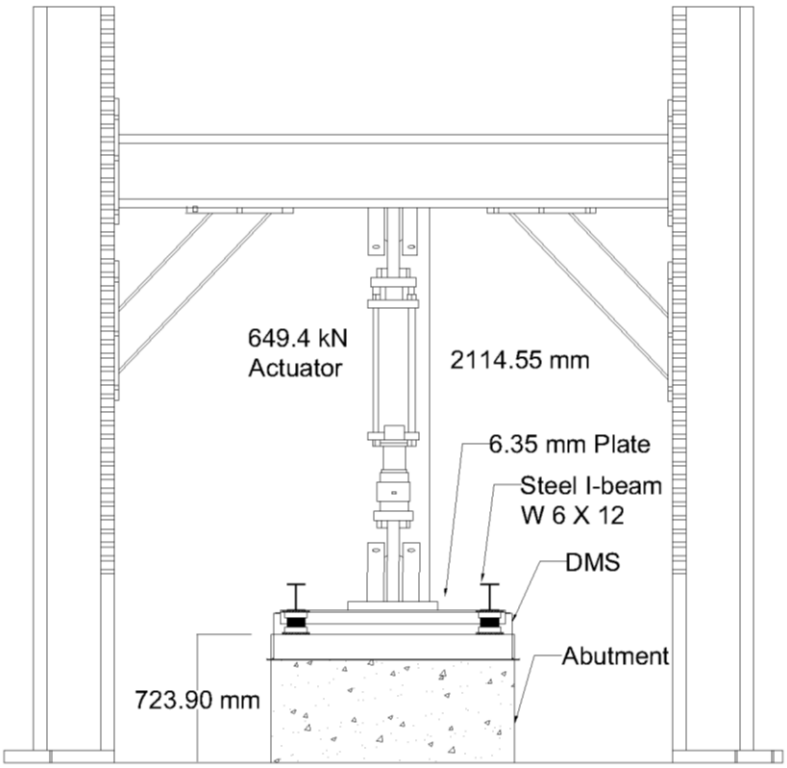

(a)

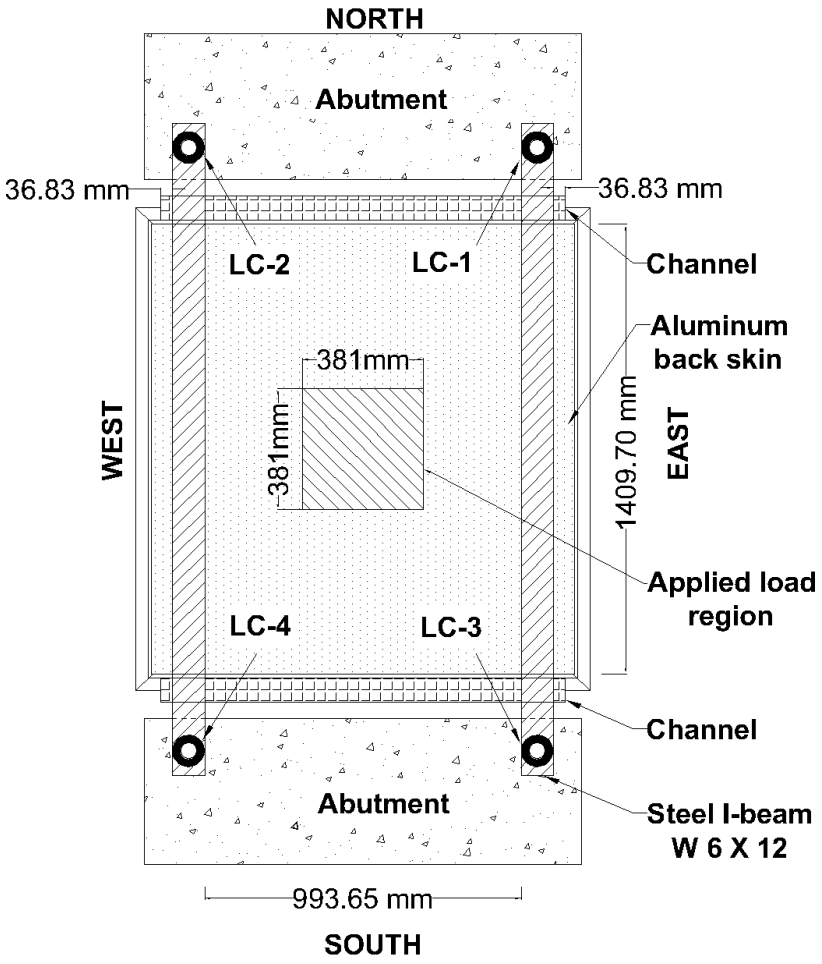

(b)

Figure 5.4: Test setup: (a) cross-section view and (b) top view.

5.3.2.1 ULTIMATE STRENGTH TESTING

As stated before, the ultimate strength of one adhesive DMS and one welded DMS were examined in this study. The ultimate strength tests were performed under displacement control by applying a monotonic load to the back-skin of the aluminum panel with a displacement rate of 0.178 mm/sec until failure. Strain, displacement, and load data were recorded until failure. A regular inspection of the DMS was conducted to

check the damage on the structure during the test. The testing setup of the adhesive DMS for the ultimate strength test is shown in Figure 5.5.

(a)

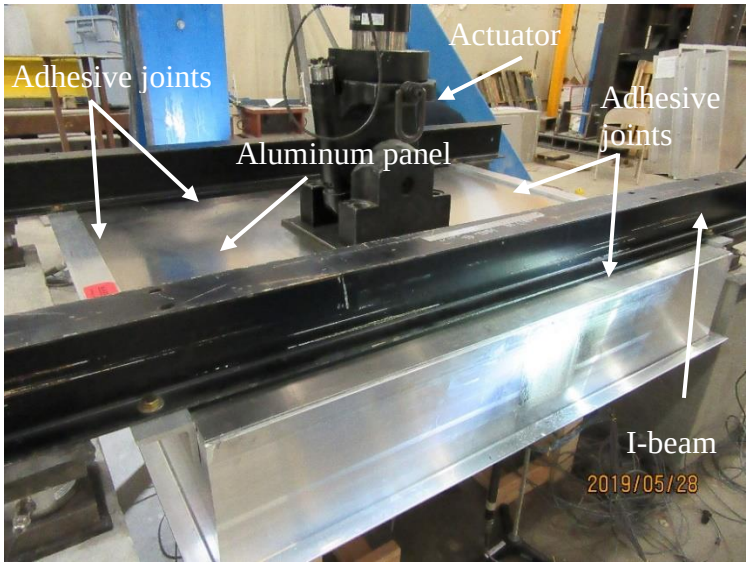

(b)

Figure 5.5: Ultimate strength test of adhesive DMS: (a) isometric view and (b) close-up view.

5.3.2.2 FATIGUE LOAD TEST

One adhesive DMS and one welded DMS were tested under a fatigue design load of 0.818kN for 500,000 cycles. The load was calculated from the AASHTO Specifications (2015) simulating the wind load exerted by natural wind gust pressure based on a yearly mean speed of 18.02 km/hr. The actuator was operated at a frequency of 1 Hz in a displacement control manner. Strain, displacement, and load responses were logged every hour during the test. Each of the DMSs was inspected for the existence of any damage every four hours initially up to 100,800 cycles, every two hours between 100,800 and 302,400 cycles, which later truncated to an hourly observation. The fatigue testing setup of the welded DMS is shown in Figure 5.6.

(a)

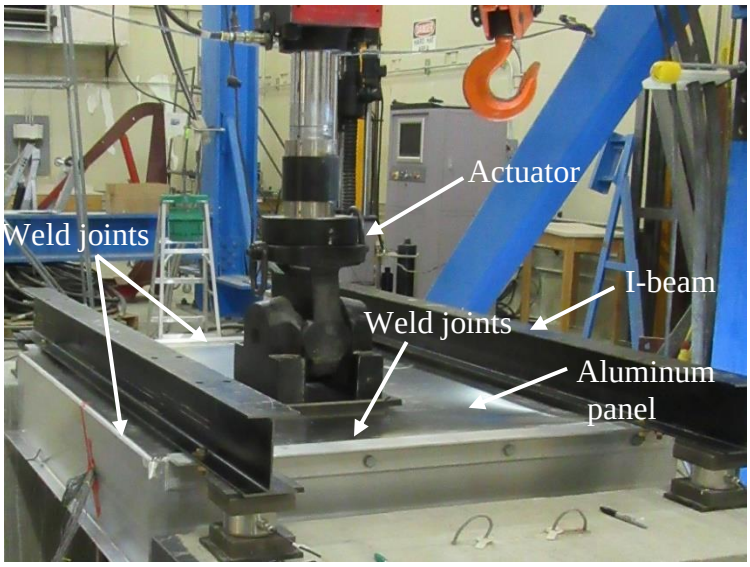

(b)

Figure 5.6: Fatigue load test of welded DMS: (a) isometric view and (b) close-up view.

5.4 RESULTS AND DISCUSSION

Results from the ultimate strength and fatigue load tests are summarized and discussed in this section. Details on the results with a focus on load-displacement curves and strain profiles are presented in the following subsections.

5.4.1 ULTIMATE STRENGTH

5.4.1.1 ADHESIVE DMS STRENGTH

A schematic for the detailed four damage states (including aluminum panel distortion) and load transferring mechanisms during the test are presented in Figure 5.7. As shown in the figure, the DMS was loaded with a square steel plate placed at the center of DMS. Load exerted by the actuator was transferred to the adhesive joints of the DMS diagonally through the aluminum panel. Adhesive debonding and distortion of the

aluminum panel were two types of primary damage observed during the test. The damage state designated as DS-1 is the first damage state observed during the test. In this damage state, adhesive debonding was initated at the north-east corner of the DMS with slight distortion of the aluminum panel. At this stage, only 0.504% of the adhesive area was found to be damaged. The second damage state labeled as DS-2 shows the propagation of adhesive debonding observed on the east side of the DMS at north east corner. The damage in the adhesive area was found to be 4.318%. Excessive damage in the adhesive area of the DMS was found at third damage state indicated as DS-3 at which damage in the adhesive area was increased to 7.535%. The final damage state, defined as DS-4 was observed at both east and north edge of the DMS as shown in the figure. At DS-4, the DMS was failed completely with 32.864% damage in the adhesive area of the DMS. The damage observed in the adhesive DMS at four damage stages is also tabulated in Table 5.2.

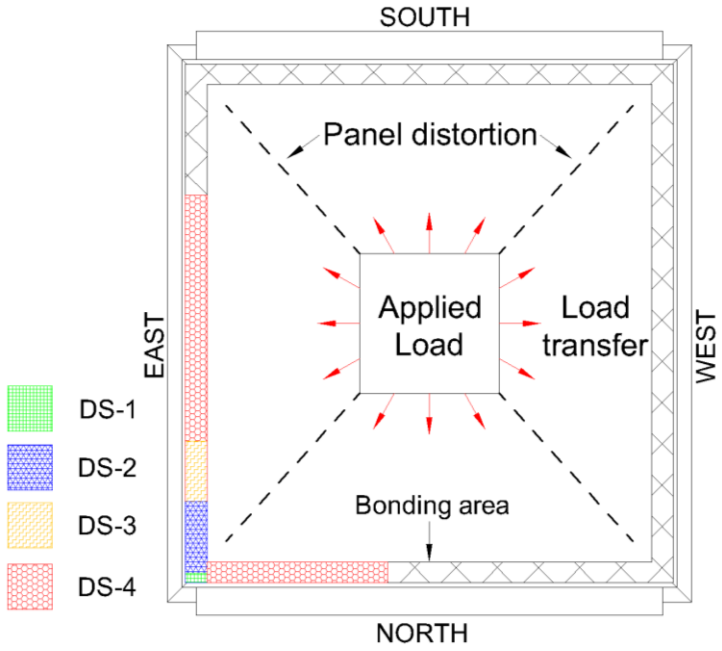

Figure 5.7: Top view of damage states in adhesive DMS.

Table 5.2: Damage in adhesive DMS at different damage states

Damage state	Distortion of panel	Adhesive debonding state	Adhesive debonding (%)
DS-1	Slight	Initiation	0.504%
DS-2	Moderate	Propagation	4.318%
DS-3	Extensive	Excessive	7.535%
DS-4	Complete	Ultimate failure	32.864%

Figure 5.8 shows the elevation views of the adhesive DMS with respect to each damage state. The DS-1 of the DMS observed is presented in Figure 5.8a. It appears that the debonding of adhesive at the east edge of panel in the north-east corner was initiated, and the aluminum panel was observed to be slightly distorted. The damage was observed when the centerline deflection was 76.2 mm and can be considered least possible damage. The DS-2 is shown in Figure 5.8b, indicating that the adhesive debonding observed in DS-1 in north-east corner is propagated significantly at the east edge of the panel with moderate distortion of the aluminum panel due to a significant transfer of load (116.50 kN) from the actuator. The DS-3 is presented in Figure 5.8c. The adhesively bonded aluminum panel was found to be debonded excessively during this damage state. At this instant, extensive distortion of the panel was observed at the center, whereas east edge of the panel was slightly lifted at the north-east corner. Figure 5.8d illustrates the DS-4, where complete distortion of the aluminum panel was spotted at the center. The excessive debonding observed in DM-3 at the east edge of the panel was found to be significantly propagated. The adhesive debonding was also observed in the north edge of the panel at the north-east corner as shown in the figure. Substantial uplift of the panel was observed at the north edge and east edge of the panel at the north-east corner. At DS-1 (see Figure 5.8a), when the actuator load in DMS was 62.05 kN, only slight distortion

in the panel was observed. At each of the following damage states DS-2, DS-3, and DS-4, distortion in the the panel was observed to be increasing correspondingly. Although the overall shape of the deflected panel was almost identical, the magnitude of distortion was found to be increased at each damage states causing high stress concentration at the edge and corner locations of DMS. The increment in the stress at corners due to rise in actuator load triggered the initiation of adhesive debonding at the north-east corner which propagated to ultimately fail.

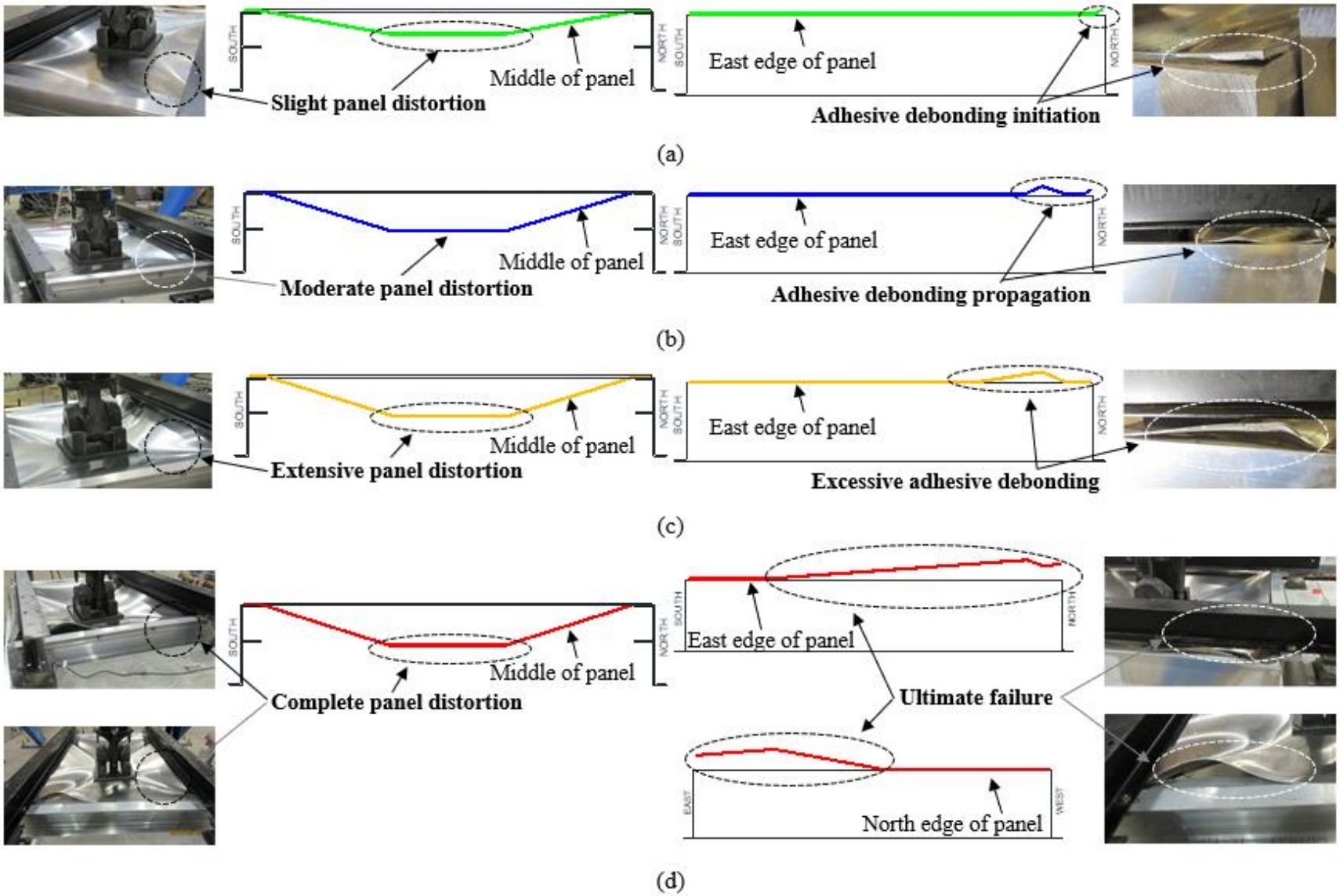

Figure 5.8: Elevation view of damage states in adhesive DMS: (a) DS-1, (b) DS-2, (c) DS-3, and (d) DS-4.

A load-displacement curve for the ultimate strength test of the adhesive DMS is presented in Figure 5.9. The adhesive DMS was loaded at the center of the back-skin aluminum of the DMS. As mentioned previously, four different damage states were observed during the test. The first damage state (DS-1) was observed when the actuator load reached to 62.05 kN. Pior to DS-1 at 62.05 kN, no visible damage was observed. An abrupt drop in the actuator load from 102.57 kN to 70.74 kN was observed as shown in this figure. The actuator was pulled up for the removal of the LVDTs that were installed at the bottom of the DMS to avoid any damage on the LVDTs which explains the unusual behavior of the load-displacement curve. The second (DS-2), third (DS-3), and fourth (DS-4) damage states were observed at 116.50 kN, 120.12 kN, and 123. 41 kN. The adhesive DMS failed at 123.41 kN when the center-line deflection was 133.35mm. The results from the ultimate strength test found that adhesive DMS can easily resist up to 62.05 kN as DS-1 with relatively small damage in the adhesive area was observed at that instant. Damage due to propagation of adhesive debonding (DS-2) was observed at 127 mm centerline-deflection of the aluminum panel. Damage states DS-3 and DS-4 were also observed when the centerline-deflection of the aluminum panel were 130.81 mm and 133.35 mm, respectively. As presented in Figure 5.9, three damage states DS-2, DS-3, and DS-4 were spotted at a narrow interval. Therefore, DS-2 (adhesive debonding propagation) was found to be the crucial damage state for the adhesive DMS, rather than DS-1 (adhesive debonding initiation). As DS-3 and DS-4 were observed immediately after DS-2, adhesive DMS can be considered unsafe after propagation of adhesive debonding (DS-2).

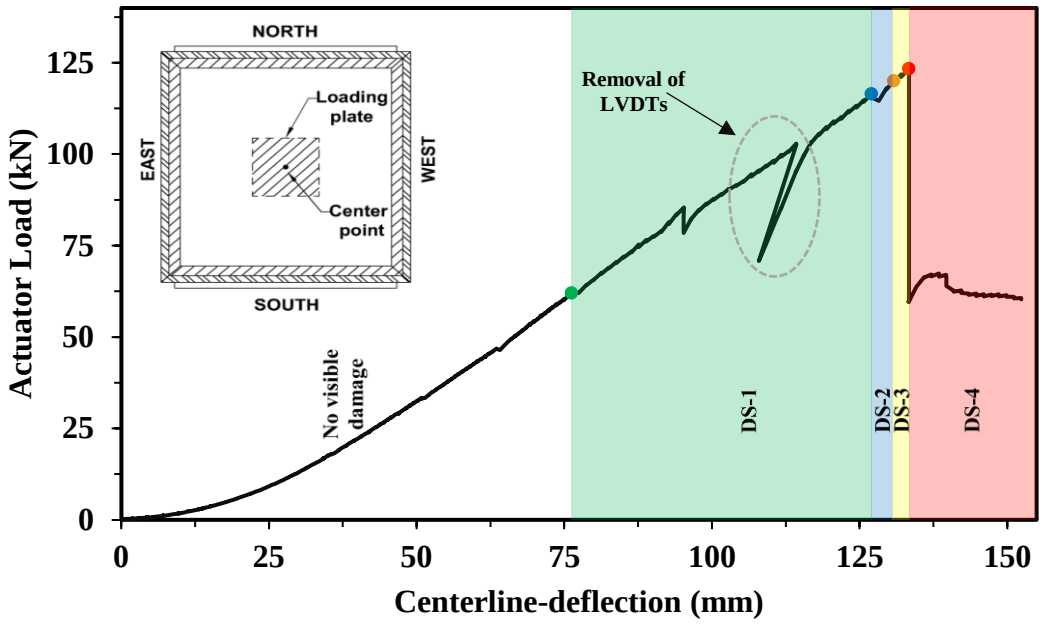

Figure 5.9: Load-displacement curve for tested adhesive DMS.

Figure 5.10 shows representative actuator load versus strains of the adhesive DMS. The representative strain profile of the strain gauges installed on the north and west end of the adhesive DMS is presented in Figure 5.10a and Figure 5.10b, respectively. It should be noted that tensile strains observed are well below the yield strains of the aluminum on the north, south, east, and west end of the adhesive DMS. The aluminum panel in all four edges experienced compression at the beginning of the test. Maximum strains observed on the aluminum panel on the north, south, east, and west end of the adhesive DMS are found to be lower than half of the yield strain of the aluminum. This result indicates that these locations are not affected significantly when subjected to the loading. In Figure 5.10a, all three strain gauges (SG-3, SG-4, and SG-5) were observed to be in compression at DS-1, however the strain at SG-4 and SG-5 were close to zero and

SG-3 was found to be tension with maximum strain. Figure 5.10c and Figure 5.10d illustrate the strain profiles at the corners in the longitudinal and transverse directions, respectively. Note, a direction along east-west is considered as the longitudinal direction, whereas a direction along north-south is deemed as the transverse direction. Strains at the corners of the adhesive DMS were found to be substantially higher than the yield values of the aluminum, as expected. Each corner of the aluminum panel was on compression at the beginning of the test, however, it was observed that there were extreme strains experienced near the failure of the DMS. At DM-4, strains in the longitudinal directions are higher than three times the yield strain of aluminum, whereas strains in the transverse directions are greater than five times the yield strain of the aluminum. At DS-4, SG-2 observed the highest strain in longitudinal direction as shown in Figure 5.10c and SG-1 recorded the highest strain in transverse direction as shown in Figure 5.10d. Strain profiles of the four strain gauges installed around the perimeter of the loading plate at the center are also shown in Figure 5.10e. The aluminum panel was found to be in tension throughout the test until failure and the peak strain was observed at SG-11 during ultimate failure. The highest tensile strains were observed for the strain gauges installed at the corners in the transverse direction followed by the longitudinally installed strain gauge group. It was found that the corner sections of the aluminum panel in the DMS play a more critical role as strain gauges installed in the corners observed highest strains than the other locations and should be designed carefully. At DS-4, SG-3 observed the maximum strain among the three strain gauges installed at the north edge of the panel, SG-2 recorded the peak strain between the four strain gauges installed at the corners in longitudinal direction, SG-1 observed the highest strain among the four strain gauges

installed at the corners in transverse direction, and SG-11 detected the maximum strain among the four strain gauges installed at the center of the panel. These results can be attributed to the failure of adhesive DMS due to adhesive debonding at the north and east edge in the north-east corner of the aluminum panel.

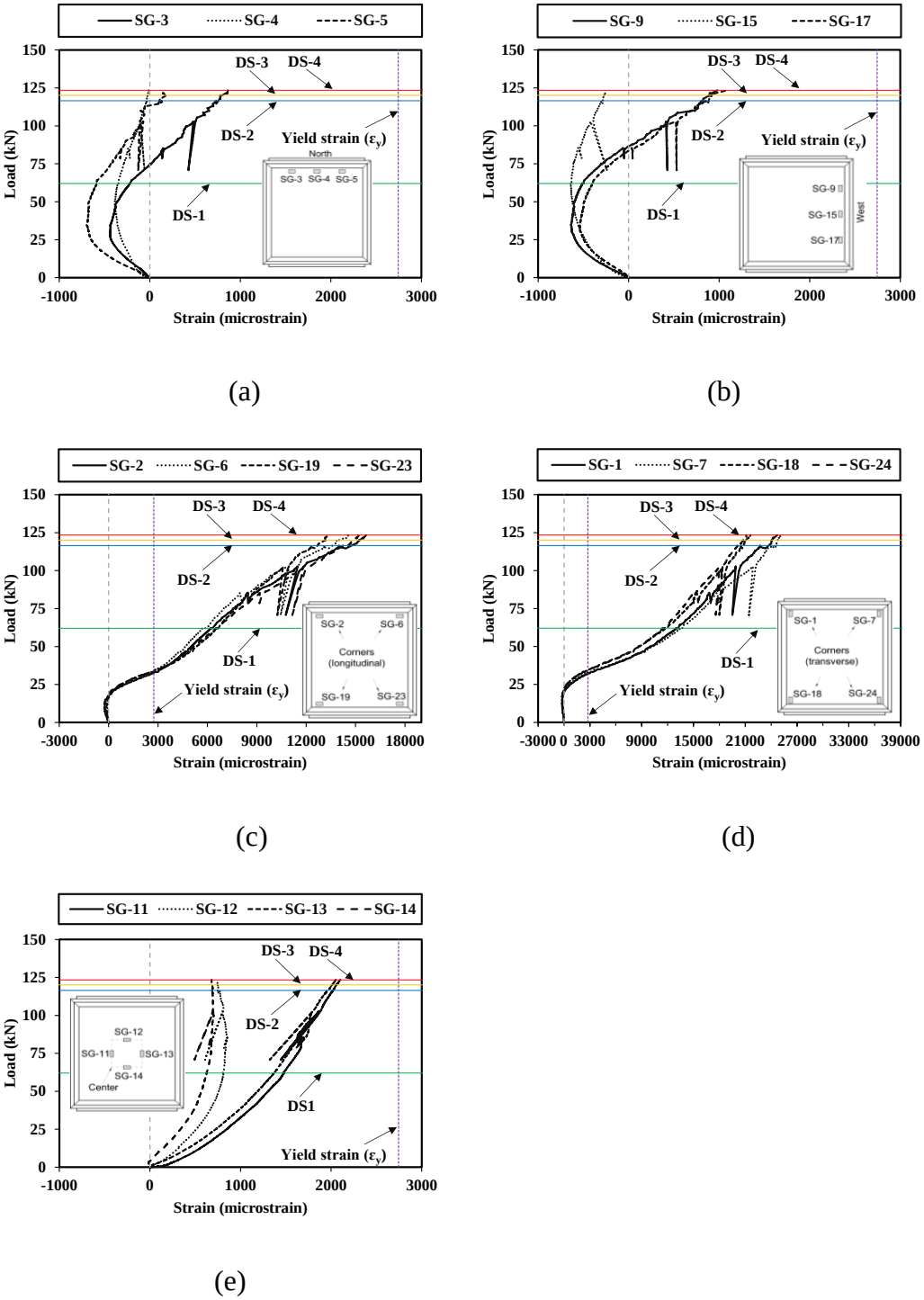

Figure 5.10: Strain profile for adhesive DMS at: (a) north end, (b) west end, (c) corners in the longitudinal direction, (d) corners in the transverse direction and (e) center

Figure 5.11 shows the load versus deflection responses at all LVDT locations in the panel. All deflection profiles are nearly linear. The LVDTs installed near the center of the adhesive DMS (V-6, V-7, V-8, and V-9) were removed at 83.04 kN, whereas the rest of the LVDTs were removed at 102.57 kN to prevent any damage to the LVDTs. The LVDTs installed near the center of the DMS (V-6, V-7, V-8, and V-9) recorded maximum deflections, followed by the LVDTs installed at the corners of the DMS (V-1, V-3, V-12, and V-14). Only DS-1 was plotted in the figure, as the LVDTs were removed before the DMS reached the damage state DS-2. Although the LVDT profile for all the damage states could not be plotted, the peak deflection prior to LVDT removal was observed near the center of the DMS for V-7 with 91.49 mm. The maximum deflection at V-7 justifies the failure observed at the north edge of the DMS to some extent.

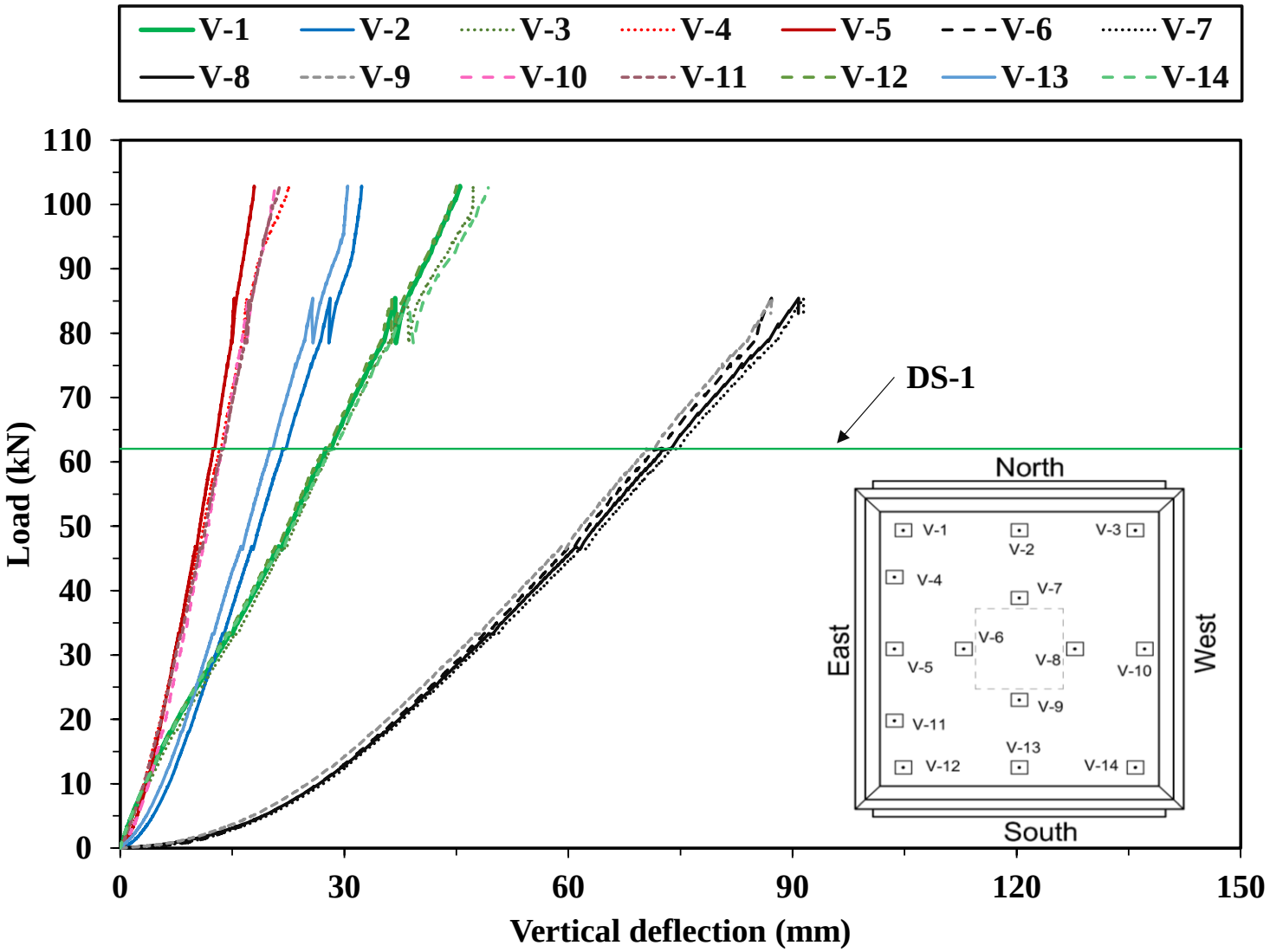

Figure 5.11: LVDT profile for adhesive DMS

Figure 5.12 shows the reaction force from the load cells installed at four ends of the adhesive DMS. The load cells were installed at each corner of the DMS. The progression of the reaction force with respect to time following different damage states is shown in Figure 5.12a. The reaction force is observed to be increasing with the increase in the actuator load during the ultimate strength test. Significant decrements in the load can be observed in all the load cells prior to DS-2. This was because the actuator was pulled up to remove LVDTs at that instant due to which load was dropped in each load cell. A bar chart for the reaction force in the four load cells when reaching the yield strength of the aluminum panel is shown in Figure 5.12b. It appears that LC-3 observed the maximum reaction force of 11.92 kN, whereas LC-4 experienced the lowest reaction force of 6.27 kN up to the yield strength. Figure 5.12c presents another bar chart of the reaction force recorded at the failure of the adhesive DMS. It turned out that the adhesive DMS experienced the maximum reaction force of 35.74 kN in LC-3 and minimum reaction force of 25.06 kN in LC-4. LC-3 installed at the south-east corner of the DMS recorded the peak load at each damage state, however LC-1 installed at the north-east corner was expected to record the highest load as failure was observed at that location. This result suggests that failure of the adhesive DMS is not only contributed by the load acting on the DMS. Failure of the DMS at the north-east corner can be considered due to better cohesion of the adhesive in other corners than in the north-east corner. As cohesion of the adhesive was lower, adhesive debonding initiated which later propagated and ultimately failed.

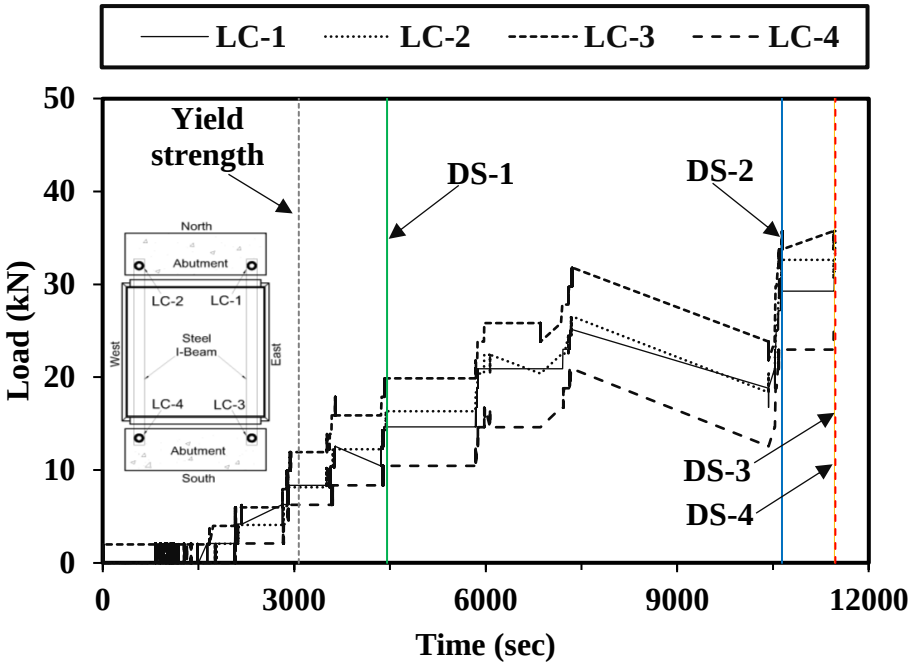
LC-1
LC-2
LC-3
LC-4
Yield strength
DS-1
DS-2
DS-3
DS-4
Load (kN)
Time (sec)
0
10
20
30
40
50
0
3000
6000
9000
12000
North
Abutment
LC-2
LC-1
Steel I-Beam
West
East
LC-4
LC-3
Abutment
South

(a)

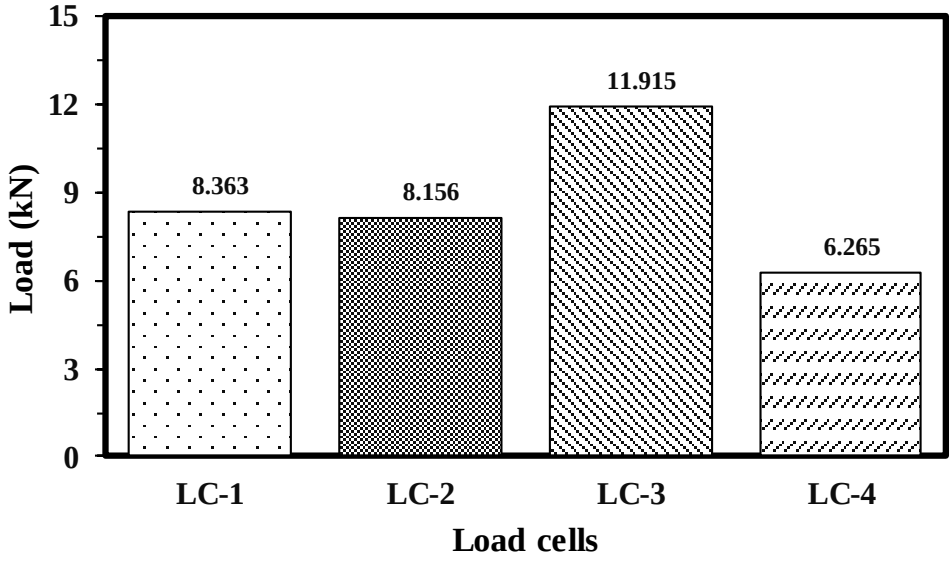
Load (kN)
Load cells
0
3
6
9
12
15
8.363
8.156
11.915
6.265
LC-1
LC-2
LC-3
LC-4

(b)

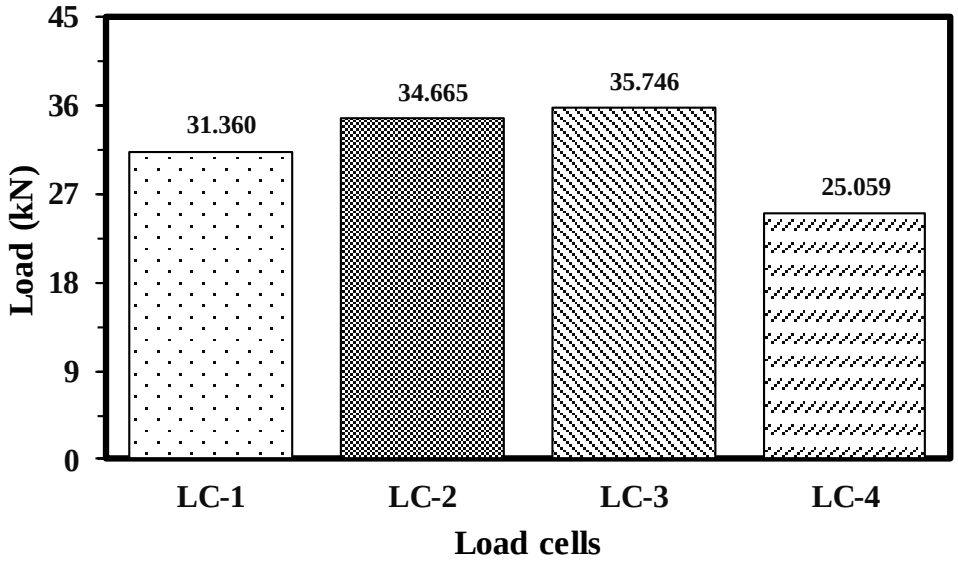

(c)

Figure 5.12: Reaction force from load cells for adhesive DMS: (a) load vs time, (b) at yield strength, and (c) at ultimate strength

5.4.1.2 WELDED DMS STRENGTH

Figure 5.13 presents the overall schematic of two failure modes and aluminum panel distortion observed for the welded DMS during the ultimate strength test of welded DMS. The first mode was observed due to failure of internal welds connecting the frame and back skin aluminum of the DMS. Specifically, the internal welds closest to the corners of the DMS were failed due to the high stress concentration at the corners. Two welds were observed to be failed at the north east corner, at the south east corner, and at the north west corner, whereas the failure of only one weld was found at the south east corner. The second failure mode was observed due to the rupture of the frame at the south-west end. At this mode, the bolt connecting the channel and frame of the DMS was detached causing the rupture of frame at that location.

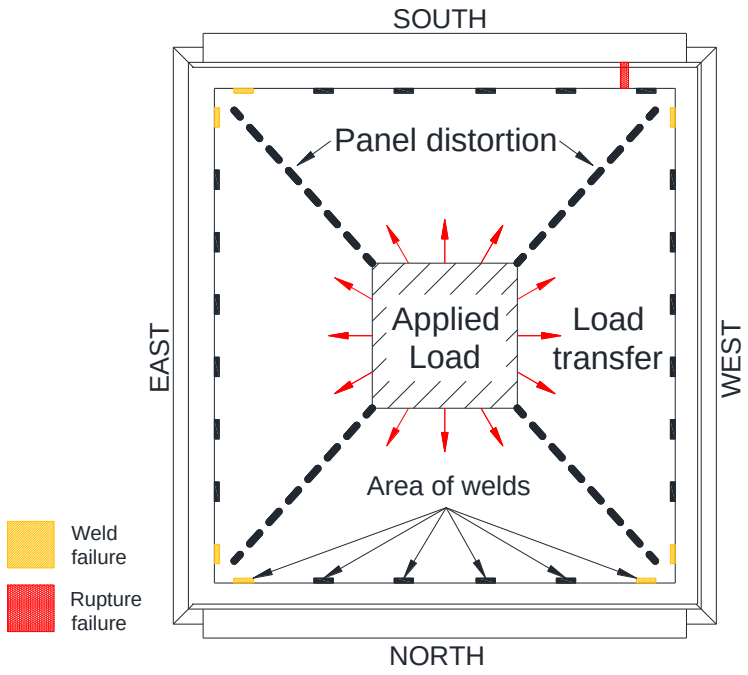

Figure 5.13: Top view of failure modes in welded DMS.

Figure 5.14 also presents the elevation views of the two failure modes observed during the test. As shown in Figure 5.14a, extensive distortion of the aluminum panel was observed with the internal weld failure as the first failure mode. Figure 5.14b displays the second failure mode of the welded DMS. The aluminum panel was observed to be distorted completely at the center and the frame was ruptured at the south-west corner of the DMS. The channel connecting the DMS and I-beam was bent as well. As in the adhesive DMS, distortion in the aluminum panel was also observed to be increased progressively with the increase in actuator load. Higher deflection of the aluminum panel was observed at diagonal directions of the DMS (see Figure 5.14a and Figure 5.14b) indicating diagonal load distribution in the aluminum panel. As the test progressed, stress

concentration at the corner locations increased owing to increment in distortion of the aluminum panel which justifies the failure of interior welds at corners of DMS. Further, increment in load amplified the stress at corners which ultimately ruptured the frame of DMS at the south-west corner.

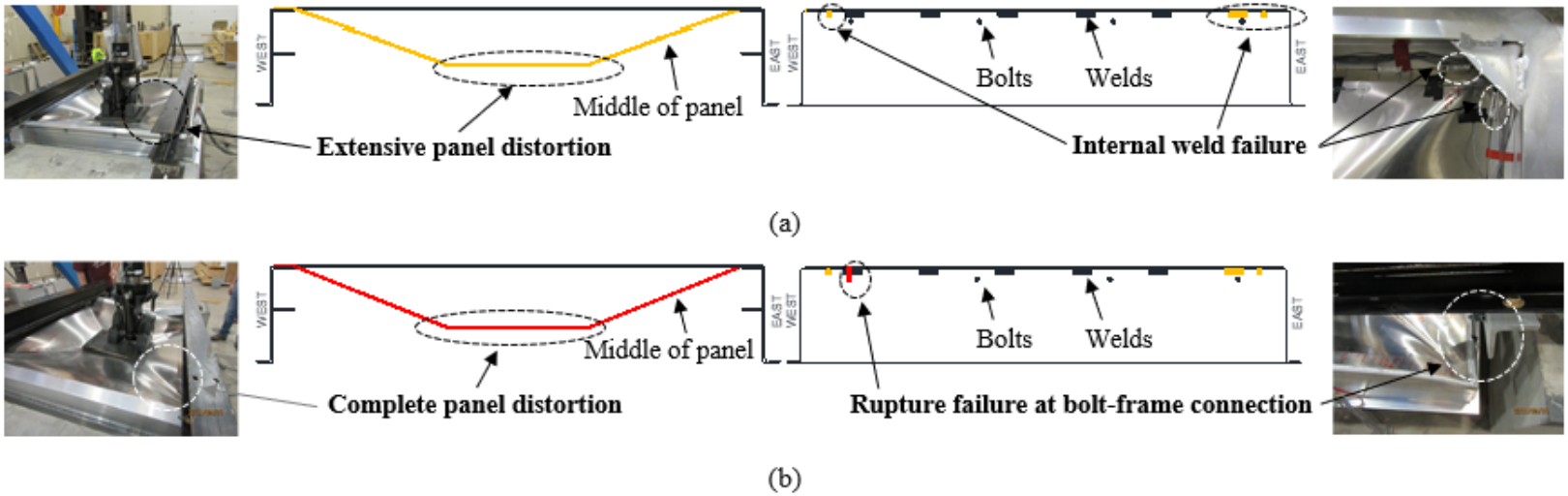

Figure 5.14: Elevation view of failure modes in welded DMS: (a) weld failure and (b) rupture failure.

Figure 5.15 shows the load-displacement curve for ultimate strength test of the welded DMS. The welded DMS was also loaded at the center of the back-skin aluminum of the DMS. The first failure due to the failure of the interior welds was observed at 153.46 kN when the center of DMS was deflected to 158.57 mm deflection. The load was decreased up to 113.38 kN after the first failure. The second failure due to the rupture of the frame was observed at 145.18 kN with center line deflection of 175.95 mm. Although the failure of internal welds were initially observed in the DMS, no damage in the exterior weld was observed during the test. Although the actuator load decreased after the first failure mode, the DMS can not be considered to be completely failed until rupture of the frame. Design shear strength of the fillet weld connecting the back skin and the frame on the exterior edge of the welded DMS calculated following the guidelines of Aluminum Design Manual (Aluminum Association 2010) was found to be 169.52 kN. The calculated design shear strength of the weld was found to be higher than the peak load (153.46 kN) resisted by the tested DMS. The DMS was failed due to the rupture of frame before the entire failure of the internal and external welds. Therefore, the design shear strength of the weld in the DMS was found to be higher than the maximum strength of the welded DMS from the ultimate strength test. The testing results demonstrated the strength of exterior weld connection higher than the strength of frame for rupture failure.

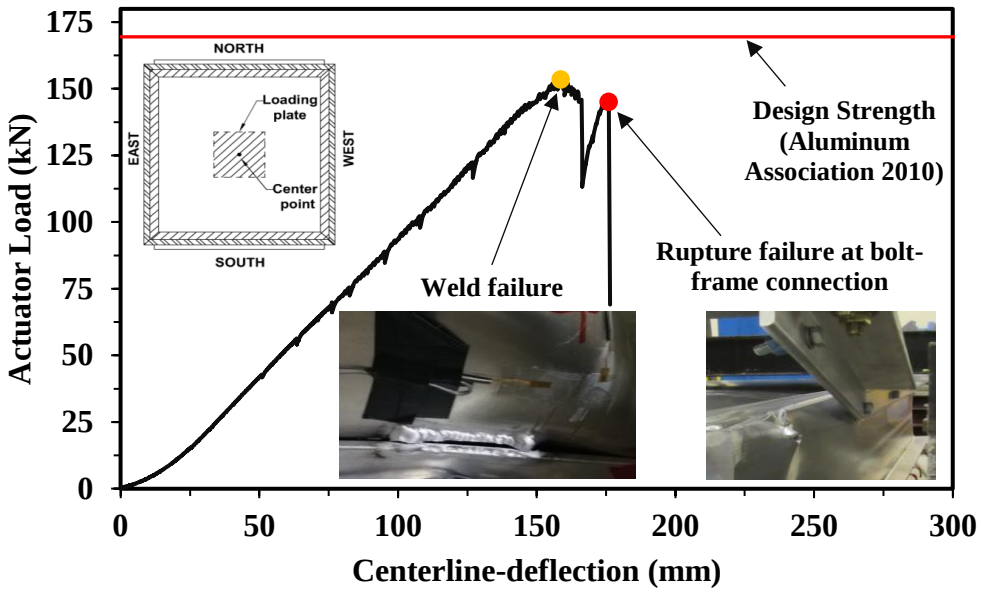

Figure 5.15: Load-displacement curve for welded DMS

With the weld failure threshold, the representative plots of the actuator load against strains observed in the aluminum panel of the welded DMS are presented in Figure 5.16. Similar to the strain profiles of the adhesive DMS, overall, tensile strains observed are less than the yield strains of the aluminum on the north, south, east, and west end of the DMS. The sample strain profiles of the strain gauges installed on the north and west end of DMS are presented in Figure 5.16a and b, respectively. The aluminum panel in all four edges experienced compression at the beginning of the test. Figure 5.16c and d illustrate the strain profiles at the corners in longitudinal and transverse directions, respectively. Strains at the corners of the DMS were found to be considerably higher than the yield values of the aluminum. Each corner of the aluminum panel was on compression at the beginning of the test, however, it was observed that the panel experienced extreme tension at the end of the test when it failed. Strain profiles of the four strain gauges

installed around the perimeter of the loading plate at the center are shown in Figure 5.16e. For the strain gauges installed near the center, the aluminum panel was found to be in tension throughout the test until failure. All four strain gauges located near the center observed strains below yield strain, excluding SG-11. The highest tensile strains were observed for the strain gauges installed at the corners in the transverse direction followed by the longitudinally installed strain gauge group. The general strain behavior of the welded DMS is found to be analogous to that of the adhesive DMS, although the strain values are different between welded and adhesive DMSs on each test and location. Particularly, in Figure 5.16c, during the weld failure, strain at SG-23 was found to be lower than the strain recorded at SG-2, SG-6, and SG-19. Longitudinal welds near SG-2 (north-east corner), SG-6 (north-west corner), and SG-19 (south-east corner) were failed which justifies the high tensile strains at those locations than in SG-2. In Figure 5.16d, strain at SG-24 was observed to be higher than strain recorded at SG-9 and SG-15. High stress concentration at SG-24 can be considered due to rupture failure of the frame.

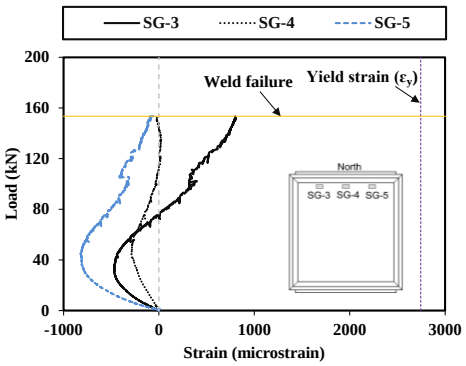

(a)

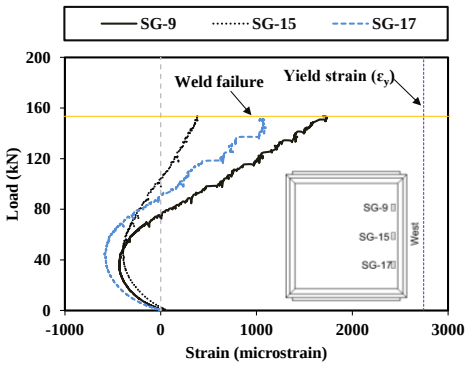

(b)

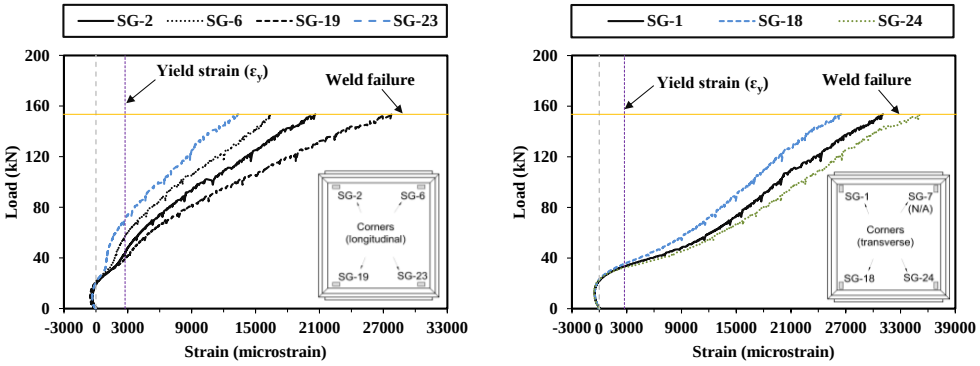

(c) (d)

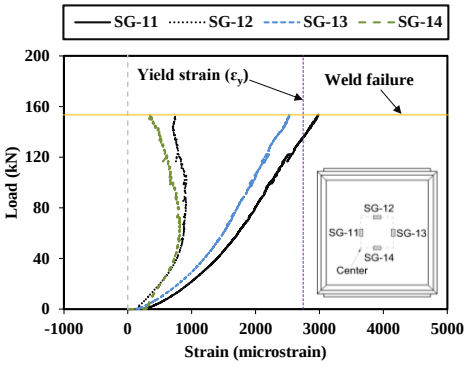

(e)

Figure 5.16: Strain profiles for welded DMS at: (a) north end, (b) west end, (c) corners in the longitudinal direction, (d) corners in the transverse direction and (e) center

For the welded DMS, the plot of the deflection responses of the aluminum panel at all LVDT locations and actuator load is shown in Figure 5.17. The deflection responses from all the LVDTs exhibited a linear behavior. The LVDTs installed near the center of the welded DMS (V-6, V-7, V-8, and V-9) were removed at 69.48 kN, whereas rest of the LVDTs were removed at 74.65 kN to prevent any damage to the LVDTs. The center LVDTs recorded maximum deflections, followed by the LVDTs installed at the corners of DMS (V-1, V-3, V-12, and V-14). The peak deflection was observed near the center of the welded DMS for V-7 with 96.14 mm. The deflection behavior of the aluminum panel

in the welded DMS is similar to that of the adhesive DMS. LVDT profile shown in this figure does not include any failure state as LDVTs were removed before the tested DMS attained any failure state. LVDTs installed at the center recorded the maximum deflection as expected, however, except for the LVDTs installed at the center, V-14 recorded the maximum deflection before the removal of LVDTs during the test. This result supports the second failure state of the welded DMS due to the rupture of frame at south-west corner.

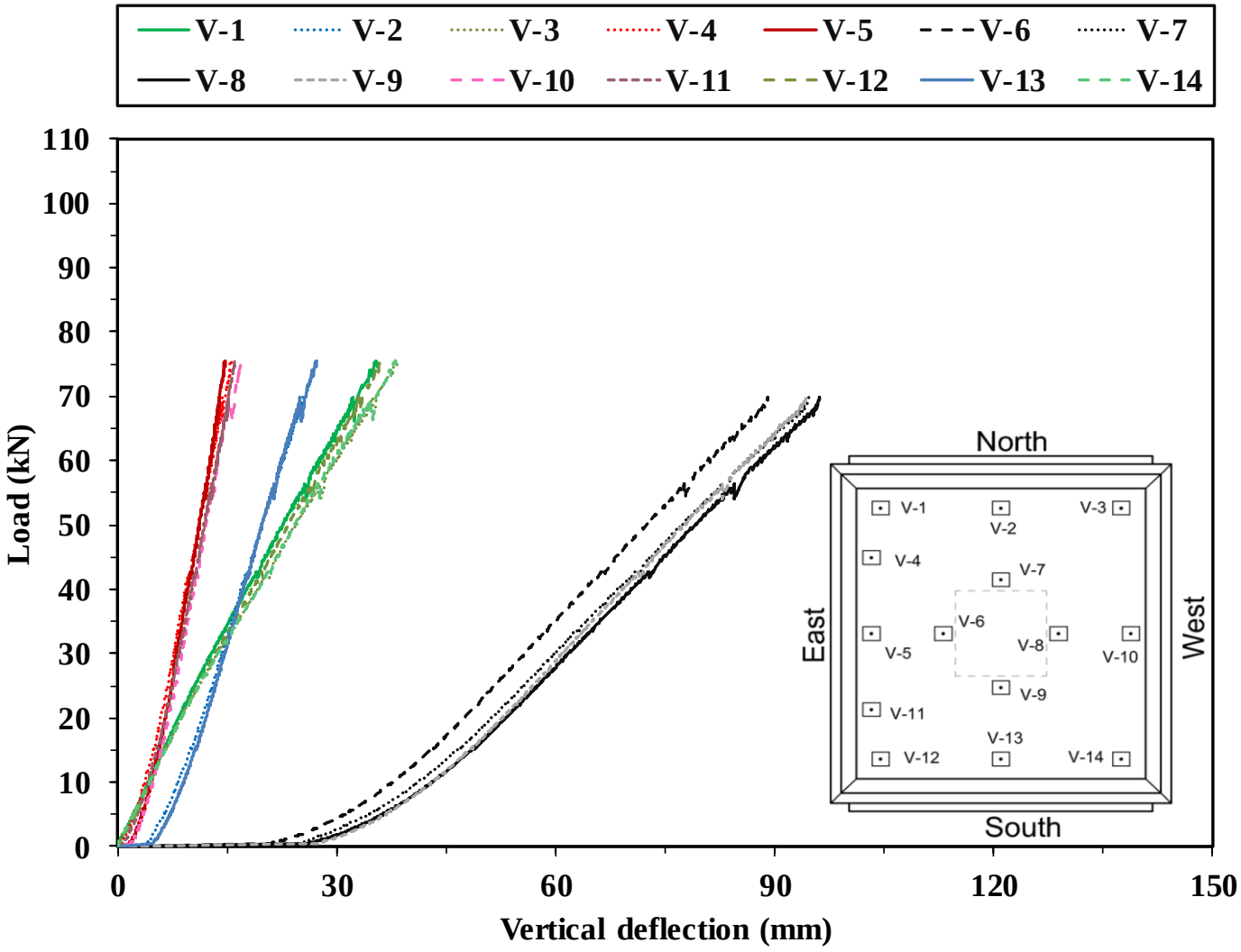

Figure 5.17: LVDT profile for welded DMS

The reaction force from the load cells installed at all the corners of the welded DMS is shown in Figure 5.18. Figure 5.18a displays the plot of the reaction force versus time during the test. The reaction force is observed to be increasing with the increase in the actuator load throughout the test. A bar chart for the reaction force in each load cell during the first yield of the aluminum panel is shown in Figure 5.18b. At the first yield of the aluminum panel, the highest reaction force of 8.36 kN is detected in LC-1, and the lowest reaction force of 5.96 kN is noted in LC-3. Figure 5.18c illustrates an additional bar chart of the reaction force at the weld failure with the maximum reaction force of 39.72 kN in LC-1 and the minimum reaction force of 35.50 kN in LC-4. Again, the failure of the welded DMS was observed due to rupture of the frame at the south-west corner (LC-4) because the reaction force recorded by LC-4 at the south-west corner was lower than the load recorded by LC-1, LC-2, and LC-3 at other corner locations.

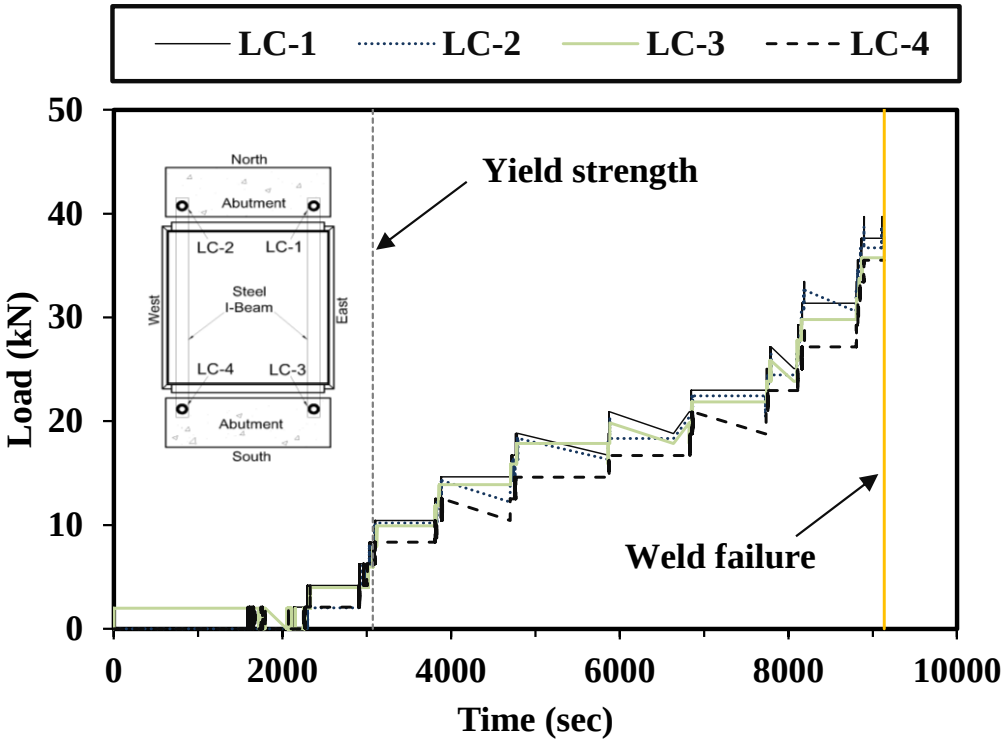
LC-1
LC-2
LC-3
LC-4
Load (kN)
Time (sec)
Yield strength
Weld failure
North
Abutment
LC-2
LC-1
Steel
I-Beam
West
East
LC-4
LC-3
Abutment
South

(a)

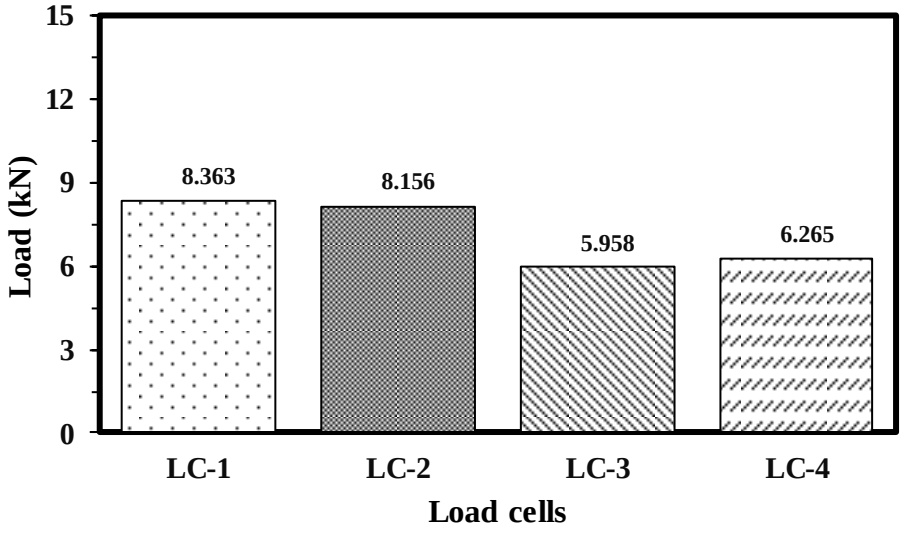
Load (kN)
8.363
8.156
5.958
6.265
LC-1
LC-2
LC-3
LC-4
Load cells

(b)

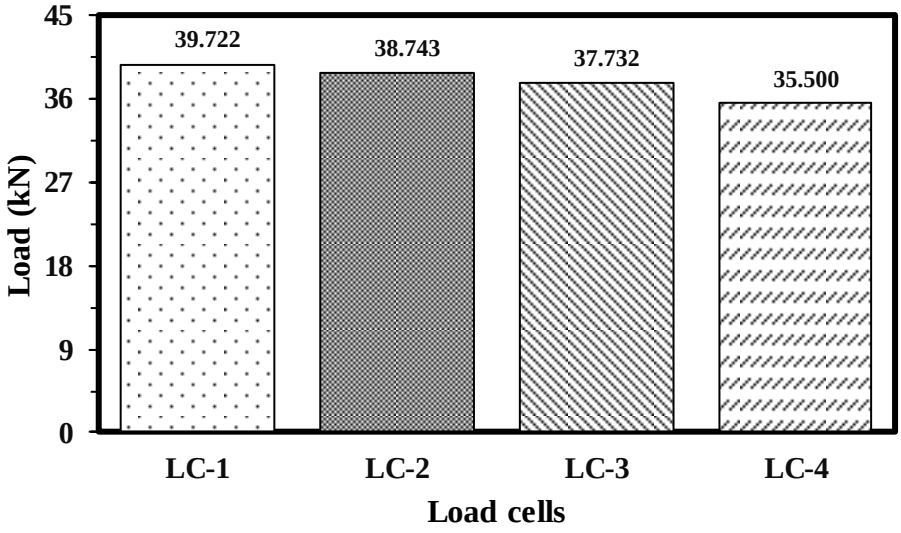

(c)

Figure 5.18: Reaction force from load cells for welded DMS: (a) load vs time, (b) at 1st yield, and (c) at weld failure

5.4.1.3 COMPARISON IN STRENGTH BETWEEN ADHESIVE AND WELDED DMSs

Figure 5.19 presents the comparative illustration of load displacement curve between adhesive and welded DMS. Adhesive DMS resisted an actuator load of 123.41 kN when center-line deflection was 133.35mm, whereas welded DMS resisted an actuator load up to 153.46 kN with center-line deflection of 158.57 mm. Load resisting capacity of the welded DMS was found to be 24% higher than the adhesive DMS. Deflection in the welded DMS was also observed to be 19% greater than in the adhesive DMS. Results from the load-displacement curve revealed higher strength of the welded DMS compared to adhesive DMS as expected. The damage states in the adhesive DMS were also found to be observed at the lower load than the failure modes in the welded DMS. From the load-displacement curve shown in this figure, it can be clearly observed that welded

DMS resisted higher strength than the adhesive DMS when compared with respect to equivalent identical centerline-deflection in the DMSs.

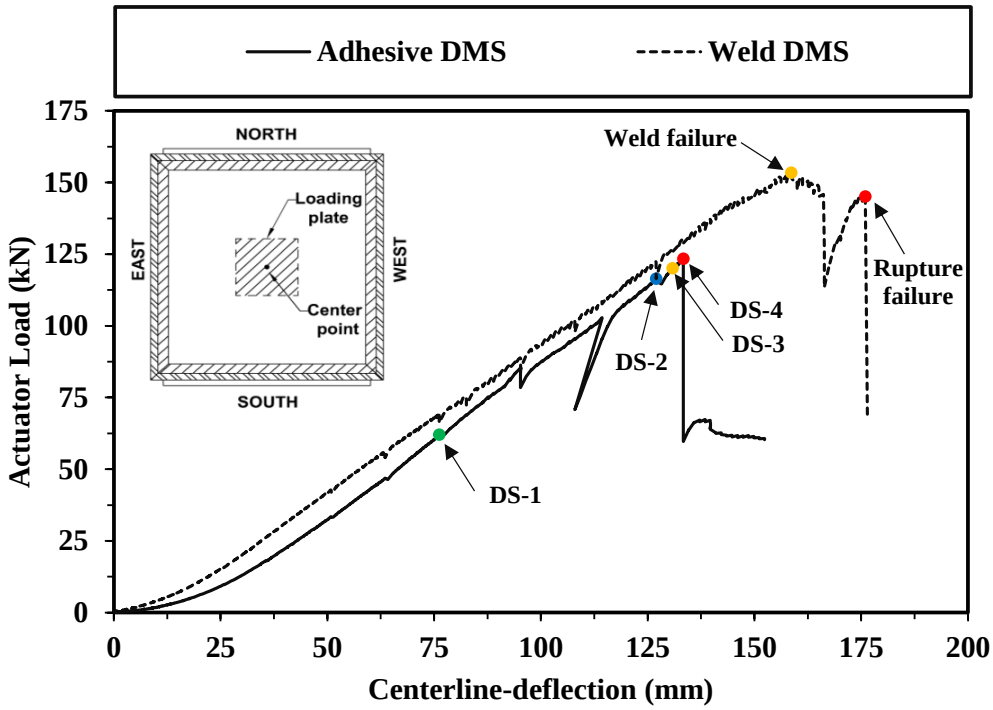

Figure 5.19: Comparison of load-displacement curve for both adhesive and welded DMS

The maximum deflections recorded by LVDTs at different locations during the ultimate strength test of the adhesive and welded DMSs are compared, and the comparison of the vertical deflections is further depicted in a bar chart showing the percent difference in Figure 5.20. It is observed that the deflection near the center of the adhesive DMS is higher (up to 8% for V-9) compared to the welded DMS. All other LVDTs excluding the LVDTs installed at the center observed lower deflections in the welded DMS than the adhesive DMS. The percent difference was found to be the least for V-4 with a 31% lower deflection in the welded DMS than the adhesive DMS. Debonding of adhesive was observed at east and north edge of the adhesive DMS at the

north-east corner. Debonding of adhesive at the north-east corner caused the slippage of aluminum panel from the original position which further increased deflection of the aluminum panel at the center. Therefore, deflections of aluminum panel recorded from LVDTs near the center was found to be greater in the adhesive DMS than in the welded DMS, although deflections at other locations were observed to have opposite phenomena. The maximum strains in both tension and compression are compared along with the percent difference. The comparison of peak strains in tension field between the adhesive and welded DMSs is also presented in

Figure 5.21. The welded DMS observed higher strain values in 15 strain gauge locations with a maximum percent difference of 240% for SG-10 located on the east side of the DMS. 6 strain gauges observed lower value of strains in the welded DMS than the adhesive DMS with a peak decrement of 100% for SG-7 installed at the north-west corner and SG-22 installed at the south end of the DMS. These results suggest that during the ultimate strength test, the elongation of the aluminum panel in the welded DMS was higher than in the adhesive DMS. Figure 5.22 displays the comparison of peak strains in compression between the adhesive and welded DMSs. The welded DMS observed higher strain values in 13 strain gauge locations with the maximum percent difference of 454% for SG-6 installed at the north-west corner in the longitudinal direction. 8 strain gauges in the welded DMS observed lower strain values compared to that of the adhesive DMS with the percent difference of 100%, which is observed in SG-7 installed at the north-west corner and SG-21 located at the south end of DMS. Percent difference values shown in Figure 5.22 also indicate that the compression of the aluminum panel observed in the welded DMS is significantly higher than the compression in the adhesive DMS. Tensile

and compression strains in the welded DMS are found to be significantly higher than in the adhesive DMS as the welded DMS resisted the higher load than the adhesive DMS during the ultimate strength test.

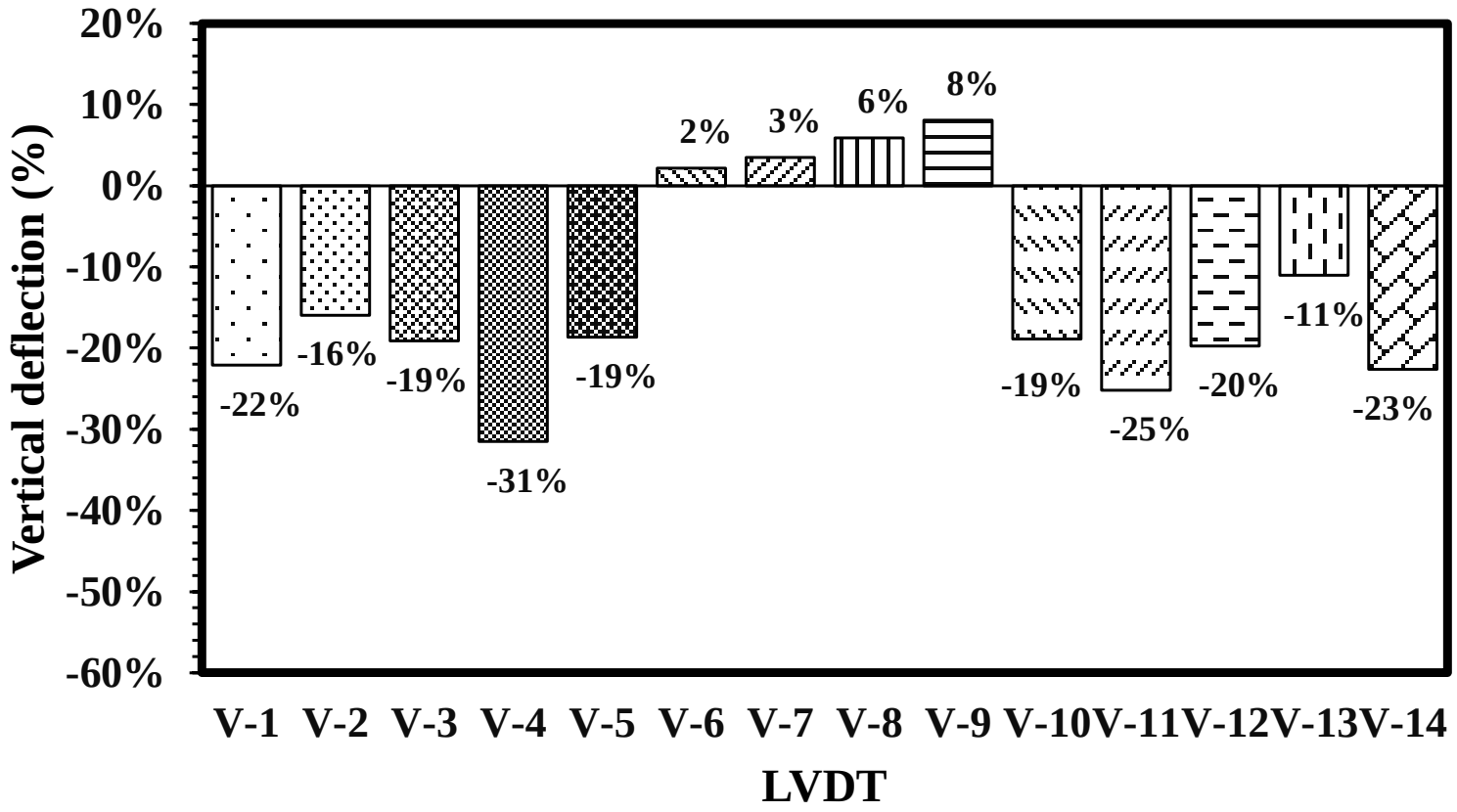

Figure 5.20: Percent difference in vertical deflection between adhesive and welded DMSs

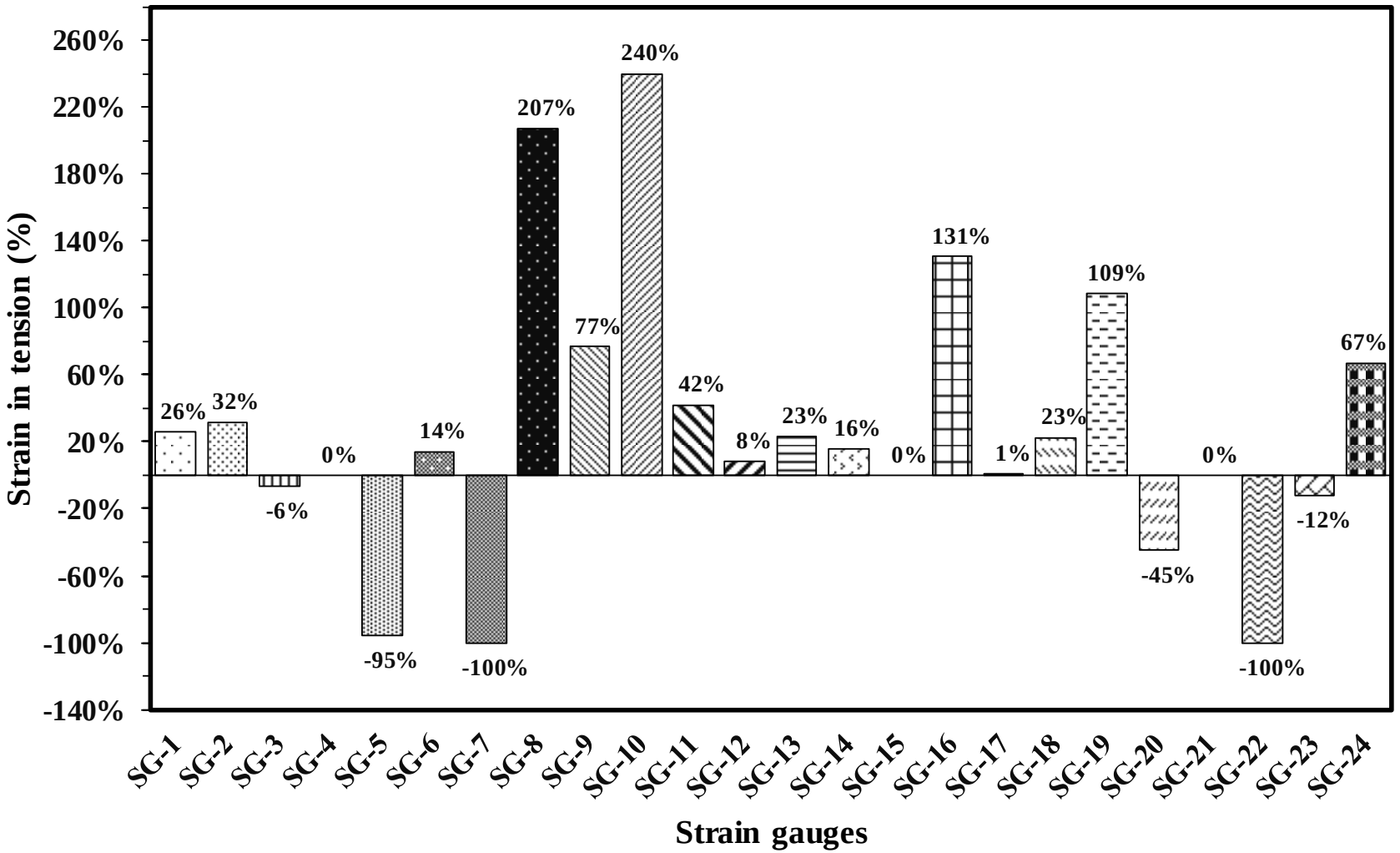

Figure 5.21: Percent difference between adhesive and welded DMSs for peak strains in tension

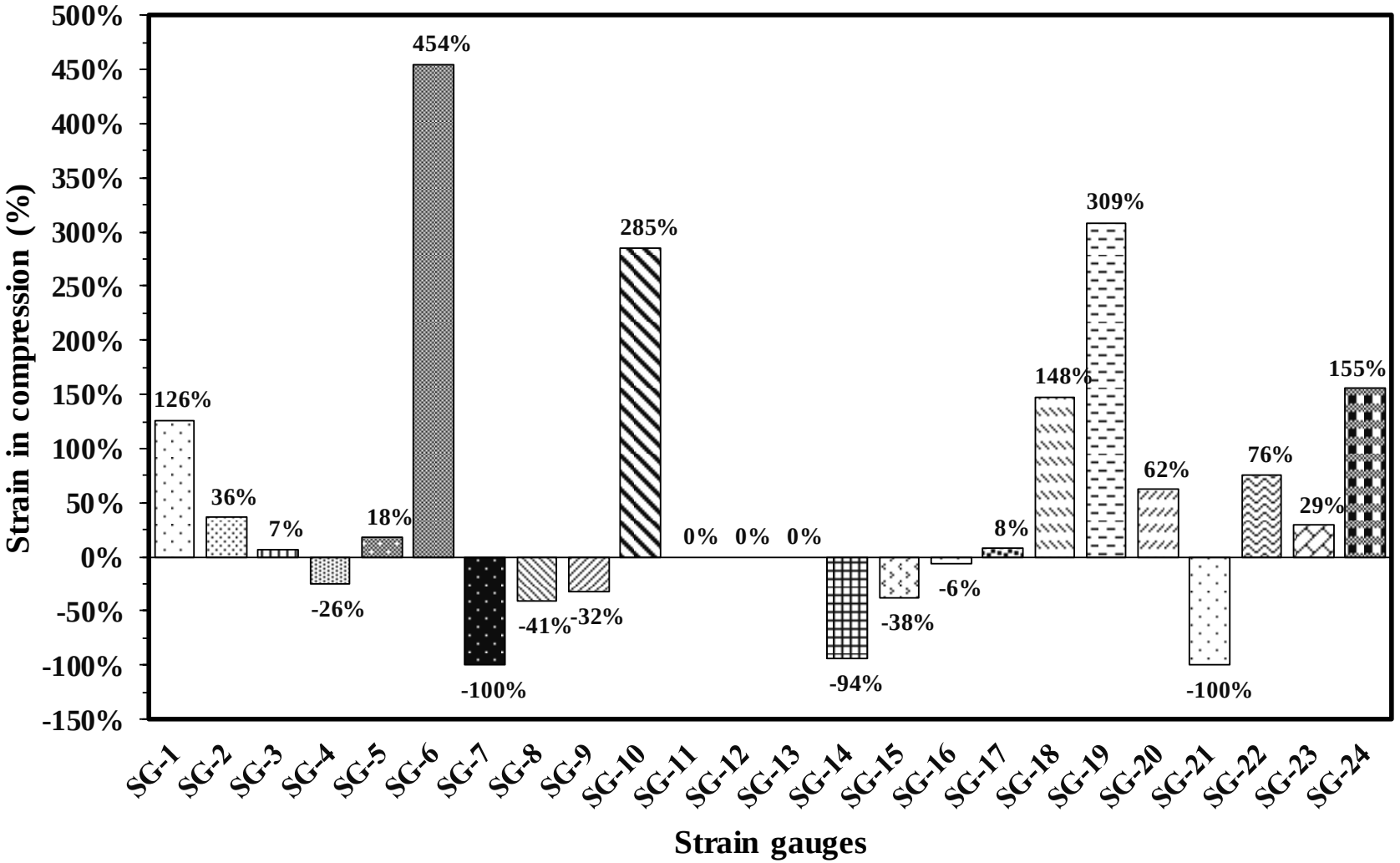

Figure 5.22: Percent difference between adhesive and welded DMSs for peak strains in compression

5.4.2 FATIGUE TESTING DATA

5.4.2.1 ADHESIVE DMS

Figure 5.23 shows the representative strain profiles for the fatigue load test of the adhesive DMS plotted against the number of cycles. The strain profile of strain gauges installed on the north and west end of the DMS is presented in Figure 5.23a and b respectively. The strains observed in all gauge locations in the DMS during the cyclic loading is significantly less than the aluminum yield strain of 2745.4 $\mu\varepsilon$. At the north end of the adhesive DMS, SG-3 is observed to be under tensile strain, whereas SG-4 and SG-5 are observed under tensile and compression cycles of strains (see Figure 5.23a). Two strain gauges (SG-9 and SG-17) installed near the west end of the DMS are under tensile and compression cycles of strains with the other strain gauge (SG-15) being completely in compression. The strain profiles of the strain gauges installed at the corners in the longitudinal and transverse directions are presented in Figure 5.23c and d, respectively. In the longitudinal direction, all the strain gauges experienced both tensile and compression strains except for SG-2, which is under tension during the test (see Figure 5.23c). In the transverse direction, two strain gauges are found to be under tension (SG-18 and SG-24) with the other two strain gauges under compression (SG-1 and SG-7). Strains recorded from the gauges installed near the center are plotted against the number of fatigue load cycles which is shown in Figure 5.23e. SG-11 and SG-14 observed both tensile and compression strains while SG 13 experienced tensile strain only, and finally, SG-12 was under compression throughout the fatigue test. The results from the strain profiles from the fatigue test suggest that the design fatigue load from the AASHTO Specifications (AASHTO 2015) is safer than expected for 500,000 cyclic loads since

strains observed in the aluminum panel are substantially less than the yield strain of the aluminum.

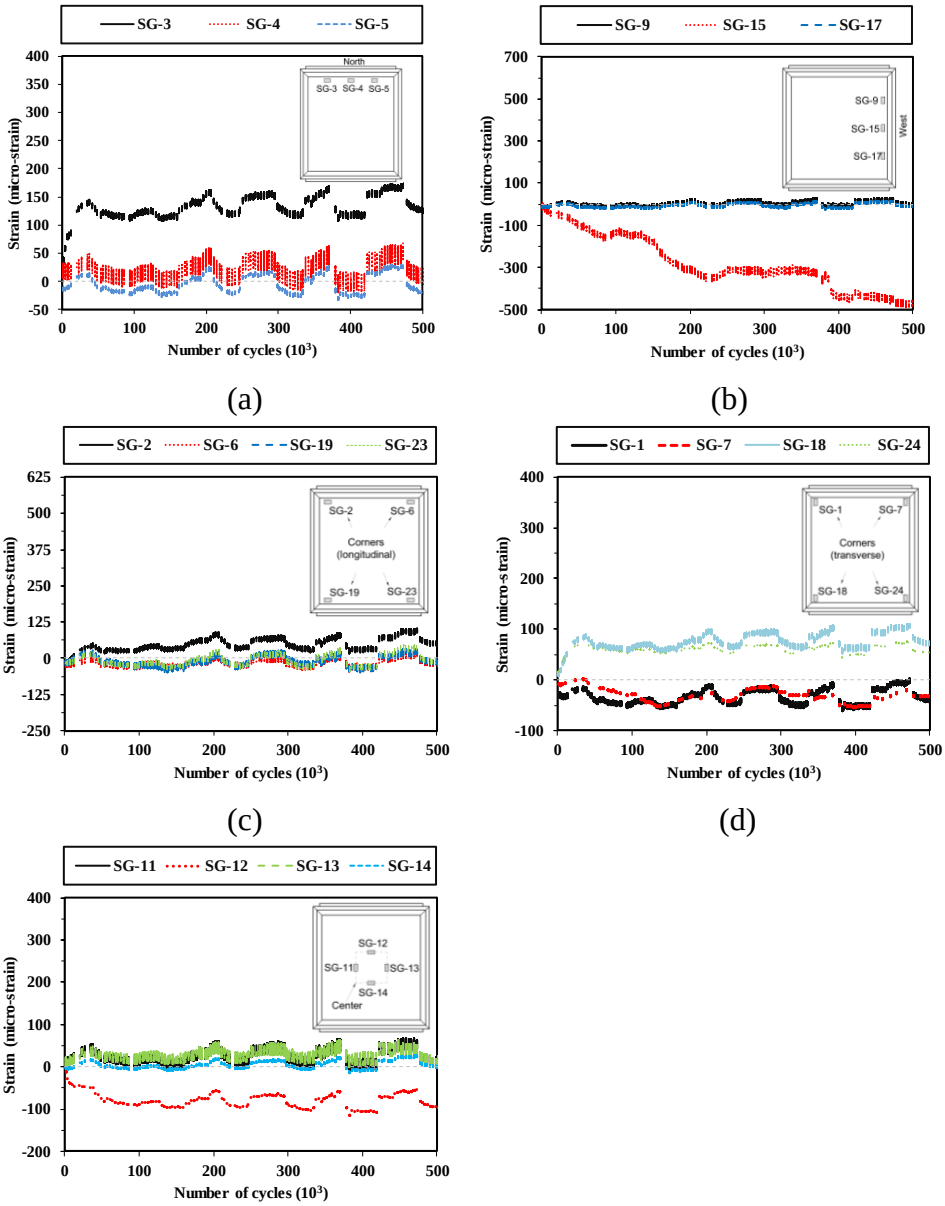

Figure 5.23: Strain profile for adhesive DMS from fatigue load test at: (a) north end, (b) west end, (c) corners in the longitudinal direction, (d) corners in the transverse direction and (e) center

Figure 5.24 presents the plot of the maximum stress range (observed in each strain gauge locations) with a S-N curve of 5052-H32 aluminum. The stress range plotted in the

figure represents the stress range observed in the aluminum back-skin at different locations of the strain gauges during the test. The S-N curve for the aluminum panel was generated utilizing the properties (ultimate tensile strength and fatigue strength) of the 5052 aluminum material (Aluminum Association 2010). The highest maximum stress range is observed for SG-10 (located at the east end) at around 316,000 cycles of fatigue load, whereas the maximum stress range is the least for SG-7 (located at north-east corner) at around 323,500 cycles of fatigue load. The stress ranges observed during the test of the adhesive DMS are not over the fatigue threshold of the aluminum panel. It can be thus concluded that the adhesive DMS is adequate for 500,000 cycles of the considered design fatigue load.

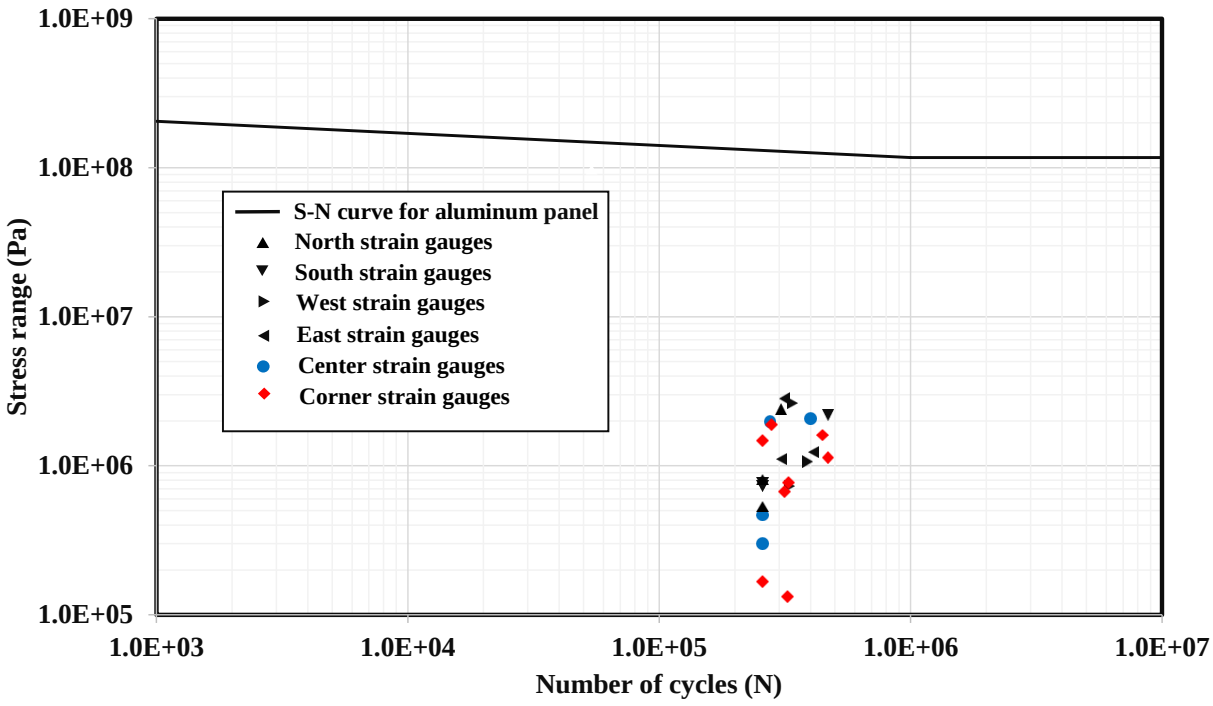

Figure 5.24: Fatigue performance of adhesive DMS with maximum stress range

The performance of the adhesive DMS during the test with respect to deflection is shown in Figure 5.25. The deflection ranges for the LVDTs located near the center of the DMS are observed significantly higher than the deflection ranges observed in the other locations. The maximum deflection range is the highest for LVDT V-8 (center) at around 469,500 cycles and is the lowest for LVDT V-12 (south end) at around 418,700 cycles of fatigue load. This indicates that the DMS is subjected to higher vibrations near the center than the other locations when encountered with cyclic wind loads. Note, no sign of damage was observed in the adhesively bonded region of the DMS as well as in all the other parts of the DMS.

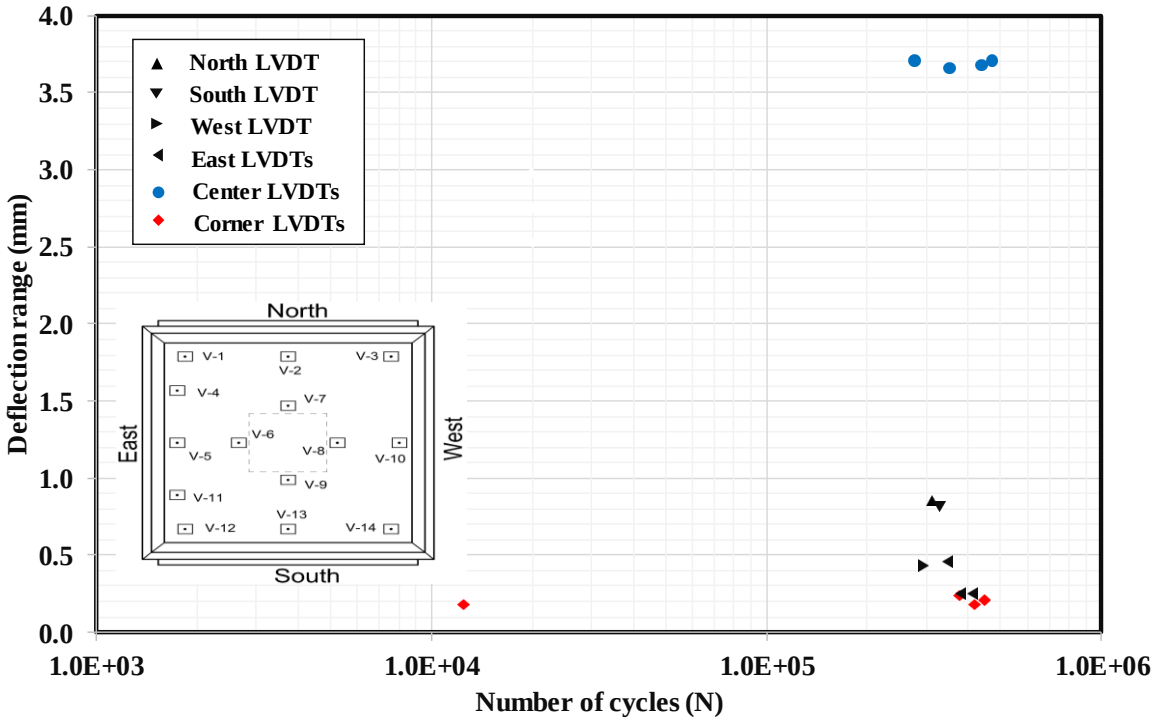

Figure 5.25: Fatigue performance of adhesive DMS with maximum deflection range at LVDT locations

5.4.2.2 WELDED DMS

Figure 5.26 shows the representative strain profiles for the fatigue load test of the welded DMS plotted against the number of cycles. The strain profiles of the gauges installed on the north and west end of the welded DMS are presented in Figure 5.26a and b, respectively. Strains observed in all gauge locations in the DMS during the cyclic loading is substantially less than the aluminum yield strain. At the north end of the welded DMS, SG-3 and SG-5 are observed to be under compression strain, whereas SG-4 is observed to be under tensile and compression cycles of strains (see Figure 5.26a). Two strain gauges (SG-9 and SG-15) installed near the west end of the DMS are completely under compression strains with the other strain gauge (SG-17) being under tensile and compression cycles. The strain profile of the strain gauges installed at the corners in longitudinal and transverse directions is presented in Figure 5.26c and d respectively. In longitudinal direction, all the strain gauges are observed to be under compression except for SG-2 which is under compression initially, however, SG-2 is found to be under tension at the end of the test (see Figure 5.26c). In transverse direction, all the strain gauges are found to be under compression (SG-1, SG-7, and SG-18) except for SG-24 which is observed to be under both tension and compression. Strains recorded from the strain gauges installed near the center are plotted against the number of fatigue load cycles and shown in Figure 5.26e. SG-12 and SG-13 observed both tensile and compression strains, whereas SG 11 and SG-14 were under compression only throughout the fatigue test. The strain profiles from the fatigue load test of the welded DMS suggest that the design fatigue load from AASHTO (2015) is safer than expected for 500,000

cyclic loads since strains observed in the aluminum panel are significantly less than the yield strain of the aluminum.

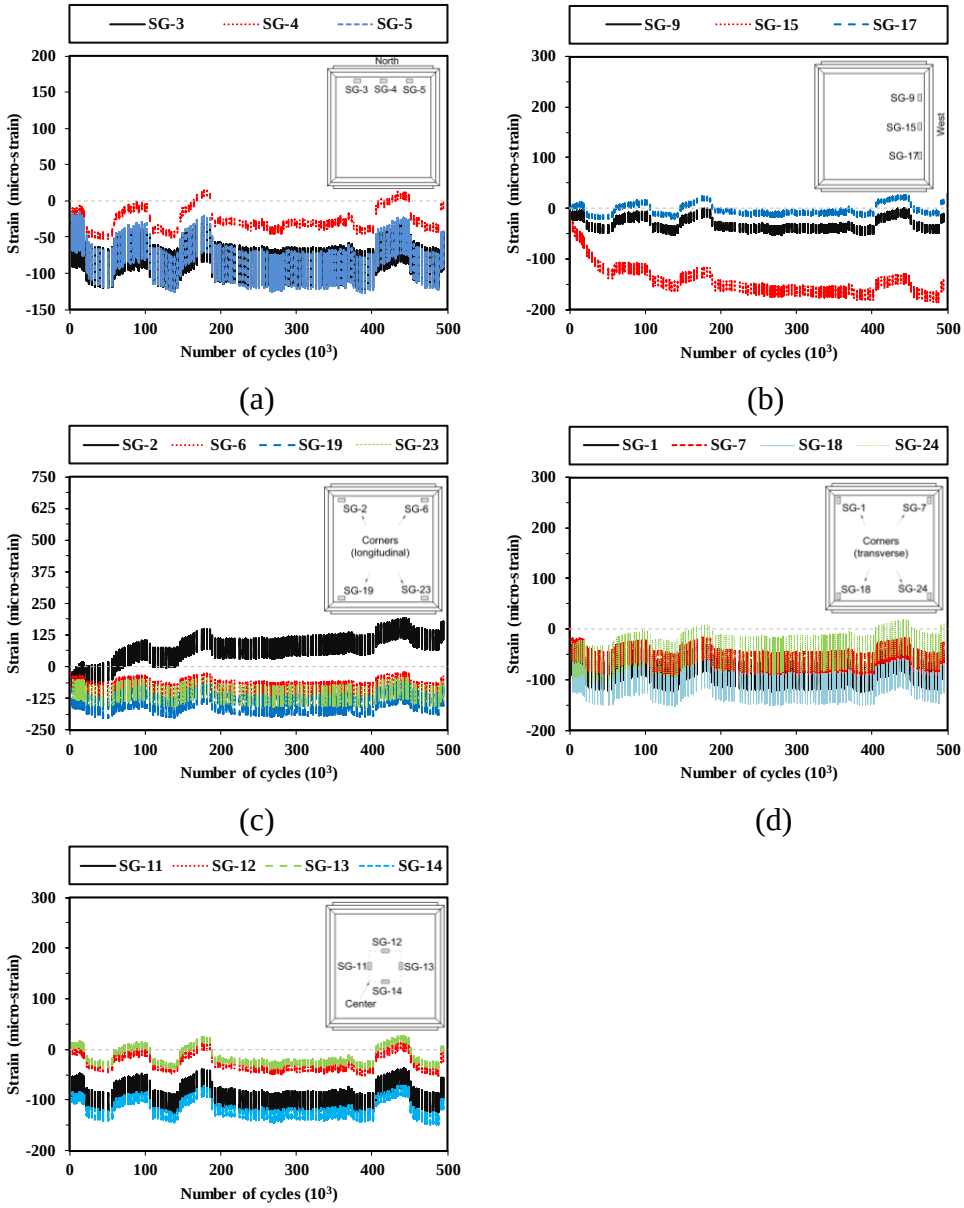

Figure 5.26: Strain profile for welded DMS from fatigue load test at: (a) north end, (b) west end, (c) corners in the longitudinal direction, (d) corners in the transverse direction and (e) center

The plot of maximum stress range (observed in each strain gauge locations) in the welded DMS with the S-N curve of 5052-H32 aluminum is shown in Figure 5.27. The highest maximum stress range is observed for SG-23 (located at the south end) at around 444,600 cycles of fatigue load, whereas the maximum stress range is the least for SG-17 (located at west end) at around 17,700 cycles of fatigue load. The stress ranges observed during the fatigue test of welded DMS are also below the fatigue threshold of aluminum panel. The results from the plot indicate the welded DMS is also reliable for 500,000 cycles of design fatigue wind load.

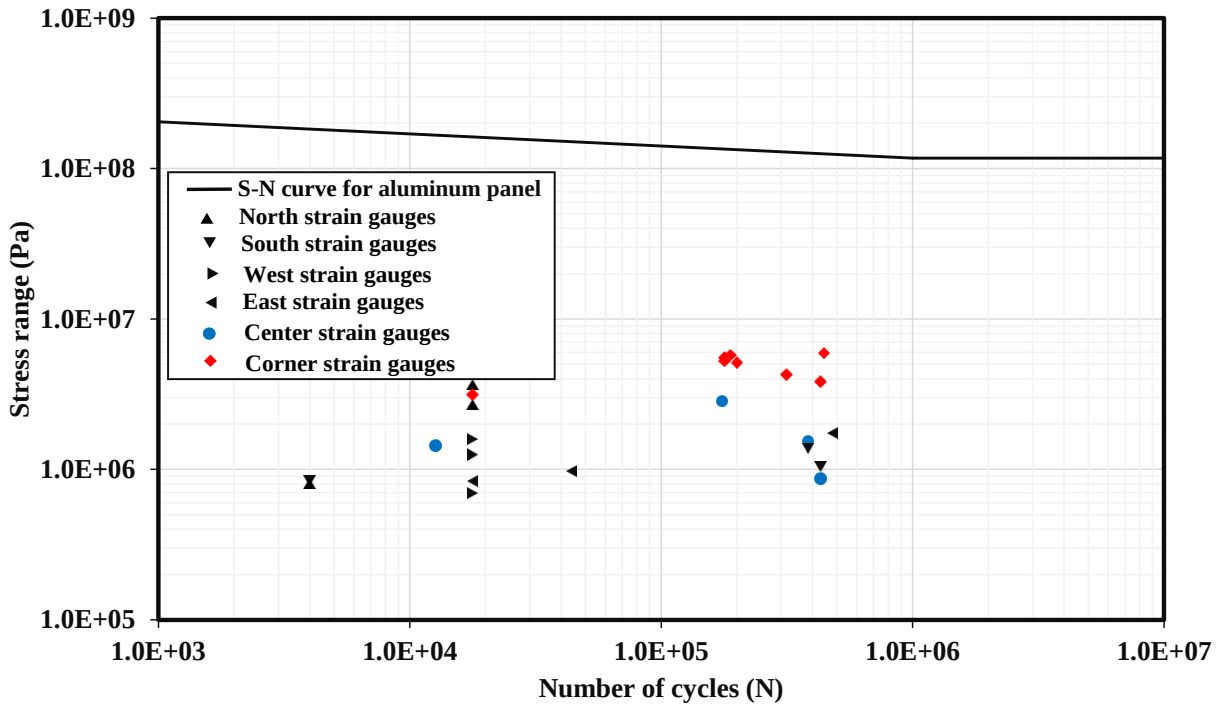

Figure 5.27: Fatigue performance of welded DMS with maximum stress range

The performance of the welded DMS for deflection criteria with respect to the fatigue load test is shown in Figure 5.28. A higher range of deflection for the LVDTs located near the center of the DMS is observed when compared with the deflection ranges observed in the other locations. The maximum deflection range is the highest for LVDT

V-6 (center) at around 22,300 cycles and is the least for LVDT V-13 (south end) at around 217,900 cycles of fatigue load. Based on the results of the deflection range, a higher vibration of aluminum panel of the welded DMS is expected near the center than in the other locations.

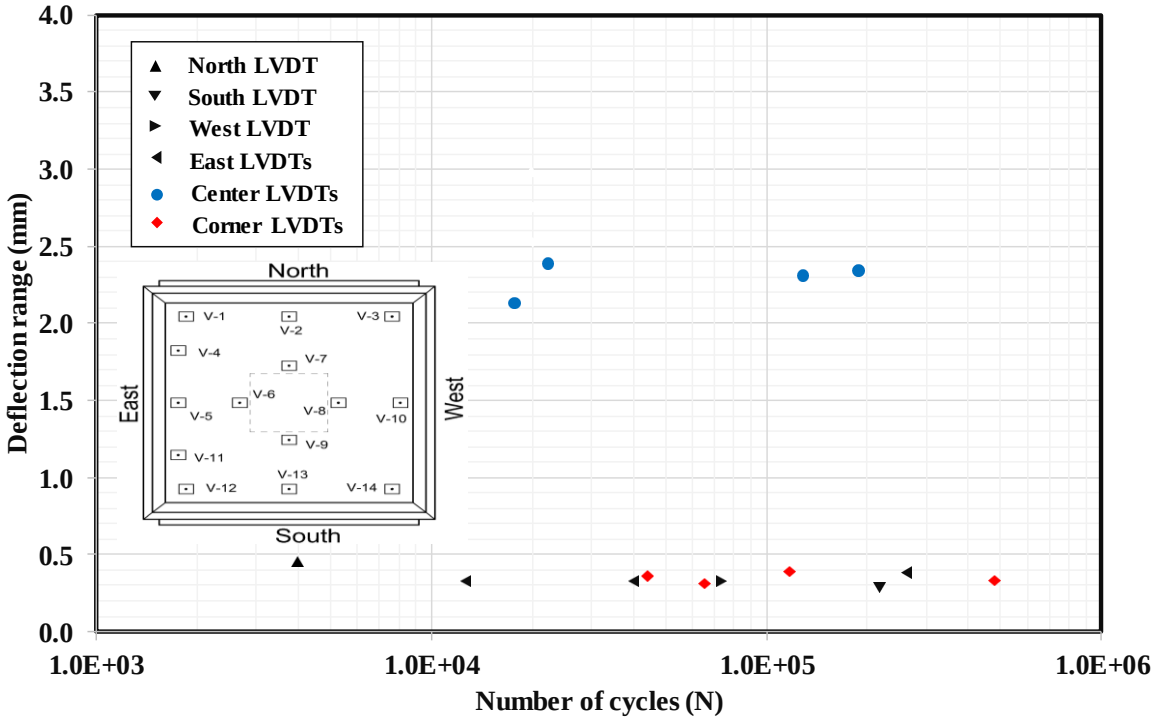

Figure 5.28: Fatigue performance of welded DMS with maximum deflection range at LVDT locations

As did in the adhesive DMS, the welded DMS did not show any type of damage in the weld as well as the other parts such as the aluminum back skin and panel. The results indicate that welded connections in DMS are appropriate with respect to fatigue wind load cycles.

5.5 CONCLUSIONS

The structural behavior of aluminium dynamic message signs (DMSs) was investigated through the ultimate strength and fatigue load testings. The ultimate strength

testing was performed on one DMS with adhesive joints and one with typical welded connections, and the fatigue testing was also performed on one DMS with adhesive joints and one with welded connections. The ultimate strength testings were performed with a monotonic load until failure, and the fatigue load testings were carried out with the application of wind-gust-based design fatigue load from the AASHTO (2015) for 500,000 cycles. Load, deflection, and strain responses were recorded for each test and analysed in depth. Based on the results from each of the tests, the following conclusions can be drawn.

1. The ultimate strength testing revealed that four different damage states through DS-1 through DS-4 were identified for the adhesive DMS of which DS-2 due to signficiant propagation of adhesive debonding was found to be utmost crucial damage state, whereas welded DMS failed with two failure modes. In the testing, the strains at the corner location of the adhesive DMS and the welded DMS were found to surpass the yield strain of the aluminum DMS panel, indicating high tensile strength at its corners. From the testing, the measured strains near the damage locations observed the highest strains in adhesive as well as in welded DMS and the strength of the adhesive DMS was found to be 24% higher than the welded DMS.

2. For the ultimate strength testing, the maximum deflection near the center of the welded DMS (V-6, V7, V8, and V9) was higher up to 8% than the adhesive DMS. The maximum deflection in the boundary and corner locations of the welded DMS (V-1 through V-5 and V-10 through V-14), however, was lower up to 31% than the adhesive DMS. The ultimate strength testing demonstrated that the maximum strain in the tension sof the welded DMS was up to 240% higher than that of the adhesive DMS, and the

maximum strain in compression of the welded DMS was up to 454% higher compared to the adhesive DMS.

3. In the fatigue strength testing, the maximum stress ranges observed in both the adhesive and welded DMSs were below the fatigue threshold of aluminum panel for 500,000 cycles according to the S-N curves. From the testing, the maximum deflection range was found to be highest near the center for both adhesive (V-8) and welded (V-6) DMSs. The results indicated that the DMSs were exposed to higher vibrations near the center than the corner or bourndary locations when encountered with the fatigue loads.

5.6 REFERENCES

AASHTO. (2015). LRFD Specifications for Structural Supports for Highway Signs, Luminaires, and Traffic Signals.

Abdel Wahab, M. M. (2012). Fatigue in adhesively bonded joints: a review. *ISRN Materials Science*, *2012*.

Agarwal, A., Foster, S. J., Hamed, E., & Ng, T. S. (2014). Influence of freeze–thaw cycling on the bond strength of steel–FRP lap joints. *Composites Part B: Engineering*, *60*, 178-185.

Alfano, M., Furgiuele, F., Lubineau, G., & Paulino, G. H. (2011). Simulation of debonding in Al/epoxy T-peel joints using a potential-based cohesive zone model. *Procedia Engineering*, *10*, 1760-1765.

Aluminum Association. (2010). *2010 Edition of Aluminum Design Manual*. Washington, D.C.

Amatya, I., Seo, J., & Letcher, T. (2020b). Peel and cleavage strength tests with adhesive connections in dynamic message signs. *International Journal of Adhesion and Adhesives, In Review.*

Amatya, I., Seo, J., Letcher, T., & Bierschbach, D. (2020a). Tensile and shear strength tests with adhesive connections in dynamic message signs. *Mechanics of Materials, In Review.*

Arabi, S., Shafei, B., & Phares, B. M. (2018). Fatigue analysis of sign-support structures during transportation under road-induced excitations. *Engineering Structures*, *164*, 305-315.

ASTM D1062-08. (2008). Standard test method for cleavage strength of metal-to-metal adhesive bonds. West Conshohocken: American Society of Testing and Materials.

ASTM D1876-08. (2008). Standard test method for peel resistance of adhesives (T-peel test). West Conshohocken: American Society of Testing and Materials.

AZEEZ, A. A. (2013). Fatigue failure and testing methods. *Häme University of Applied Sciences*.

Bolton, R. W., Phares, B., & Wipf, T. J. (2011). Response Measurements of DMS Cabinets and Supporting Truss Structures under Environmental and Transient Wind Loads. In *Linking Models and Experiments, Volume 2* (pp. 411-416). Springer, New York, NY.

Broughton, W. R., Mera, R. D., & Hinopoulos, G. (1999). Creep Testing of Adhesive Joints T-Peel Test. *NPL Report CMMT (A)*, *193*.

Campilho, R. D. S. G., Pinto, A. M. G., Banea, M. D., & da Silva, L. F. (2012). Optimization study of hybrid spot-welded/bonded single-lap joints. *International Journal of Adhesion and Adhesives*, *37*, 86-95.

Chang, B., Phares, B. M., Zou, H., & Couch, T. (2014). Thermal analysis of highway overhead support structures. *Transportation Research Record*, *2406*(1), 32-41.

Connor, R. J., & Altstadt, S. (2013). After-Fracture Reserve Strength of Two Four-Chord Aluminum Sign Trusses. *Journal of Structural Engineering*, *140*(1), 04013030.

Da Silva, L. F., Carbas, R. J. C., Critchlow, G. W., Figueiredo, M. A. V., & Brown, K. (2009). Effect of material, geometry, surface treatment and environment on the shear strength of single lap joints. *International Journal of Adhesion and Adhesives*, *29*(6), 621-632.

Da Silva, L., El-Sharif, M., Chisholm, C., & Laidlaw, S. A Novel Adaptation of the T-Peel Bimetal Bond Test based on the Thin Film Bonding Theory Using Cold Roll Bonded AlSn/Steel Bimetal Laminates.

De Freitas, S. T., & Sinke, J. (2014). Adhesion properties of bonded composite-to-aluminium joints using peel tests. *The Journal of Adhesion*, *90*(5-6), 511-525.

Fouad, F. H., & Calvert, E. (2005). Design of cantilevered overhead sign supports. *Transportation research record*, *1928*(1), 39-47.

Goglio, L., & Rezaei, M. (2014). Variations in mechanical properties of an epoxy adhesive on exposure to warm moisture. *Journal of Adhesion Science and Technology*, *28*(14-15), 1394-1404.

Hamilton III, H. R., Riggs, G. S., & Puckett, J. A. (2000). Increased damping in cantilevered traffic signal structures. *Journal of Structural Engineering*, *126*(4), 530-537.

Hosch, I. E., & Fouad, F. H. (2009). Fatigue design of sign support structures for loading caused by natural wind loads. *Transportation research record*, *2131*(1), 15-22.

Huckelbridge Jr, A. A., & Metzger, A. T. (2009). Investigation of the Dayton, Ohio, IR 75 sign truss failure of September 11, 2006. *Journal of Performance of Constructed Facilities*, *23*(5), 372-378.

Kim, K. S., & Aravas, N. (1988). Elastoplastic analysis of the peel test. *International Journal of Solids and Structures*, *24*(4), 417-435.

Kim, Y. J., Hossain, M., & Yoshitake, I. (2012). Cold region durability of a two-part epoxy adhesive in double-lap shear joints: Experiment and model development. *Construction and Building Materials*, *36*, 295-304.

LORD Corporation. (2018). LORD® 406 Acrylic Adhesive. Retrieved November 29, 2018, from https://www.lord.com/products-and-solutions/adhesives/lord-406-acrylic-adhesive.

Noori, H., Jain, M., Nielsen, K., & Brandys, F. (2016). Effect of Deformation-induced Residual Stress on Peel Strength of Polymer Laminated Sheet Metal. *The Journal of Adhesion*, *92*(10), 862-876.

Park, J. S., & Stallings, J. M. (2006). Fatigue evaluations of variable message sign structures based on AASHTO specifications. *KSCE Journal of Civil Engineering*, *10*(3), 207-217.

Puckett, J. A., Erikson, R. G., & Peiffer, J. P. (2010). Fatigue testing of stiffened traffic signal structures. *Journal of Structural Engineering*, *136*(10), 1205-1214.

Savvilotidou, M., Vassilopoulos, A. P., Frigione, M., & Keller, T. (2017). Development of physical and mechanical properties of a cold-curing structural adhesive in a wet bridge environment. *Construction and Building Materials*, *144*, 115-124.

Schijve, J. (2001). *Fatigue of structures and materials*. Springer Science & Business Media.

Silva, P., Fernandes, P., Sena-Cruz, J., Xavier, J., Castro, F., Soares, D., & Carneiro, V. (2016). Effects of different environmental conditions on the mechanical characteristics of a structural epoxy. *Composites Part B: Engineering*, *88*, 55-63.

Sousa, J. M., Correia, J. R., & Cabral-Fonseca, S. (2018). Durability of an epoxy adhesive used in civil structural applications. *Construction and Building Materials*, *161*, 618-633.

Zheng, X. L., Zhang, M. S., You, M., Yu, H. Z., & Li, Z. (2007). A Study on Normal Stress Distribution and Failure of Adhesively Bonded Joint under Cleavage Loading. In *Key Engineering Materials* (Vol. 348, pp. 949-952). Trans Tech Publications.